Space Sciences Laboratory
University of California
Berkeley, California

STUDY OF DETONATION OF MIXTURES OF GASEOUS HYDROGEN AND GASEOUS OXYGEN

by

A. J. Laderman

A. K. Oppenheim
Faculty Investigator

Final Report on Contract NAS8-2634
Covering the Period from
June 1, 1962 to February 18, 1965

Series No. 6
Issue No. 11

April 1965

ACKNOWLEDGMENT

This report was prepared by Propulsion Dynamics Laboratory of the University of California under Contract No. NAS8-2634, "Study of Detonation of Mixtures of Gaseous Hydrogen and Gaseous Oxygen," for the George C. Marshall Space Flight Center of the National Aeronautics and Space Administration. The work was administered under the direction of the Propulsion and Vehicle Engineering Division, Engineering Materials Branch of the George C. Marshall Space Flight Center with Dr. J. B. Gayle, Mr. C. H. Blakewood, and Mr. Harold Perkins acting as project engineers.

Special acknowledgment is due for the success of this work to the numerous contributions of the Staff of the Propulsion Dynamics Laboratory; in particular to Drs. P. A. Urtiew and G. T. Williams, and to Messrs. C. W. Busch, C. Jako, K. Jakus, L. S. Nawroczynski, MacKenzie Patterson, and G. B. Steel for their help in the design of the experimental apparatus and/or preparation of this report; to Messrs. K. Hom, W. T. Giba, and K. F. Voak for their assistance in the installation of the experimental apparatus and instrumentation; to Messrs. W. E. Amend, R. L. Panton, J. R. Peterson, W. G. Struck, A. C. Riggin, R. D. Wing, and H. Zaklad for their aid in carrying out the test program; and last, but by no means least, to Mrs. M. P. Perrault, without whose able administrative assistance the burden of the job would have been unmanageable.

TABLE OF CONTENTS

TABLES

1. INTRODUCTION

This report describes the work performed under Contract NAS8-2634 during the period from July 1, 1962 to February 18, 1965, and presents the results of the entire test program. Annual Report No. 1, covering the period from June 1, 1962 to June 30, 1963, described essentially the design and construction of experimental equipment and facilities and presented results of initial tests. At the risk of some repetition, this material has been included in the present report in order to provide a more definitive exposition of the subject matter.

Due to the possibility of venting or accidental leakage into interstage compartments, the use of liquid hydrogen and liquid oxygen as propellants for launch vehicles presents a potential explosive hazard. This hazard prevails both at the launch site and in subsequent flight in space and is amplified by the existence of a multitude of devices capable of initiating reaction, ranging from explosive actuators to lower energy sources, which are present during the normal course of operation.

The primary objective of this investigation was to determine the detonability of hydrogen-oxygen mixtures of various compositions, in vessels of size comparable to interstage compartments, under selected environmental conditions. In addition it was concerned with the study of the influence of the ignition source and of the geometry of the reaction chamber on the development and sustenance of detonation and with the detailed

observation of related effects, such as the wave velocity and pressure variation during the course of the combustion process. The results of this program, in addition to contributing toward a more thorough understanding of the influence of external effects on the detonation process, should be of significant value, not only in defining the hazards associated with the handling of hydrogen-oxygen mixtures, but also in the establishment of design criteria for launch vehicles using these substances as propellants.

Tests were performed in three detonation vessels with the following dimensions: 3 ft diam x 20 ft long, 2 ft diam x 20 ft long, and 2 ft diam x 40 ft long. Mixtures of $n\,H_2 + O_2$ (n = 1, 2, and 3) were used at initial pressures and temperatures ranging respectively from 0.1 to 760 mm Hg and -180 to +200°F.

Similar studies with fuel-air mixtures in large vessels have been carried out by Seamans and Wolfhard (1), who used a tube 54 cm in diam x 10 meters long, and Gerstein, et al. (2), who used a 2 ft diam x 300 ft long chamber. However, the former were concerned primarily with initial pressures greater than 1 atmosphere while the latter were interested in the ranging of initial pressures from 0.2 to 0.4 atmospheres and both investigations were restricted to mixtures at room temperatures.

It has been well established recently that the structure of detonation is characterized by a multiplicity of transverse shock wave interactions, whose effects become significant at low initial pressures of the reactive mixture. However, the classical Chapman-Jouguet hypothesis should be still valid for the bulk

average state behind an unconfined fully established, self-sustaining, detonation wave. Consequently, the C-J parameters, determined from a thermodynamic equilibrium analysis (3), were used for comparison with experiment.

The C-J hypothesis is in fact the only reasonable criterion for the identification of a truly detonative process and in the present investigation represents the most accurate means of establishing whether or not it has occurred. Only the relatively small length-to-diameter ratio of the vessels prevented a more definitive conclusion from being reached.

The experimental program was comprised of two distinct phases. The first, discussed in Section 3, was devoted primarily to determining steady detonation parameters, and made use of a high energy ignitor consisting essentially of a 2 inch length of 400 grain "Primacord"--a commercial detonating fuse. Depending on whether or not the reactive mixture could sustain a steady detonation wave, the Primacord explosion produced either an overdriven detonation wave or a strong shock wave whose velocity and pressure exceeded the theoretical Chapman-Jouguet properties. In both cases, then, the process was characterized by a wave front which decayed in strength along the length of the vessel, acquiring eventually a constant velocity in detonable mixtures or continuing to decelerate in mixtures unable to support a steady detonation. Test results are reported in the form of graphs showing variation of wave velocity and peak pressure as a function of distance from the ignitor. To allow maximum travel for the establishment of a steady wave, the wave properties observed

at the last position in the vessel are compared with the theoretical C-J parameters.

The second phase of the program, described in Section 4, was concerned with the use of weak ignitors and provided information on the detonability of hydrogen-oxygen mixtures in the absence of externally produced shock waves. In this case, however, shock waves were generated by the action of the accelerating flame itself. Observations were directed then toward examination of predetonative phenomena, including observation of the initial acceleration of the flame as it expanded to fill the cross-section of the vessel, the development of the precursor shock generated by the flame front, and the subsequent establishment of detonation, either behind the precursor shock or as a consequence of its reflection from the end wall of the vessel. Results, presented primarily in the form of space-time diagrams of the process, include information on flame velocity and precursor shock strength and on the limiting initial pressure below which detonation is initiated only by reflection of the precursor shock.

In both portions of the program the velocity and pressure measurements were supplemented, on several occasions, by streak Schlieren photographs. However, the photographic records were of limited assistance in interpreting the experimental data, since, for practical reasons, the field of view of the optical system was restricted to approximately one tube radius. Hence, observations of shock-flame interactions were obscured by the extent of the reaction zone, which, for deflagrations, was also

of the order of a tube radius.

In addition to the information contained here, the following technical notes have been issued during the duration of the program:

(1) Austin, A. L., "Dynamic Elastic Response of a Thin-walled Cylindrical Tube to an Axisymmetric Internal Transient Pressure," Tech. Note #1, June 1962.

(2) Laderman, A. J., Williams, G. T., and Peterson, J. R., "Analysis of Flame Ionization During the Development of Detonation," Tech. Note #2, September 1962.

(3) Laderman, A. J., and Urtiew, P. A., "Design of Gas Handling System," Tech. Note #3, October 1963.

(4) Laderman, A. J., Jako, Chris, and Panton, R. L., "Design of Vacuum Pump System for Detonation Vessels," Tech. Note #4, November 1962.

(5) Laderman, A. J., Struck, W. G., and Urtiew, P. A., "Design of Primacord Ignition System," Tech. Note #5, October 1963.

(6) Busch, C. W., and Laderman, A. J., "Computation of Gaseous Detonation Parameters," Tech. Note #6, August 1964.

(7) Struck, W. G., and Urtiew, P. A., "Analysis of the Spherical Flow Field Generated by a Solid Explosive," Tech. Note #8, August 1964.

(8) Wing, R. D., de Malherbe, M. C., and Laderman, A. J., "Investigation of Dynamic Stresses in Detonation Tubes," Tech. Note #7, August 1964.

(9) Amend, W. E., and Laderman, A. J., "Dynamic Performance of Pressure Transducers in Shock and Detonation Tubes," Tech. Note #9, September 1964.

2. DESCRIPTION OF THE EXPERIMENTAL APPARATUS

2.1. Detonation Vessels

2.1.1. Design

The dimensions of the three cylindrical detonation chambers were as follows:

(1) 2 ft diam x 20 ft long

(2) 2 ft diam x 40 ft long

(3) 3 ft diam x 20 ft long

The first of these vessels was made of type 304 stainless steel with provisions for temperature control from -180°F to 200°F. It had, in addition, a number of 4 inch diam optical observation ports extending along half its length to be used for Schlieren photography. The second chamber was obtained by adding to the stainless steel vessel a 20 ft long carbon steel extension. The third chamber was also made of carbon steel. All three vessels were fitted with a number of access ports of uniform dimensions for installation of instrumentation and other accessory equipment. The location of the vessels is shown in the laboratory floor plan, Figure 1.

The design of the vessels was based essentially on the magnitude of peak pressures observed during previous studies carried out in this laboratory. From these measurements it appeared that for a $2H_2 + O_2$ mixture, initially at 1 atmosphere and room temperature, a maximum pressure of 1250 psi, four times larger than the C-J pressure and slightly greater than the reflected detonation pressure, was attained during the development process,

prior to the establishment of the steady wave. An analysis of the dynamic response of the vessel to this pressure pulse (4) indicates that it is equivalent to a static pressure of 1000 psi, while the maximum static pressure produced by adiabatic constant volume combustion of the test mixture, which occurs for an initial temperature of -180°F, is 250 psia.

In order to reduce fabrication and material costs, minimum wall thicknesses were used: 1/2 inch and 3/4 inch, respectively, for the 2 and 3 ft diam carbon steel vessels, and 3/8 inch for the stainless steel cylinder. The maximum stresses associated with the 1000 psia static pressure were then 30,000 psi for the stainless steel and 24,000 psi for the carbon steel vessels. Comparing these values with the 30,000 and 25,000 psi yield stresses associated with type 304 stainless and mild carbon steel, respectively, the wall thicknesses appear marginal. However, since the maximum pressure for tests with initial pressures of 100 mm Hg and lower would not be expected to exceed 250 psia, the selected wall thicknesses provided adequate safety factors, with the possible exception of the 760 mm Hg initial pressure tests. The performance of the 1 atmosphere tests then was contingent on the information obtained from dynamic strain gauge measurements made at initial pressures intermediate to 100 and 760 mm Hg. It was planned to take safety precautions such as barricading the vessel and removing personnel from hazardous areas if strain measurements indicated that the yield condition was approached. As it turned out, this procedure was not necessary since maximum stresses did exceed the yield point.

The following designations are used to identify the vessels:

Vessel A	3 ft x 20 ft carbon steel
Vessel B	2 ft x 20 ft carbon steel
Vessel CD	2 ft x 20 ft stainless steel

Assembly drawings of the vessels reflecting the final design are shown in Figures 2, 3, and 4. Figures 5 and 6 show the completed vessels installed in the laboratory.

All vessels had instrumentation ports for both pressure transducers and ionization gauges located at 2 ft intervals along their length, as well as other access openings to the interior of the chamber. Furthermore, vessel CD was provided with 23 pairs of 4 inch window ports for Schlieren photography. These ports extended over a 10 ft section of the vessel so that observation of any portion of the process in the 20 ft section was possible by igniting the test mixture from the appropriate end of the vessel. When vessels B and CD are used together, the last 10 ft may also be observed, affording thus the opportunity to investigate by optical means three-quarters of the entire 40 ft length. To accommodate the windows, special design features had to be incorporated in order to avoid sharp discontinuities in the interior of the chamber. This was accomplished by inserting plane optical windows into a flat-surfaced bar welded into the side of the vessel and by welding blank inserts, approximately 6 inches wide, along the remainder of the inner wall of the tube. Thus the internal cross-section is not exactly circular, but in the form of a circle segmented on two opposite sides. Minnesota Rubber

Company type A 245 O-ring seals, a special low temperature silicon rubber compound, were provided at all flange and port openings.

Because of the possibility of frosting of the glass at low temperatures, a double window arrangement, illustrated in Figure 7, was used for the observation ports. An insulating cylinder was attached to the window port block with a second window fitted in its outer end. Thus the temperature of the outer window could be kept above the dew point of the room air while the space between the two windows was evacuated.

2.1.2. Testing

All three vessels were subjected to several acceptance tests and checks both before and after delivery. All critical welds were subjected to X-ray photography. Hydrostatic testing to 300 psi on vessel A and 500 psi on vessles B and CD was performed with a number of SR-4 strain gauges attached to the surface of the vessel in order to measure maximum stresses and locate critically stressed areas. Locations of the strain gauges with respect to the vessels and stresses calculated from static strain measurements are shown in Figures 8, 9, and 10 for vessels A, B, and CD, respectively. The stress measurements were obtained with Baldwin-Lima-Hamilton type A-5 and A-7 standard SR-4 resistance strain gauges and a BLH type L strain indicator. It was found that the critical stress concentration in vessel A occurred at the weld joining the 18 inch flange neck to the elliptical head, while the maximum stress in vessel CD was developed at the weld between the window port block and the vessel wall. Stresses

in vessel B were found to be considerably below the critical level.

2.1.3. Vacuum Performance

In order to satisfy vacuum requirements of the vessels, two methods of leak detection were employed. Initially, a halogen-sensitive detector, Distillation Products Industries type LD-01, was used to locate moderate to large sized leaks. This was followed by more sensitive testing in which the leakage rate of helium into the chamber was measured with a VEECO type MS-9 mass spectrometer. The two-stage pump system used in the vacuum tests consisted of a Roots-type blower backed by a rotary oil pump. The system, described in detail in Section 2.3, was designed to reduce pressure in a 150 cu ft chamber from 1 atmosphere to 1 mm Hg in 15 minutes.

Vessel A was found to be in good condition with respect to vacuum service, with a maximum pressure rise of several μHg/hr in the range of pressures from 1 to 100 μ Hg. The pump-down curve of vessel A, illustrated in Figure 11, shows that after 15 minutes of pumping time the pressure in the chamber was reduced to 7 μ Hg. Considering that the vessel interior was not perfectly clean and that the pump performed below predictions, this value was found to be quite satisfactory.

Initial tests of vessels B and CD revealed that pumping times were excessive and that base pressures were not sufficiently low. To improve the performance of the vessels, all leaks which could be localized were eliminated. Following this, the leak rate of the entire vessel was determined by surrounding

it with a helium atmosphere and obtaining measurements with the mass spectrometer. The leak rates thus determined were approximately 0.007 μ-ft^3/hr for vessel CD and 0.006 μ-ft^3/hr for vessel B, within the allowable limit.

Subsequent to the leak rate tests, pump-down rates were established for vessel CD and for the 2 ft x 40 ft chamber obtained by combining vessel CD with vessel B. In addition, the pressure rise in the blanked off vessels was observed. The results are shown in Figure 12 for vessel CD and in Figure 13 for vessels B and CD combined.

The excessive pressure rise indicated in these figures could not be accounted for by leakage from the atmosphere, consequently it was considered as due to outgassing within the chambers. Sources for the outgassing were established at a number of small cracks and holes resulting from weld porosities opened up during grinding of the internal welds in both vessels. In fact, some of the cracks located along the 6 inch wide filler strips possibly provided gas passage to the small void between the strip and the vessel wall, thus seriously impairing the vacuum characteristics of the vessels.

This condition was corrected in vessel CD by repeated welding and grinding of the cracks. Standard dye techniques were used to detect new cracks after each grinding operation. Repetition of the vacuum tests indicated an approximate pressure rise of 13 μ Hg/hr, an acceptable value considering that the resulting change in initial pressure of the test gases would be insignificant during the time required to perform the test.

Final pump-down characteristics and pressure rise curve are also shown in Figure 12.

Similar repairs performed on vessel B were unsuccessful because the additional welding of the cracks produced surface irregularities which were considered excessive from the standpoint of interference with the wave process under observation. Consequently, it was necessary to eliminate the source of the outgassing by removing the entire weld on both sides of the two filler strips and rewelding the strips to the vessel. This operation was successful in reducing the pressure rise from 20.6 μ Hg/hr to 3.4 μ Hg/hr in the 40 ft long chamber, as indicated in Figure 13. The increase in the final pump-down time, also apparent from this figure, reflects only the deterioration of the vacuum pump system, rather than the condition of the vessels.

2.2. Temperature Control System

In order to vary the initial gas temperature, vessel CD was provided with a system designed to control its temperature from -180°F to 200°F. In fact, the low temperature service dictated the use of type 304 stainless steel for this chamber.

Heat transfer characteristics of the stainless steel vessel with appropriate insulation were calculated and the results used to design the temperature control system. The insulation was comprised of a 1 inch layer of mineral wool covering the vessel surface and, over this a 3 inch layer of polyenethane foam which in turn was completely sealed with a water-impervious canvas sheet. Figure 14 shows vessel CD after installation of the insulation.

Temperature control was achieved in the following manner. Subzero temperatures were maintained by spraying controlled quantities of liquid nitrogen into a 1 inch annular space formed around the vessel by a 12 gauge stainless steel cover. Heating to 200°F was accomplished by means of electric heating elements attached to the surface of the vessel. The heaters were attached with Thermon, a heat-conducting graphite-based epoxy.

Twenty-six thermocouples, described later, were attached to the surface of the vessel. Fourteen of these were connected to a Brown recorder for rapid visual audit of the magnitude and uniformity of the vessel temperature. The remaining twelve were connected, through a selector switch, to a Bustol automatic controller, series 536, which regulated the heating and cooling systems. Of the latter thermocouples, a single one, which was observed to record the approximate average temperature of the entire group of twelve, was used to drive the control unit. The controller operated in an on-off mode, actuating either a solenoid valve installed in the LN inlet line of the cooling system or the contactor switch of the electric heating system. Schematic diagrams of the temperature control systems are shown in Figures 15 and 16.

During transient operation temperature differences over the length of the vessel were as large as 50°F. However, during steady state the vessel temperature was uniform within 10°F. Heating to 200°F required approximately 6 hours while cooling to -50 and -180°F was accomplished in 6-8 and 20 hours, respectively.

Gas temperature within the vessel was recorded by thermocouples located at both ends, extending several inches into the interior. Several feet of the mixture inlet line were welded to the outer surface of the steel shell, which, according to heat transfer calculations, was sufficient to cool (or heat) the mixture to the vessel temperature during the filling process.

2.3. Vacuum Pump System

2.3.1. Description

Prior to admission of the test gas mixture, residue gases were removed from the detonation vessel by means of a vacuum pump. The primary factors influencing the design of the pumping system and the selection of its components were the ultimate base pressure required, the gas load, and the pump-down time. The first two requirements governed the type of pump to be used, while the last determined the capacity of the pump.

The pump-down time for a given pump is, of course, dependent upon the volume of the chamber to be evacuated, which in this case ranged from 62 cu ft for vessel CD to 150 cu ft for vessel A. To provide adequate performance for all conditions, the design of the pumping system was based on the largest volume of 150 cu ft.

The initial pressure of the test mixture ranged from 100 mm Hg to 0.1 mm Hg. Consequently, to insure that the maximum impurity level did not exceed 1%, the pumping system had to be capable of evacuating the vessel to a pressure of at least 0.001 mm Hg. In view of the large number of tests to be performed, it was desired that the time required to reach this pressure be kept to

a reasonable minimum, which was arbitrarily set at 15-20 minutes. To facilitate leak detection tests, an ultimate pressure of 10^{-4} mm Hg was required. Here, however, the pumping time was not important, although the pump should have sufficient capacity at the ultimate pressure to overcome the leaks.

The vacuum pressure requirements dictated the use of a two-stage pumping system. Consequently, a high vacuum pump backed by a mechanical rotary oil seal pump was chosen for use. These pumps are hereafter referred to as HVP and MP, respectively. The function of the MP was twofold: first, it reduced the pressure in the chamber to a level where the HVP could be safely operated; secondly, it provided a sufficiently low exhaust pressure for efficient operation of the HVP.

The pumping system had to be also capable of handling the large volume of water vapor produced by the combustion process. For example, several pounds of water vapor result from the reaction of a stoichiometric mixture of hydrogen and oxygen initially at NTP. The presence of the water vapor introduces two serious problems. First, if a portion of the water vapor condenses in the vessel, it will evaporate when the pump reduces the pressure in the vessel below the equilibrium vapor pressure, thereby reducing the effective pumping speed of the system. In fact, when the rate of evaporation equalizes the rate of evacuation, the pressure in the vessel is maintained constant until the condensed phase is entirely evaporated. Secondly, the water vapor passing through the mechanical pump condenses in the oil. When the pressure in the pump is reduced below the vapor pressure of the

water, evaporation occurs and limits the ultimate pressure which can be attained regardless of conditions in the vessel. The first problem is independent of the pumping system; the second is largely influenced by the pressure at which the MP operates when backing the HVP.

In consideration of the ultimate pressure requirements and the capability to handle large water vapor loads, a Roots-type compression blower was selected for use as the HVP in preference to a vapor diffusion pump. The diffusion pump, which cannot be operated until the fore pressure is reduced to several hundred microns Hg, does not attain its maximum pumping speed until a pressure of 1 μ Hg. On the other hand, the compression blower can be operated at a fore pressure of 50 mm Hg and is in fact designed for operation in the range from 1 μ to several mm Hg. The Roots-type blower offers the further advantages over the diffusion pump of simpler operation and the capability of handling large volumes with a moderate sized pump.

Since the compression blower operated at higher back pressures than the diffusion pump, the problem of contamination of the oil in the MP was alleviated, although not entirely eliminated. Contamination of the oil was minimized by the installation of a cold trap between the vessel and the HVP and by providing a gas ballast feature on the MP. In spite of these precautions, it was found later that the pump performance was seriously impaired by slight oil contamination after 10-20 detonation tests at high initial pressures. Thus, frequent oil changes were necessary.

The selection of the MP was not critical and was governed primarily by the desired pumping speed in conjunction with the HVP and the compression ratio of the HVP at the desired base pressure. The MP had, of course, to have the gas ballast provisions necessary to handle the heavy water vapor load. For the present range of pressures a single stage mechanical pump was found to be adequate.

The pumping system assembly is shown schematically in Figure 17. The MP selected for use was the Stokes model 212-H rotary oil pump while the HVP was the Roots-Heracus model VPRG 350-A. The manufacturer's published performance curve for the combination is shown in Figure 18. The cold trap between the HVP and the vessel, in addition to condensing the water vapor evacuated from the vessel, also served to reduce backstreaming of oil from the HVP into the detonation chamber. A schematic diagram depicting the construction of the cold trap is shown in Figure 19. The two pumps were mounted on a common steel support and were connected by a 4 inch steel pipe. Vibration transmission between pumps was reduced by vibration mounts and a flexible bellows in the connecting pipe.

At the start of the pumping operation the MP operated by itself until the pressure in the chamber was reduced below 50 mm Hg. A pressure switch actuated the HVP at this point and reduced the pressure further until the desired base pressure was reached.

Isolation of the pump system from the detonation vessel was achieved through a Hydromatics type 703, 300 lb ASA, 4 inch

ball valve, with an actual opening of 3 inches. The valve was constructed of stainless steel, with extended stem for cryogenic operation, and teflon seats.

2.3.2. Performance

A theoretical performance analysis of the entire pumping system has been presented in reference 5. Results are shown as curve B in Figure 18. The actual performance of the system depends to a large extent on the cleanliness and vacuum tightness of the chamber to be evacuated; furthermore, these factors determine the ultimate attainable vacuum pressure. In the calculation of the performance (curve B, Fig. 18), a total leakage and outgassing rate of 1.0 μ-cfm was assumed. Subsequent vacuum tests revealed, however, that while leakage into the system was almost negligible, outgassing occurred at a much higher rate than the assumed value. This fact was established by pressure rise measurements in the blanked-off chambers, illustrated in Figures 12 and 13. As a consequence of the heavy interior gas formation of the vessels, the pumping speed diminished rapidly below a pressure of 10 μ Hg, causing total pumping time to be in excess of the expected value. Figure 11 shows the measured pressure-time curve for vessel A both with and without the LN cold trap. The leveling off of the curve at several microns was the result of the outgassing discussed above.

Figure 20 shows the measured pump speed for the vacuum system with vessel A in the range of pressures from 1 to 100 μ Hg. It compares favorably with the manufacturer's curve which was obtained, however, with a 47 cfm forepump. The total pumping

speed of the system, as measured in the laboratory, is also shown, as well as the predicted system performance. Although limitations of the measuring apparatus forced a termination of the pump speed tests at a system pressure of 7 μ Hg, sufficient information was obtained to show that the actual system speed becomes less than the predicted speed at 10 μ Hg. In view of the more than adequate pump speed, and the fact that the calculated flow resistances should be accurate within at least a factor of two, the drastic reduction in system speed was felt to be the effect of excessive outgassing.

The increase in base pressure, however, did not affect the performance of the detonation tests. For the 100 μ Hg tests, the vessel was pumped to its ultimate pressure, filled to 50 or 100 μ Hg, pumped again to 10-15 μ Hg, and finally filled to 100 μ Hg, the entire time required for this procedure being short enough to assure that impurities introduced by outgassing and leaks were less than 1%.

2.4. Gas Handling System

2.4.1. Design

The two most important features considered in the design of apparatus to prepare and handle explosive gas mixtures were (1) safety of the operating personnel and protection of other equipment, and (2) control of the composition of the mixture. To a large extent, explosion hazards can be minimized by the use of high strength components, judicious location of the apparatus, and proper operating procedure. Adequate control of the com-

position involves the ability to reliably and reproducibly prepare mixtures of known composition and known purity. Accuracy of the composition is limited only by the precision of the metering instruments, while very high purity is possible by means of several standard techniques. The type of gas handling system selected for this work met both these requirements quite satisfactorily. A brief description of the system is presented below while more detailed information is given in reference 6.

The obvious method of preparing the explosive mixtures directly in the detonation vessel, by monitoring the partial pressure of the component gases, was discarded because of difficulties associated with producing uniform composition throughout the vessel. Mixing devices located within the detonation vessel could not be employed and the time required to assure uniform composition by diffusion alone would be excessively long. While the equilibration time could be reduced somewhat by means of an external recirculation pump, the increased complexity of the apparatus was considered unwarranted in view of the advantages afforded by the system which was adopted.

Initially, because of the large variation in the quantity of mixture required at varying initial conditions, two different systems were considered. For tests at subatmospheric initial pressures a "mixing chamber" system was designed which provided for the preparation, storage, and control of 4200 cu in. of gas mixture at 400 psi maximum pressure. For the 1 atmosphere initial pressure tests it was planned to feed gases, mixed in proper proportion, from commercial cylinders directly into the

detonation vessel. During subsequent operation it was found, however, that the small number of the 760 mm Hg tests could be handled by repetitive filling from the "mixing chamber" system; thus, plans for the "continuous flow" system were abandoned.

The explosive mixture was prepared and stored in a container, hereafter referred to as the mixing chamber, from which it was then transferred to the detonation vessel as required. Because of its large explosive content, the mixing chamber presented the greatest explosion hazard. Any attempt to design a mixing chamber sufficiently strong to withstand the pressures generated during an explosion within the chamber would be based on questionable data. This required, then, the introduction of arbitrarily large safety factors, leading to prohibitive costs. If we consider detonation to represent the most severe explosive process to occur within the chamber, then it is an easy matter to compute with fair accuracy the pressures corresponding to the von Neumann spike, the Chapman-Jouguet state, and the state behind the reflected detonation. The maximum pressure, however, occurs during the development of the detonation wave and can only be determined experimentally. For example, for a stoichiometric mixture of hydrogen and oxygen initially at NTP, pressures of 40, 20, and 67 atmospheres correspond to the von Neumann spike, the C-J point, and the reflected detonation, respectively, while a peak pressure of at least 85 atmospheres has been measured at the instant the detonation is generated. If we assume that an explosion occurs within the mixing chamber when the pressure there is 400 psi, a reaction pressure as high as 34,000 psi could

be expected, and even higher pressures may be produced by wave reflections. A relatively thick-walled chamber would be required which, if it should rupture, would give rise to high kinetic energy shrapnel.

It was, therefore, considered more expedient to use a thin-walled chamber without attempting to contain an explosion. An inexpensive barricade, such as sand bags, would provide efficient means of absorbing the lower kinetic energy particles (resulting from reduced mass) produced if the chamber is shattered. Such chambers were readily available as surplus oxygen-breathing cylinders with standard volumes of 500, 2100, and 18,000 cu in. and with a working pressure of 400 psi. Two 2100 cu in. cylinders, charged to the maximum pressure, would contain 3 lbs of equimolar hydrogen-oxygen mixture, almost four times the maximum quantity required for a single experiment in the largest vessel at an initial pressure of 100 mm Hg. Consequently, at least three experiments could be performed from a single charging of the mixing chamber. For a given initial temperature, the weight of mixture used in a single experiment is directly proportional to the initial pressure. Since only several experiments were required at each operating condition, the amount of mixture required for the 10, 1, and 0.1 mm Hg initial pressure tests did not exceed the amount needed for a single experiment at 100 mm Hg. Depending then on the number of unsuccessful shots, in most instances a single charging of the mixing chamber was sufficient for all tests at a given composition.

The maximum chemical energy content is obtained when the

mixing chamber is charged to 400 psia with a stoichiometric hydrogen-oxygen composition. At room temperature this corresponds to 2.1 lbs of mixture which, assuming the higher heating value of 5760 BTU/lb of mixture, yields a theoretical energy content of 12,100 BTU.

The mixing chamber was located in a cell constructed of 2 ft thick reinforced steel concrete walls with blow-off roof, isolating it from the rest of the laboratory. All operations during preparation and storage of the mixture were controlled from outside the cell. A flow diagram of the gas handling system is shown in Figure 21 while details of the mixing chamber and its controls are shown in Figure 22. To minimize corrosion and maintain mixture purity, that part of the system exposed to the mixture was constructed entirely of stainless steel. With the exception of the component gas lines, the housing for the gas filter, the mixing chamber, and the solenoid valves, all components were rated at 30,000 psi.

Gas cylinders, located outside the building, were connected by 15,000 psi aluminum tubing through a manifold and valve system to the mixing chamber, Figure 21. From the mixing chamber a line led to a manifold which distributed the mixture to the detonation vessels. Manually operated high pressure valves were located on both sides of the manifold to isolate the vessels from the mixing chamber. When a vessel was in use, the upstream valve and the downstream valve connecting to the vessel were open and the remaining downstream valves were closed. The line feeding the detonation vessel was also equipped with a 500 psi

normally closed solenoid valve, for admitting the mixture to the vessel, and a 30,000 psi normally closed air-operated shut-off valve, to provide positive closure of the vessel during an experiment. After filling, the line between these valves was evacuated to provide isolation of the detonation vessel from the rest of the system.

Each of the aluminum lines from the gas cylinders terminated in a high pressure stainless steel valve connected to the manifold. Installed in the line between the manifold and the mixing chamber was a high pressure metering valve for control of the gas flow rate, and a molecular sieve to remove trace impurities, particularly water vapor, Figure 22. The mixing chamber was comprised of two 2100 cu in. surplus oxygen-breathing bottles connected in parallel. Manually operated high pressure valves located at both ends of each bottle served to isolate either bottle from the system when a smaller volume was desired. To insure uniform composition, each bottle was provided with a jet mixer. The mixer, a piece of tubing several inches shorter than the chamber length, was closed at one end and had a series of small holes drilled through the tube wall, the total area of these holes being equivalent to the cross-sectional flow area of the tube. The mixer inlet was attached to the feed line so that the incoming gas could only enter the mixing chamber through the orifices. At inlet pressures lower than the pressures encountered during mixing, the gas jets were of more than sufficient extent to reach the chamber walls; hence, mixing was further enhanced by the turbulence produced by jet impingement on the walls of the chamber.

The mixing chamber was mounted with its axis horizontal; the effects of gravity on the uniformity of the composition could be ignored since the chamber was only 12 inches in height.

From the other end of the mixing chamber a line led to an atmospheric vent, a vacuum pump, and the pressure gauges used for composition metering. Gauge savers installed upstream of each pressure gauge would automatically close if the pressure would exceed the maximum range of the gauge and served to protect the gauge in the event of an explosion.

Since the mixing chamber pressure was considerably greater than the highest pressure to which the detonation vessel was filled, the flow into the vessel was choked and was determined by the mixing chamber pressure alone. At an initial pressure of 100 mm Hg, the filling time, which is proportional to the ratio of the final vessel pressure to the mass flow rate, was of several minutes' duration, which provided sufficient time for adequate control of the pressure. However, since the feed line was sized for the high initial pressure tests, filling times of less than 1 second resulted for the low initial pressure tests. To circumvent this, an intermediate chamber, also a 2100 cu in. surplus oxygen bottle, was installed in the line between the mixing chamber and the distribution manifold. After the mixture had been prepared, a portion of it was transferred at lower pressure to the intermediate tank which then served as the storage chamber for the low initial pressure tests. The pressure in this chamber, determined by the change of pressure in the mixing chamber, was adjusted so that the proper filling time could be obtained.

2.4.2. Selection of Components

A. The Mixing Chamber. As stated before, surplus oxygen-breathing bottles in sizes of 0.3, 1.2, and 10.5 cu ft, available commercially, were chosen for use as the mixing chambers. The bottles, made of stainless steel, had a wall thickness of 40 mils and a maximum working pressure of 400 psia. The size of the mixing chamber was specified by the requirement that it contain sufficient mixture for at least three experiments, and was given by:

$$V_c = 3 V_v \frac{P_v T_c}{P_c T_v}$$

where V is the volume, P the pressure, T the temperature, and the subscripts c and v denote conditions in the mixing chamber and detonation vessel, respectively. The largest volume required was 2.2 cu ft and resulted when the chamber was charged to 400 psia at room temperature and the mixture was tested in the 3 ft diam x 20 ft long chamber at an initial pressure of 100 mm Hg and initial temperature of 520°R. Consequently, two of the 1.2 cu ft bottles connected in parallel satisfactorily met the storage requirements.

B. Composition Control. Explosive mixtures were prepared by evacuating the chamber to several hundred microns Hg, then filling the chamber first with hydrogen, then with oxygen and measuring the partial pressure of the hydrogen and the total pressure of the mixture. Measurements were made by means of two bourdon tube pressure gauges, with maximum ranges of 300 and

600 psi and least readings of 1 and 2 psi, respectively. The gauges were protected with pressure-actuated shut-off valves which were adjusted to automatically isolate the gauge from the system when its maximum range was exceeded. Both gauges were mounted in explosion-proof cases, with blow-out backs, and were accurate to within 1/4%. Since the mixing chamber was charged to a total pressure of 400 psi, the minimum partial pressure of hydrogen was 200 psi, which could be read with an accuracy of 1/2% on the 300 psi gauge. The total pressure, read on the 600 psi gauge, was accurate to 1/2% for all mixture ratios. With this system, the accuracy with which the concentration of hydrogen could be determined was within 1%.

The pressure gauges were located in the same cell as the mixing chamber and observed through a periscope mounted on the cell door, a 1/2 inch thick steel panel. Due to the rise in gas temperature which accompanied the filling of an evacuated tank, after filling was stopped, the gas pressure dropped as the gas cooled, requiring an additional quantity of gas to maintain the desired pressure. The metering valves had sufficient sensitivity to allow the delivery of small quantities of gas with relative ease, and the entire filling process required about 15-20 minutes with most of this time being necessary for the gas to cool. Oxygen was not added until the pressure of hydrogen was constant with time, and the pressure of the final mixture was allowed to reach a steady value before the mixture was used.

All control valves were equipped with extension handles which passed through a slot in the concrete wall so that they

could be operated outside the cell. The slot was covered on both sides of the wall with 3/4 inch steel plates, the holes in the plates being smaller in diameter than the coupling to the valve stem, for safety in the event of explosion.

C. Filter. The molecular sieve used to filter trace impurities, particularly water, from the test gases possesses several distinct advantages over other adsorptive desiccants. Most important, the sieve has a greater drying capacity, especially at low relative humidities. For example, at 1% relative humidity, the molecular sieve adsorbs approximately six times more water than either alumina- or silica-type desiccants, even under dynamic conditions. In contrast to other desiccants, the molecular sieve is most efficient under adiabatic rather than isothermal conditions, eliminating the necessity for cooling the adsorbent bed. In addition, by proper design of the bed, the molecular sieve can also be used to adsorb other impurities. Since the sieve has a much stronger affinity for water, then as water is adsorbed at the inlet of the adsorbent column it displaces other impurities previously adsorbed. However, these impurities are then readsorbed further on in the column. If the column is long enough, these impurities are retained on the adsorbent, rather than re-entering the purified stream.

The general design requirements for the molecular sieve bed were:

Minimum bed depth	2.5 ft
Maximum superficial gas velocity	2.0 ft/sec

Minimum bed to pellet diameter ratio	20:1
Maximum inlet gas temperature	100°F

Commercial gases can be supplied with a water content much less than one mole per cent. Since this is considerably less than the capacity of the adsorbent, the minimum bed depth of 2.5 ft was chosen. In addition, Linde type 4A pellets were used. These pellets are 1/8 inch in diameter and adsorb molecules of diameter less than 4 angstroms. The pellet diameter also imposed a lower limit on the bed diameter, i.e., the bed must have a diameter greater than 2.5 inches. To insure adequate residence time and adsorbent surface area, a bed diameter of 4 inches was chosen, satisfying also the requirement posed by the pellet size.

D. Lines, Valves, and Fittings. All lines, valves, and fittings which were exposed to the mixture, with the several exceptions noted previously, were standard autoclave components made of stainless steel rated for 30,000 psi. Although the components were rated at a pressure slightly less than the maximum pressure expected in the event of an explosion in the mixing chamber, several factors indicated that they were suitable for use. First, rupture of the mixing chamber would aid in reducing the explosion pressure. Secondly, since the rated pressure was considerably less than the yield strength of the components, it was doubtful that rupture of the components would result from an explosion.

To provide adequate capacity over the entire range of operating conditions, 1/8 inch ID x 1/8 inch wall lines were used.

Assembly of the components was accomplished by means of threaded couplings. The couplings provided a metal-to-metal seal which minimized leak rates, both pressure and vacuum, to an acceptable level. Care was taken, however, to insure that the sealing surfaces were free from scratches, burrs, and foreign particles before assembly. The valves were constructed with floating stems so that their operation did not produce motion of the stem tip relative to the valve seat.

The lines from the gas cylinders to the manifold which admitted the component gases to the mixing chamber were 5/16 inch ID x 1/8 inch wall, 15,000 psi aluminum tubing. Assembly again was accomplished by a threaded coupling with a metal-to-metal seal. The line from the manifold to the mixing chamber was also 1/8 inch ID stainless steel and consequently controlled the rate of flow to the chamber. The size of the feed lines was determined from an approximate analysis of the transient flow process during the filling of the mixing chamber and the detonation vessels. These calculations can be found in detail in reference 4.

2.5. Ignition Systems

Three ignition systems were designed and constructed. The Primacord system provided a high energy source while the hot plate and spark ignitors were built essentially to study the effects of weak ignition sources.

2.5.1. Primacord System

A. Description. The ignition system used in this work consisted of a 2 inch length of 400 grain Primacord initiated by

a standard No. 6 electric blasting cap.

"Primacord" is a linear detonating cord of fuse used primarily for initiating commercial explosives (7). Basically, it is a strong flexible cord with a core containing a high explosive, PETN (pentaerythrite tranitrate), a non-hygroscopic, crystalline solid. When Primacord is initiated with a blasting cap, it detonates along its entire length at a velocity of approximately 21,000 ft/sec. The core covering, or encasement, comes in many materials and the quantity of PETN per foot of Primacord varies for different grades. The Primacord used in the present work had a core loading of 400 grains of PETN and was covered and end-sealed with a plastic encasement. For this grade Primacord the density of the PETN is about 1 gm/cm^3 and the pressure and temperature behind a detonation wave in such a material are 73×10^3 atmospheres and 5000°K, respectively, while the energy of explosion is 22 BTU for the 2 inch length used in these experiments (8). The Primacord was located end-on to the blasting cap, which was initiated by the passage of an electric current of approximately 0.5 amps.

The Primacord was obtained from the Ensign Bickford Company of Simsbury, Connecticut, and the blasting caps from the Hercules Powder Company, Hercules, California. The 2 inch lengths of Primacord were cut at the factory, the ends of each piece being sealed with plastic caps to retain the PETN within the encasement. The outer diameter of the Primacord was 0.425 inch while the blasting caps, sheathed in copper, were about 0.25 inch in diameter and about 1-1/2 inches long.

Due to the strength of the ignition system and to the amount of debris produced by fragmentation of the copper sheath of the blasting cap, tests were performed (a) to determine means of containing the fragments of the blasting cap in order to reduce damage to the interior surface of the vessels, and (b) to evaluate the effects of the blast wave, produced by the Primacord, on the detonation vessels. Results are described in reference 9.

B. Design of the Primacord Holder. During the pressure tests it was noticed that large fragments of copper were ejected from the blasting cap with sufficient velocity to embed themselves in the surface of a stainless steel plate placed at a radial distance of 1 ft from the cap. In order to minimize damage to the interior surface of the detonation vessel, the blasting cap was shielded by inserting it in a 1/2 inch wall rubber hose and enclosing the assembly in a steel cylinder. A steel plate 1/4 inch thick with a 1/32 inch diam hole drilled through it was placed over the end of the steel cylinder, and the Primacord placed immediately adjacent to the end plate. It was possible to detonate the Primacord by means of the shock wave transmitted through the orifice, and at the same time contain most of the copper fragments. The initial version of the Primacord holder with the encased blasting cap is shown in Figure 23. Thin strips of Scotch Tape passing over the head of the Primacord were used to hold the high explosive firmly against the hole in the top plate.

During subsequent use of the holder, however, it was found that the excessive pressures developed by detonation of the

blasting cap caused deformation of the walls of the holder. This resulted in seizure of the threaded parts, making it extremely difficult to disassemble the holder. This problem was alleviated by modification of the design of the ignition holder, Figure 24. The new design incorporated an increased wall thickness and uses a bolted, rather than threaded, method of assembly.

Measurements were made in free air to determine the strength of the blast wave generated by the Primacord at various positions about the center of the explosion. In particular, measurements were made along the blasting cap-Primacord axis and at radial distances from this axis. The pressure transducer, a Kistler Instrument Corporation, type 601 pressure pickup, was installed in a stainless steel instrument mount (in which it was shock-tube calibrated), the mount being bolted to a rigid steel plate at a height of 3 ft from the ground. The Primacord was held at the same height on an independent movable support.

Maximum peak pressures were observed in the radial direction and were found to be 200 psi and 70 psi at distances of 12 and 18 inches, respectively. Since this was less than the 250 psi design pressure, it was concluded that the Primacord explosion would not affect the structural integrity of the detonation vessels. The maximum pressure measured in the axial direction at a distance of 6 inches from the Primacord was 250 psi. Although the distance between the ignitor and the end wall of the vessel was also 6 inches, due to the shielding effect of the massive Primacord holder, the pressure exerted on the end was less than the above value.

In spite of the precautions which were taken, it was found to be virtually impossible to completely eliminate the generation of copper fragments. A considerable amount of debris was ejected through the small 1/32 inch orifice separating the blasting cap from the Primacord. The concentration of fragments was highest at the opposite end of the vessel and, surprisingly enough, in a band approximately 12 inches wide on the vessel walls immediately adjacent to the ignitor. While the amount of debris thus deposited in the vessel was tolerable, requiring only the occasional cleaning of the vessel interior, the copper fragments were highly undesirable because they were capable of damaging Schlieren windows and pressure transducers by their impact. During the test program several windows were, in fact, severely cracked and chipped by copper particles.

2.5.2. Spark Ignitor

Spark ignition was obtained by discharging a 0.2 μfd capacitor, charged to 6000 volts, across the electrodes of an automotive spark plug installed in the end flange of the vessel. The circuit diagram is shown in Figure 25. Losses are estimated to be 50% of the stored energy so that 1.8 joules were deposited in the mixture.

2.5.3. Hot Plate Ignitor

The "hot plate" ignitor consisted of a hollow cylinder capped at one end with a thin plate. The closed end was inserted into the chamber and heated to several thousand degrees F using at first an acetylene-oxygen torch. The high temperature of the cap ignited the test mixture.

Subsequently, the torch was replaced with an electrical circuit, consisting essentially of a commercial 2700 watt soldering unit. The operation of this system was based on the high temperatures created by a current of approximately 150 amps passing through the contact resistance of a carbon tip touching the plate. The main advantage of this system was the relative ease in controlling the heating rate of the plate and the elimination of the explosion hazard associated with the acetylene-oxygen torch. The hot plate ignitor is shown in Figure 26 and a typical temperature time history of the hot plate is presented in Figure 27.

2.6. Instrumentation

Instrumentation of the detonation vessels consisted in part of piezoelectric pressure transducers located every 2 ft axially along the inside chamber walls. In addition, a pressure transducer with sensing direction parallel to the chamber axis was located at the end of the vessel opposite the ignitors. Additional instrumentation consisted of ionization probes, located in the walls of the vessel opposite the pressure transducers, thermocouples for temperature measurements in the gas mixture and the vessel walls, and strain gauges for monitoring the dynamic response of the vessel.

2.6.1. Pressure Measurements

Since accurate pressure measurements were of crucial importance to the successful performance of the work, a systematic program of performance evaluation of the most advanced commercial transducers was undertaken prior to the test program. The pressure

measuring systems included in this investigation were:

Kistler Instrument Company types 601, 601A, 704, and 603 piezoelectric transducers, and types 568 and 553 amplifiers;

Atlantic Research Corporation model LD-80M1 piezoelectric transducer; and

Omega Dynamics Corporation type 17 capacitance pressure sensor.

The performance evaluation involved the determination of the sensitivity, natural frequency, rise time, and noise level of the various transducers. This was done using a dead weight tester for sensitivity and linearity, and a shock tube for rise time and sensitivity. Both methods showed essentially the same gain characteristics. In addition tests were performed in a detonation tube to examine the temperature sensitivity of the transducers. Detailed results of the performance evaluation program may be found in Technical Note #9.

On the basis of these experiments, it was concluded that the Kistler 601A transducer, together with both the 568 and 553 amplifiers to cover the entire pressure range, was best suited to our requirements. Unfortunately, the 601A was found to be extremely temperature sensitive. Hence, the 601 transducer, which has the same natural frequency of 150,000 cps but only one-half the gain of the 601A, was selected instead and five units were obtained, as well as a number of 568 and 553 amplifiers. Several PZ 14 transducers with PT-6 amplifiers were already on hand in the laboratory.

The published performance specifications of the transducers and amplifiers are listed in Table 2.

Experiments were carried out also to minimize the effects of gauge mounting on performance. The resulting design, Figure 28, involved the suspension of the transducer within the instrument plug. To increase its mass, the transducer was housed within a heavy brass mount which, in turn, was inserted into the standard instrument plug but isolated from it by a number of O-rings. In this manner the "ringing" of the transducer was reduced well below the useful signal. Finally, performance tests were conducted at temperatures of -180°F. Deviations in the response of the transducers from that at room temperatures were found to be negligible.

Although a total of twelve pressure measuring channels were available initially, it was found in the course of the test program that sufficient signal at the low initial pressure condition could be obtained only from the Kistler 601 and PZ 14 transducers. The number of available oscilloscope channels further limited simultaneous pressure measurements to a total of six.

A further reduction in the number of available pressure transducers occurred at low temperature, where severe icing continually shorted the sensors and particularly the cables. However, the excessive delay which would have resulted from de-icing the transducers prior to each shot was considered unwarranted and tests at these conditions were performed with essentially incomplete pressure data. Since the data that were obtained--at least two transducers were always operating satisfactorily--were consistent with other test results, the lack of more detailed information was not considered serious.

A Kistler type PT-6 unit in conjunction with a PZ 14 transducer was used to measure reflected pressures. An improvement in the quality of these measurements was obtained by the use of an Elastronics Corporation "Transductron" electronic compensating unit. This instrument served essentially to eliminate from the output of the pressure sensor the "ringing" produced by excitation of the natural frequency of the transducer, which was approximately 47.5 Kc. When the "Transductron" unit was properly adjusted, the resulting pressure record yielded a relatively accurate representation of the applied pressure pulse.

Typical oscilloscope pressure records are shown in Figure 29, obtained during detonation of a stoichiometric hydrogen-oxygen mixture initially at 100 mm Hg pressure. While a signal similar to the one illustrated provided fairly good accuracy, at low initial pressures serious problems were encountered with the pressure transducers as a consequence of the acceleration sensitivity of the piezoelectric elements. Since the detonation vessel was essentially a thin-walled cylinder, its response to the explosion of the Primacord, as well as to the detonation wave, approached that of an elastic shell rather than a rigid wall. The subsequent motion of the walls was detected by the pressure transducers and, at an initial pressure of 100 μ Hg, the spurious signal was larger than the useful output. In fact, it was only because the shock wave signal appeared as a discontinuity compared with the low frequency acceleration induced signal (to a good approximation, the response of the transducer can be considered as the linear superposition of the two signals)

that measurement of the shock pressure was at all possible.

In addition to pressure measurements, signals from the transducers also provided a convenient check on the detonation velocities obtained from ionization probes.

Depending on its value, the initial pressure of the mixture in the vessel was determined using either a 0-760 mm Hg Wallace and Tiernen precision pressure gauge, a 0-200 mm Hg W&T gauge, or a McLeod gauge calibrated Pirani system. Vacuum pressure within the vessel was recorded by a Pirani gauge.

2.6.2. Ionization Gauges

Measurements of flame velocities were made using a twelve channel ionization detection system previously developed in the laboratory (10). The ionization probe, Figure 31, consisted of a 1/32 inch diam brass electrode inserted through a 1/8 inch diam teflon insulator which was mounted in a brass housing installed and vacuum sealed in the standard instrument plug. In operation, a potential of 70 volts was placed across the gap and changes in gas conductivity were detected as variations in the gap voltage. The output of the probe was fed through a cathode follower to a high gain amplifier which triggered a thyratron. The threshold level of the circuit was 0.005 volts at the output of the cathode follower. The thyratron output could be displayed individually or, for greater than 1% precision, could be mixed and displayed on a raster sweep. However, for reasons described below, the raster display was not used in these tests.

Several problems were encountered during the detonation tests. First, pickup of high frequency noise, characteristic of

high gain, wide band-pass circuits, was made particularly severe by the long cables required for instrumentation. This was eventually overcome by raising the bias voltage on the thyratron tube and adequate grounding of the electronics through a trial and error procedure. Second, the cathode follower circuit was highly microphonic and, as a result of the high gain of the amplifier circuits, spurious signals were introduced by the acoustical noise generated by the explosion and by the accompanying vibration of the walls of the vessel. Efforts to isolate acoustically the cathode followers were only partially successful in the elimination of this problem. Thus, it became necessary to observe ionization signals directly on individual oscilloscope channels. Since the spurious signals could easily be differentiated from the real signals, this procedure provided a satisfactory technique for the measurement of wave velocities although results obtained in this manner were far less accurate than the 1/2% accuracy associated with the raster sweep. As a further drawback, the requirement for eight oscilloscope channels reduced the number of pressure measuring channels available in the laboratory to a total of six.

During performance of the tests with air it was found that at low initial pressures the shock wave induced ionization was of sufficient magnitude to be detected by the ionization probe circuits. Indeed, calculations based on equilibrium conditions behind the shock indicated that for the 0.1 mm Hg tests the degree of ionization was considerably larger than the minimum detectable by the ion probe circuits, although for the 1.0 mm Hg

tests the calculations were inconclusive.

A typical oscillograph of the ionization probe outputs is illustrated in Figure 30.

2.6.3. Dynamic Strain Measurements

The design of the vessels included sufficient safety factors for the detonation pressures developed with 100 mm Hg test mixtures. For tests at 760 mm Hg initial pressure, however, the strength of the vessel was known to be marginal. To determine the initial pressure which would result in detonation pressures sufficiently high to cause failure of the vessel, dynamic strains were monitored at critical points on the vessel surfaces during tests performed with initial pressures intermediate to 100 and 760 mm Hg. In order to minimize the cost and complexity of the instrumentation, the BLH type SPB2-18-12 semiconductor strain gauge, which has a gain fifty times greater than that of a standard SR-4 gauge, was used. The semiconductor unit, consisting of a temperature compensated P-type silicon crystal element mounted on a bakelite base, was attached to the vessel by means of EPY 400 epoxy. The gauges were connected at the position where, on the basis of hydrostatic tests, maximum stress was expected. This corresponded, for vessel A, to the weld between the 18 inch neck and the hemispherical cap, and, for vessel CD, to the weld between the window block and the wall. In addition several gauges were attached to the cylindrical portion of vessel CD to provide an experimental verification for the analysis of reference 11, which describes a method of predicting the cylinder's stress response on the basis of a simple dynamic model of the vibrating

system and an approximate expression for the shape of the blast loading wave. Details of the method, which were considered too lengthy to include here, are completely described in reference 11, where it is demonstrated that analytical results compare satisfactorily with experimental stress measurements.

For the tests with vessel A the strain gauge was used as one leg of a wheatstone bridge, Figure 32. A typical output is shown in Figure 33 which shows also the record obtained with the neighboring pressure transducer, located several inches upstream. The response of the strain gauge, before the arrival of the detonation wave, is due to the wall vibration caused by bending stresses induced by the compressed gases behind the wave as well as oscillations produced by the Primacord explosion. Figure 34 shows the peak dynamic stress plotted as a function of initial pressure and indicates that the yield stress may have been exceeded at 760 mm Hg.

For tests with vessel CD a constant current circuit, Figure 35, was used. A typical strain record is shown in Figure 36 and peak dynamic stress at the critical location is plotted against initial pressure in Figure 37.

2.6.4. Temperature Measurements

Initial temperature of the test gas mixture was measured by means of two copper-constantan thermocouples, Thermo-Electric Company type Ce S 16-18-Dt, inserted into the vessel through appropriately drilled instrument plugs located at each end of the vessel to an approximate depth of 4 inches. Vessel wall temperatures were monitored by 20 copper-constantan thermocouples,

Honeywell type 9B1T4, attached with epoxy to the vessel surface. Since the semiconductor strain gauges employed for dynamic stress measurements are highly temperature sensitive, six additional thermocouples indicated temperatures immediately adjacent to these devices.

2.6.5. Schlieren System

Observations were made by a double mirror Schlieren system whose main components are shown on the schematic diagram of Figure 38. The two 12 inch diam spherical mirrors, M_1 and M_2, of 155 inch focal length, provide the collimated light beam through the test section which then focused at the knife edge, KE. The test section was focused on the film plane, FP, by the condenser lens, L_3. Deviations of the light beam caused by density gradients produced by disturbances in the field of view, led thus to a local increase and decrease in light intensity on the film plane, depending on the exact geometric arrangement of the system.

Schlieren light was supplied by the light source, LS. The condenser lens, L_2, focused this light at an opening, S, which then acted as a point light source for the system. Initial adjustment was produced by means of an ordinary projector lamp, PL, located in such a fashion that the condenser, L_1, focused the filaments of the lamp directly on the two electrodes of the light source, LS.

An air spark discharge light source was used, consisting of two 1/4 inch diam tungsten electrodes mounted on the same axis, with the gap separation between them maintained at approximately

1/8 to 3/16 inch. The discharge energy was supplied from an 1800 joule delay line circuit which produces a rectangular pulse of light for a duration of 1 msec. The breakdown of the air gap was achieved by raising momentarily the potential of a third trigger-electrode to 15 KV.

Photography was accomplished using the Southern Instruments model M 1020 rotating drum camera with a maximum writing speed of 2500 inches/sec. Seventy millimeter Tri X film with an ASA rating of 400 was used to record the process.

Detailed information on the Schlieren system is presented in reference 12, while a complete description of the light source can be found in reference 13.

2.7. Test Procedure

Schematic drawings of vessels A and CD are shown, respectively, in Figures 39 and 40, which show the location of the instrumentation, installed at 2 ft intervals along the length of the tube, with respect to the ends of the vessel and to the ignitor. Pressure transducers and ionization probes were located in the same axial position, but separated by 180°. For convenience, the instrument locations were numbered consecutively starting with position closest to the ignitor.

The experimental apparatus is shown schematically in Figure 41, while a block diagram of the instrumentation is presented in Figure 42. The detonation vessel was evacuated, then filled with combustible mixture to the desired pressure as indicated on the Wallace and Tiernan pressure gauge. The vessel was isolated from the mixing chamber by a 30,000 psi valve immediately adjacent

to it. Evacuating the gas feed line served to prevent flashback in case of failure of the valve. Final adjustments to the instruments were made and personnel were evacuated from the test area when a warning signal was sounded. Following this, the ignitor was actuated electrically from a protective enclosure. Then, the ball valve isolating the vacuum pump from the detonation vessel was opened and the combustion products were evacuated, preparing the vessel for the next test.

Wave velocities were measured by displaying signals from eight ionization probes on an eight channel oscilloscope, Tektronix type 551, with two type M plug-in units. The pressure transducer signals were displayed on two Tektronix type 533-A oscilloscopes, with types B and M plug-in units, providing a total of six measuring channels. This arrangement was subject to some variation, depending on the availability and state of repair of the equipment. Permanent oscilloscope records were obtained with Polaroid Land cameras. An amplified signal from the ionization probe adjacent to the ignitor served as trigger for all three oscilloscopes.

3. DETONATION TESTS

3.1. Data Reduction Method and Estimation of Errors

Due to the explosive nature of the Primacord ignitor, predetonative phenomena were essentially eliminated. At high initial pressures, an overdriven detonation was established almost immediately while at low initial pressures, where the Primacord energy was significant compared to the energy content of the reactive gases, a strong blast wave was generated. In both cases, then, the observed process consisted basically of a wave front which decayed in strength as it propagated along the length of the vessel. For this reason the experimental results are presented, in Figures 44 to 91, in the form of wave velocity and peak wave pressure plotted as a function of distance from the ignitor. For comparison the corresponding C-J parameters, obtained from reference 3, are also shown. To provide an estimate of the overpressures developed in the hydrogen-oxygen mixtures, the variation in shock velocity and pressure obtained from blank shots in air have been included with the room temperature results. Although for other initial temperatures air shock wave velocities and pressures are available only at the farthest position from the ignitor, these measurements together with the room temperature data provide sufficient information to assess the overpressures generated by the reactive mixtures over the entire range of environmental conditions.

The problems associated with the microphonic pickup of the ionization detection circuit, described in Section 2.6, precluded

the use of the raster sweep display of the signals. The use of individual oscilloscope channels in place of the raster resulted then in significant uncertainties in the flame velocity measurements, depending on the initial pressure. To compensate for the reduced accuracy, which in large part resulted from errors in reading the oscilloscope record, an improved method of data reduction was developed.

Initially, reduction of the data consisted primarily of reading time intervals between the signals from the ion gaps and pressure transducers, which were permanently recorded by a Polaroid Land camera on 2-1/2 x 3-1/2 inch positive prints. The wave velocity, V_g, was given then by the ratio $\Delta x/\Delta t$, where Δx is the separation between instruments, and Δt the measured time interval. Since Δx can be measured with negligible error, the accuracy of the velocity calculation, given to the first approximation by $\delta V_g/V_g = 2\delta t/\Delta t$, is determined by the precision, δt, with which the time axis of the record can be resolved. For example, if consecutive signals are separated by 1 cm on the record and the beam width is 0.5 mm, the accuracy of the calculated velocity is ±5%.

To minimize the error and eliminate at the same time the zigzag velocity distribution associated with it, the time of arrival of each signal, measured from a common origin and including the uncertainty, δt, was plotted against position of the ion gauge on the space-time plane, determining in essence the flame world-line, i.e., its trajectory in the t-x diagram such as that of Figure 43. Since the characteristic length of local changes

in the process should be much smaller than the distance between instruments, a smooth curve could be drawn through the points, within their regions of uncertainty, from which average wave velocities over each interval were then deduced by differentiation. In this manner local variations could be recognized as abrupt changes in the shape of the world-line.

In order to insure the validity of the results, a minimum of two tests were performed at each condition. When necessary, additional tests were performed to establish the pressure measurements within an accuracy of 25%. However, the considerable range* of measurements indicated by the vertical bars in Figures 44 to 120 showed that, in general, reproducibility was poor. This is attributed primarily to variations in the initiating process, as evidenced by the fact that the relative spread of data became greater at lower initial pressures where the explosive energy of the Primacord ignitor was significantly large in comparison with the chemical energy of the reactants.

It was intended originally to check the detonation velocities deduced from the ion probe signals with those calculated from time intervals measured between successive pressure transducers. However, velocities based on pressure records were consistently larger than those determined from the ionization gauges, the difference often exceeding the uncertainty in the two measurements. This discrepancy cannot be explained on the basis of such

---

*Here the term range denotes the maximum uncertainty in the observed quantity including both the inaccuracy in the individual measurement and the maximum difference between a group of measurements.

effects as tilting of the wave front with respect to the axis of the vessel, and, as yet, remains unsolved. Since the ion gaps were considered more reliable, the flame velocities presented in Figures 43 to 91 are restricted to these data, with the exception of the +200 and -50°F tests where both measurements are shown to illustrate the differences between the two.

A typical pressure transducer oscillograph is illustrated in Figure 29. Accuracy of pressure measurements was affected by three factors. First, it was unlikely that the sharp spike present in the initial signal represented an actual pressure, but rather it was characteristic of the response of the transducer. Second, the oscillation of the signal following the initial pulse, caused in all probability by the ringing of the transducer, often degraded the readability of the records. Last, at low initial pressures the magnitude of spurious signals generated by the vibration of the vessel walls was comparable to the true signal, thus obscuring the latter seriously. On the basis of calibration tests performed with the transducers, it was estimated that the accuracy of the pressure measurements ranged from 5-10% for 100 mm Hg initial pressure tests to 25-30% for the 0.1 mm Hg conditions. The shock tube calibration also provided correction factors applicable to the nominal response characteristics of the transducers.

3.2. Experimental Results

Measured wave velocities and pressures are plotted against distance from the ignitor in Figures 44 to 67, 68 to 77, and 78 to 91 for the 2 x 20, 3 x 20, and 2 x 40 vessel, respectively.

Since for nearly all conditions the wave properties were observed either to decay with distance or to remain relatively constant, the measurements obtained at the last instrument position were chosen for comparison with the corresponding C-J parameters, whose values have been indicated on the figures.

It should be noted that results of the 10 mm Hg initial tests are inconclusive with respect to the establishment of a steady wave, since the room temperature results in the 20 ft vessel indicate that such a wave is formed, while tests in the 40 ft vessel indicate a decaying wave whose velocity at the end of the tube is less than the C-J velocity. The results are further obscured by an inconsistency in the two sets of experimental data, wherein the wave velocity at the beginning of the second half of the 40 ft vessel exceeds that at the end of the 20 ft vessel. In addition, the apparently good agreement between experimental and theoretical velocities at 1 mm Hg initial pressure is entirely coincidental and, as shown later, a consequence of the method of ignition.

Tests at an initial pressure of 0.1 mm Hg were performed at room temperature only. As a consequence of the strong ignition, wave velocity and peak pressure, while considerably in excess of the corresponding C-J values, were nearly the same as those in air. In view of this, and since the wave pressures were of the order of only a few mm Hg, it was concluded that these results would not contribute information of significant value to the objective of the overall program. On this basis, 0.1 mm Hg tests at other initial temperatures were excluded from the remainder of the experimental schedule.

Test results of the complete program are discussed below.

3.2.1. 2 ft diam x 20 ft long Vessel

3.2.1.1. Room Temperature Tests

A. 100 mm Hg initial pressure

Figures 44 and 45, respectively, show wave velocities and peak pressures developed in the four test media at an initial pressure of 100 mm Hg. Steady detonation in the reactive mixtures was established at a distance of from 8 to 12 ft from the ignitor, varying slightly with composition, although the wave velocity was 5-7% less than its theoretical value. The peak pressures developed in equimolar and stoichiometric mixtures decayed along the length of the vessel acquiring, at the last position, values in agreement with the theoretical C-J pressures. In contrast to this, an increase in pressure over the wave path was observed in $3H_2 + O_2$ mixtures, from 25 psia at the initial point of measurement to 32.5 psia, or nearly 7% below C-J pressure, at the last position.

Results of the blank shots show both velocity and pressure of the air shock wave generated by the Primacord explosion are roughly 4 times less than those corresponding to the detonation in the reactive mixtures.

B. 10 mm Hg initial pressure

Velocities measured at 10 mm Hg initial pressure, Figure 46, exhibited characteristics similar to those observed at 100 mm Hg: after an initial decay a steady wave formed at a distance of about 10 ft from the ignition point, although the average velocities were from 3 to 12% below C-J values. Measured

peak wave pressures, Figure 47, were in good agreement with the theoretical C-J pressure in equimolar mixtures. Pressures measured in $2H_2 + O_2$ and $3H_2 + O_2$ mixtures exhibited, however, a gradual decay from the point of ignition and at the last position were 16 and 26%, respectively, above the theoretical values.

With the reduction in initial pressure from 100 to 10 mm Hg, the air shock wave generated in the blank shots becomes stronger, with both velocity and pressure now half as large as their corresponding values in the reactive mixtures.

C. 1 mm Hg initial pressure

The measured wave velocities, Figure 48, indicated that a steady wave was not established within the available 20 ft of travel since at the end of the vessel the velocities were still decaying although, coincidentally, they were in good agreement with the C-J values. Average pressures, Figure 49, however, were about twice the corresponding C-J values at the last position and also showed a tendency for further decay.

At this initial pressure, both the velocity and pressure of the air shock wave are comparable in magnitude to those observed in the hydrogen-oxygen mixtures. This indicates the significant influence of the initiating blast on subsequent wave propagation and suggests that appreciable chemical reaction does not occur even in the shock compressed medium.

D. 0.1 mm Hg initial pressure

Both wave velocities, Figure 50, and peak wave pressures, Figure 51, are nearly independent of the composition of the hydrogen-oxygen mixtures and exceed the corresponding C-J values

by 1.5-2.0 and 6-10 times, respectively. Similar to the 1.0 mm Hg tests, results of blank shots are nearly identical to those obtained with the reactive mixtures. Included in Figures 50 and 51 are results of calculations based on one-dimensional blast wave theory. A more detailed discussion of these calculations is presented in Section 3.3.3.

3.2.1.2. +200°F Tests

A. 100 mm Hg initial pressure

Figures 52 and 53, respectively, show wave velocities and peak pressures as a function of distance from the ignitor in a $3H_2 + O_2$ mixture. The wave velocity plot, Figure 51, shows measurements based on both the ionization probes and the pressure transducers. Both measurements are in good agreement with the theoretical C-J value, although results obtained from the pressure transducers are about 4% higher than those determined from the ion probe data. In contrast to the room temperature tests, a steady wave is established less than 5 ft from the ignitor.

The peak pressure measurements, Figure 53, show the same trend of a gradually increasing pressure observed for the room temperature tests. Within the experimental accuracy, the peak pressures recorded at distances 13.5 and 15.5 ft from the ignitor agree with the theoretical C-J values, although the average measured pressure is 7% less.

B. 10 mm Hg initial pressure

Measured wave velocities, Figure 54, show evidence of an initially overdriven wave, although a steady wave is

apparently established at a distance 10 ft from the ignitor. Again velocities based on the pressure transducers are 4% greater than those obtained from the ion probe measurements, although both are again in good agreement with the theoretical C-J value.

The variation of peak wave pressure along the length of the vessel, Figure 55, is similar to that observed for a $3H_2 + O_2$ mixture at room temperature. In contrast to the velocity measurements, however, the peak pressure recorded 17 ft from the ignitor was about 20% in excess of the C-J pressure.

C. 1.0 mm Hg initial pressure

Both the magnitude of the measured wave velocities and pressures, Figures 56 and 57, respectively, and their variation along the length of the vessel were quite similar to those observed at room temperature. This demonstrates again that the Primacord explosion plays a prominent role in the subsequent wave propagation at initial pressures below 10 mm Hg.

3.2.1.3. -50°F Tests

A. 100 mm Hg initial pressure

Figure 58, showing wave velocity plotted along the length of the vessel, indicates a steady wave is established within 10 ft of the ignitor, in agreement with previous results for a $3H_2 + O_2$ mixture. The wave velocity is now, however, several per cent greater than the corresponding C-J value and again measurements based on the pressure transducer records are about 4% higher than those determined from the ion probe signals.

Figure 59 shows that the peak wave pressure remains relatively constant over the span of the vessel, although pressure

measurements were not available over the last 7 ft of travel. In contrast to results at higher temperature, however, the wave pressure is larger than the theoretical C-J pressure, exceeding it by approximately 20%.

B. 10 mm Hg initial pressure

Wave velocity measurements, Figure 60, are in agreement with results at higher initial temperatures, indicating the establishment of a steady wave at a distance of 8-10 ft from the ignitor and showing the same discrepancy between the pressure transducer and ionization probe data. The steady wave velocity is about 5% less than the C-J value for a $3H_2 + O_2$ mixture. Because of icing problems discussed earlier, only two pressure measurements are available, Figure 61, both at positions less than 10 ft from the ignitor.

C. 1.0 mm Hg initial pressure

Results, Figures 62 and 63, are similar to those obtained at higher initial pressures, showing gradual deceleration of the wave along the length of the vessel. Pressure measurements are again restricted to two transducers, both indicating pressures nearly twice as large as the theoretical C-J value.

3.2.1.4. -180°F Tests

A. 100 mm Hg initial pressure

At an initial pressure of 100 mm Hg and initial temperature of -180°F, it was possible to generate detonation in the three hydrogen-oxygen mixtures with the spark ignitor. Consequently, tests with the Primacord ignitor were not performed at this condition.

Figure 64, the wave velocity measurements, indicates the establishment of a steady wave at a distance of 5-7 ft from the ignitor and shows in each case that the experimental velocity is within several per cent of the corresponding C-J values. The peak wave pressures, Figure 65, are also relatively constant over the last 15 ft of travel, but are roughly 1/3 to 1/2 larger than the C-J pressures.

B. 10 mm Hg initial pressure

The variation of wave velocity along the length of the vessel, Figure 66, is similar to that observed at higher initial temperatures, with a steady wave established within 10 ft of travel from the ignitor. For each mixture, however, the steady wave velocity was 10-14% less than the corresponding C-J value, the largest discrepancy occurring for the equimolar mixture. In addition, for a stoichiometric hydrogen-oxygen mixture the wave velocity increased slightly near the end of the vessel. The pressure transducer records, which were much more difficult to interpret at the -180°F condition, indicate peak pressures, Figure 67, ranging from 30 to 50% greater than the theoretical C-J pressures over the last 10 ft of the vessel.

3.2.2. 3 ft diam x 20 ft long Vessel

Tests in the 3 ft vessel were restricted to room temperature experiments in equimolar mixtures at initial pressures ranging from 760 to 0.1 mm Hg. Taking into account the increased diameter, results are similar to those obtained in the 2 ft vessel.

Wave velocities and peak pressures for the 760 mm Hg test are shown, respectively, in Figures 68 and 69. Although a steady

wave would be expected, the velocity measurements, Figure 68, are erratic, varying from 1 to 3% less than the C-J velocity. The peak wave pressures, Figure 69, are more nearly constant, although approximately 4% less than the C-J pressure.

Results at 100 and 10 mm Hg, shown in Figures 70 and 71 and Figures 72 and 73, respectively, are in good agreement with those obtained in the 2 ft vessel and are not discussed further. At 1.0 and 0.1 mm Hg initial pressure, test results, shown in Figures 74 and 75 and Figures 76 and 77, respectively, are similar to those for the 2 ft vessel although, due to the increase in tube diameter, both wave velocity and pressure are slightly smaller than obtained previously.

3.2.3. 2 ft diam x 40 ft long Vessel

Tests in the 40 ft vessel were restricted to equimolar mixtures initially at room temperature and at initial pressures ranging from 600 to 1.0 mm Hg.

Due to the limited number of instruments available, measurements in the 40 ft vessel were restricted to the last 20 ft, since it was felt that they could be combined with the results of tests in the 20 ft vessel to provide a complete set of data over the entire span of the detonation tube. As shown below, this procedure was not particularly successful.

At 600 mm Hg, tests were performed with both Primacord and spark ignition and results are shown in Figures 78 and 79 and Figures 80 and 81, respectively. With Primacord ignition, wave velocities, Figure 78, were constant at each instrument position, although, while the measurements based on the ionization probes

were in agreement with the C-J velocity, those based on the pressure transducers were 8% higher. On the other hand, with spark ignition, Figure 80, the pressure records indicated a constant velocity 3% greater than the C-J value while the ion probe measurements did not indicate a steady wave. In both instances the peak wave pressures were not constant along the length of the vessel, with slightly larger pressures evident in the case of spark ignition.

At an initial pressure of 400 mm Hg, the velocity measurements, Figure 82, made with pressure transducers and ionization probes were in agreement, although both indicated an overdriven wave over the distance from 25 to 38 ft from the ignitor. This is somewhat surprising since previous results in the 20 ft vessel would indicate that a steady wave should have been established earlier. Peak wave pressures, Figure 83, are again less than the C-J pressure, by amounts ranging from 30% at a distance 25 ft from the ignitor, to 15% at 37 ft from the ignitor.

Wave velocity measurements at 200 mm Hg initial pressure, Figure 84, again indicate an overdriven wave which steadies out to the C-J velocity at the end of the vessel. Again, however, measurements based on the pressure transducers are about 7% higher than the velocities deduced from the ionization probes. The peak wave pressures, Figure 85, follow roughly the same trend observed at higher initial pressures and are 10 to 15% less than the C-J pressure.

Tests in the 40 ft vessel gave the first indication that a steady wave cannot be sustained at an initial pressure of 10 mm Hg.

At this condition both wave velocities, Figure 86, and peak pressure, Figure 87, continually decay over the distance from 20 to 40 ft from the ignitor and are significantly less than the C-J values at the end of the vessel.

The 1.0 mm Hg initial pressure tests, however, yielded results in contradiction to those above as well as the previous results in the 20 ft vessel. The wave velocity measurements, Figure 88, indicate that a steady wave, which propagates at the C-J velocity, is established 30 ft from the ignitor. The peak wave pressures, Figure 89, are about 75% greater than the C-J pressure over the last 8 ft, although it falls abruptly to the C-J value at the end of the vessel. These results, together with those obtained in the 20 ft vessel, Figures 48 and 49, are replotted in Figures 90 and 91. These diagrams, in particular the wave velocity measurements, Figure 90, show quite clearly that the results of the two tests do not match. This suggested the possibility that, in spite of precautions taken during fabrication, an irregularity may have existed at the junction between the two 20 ft sections, which, in turn, could have disturbed the process. However, the results of later tests, performed under conditions which were felt to be more sensitive to variations or discontinuities in the cross-sectional area, did not support this premise.

3.3. Discussion of Results

3.3.1. Reliability of Pressure Measurements

In addition to providing a basis for estimating the overpressures in hydrogen-oxygen mixtures, the Primacord shots in air were useful in establishing the reliability of the pressure measurements.

As stated earlier, wave velocities and pressures in the reactive mixtures were observed to decay slightly or remain relatively constant over the latter portion of all the vessels used in the test program. Consequently, the parameters measured at the last position in the vessel were chosen for comparison with the properties of the theoretical C-J state. Velocities measured at the end of the 2 x 20 vessel are plotted against initial pressure in Figure 92 for all four test media. The air data are replotted in Figure 93, which includes also the results of blank shots in the 3 x 20 vessel, the difference between the two arising from the change in tube diameter.

Using the experimental velocities shown in Figure 92 for air, the corresponding pressures were calculated from the normal shock relations:

$$\frac{P_2}{P_1} = 1 + \frac{2\gamma(M_1^2-1)}{\gamma+1} \qquad (1)$$

where P_1 and P_2 are the upstream and downstream pressures, respectively, M_1 is the upstream Mach number of the shock, and $\gamma = 1.4$, the specific heat ratio. The results of these calculations are plotted in Figure 94 together with the pressures measured at the last instrument position.

A similar comparison was made between the experimentally measured reflected pressure and those computed from the incident shock velocity in air, using the following relation between incident pressure, P_2, and reflected pressure, P_r (14):

$$\frac{P_r}{P_2} = \frac{\left(2\mu^2+1\right)\frac{P_2}{P_1} - \mu^2}{\mu^2 \frac{P_2}{P_1} + 1} \qquad (2)$$

where P_1 is the initial pressure and $\mu^2 = \frac{\gamma-1}{\gamma+1} = 0.1668, \gamma = 1.4$ denoting the ratio of specific heats. Results of the calculations, together with measured reflected pressures, are shown in Figure 95.

These plots, Figures 94 and 95, show that at initial pressures above 1 mm Hg, agreement between calculated and measured pressures was within the experimental accuracy. For initial pressure 1 mm Hg and less, measured pressures were in some cases slightly less than those calculated from the shock velocity although, in general, a fair agreement between the two was obtained.

A similar check was performed for the other initial temperature conditions where, however, measurements were restricted to the pressure behind the incident shock wave at the last instrument position. Results, shown in Figure 96 for initial temperatures of +200 and +70°F (repeated here for direct comparison) and Figure 97 for initial temperatures of -50 and -180°F, show that in most cases the measured and calculated values agree to within the experimental accuracy. The results of the blank shots then demonstrate the consistency of the pressure measurements and establish a reasonable level of confidence in the results obtained with the reactive mixtures.

3.3.2. Influence of Primacord Ignitor

The influence of the blast wave generated by the Primacord ignitor on the subsequent wave propagation process can be observed

in Figure 93, where wave velocities measured at the last position in both the 2 x 20 and 3 x 20 vessels have been plotted as a function of initial pressure for air and the equimolar hydrogen-oxygen mixture. The air curves show clearly the effect of the size of the vessel on the strength of the shock wave in a chemically inert medium. For the reactive mixture at initial pressures above 10 mm Hg, the wave velocity is independent of the size of the vessel, indicating that the wave propagation process is dominated by the chemical reaction which it initiates. It is of interest to note that while the velocities in the two vessels are nearly identical at these conditions they are both about 7% less than the corresponding C-J values. The constancy of the wave velocity over the last few feet of travel and the fact that the size of the vessel has no apparent effect on it, would seem to indicate that a steady detonation can be sustained at an initial pressure of 10 mm Hg, although both the velocity deficit and the results with the 40 ft vessel tend to contradict this. This point remains unresolved.

At an initial pressure of 1.0 mm Hg, the wave velocity in both vessels, and in particular in the 2 ft vessel, is slightly larger than what would be expected from extrapolation of the results at high initial pressures. Since the inert shock velocities are already quite large at this pressure, it is difficult to assess to what extent chemical reaction proceeds in the hydrogen-oxygen mixture, although, on the basis of results with $2H_2 + O_2$ and $3H_2 + O_2$ mixtures in the 2 ft vessel, Figure 92, it apparently does contribute to the wave propagation.

At an initial pressure of 0.1 mm Hg the wave velocities in each vessel are nearly identical to those of the air shocks indicating clearly that the Primacord explosion completely dominates the wave process. This is further substantiated by measurements in $2H_2 + O_2$ and $3H_2 + O_2$ mixtures in the 2 ft vessel, Figure 92. It appears then that the effects of the Primacord explosion become significant at an initial pressure of a few mm Hg. This also explains the apparent agreement between experiment and theory at an initial pressure of 1.0 mm Hg. By sheer coincidence, the blast wave generated by the Primacord at this condition acquires a velocity, at the end of the 20 ft vessel, which is comparable to the C-J velocity.

3.3.3. <u>One-dimensional Blast Wave Theory</u>

On the basis of the foregoing discussion an attempt was made to rationalize the results obtained at low initial pressures by means of one-dimensional blast wave theory. Assuming a perfect, inviscid gas, the one-dimensional equations of conservation of mass, momentum, and entropy, valid in the region bounded by the blast wave, are given by (15):

$$\frac{\partial \rho}{\partial t} + \frac{\partial}{\partial r}(\rho u) = 0 \tag{3}$$

$$\frac{\partial u}{\partial t} + u\frac{\partial u}{\partial r} + \frac{1}{\rho}\frac{\partial p}{\partial r} = 0 \tag{4}$$

$$\frac{\partial}{\partial t}\left(\frac{p}{\rho^{\gamma}}\right) + u\frac{\partial}{\partial r}\left(\frac{p}{\rho^{\gamma}}\right) = 0 \tag{5}$$

where ρ is the density of the gas, p the pressure, u the particle

velocity, γ the specific heat ratio, and the independent variables r and t stand for distance and time, respectively.

For intense blasts only E, a function of the energy release, and ρ_1, the initial gas density, affect the motion and the independent variables are so related that the above equations can be reduced to ordinary differential equations for which exact self-similar solutions are possible. The boundary conditions which have to be satisfied are that the particle velocity remain zero at the origin and that the Rankine-Hugoniot equations are satisfied across the shock front. For intense blasts the above equations reduce to the following (15):

$$u_2 = \frac{2}{\gamma+1} C \tag{6}$$

$$\rho_2 = \frac{\gamma+1}{\gamma-1} \rho_1 \tag{7}$$

$$p_2 = \frac{2}{\gamma-1} \rho_1 C^2 \tag{8}$$

where C is the shock velocity and subscripts 1 and 2 identify conditions ahead of and behind the shock.

The motion of the shock front is given by (15, 16):

$$r = \left(\frac{E}{\rho_1}\right)^{1/3} t^{2/3} \tag{9}$$

from which the shock velocity can be found:

$$C = \frac{dr}{dt} = \frac{2}{3}\left(\frac{E}{\rho r}\right)^{1/2} \tag{10}$$

Substituting Eq. 10 into Eq. 8 yields finally an expression for the pressure, p_2 , behind the shock wave:

$$p_2 = \frac{8}{9} \frac{E/r}{\gamma+1} \tag{11}$$

which is independent of the initial pressure, p_1 .

The value of E used in the above equations is given by (13):

$$E = \frac{E_0}{\alpha A}$$

where E_0/A represents the energy release per unit area, and the constant $\alpha = \alpha(\gamma)$ is determined from the assumption that the total energy of the medium disturbed by the wave is invariant. For $\gamma = 1.4$ it is found that $\alpha = 1.08$ (reference 16).

The results of the blast wave theory are not directly applicable since the analysis assumes a plane explosive source, whereas the Primacord ignitor closely resembles a point source. Thus in the immediate vicinity of the ignitor, the initial shock wave is spherical in nature and the one-dimensional analysis would be applicable only at some distance from the ignitor. In addition, the blast energy absorbed by the vessel walls and the ignition holder has not been taken into account.

A number of investigators (see, e.g., Glass (15) and Brode (17)) have pointed out that, although the explosion is influenced by its initial history, the shock wave decay can be expressed eventually by inverse laws of the type given in Eqs. 10 and 11. Hence the parameter E/r was adjusted by a scaling factor, B ,

to provide a satisfactory fit between the calculated peak pressures and those measured in air at an initial pressure of 0.1 mm Hg. The value of B was found to be 0.22. Since, at this condition, the pressures measured at the last instrument position were nearly identical for all four test media, agreement with calculated pressures in the hydrogen-oxygen mixtures was obtained also, Figure 51. This result is in agreement with Eq. 11, which shows that the blast pressure is independent of initial gas density.

The wave velocities calculated on the basis of $B = 0.22$ did not provide as good an agreement with experimental data as did the pressures, yielding values within 20-30% of the velocities measured at the last position in the vessel, Figure 50. Furthermore the calculations for air were less than the measured velocities while those for the hydrogen-oxygen mixtures were greater than the observed values, indicating the limited applicability of the theory.

3.3.4. Correlation of Results

A check similar to that performed with the results of the air shots was carried out for the pressures measured in the reactive gas mixtures. For the room temperature tests with $H_2 + O_2$ mixtures, incident peak wave pressure, measured at the last position in the vessel, and reflected wave pressure are plotted as a function of initial pressure in Figures 98 and 99, respectively. Results in both the 2 and 3 ft diam vessels are shown and included also are the theoretical C-J pressures and the pressures calculated from the velocities of Figure 92, assuming a non-reactive shock wave.

At initial pressures of 100 and 10 mm Hg the experimental measurements are somewhat greater than the theoretical pressures. In addition, for the 10 mm Hg test in the 3 ft vessel the measured pressure exceeds even that calculated for a non-reactive shock. At initial pressures of 1.0 and 0.1 mm Hg, the 2 ft vessel data are in fair agreement with the non-reactive shock pressures while the data from the 3 ft vessel again exceed the calculated shock pressures.

Curves of incident and reflected pressures as a function of initial pressure are plotted in Figures 100 and 101 and Figures 102 and 103 for $2H_2 + O_2$ and $3H_2 + O_2$ mixtures, respectively. They include also the C-J pressures and those calculated from the velocities of Figure 92 for a non-reactive shock. At initial pressures of 100 and 10 mm Hg, the figures show a similar comparison between measured pressures and the corresponding C-J values as observed for $H_2 + O_2$ mixtures while at lower initial pressure the experimental data exceed slightly the non-reactive shock pressures. This trend was observed, in fact, for all tests and is somewhat surprising, since the air shots, which served also as a calibration of the transducers, showed that the pressure pickups indicated slightly lower pressures than those calculated from the shock velocity. For direct comparison with results of tests at other temperatures, Figure 92 has been replotted in Figure 104 where now the velocities based on the pressure transducers have been included with the ion probe measurements. In addition, Figures 98-103 have been combined into a single diagram, Figure 105, where the non-reactive shock calculations have been omitted.

Similar diagrams of wave velocity and peak incident wave pressure plotted as a function of initial pressure for the +200, -50, and -180°F tests are presented, respectively, in Figures 106 and 107, Figures 108 and 109, and Figures 110 and 111. In general, the agreement between experiment and theory is similar to that observed at room temperature although the discrepancies are somewhat larger and it becomes apparent that the measurements are less consistent at the lower initial temperatures. This is indicated more clearly in the plots of wave velocity and wave pressure versus initial temperature which are shown in Figures 112 and 113, Figures 114 and 115, and Figures 116 and 117 for the 100, 10, and 1.0 mm Hg tests, respectively.

A final correlation presenting wave velocity and wave pressure as a function of hydrogen concentration is given in Figures 118 and 119 and Figures 120 and 121 for the +70 and -180°F initial temperature tests. Since only the 100 and 10 mm Hg initial pressure tests provided evidence of steady wave propagation, they are the only results included. These figures illustrate quite clearly that in general the measured velocities are lower than the theoretical C-J values, with the differences becoming larger at lower initial pressures where it is unlikely that detonation is self-sustaining. The measured pressures, however, which are in fair agreement with theory at room temperatures, exceed the corresponding C-J values by as much as 50% at the low initial temperature conditions. While the few exceptions to this may not be significant, they prevent any specific conclusions from being reached. On the basis of the present data it is difficult to

attribute the observed discrepancies to any particular cause such as wall effects or wave structure. In fact, because of the large diameter of the vessel, boundary layer effects should be minimized leading to a smaller velocity deficit than observed in conventionally sized laboratory equipment. However, in view of the excessive wave pressures, which are approximately 50% larger than the C-J values at low initial temperatures, it is felt that further investigation is warranted, particularly at low temperatures where the effect is most pronounced.

3.3.5. Schlieren Photographs

To supplement the velocity and pressure measurements described above, several photographs of the wave process were obtained using the streak Schlieren technique. Optical observations were restricted to the 100 and 10 mm Hg initial pressure tests, since the sensitivity of the Schlieren system was inadequate at lower pressures. In addition, on the basis of the velocity and pressure measurements it was concluded that the process was not altered significantly by changes in the initial temperature. Consequently, the Schlieren observations were further restricted to the room temperature tests.

A typical Schlieren record, representing the space-time history of the wave process in a $3H_2 + O_2$ mixture initially at 100 mm Hg is shown in Figure 122. The abscissa represents the distance along the axis of the vessel and the ordinate denotes the time while the field of view was 18 ft from the Primacord ignitor. The photograph shows a steady detonation wave propagating to the right, depicted by the dark diagonal line emanating

from the origin and, approximately 0.7 msec later, the reflected shock was traveling to the left. The wavy appearance of the detonation and the short bright streaks which follow it are manifestations of wave structure usually observed under these conditions.

The complete space-time diagram of this test is shown in Figure 123 where the space-time location of Figure 122 is shown as an insert. For comparison, the wave trace, as determined from both ion probe and pressure transducer measurements and from the photograph of Figure 122, is included. While slight differences are apparent and may be accounted for by experimental inaccuracies, on the whole the various methods of observation provide a consistent representation of the process.

4. PREDETONATION STUDIES

4.1. Flame Acceleration

When weak ignitors, such as spark discharge or heated plate, are used, the establishment of detonation is preceded by an induction period whose duration is determined by the composition and initial conditions. Figure 124 shows a number of streak Schlieren photographs, representing the space-time history of the process, of an accelerating flame in an equimolar mixture of hydrogen and oxygen initially at 100 mm Hg and 70°F. The mixture was contained in the 2 x 20 vessel and ignition was by means of spark discharge. The abscissa represents distance from the ignitor and the ordinate denotes the time. The flame front is depicted by the bright line curved diagonally up to the right. Similar traces behind the front are manifestations of the structure of the flame surface, although it is apparent that the flame propagation is relatively laminar. The trace of the flame front of Figure 124 has been replotted in Figure 125 where the photographs of Figure 124 are included as inserts. The single dashed line represents the front of the flame while the double dashed line corresponds to the structure observed in Figure 124. The solid lines at the top of the diagram denote the pressure wave and the flame path deduced from the ionization probe signals.

Similar space-time diagrams for $2H_2 + O_2$ and $3H_2 + O_2$ mixtures initially at 100 mm Hg and 70°F are shown in Figures 126 and 127. Inserts show the space-time location of streak Schlieren photographs which, because of their resemblance to those of Figure 124, have not been shown.

The flame path of Figure 126 has been reproduced in Figure 128 where the pressure profiles measured at four adjacent instrument positions have been included to depict the growth of the pressure pulse generated by accelerating flame. The process was analyzed using the method developed in previous studies in small sized equipment (18, 19, 20). The combustion front, expanding in space about the ignition source, is considered to act as an equivalent plane, moving heater, which releases heat at the same rate as the flame. The generation of pressure waves is then attributed to the increase in the rate of heat release per unit cross-sectional area of the vessel. Under the present circumstances, where ignition occurs at a point and the flame grows in the form of a hemisphere, the flow velocity immediately ahead of the flame is given by the expression:

$$U \equiv \frac{u}{a_o} = 2KVX_f^2 \qquad (12)$$

where

$$K = \frac{\mathcal{R}}{\Gamma_2} \Big/ \left(1 + \sqrt{\frac{\gamma_1}{\gamma_2}\,\frac{\mathcal{R}+\Gamma_1}{\Gamma_2}}\right)$$

$$\mathcal{R} = \gamma_1 q / a_o^2 \qquad V = S/a_o$$

$$\Gamma = \frac{\gamma}{\gamma - 1} \qquad X_f = \frac{x_f}{r}$$

γ being the specific heat ratio of the mixture, q the heat of combustion, a_o the sound speed of the undisturbed medium,

S the constant relative speed of propagation of the flame front, x_f the axial distance traveled by the flame, r the radius of the vessel, and subscripts 1 and 2 denote conditions immediately ahead of and behind the front, respectively.

The flame world-line--its path in the space-time plane--is found from

$$T_f = \int_0^{X_f} \frac{dX_f}{V+U} \tag{13}$$

where $T_f = \frac{a_c t_f}{r}$. With Eq. (12), Eq. (13) becomes

$$T_f = \frac{X_f^2 \sqrt{2K}}{U} \tan^{-1} X_f \sqrt{2K} \tag{14}$$

Defining now $Y = T_f U$, we obtain finally:

$$Y = X_f^2 \sqrt{2K} \tan^{-1} X_f \sqrt{2K} \tag{15}$$

which depends only upon the parameter K, independent of the relative flame propagation speed. Equation (15) can be used to evaluate K and subsequently, through Eq. (12), the flame speed, S.

Equation (15) is plotted on the Y-X plane with K as a parameter, Figure 129. On the same plane the world-lines of the simple pressure wave deduced from the pressure records of Figure 128 are mapped. For this purpose each is expressed in the form

$$Y = \left[\frac{1}{U} + \frac{\gamma - 1}{2} \right]^{-1} X + UT^{\circ} \tag{16}$$

where τ^o is the non-dimensional value of the time coordinate of the intersection of the wave world-lines with the $X = 0$ axis of Figure 128. They appear in Figure 129 as a family of straight lines for $U = 0.035$, 0.069, and 0.101, respectively. Finally, the Y-X coordinates of the intersection of the pressure waves with the observed flame world-line are plotted in Figure 129, as denoted by the small crosses. Their location indicates that the value of K lies between 0.6 and 0.7 corresponding to $\mathcal{R} = 9.6$ and 11.7, respectively. Assuming that the flame is characterized by $\mathcal{R} = 11.0$ the value of S determined from Eq. (12) is 50 m/sec.

With these parameters the flame world-line is evaluated according to Eq. (14), while the pressure profiles at the first three instrument positions are computed from the simple wave relation

$$t = \left[\left(1 + \tfrac{\gamma+1}{2} U\right) a_o \right]^{-1} (x - x_f) + t_f$$

where x is the distance between the transducer and the ignitor. Results, denoted by the small circles in Figure 128, are in remarkable agreement with experiment, demonstrating that the theory provides a valid rationalization of initial flame acceleration regardless of the size of the apparatus. It is of interest to note, however, that the value of $\mathcal{R}$ deduced above is approximately 1/3 of that determined from analysis of earlier results (20) obtained at 1 atmosphere in a 1 x 1-1/2 inch tube. While reduction in initial pressure and increased tube size may contribute to changes in $\mathcal{R}$, the exact significance of the large

difference in its magnitude is not yet understood. It should be emphasized, however, that the parameter $\mathfrak{P}$ reflects the consequences of ideal gas behavior assumed for the combustible mixture and thus may not be exactly equivalent to the heat of reaction.

A space-time diagram of the flame acceleration process over the entire length of the 2 x 20 vessel is shown in Figure 130 for an equimolar hydrogen-oxygen mixture initially at 100 mm Hg and 70°F and ignited by spark discharge. The flame, after an initial period of acceleration during which it generates a pressure with peak strength, ΔP, of 3 psi, acquires a nearly constant velocity of 1240 ft/sec. The reflection of the precursor shock and its subsequent interaction with the flame front are shown in detail. A similar diagram showing results obtained with hot plate ignition is shown in Figure 131. The close resemblance to Figure 130 demonstrates that the process is independent of the method of ignition, which is to be expected in the present instance where both ignitors behave essentially as point sources.

Figure 132 shows results obtained in the 3 ft vessel under the same conditions as those of Figure 130. In view of the increased vessel diameter the faster flame speed is somewhat surprising, although it may be due to re-enforcement of the pressure wave by the concave shape of the end-cap of the vessel.

The most significant feature of the foregoing results is the fact that transition to detonation does not occur in the 20 ft long vessel when the initial pressure is 100 mm Hg or less. Figure 132, however, shows the appearance of a strong shock wave approximately 40 msec after ignition, indicating that an explosive

process takes place near the far end of the tube after a number of interactions between the flame and re-reflected shock waves.

A final space-time diagram of the process, for initial conditions identical to those of Figure 130, in the 2 x 20 vessel is shown in Figure 133. It indicates the location of the streak Schlieren photograph of Figure 134 which reveals the details of a typical interaction between the flame and shock waves reflected from the end of the vessel. Shock waves traveling to the right appear as bright straight lines, while those moving to the left, after reflection from the end of the vessel, are represented by dark lines. The reaction zone, which occupies nearly 70% of the record, appears as a distinct front moving diagonally up to the right, followed by a great number of wavy streaks which are indicative of the structure of the flame surface. The record demonstrates quite clearly the limitations imposed on this method of observation when the field of view is comparable to the diameter of the vessel.

4.2. Initiation of Detonation

To provide a greater length of travel, a number of tests were performed with spark ignition in the 2 x 40 vessel at initial pressures ranging from 100 to 400 mm Hg and initial temperatures of +70°F. In these tests detonation was always initiated either behind the incident precursor shock wave or as a result of its reflection from the end wall. Results are presented in Figures 135-150, in the form of space-time diagrams.

Figure 135 shows a composite space-time diagram of the wave

interaction pattern observed in a spark-ignited $H_2 + O_2$ mixture initially at 100 mm Hg and 70°F. It includes data from both the 2 x 20 and the 2 x 40 vessels, demonstrating the consistency of the experimental measurements and, more significantly, illustrating the influence of the length of travel on the initiation of detonation. In the former instance the pressure wave preceding the flame reflected from the end of the vessel and caused a gradual slowing down of the flame and, after re-reflection from the ignitor end, a subsequent acceleration of the reaction zone. On a number of occasions, an explosive process was observed at the far end after several such reflections. However its exact nature could not be determined from the experimental records. In the latter case, however, with the greater length of travel available, the flame-generated pressure waves coalesced to form a shock front which initiated detonation upon its reflection from the far end of the vessel. The difference can be attributed to the character of the pressure waves. For both cases, the strength of the incident waves was nearly identical, with a maximum of 5 psia being attained. In the 2 x 20 vessel, the compression process was continuous and, if considered isentropic, would have produced a temperature upon reflection of approximately 490°K, while in the 2 x 40 vessel a temperature of about 520°K was calculated behind the reflected shock wave. The slightly increased temperature and abrupt heating rate associated with the shock compression process are apparently sufficient to initiate reaction. However, the relatively low magnitude of the calculated ignition temperature indicates that initiation may have resulted from other

effects, most probably by shock re-enforcement produced by a small cavity in the reflecting wall. Fay (21), who studied shock initiation of detonation in stoichiometric hydrogen-oxygen mixtures, found that temperatures several hundred degrees greater than that produced by a simple reflection can be attained in this manner and, in fact, was able to rationalize his results on the basis of shock amplification within a small clearance volume at the end of his chamber. The effect of shock re-enforcement on initiation of detonation is discussed later in detail. It does not, however, detract from the present results since the distinction between the character of the compression processes is still valid.

Details of the shock reflection process in the 2 x 40 vessel are shown in Figure 136, which includes the pressure records obtained at distances 32-1/2 and 38-1/2 ft from the ignitor. It appears that detonation was initiated adjacent to the end wall, after a delay of approximately 1.5 msec. The record shows also an anomaly in the detonation velocity measurements which was observed on all the tests in this series. While both the ion probe and pressure transducer data yielded velocities which agreed within the experimental accuracy, the former consistently indicated a lag in the time of arrival of several hundred microseconds. Since the ion probes were located vertically above the pressure pickups, this discrepancy was attributed to wave tilt, although there is no obvious explanation for it.

Space-time diagrams constructed for tests with equimolar mixtures at initial pressures of 200, 250, and 300 mm Hg are shown in Figures 137 to 140. At a pressure of 200 mm Hg, two modes of

initiation were observed. Figure 137 shows the initiation of detonation approximately 1 msec after the reflection of the precursor shock wave from the end of the vessel, while, for the same conditions, Figure 138 shows the onset of detonation at a distance of about 29 ft from the ignitor. This suggests that for an equimolar mixture of hydrogen and oxygen at room temperature, the limiting initial pressure for the natural transition from deflagration to detonation with a weak ignition source is about 200 mm Hg. Below this pressure, detonation is initiated only behind the reflected precursor shock wave. This conclusion, however, must be interpreted in consideration of the geometry of the chamber used in the present experiments.

At 250 mm Hg, Figure 139, detonation was initiated at about 26-1/2 ft from the ignitor and the detonation overtook the precursor shock wave at about 35 ft. At 300 mm Hg, Figure 140, initiation occurred before the last 15 ft and the detonation wave overtook the shock wave at about 30 ft from the ignitor.

A space-time diagram of the wave interaction pattern observed in a $2H_2 + O_2$ mixture initially at 100 mm Hg and 70°F is shown in Figure 141. Here again, initiation of detonation occurred behind the reflected shock wave after a delay of approximately 1.1 msec.

Results obtained with $3H_2 + O_2$ mixtures at initial pressures of 200, 250, and 300 mm Hg showing initiation behind the reflected shock wave are presented in Figures 142 to 144. Figure 145, also obtained at 300 mm Hg, shows the onset of detonation at a distance of 28 ft from the ignitor. This indicates, then, that the limiting pressure for natural transition to detonation in $3H_2 + O_2$ mixtures is 300 mm Hg, 50% greater than for $H_2 + O_2$ mixtures.

The detonation velocities in all the above-discussed spark ignition tests have been calculated, taking account of the conditions which exist in the medium behind the precursor shock wave. The results are summarized in Table 3 with the measured values. The discrepancy between measured and calculated velocities ranged from less than 1.0 to about 20%. This, however, was considered a reasonable agreement since the accuracy of the measurements is estimated at 5 to 10%, while the state of the medium into which the detonation propagated, which formed the basis for the calculation of the wave velocity, may not have been uniform throughout.

Figures 146, 147, and 148 show, respectively, the space-time diagrams obtained from tests in the 2 x 20 vessel, depicting the wave interaction pattern in $H_2 + O_2$, $2H_2 + O_2$, and $3H_2 + O_2$ mixtures initially at 100 mm Hg and -180°F. In each case, detonation occurred behind the incident precursor shock wave at distances of 8-10 ft for the $H_2 + O_2$ and $2H_2 + O_2$ mixtures and 16 ft for the $3H_2 + O_2$ mixture. At -180°F, then, the limiting pressure for natural transition to detonation is less than 100 mm Hg for all three mixtures.

Two final $x-t$ diagrams constructed for $3H_2 + O_2$ mixtures are shown in Figures 149 and 150. The former, obtained at -260°F, shows that the flame front follows almost immediately behind the precursor shock for the last 14 ft of travel, with detonation established adjacent to the end wall. The measurements did not resolve whether initiation occurred behind the incident wave or its reflection, although the interaction between the flame and

the reflected pressure wave probably enhanced the formation of detonation. The difference between this result and those at high initial temperatures is most probably the consequence of air dilution of the mixture caused by the excessive leakage encountered at this condition. The latter figure, obtained at -50°F, shows the initiation of detonation behind the reflected precursor shock wave after a delay of 2 msec.

The ignition delay times indicated in Figures 135-145 were compared to the data of Schott and Kinsey (22) and Strehlow and Cohen (23). The former measured delay times behind incident shock waves in hydrogen-oxygen mixtures highly diluted with argon, while the latter used the reflected shock technique in similar mixtures but with large O_2 concentration. In both cases the ignition temperatures ranged from 1000 to 3000°K. Results of the two studies, which were in good agreement, are represented in Figure 151 where the products of oxygen concentration and delay time are plotted against the inverse of the ignition temperature--the solid lines delineate the spread of their experimental data. Results of the present study, for which temperatures ranged from 475-630°K, are indicated by the small circles. Although Strehlow and Case (24) have pointed out that as a result of boundary layer effects, the temperature behind the reflected shock is higher than that predicted on the basis of ideal shock tube theory, these corrections have not been applied here since they were felt to be less than the experimental accuracy.

In spite of the temperature range involved, the present results, which fall below the extrapolation of the data of references

22 and 23, are grouped together at a value of 10^{-5} mole sec/liter. In the work of Schott and Kinsey, delay times were determined from measurements of OH absorption, whereas Strehlow and Cohen used photographic means to detect the initiation of reaction. In our tests, delay times were deduced from detection of both reaction-generated pressure waves and ionization signals. While the location of the plane of initiation was not observed directly, time of arrival measurements from both the ionization probes and the pressure pickups indicated that it occurred adjacent to the end wall.

The discrepancy between the present results and those of references 22 and 23 is most probably a consequence of shock re-enforcement within a small cavity in the end wall. Located in the center of the end wall where wave reflection occurred was the 3 inch opening to the vacuum pump. In order to protect the shut-off valve from metal fragments generated by the Primacord explosion, a thin plate, about 4 inches square, was installed several inches ahead of the opening. While the plate and cavity would have produced a negligible perturbation on the gross one-dimensional flow, it would have caused local shock wave re-enforcement with a corresponding increase in temperature. On the basis of Fay's experiments (21) it is quite likely that detonation was initiated in the hotter gases within the cavity rather than behind the reflected shock. Since shock re-enforcement would lead to increased initiation temperature and oxygen concentration and decreased induction time, the overall effect would shift the data points to the left on Figure 151, yielding a better agreement with the high temperature data.

5. SUMMARY AND CONCLUSIONS

In tests with the high energy ignitor, the initiating blast wave completely eliminated predetonative phenomena. At initial pressures of 100 and 10 mm Hg, an overdriven detonation-like wave was produced, which acquired a constant velocity of propagation within 20 ft of travel. In both cases the measured final wave velocities and pressures were in fair accord with the corresponding C-J values. In general the measured velocities were slightly less (5-10%) and pressures somewhat greater (10-50%) than the theoretical parameters, with discrepancies increasing at lower initial pressures and particularly at low initial temperatures where, in addition, the measurements were less consistent. This yields, then, a specific confirmation of the rule that the classical theory can be used only to predict the lower, i.e., the non-conservative, bound for the magnitude of peak pressure attained by a detonative process.

Exceptions to the above findings were observed for the 100 mm Hg, -180°F and -50°F conditions where the measured velocities exceeded the theoretical values for all compositions. Furthermore, although a constant wave velocity was observed at the 10 mm Hg condition in the 20 ft vessel, it is quite unlikely that a self-sustaining detonation can exist at this pressure. This contention is supported by the fact that the measured velocity was 10% less than the corresponding C-J value, and the indication of subsequent, albeit gradual, wave decay in the 40 ft vessel tests.

At initial pressure less than 10 mm Hg, the influence of the

blast wave generated by the Primacord ignitor becomes significant. Test results at an initial pressure of 1.0 mm Hg indicate that, although there is some contribution from energy released by chemical reaction of the hydrogen-oxygen mixtures, the wave propagation is supported primarily by the Primacord explosion. However, at 0.1 mm Hg, chemical reaction is apparently negligible and the observed process represents essentially the decay of the Primacord blast. The maximum reflected wave pressure at the 1.0 mm Hg condition was of the order of several psia which may be marginal with respect to the structural integrity of some components of launch vehicles. This pressure loading, however, is entirely a consequence of the method of ignition and not of detonation phenomena.

In conclusion, then, a strong shock wave initiation will produce detonation in mixtures at initial pressures greater than 10 mm Hg. The C-J theory, however, yields only a lower bound to the peak wave pressures, measurements indicating pressures as large as 50% greater being attained. Below 10 mm Hg initial pressure, chemical reaction is negligible and no amplification of the initiating blast wave occurs.

Information on the detonability of hydrogen-oxygen mixtures in the absence of external shock waves was provided by the weak ignition test series. In this case, however, shock waves were generated by the action of the accelerating flame itself. At room temperature the minimum initial pressure above which detonation was initiated behind the flame-generated precursor shock wave was in the neighborhood of 200-300 mm Hg, depending on the

composition of the mixtures. This result, however, must be interpreted in consideration of the geometry of the vessel, since, at lower pressures, the induction distance may exceed 40 ft, the maximum length available. At an initial temperature of -180°F, the minimum pressure was less than 100 mm Hg, although tests to determine its exact value were not performed. The ratio of induction distance to vessel diameter determined in these tests was approximately 15-20 at the minimum initial pressure. Since both large diameter and low initial pressure tend to increase the induction distance, these results are surprisingly low compared to those observed in 1 inch ducts at 1 atmosphere, where $L/D \approx 30$.

Perhaps the most significant results of the entire study were obtained from the reflected detonation experiments. At initial pressures of 100 mm Hg, which is below the minimum value discussed above, detonation was observed behind the reflected precursor shock wave, after an induction period of approximately 1.0 msec. The strength of the incident precursor shock was quite modest, corresponding to a Mach number of approximately 1.50. The detonation was formed almost instantaneously following initiation of reaction adjacent to the end wall, although the measurements did not resolve the precise details of the process.

The observed induction times were correlated with known kinetic data. For the comparatively low temperatures attained behind the singly reflected shock waves, they were appreciably below the values extrapolated from higher temperature data reported in the literature. This indicated the possibility of multiple reflections, which could have been indeed produced by the

irregular internal geometry of the enclosure. Although at this stage scientifically incomplete, and hence somewhat dissatisfying, these results have an important practical implication since the actual hardware must also possess irregular internal geometry that should similarly enhance the wave amplification process. The actual magnitude of pressure attained by shock re-enforcement is not important since the volume of the cavity and duration of the pulse are relatively small. However, the additional compression produced by the irregular geometry may initiate detonation in systems that may otherwise be considered safe.

Finally, as an outgrowth of measurements used to monitor stresses induced by the detonative process a method for prediction of the cylinder's stress response to a symmetric internal blast load has been developed. Based on a simple dynamic model of the vibrating cylinder and an approximate expression for the wave shape of the blast load, the analysis yielded results in satisfactory agreement with experimental data. Full details of this study are presented in reference 11.

10. Hecht, G. J., Laderman, A. J., Stern, R. A., and Oppenheim, A. K., "Determination of Flame Velocities in Gaseous Predetonation," Review of Scientific Instruments, 31, 1107-1111, 1960.

11. Wing, R. D., de Malherbe, M. C., and Laderman, A. J., "Investigation of Dynamic Stresses in Detonation Tubes," SSL TN #7, Series 5, Issue 46, University of California, Berkeley, August 1964.

12. Laderman, A. J., and Oppenheim, A. K., "Experimental Study of the Development of Detonation," TN DR #9, AFOSR TN 60-1303, University of California, Berkeley, November 1960.

13. Hecht, G. J., Lilleston, C. T., and Oppenheim, A. K., "Long Duration Spark Light Source for Streak Schlieren Photography of High-Speed Events," ISA Transactions, 3, 2, 100-107, 1964.

14. Courant, R., and Friedrichs, K. O., Supersonic Flow and Shock Waves, Interscience Publishers, Inc., New York, 1948, xvi + 464 pp.

15. Glass, I. I., "Aerodynamics of Blast," Canadian Aeronautical Journal, 7, 3, 109-135, 1961.

16. Sedov, L. I., Similarity and Dimensional Method in Mechanics, Academic Press, New York, 1959, 363 pp.

17. Brode, H. L., "The Blast Wave in Air Resulting From a High Temperature, High Pressure Sphere of Air," Rand Corporation Report RN-1825-AEC, 1956.

18. Laderman, A. J., and Oppenheim, A. K., "Initial Flame Acceleration in an Explosive Gas," Proc. Roy. Soc. (London) A268, 153-180, 1962.

REFERENCES

1. Seamans, T. F. and Wolfhard, H. G., "Detonation and Suppression of Detonation in Fuel-Air Mixtures at Elevated Pressures," Research Abstracts and Reviews, 4, 112, 1962.
2. Gerstein, Melvin, Carlson, E. R., and Hill, F. U., "Natural Gas-Air Explosions at Reduced Pressure," Industrial and Engineering Chemistry, 46, 12, 2558-2562, 1954.
3. Busch, C. W., Laderman, A. J., and Oppenheim, A. K., "Computation of Gaseous Detonation Parameters," SSL TN #6, Series No. 5, Issue No. 42, and IER Report No. 64-12, University of California, Berkeley, August 1964.
4. Austin, A. L., "The Dynamic Response of a Thin-Walled Cylindrical Tube to an Axisymmetric Internal Transient Pressure," SSL TN #1, University of California, Berkeley, June 1962.
5. Laderman, A. J., Jako, G., and Panton, R. L., "Design of Vacuum Pump System for Detonation Vessels," SSL TN #4, University of California, Berkeley, November 1962.
6. Laderman, A. J., and Urtiew, P. A., "Design of Gas Handling System," SSL TN #3, University of California, Berkeley, October 1962.
7. "Primacord-Bickford Detonating Fuse," Ensign Bickford Co., Simsbury, Connecticut, 3rd Printing, 1960.
8. Taylor, J., "Detonation in Condensed Explosives," Oxford Press, London, 1952, 186 pp.
9. Laderman, A. J., Struck, W. G., and Urtiew, P. A., "Design of Primacord Ignition System," SSL TN #5, Series 4, Issue 77, University of California, Berkeley, October 1963.

19. Laderman, A. J., Urtiew, P. A., and Oppenheim, A. K., "On the Generation of a Shock Wave by Flame in an Explosive Gas," Ninth Symposium (International) on Combustion, Pergamon Press, New York and London, 1963, pp. 424-441.

20. Urtiew, P. A., Laderman, A. J., and Oppenheim, A. K., "Dynamics of the Generation of Pressure Waves by Accelerating Flames," Tenth Symposium (International) on Combustion, Cambridge, England, August 17-21, 1964 (in press).

21. Fay, J. A., and Hooker, W. J., Comment to paper #74, Fifth Symposium (International) on Combustion, Reinhold Publishing Co., New York, 1955, pp. 671-672. See also Fay, J. A., "Some Experiments on the Initiation of Detonation in $2H_2 + O_2$ Mixtures by Uniform Shock Waves," Fourth Symposium (International) on Combustion, Williams and Wilkins Co., Baltimore, 1953, pp. 501-507.

22. Schott, G. L., and Kinsey, J. L., "Kinetic Studies of Hydroxyl Radicals in Shock Waves. II. Induction Times in the Hydrogen-Oxygen Reaction," Journal of Chemical Physics, 29, 5, 1177-1182, 1958.

23. Strehlow, R. A., and Cohen, Arthur, "Initiation of Detonation," Phys. of Fluids, 5, 1, 97-101, 1962.

24. Strehlow, R. A., and Case, C. T., "Limitations of the Reflected Shock Technique for Studying Fast Chemical Reactions," J. of Chem. Phys., 35, 4, 1506-1507, 1961.

TABLE 1

Summary of Operating Conditions

Vessel	Initial Temperature °F	Composition	Ignitor	Initial Pressure mm Hg
2 x 20	70	$H_2 + O_2$	P,S,H	100
		$2H_2 + O_2$	P,S	100
		$3H_2 + O_2$	P	100
		$H_2 + O_2$ $2H_2 + O_2$ $3H_2 + O_2$	P	10 1 0.1
	200	$3H_2 + O_2$	P	100 10 1.0
	-50	$3H_2 + O_2$	P,S	100
			P	10 1.0
	-180	$H_2 + O_2$ $2H_2 + O_2$ $3H_2 + O_2$	S	100
			P	10
	-260	$3H_2 + O_2$	S	100
3 x 20	70	$H_2 + O_2$	P	760
			P,S	100
			P	10 1.0 0.1
2 x 40	70	$H_2 + O_2$	P,S	600
			P	400
		$H_2 + O_2$ $3H_2 + O_2$	S	300
		$H_2 + O_2$ $3H_2 + O_2$	S	250
		$H_2 + O_2$	P,S	200
		$3H_2 + O_2$	S	
		$H_2 + O_2$ $2H_2 + O_2$	S	100
		$H_2 + O_2$	P	10 1.0

P--Primacord, S--spark ignitor, H--hot plate ignitor.

TABLE 2

a. Specifications of Amplifiers Used With Pressure Transducers

	Kistler Type 568	Kistler Type 553-A	Kistler Type PT-6
Range	100 to 10^5 psi	5 pCb to 230 pCb peak to peak	100 to 10^4 psi
Output signal	-5 V to 10 V	5 V peak to peak	max. 6 V
Output impedance	100 ohms	120 ohms	200 ohms
Frequency response	dc to 150 Kc	10 cps to 30 Kc	dc to 150 Kc
Linearity	0.1%	0.1%	1%
Noise	1 mV	1.2 mV at 100 pf	2 mV
Power source	115 V, 60 cps	28 V dc	8 V dc

TABLE 2 (Continued)

b. Specifications of Pressure Transducers

	Kistler Type 601	Kistler Type PZ 14
Range	to 5000 psi	to 3000 psi
Resolution	0.01 psi	0.01 psi
Sensitivity	0.5 pCb/psi	4 pCb/psi
Linearity	1%	1%
Natural frequency	150,000 cps	50,000 cps
Rise time	3 sec	
Temperature range	-400° to +500°F	Max. 600°F
Max. gas temperature (intermittent)	3000°F	3000°F
Insulation resistance	10^{14} ohms	10^{14} ohms
Acceleration sensitivity	0.02 psi/g	0.05 psi/g

TABLE 3

Detonation Velocities

Mixture	Fig. No.	Initial Pressure mm Hg	Pressure Behind Precursor Shock mm Hg	Detonation Velocity (in lab coordinates)	
				Calculated	Measured
$H_2 + O_2$	137	200	424	6700	6600
	138	200	625	9000	10000
	139	250	800	9100	8340
	140	300	870	8900	9900
$3H_2 + O_2$	142	200	500	8400	8350
	143	250	825	8200	9090
	144	300	845	8400	10000
	145	300	845	10100	12000

FIGURES

Fig. 61. Wave pressure as a function of distance from Primacord ignitor in vessel CD. $3H_2 + O_2$ composition, initial pressure 10 mm Hg, initial temperature -50°F.

Fig. 62. Wave velocity as a function of distance from Primacord ignitor in vessel CD. $3H_2 + O_2$ composition, initial pressure 1.0 mm Hg, initial temperature -50°F.

Fig. 63. Wave pressure as a function of distance from Primacord ignitor in vessel CD. $3H_2 + O_2$ composition, initial pressure 1.0 mm Hg, initial temperature -50°F.

Fig. 64. Wave velocity as a function of distance from spark ignitor in the 2 ft diam x 20 ft long vessel. Initial pressure 100 mm Hg, initial temperature -180°F.

Fig. 65. Wave pressure as a function of distance from spark ignitor in the 2 ft diam x 20 ft long vessel. Initial pressure 100 mm Hg, initial temperature -180°F.

Fig. 66. Wave velocity as a function of distance from Primacord ignitor in vessel CD. Initial pressure 10 mm Hg, initial temperature -180°F.

Fig. 67. Wave pressure as a function of distance from Primacord ignitor in vessel CD. Initial pressure 10 mm Hg, initial temperature -180°F.

Fig. 68. Wave velocity as a function of distance from Primacord ignitor in vessel A. Initial pressure 760 mm Hg, initial temperature 68°F.

Fig. 69. Wave pressure as a function of distance from Primacord ignitor in vessel A. Initial pressure 760 mm Hg, initial temperature 68°F.

Fig. 52. Wave velocity as a function of distance from Primacord ignitor in vessel CD. $3H_2 + O_2$ composition, initial pressure 100 mm Hg, initial temperature +200°F.

Fig. 53. Wave pressure as a function of distance from Primacord ignitor in vessel CD. $3H_2 + O_2$ composition, initial pressure 100 mm Hg, initial temperature +200°F.

Fig. 54. Wave velocity as a function of distance from Primacord ignitor in vessel CD. $3H_2 + O_2$ composition, initial pressure 10 mm Hg, initial temperature +200°F.

Fig. 55. Wave pressure as a function of distance from Primacord ignitor in vessel CD. $3H_2 + O_2$ composition, initial pressure 10 mm Hg, initial temperature +200°F.

Fig. 56. Wave velocity as a function of distance from Primacord ignitor in vessel CD. $3H_2 + O_2$ composition, initial pressure 1.0 mm Hg, initial temperature +200°F.

Fig. 57. Wave pressure as a function of distance from Primacord ignitor in vessel CD. $3H_2 + O_2$ composition, initial pressure 1.0 mm Hg, initial temperature +200°F.

Fig. 58. Wave velocity as a function of distance from Primacord ignitor in vessel CD. $3H_2 + O_2$ composition, initial pressure 100 mm Hg, initial temperature -50°F.

Fig. 59. Wave pressure as a function of distance from Primacord ignitor in vessel CD. $3H_2 + O_2$ composition, initial pressure 100 mm Hg, initial temperature -50°F.

Fig. 60. Wave velocity as a function of distance from Primacord ignitor in vessel CD. $3H_2 + O_2$ composition, initial pressure 10 mm Hg, initial temperature -50°F.

Fig. 70. Wave velocity as a function of distance from Primacord ignitor for vessel A. Initial pressure 100 mm Hg, initial temperature 73°F.

Fig. 71. Wave pressure as a function of distance from Primacord ignitor in vessel A. Initial pressure 100 mm Hg, initial temperature 73°F.

Fig. 72. Wave velocity as a function of distance from Primacord ignitor for vessel A. Initial pressure 10 mm Hg, initial temperature 73°F.

Fig. 73. Wave pressure as a function of distance from Primacord ignitor for vessel A. Initial pressure 10 mm Hg, initial temperature 73°F.

Fig. 74. Wave velocity as a function of distance from Primacord ignitor for vessel A. Initial pressure 1.0 mm Hg, initial temperature 72°F.

Fig. 75. Wave pressure as a function of distance from Primacord ignitor for vessel A. Initial pressure 1.0 mm Hg, initial temperature 72°F.

Fig. 76. Wave velocity as a function of distance from Primacord ignitor for vessel A. Initial pressure 0.1 mm Hg, initial temperature 70°F.

Fig. 77. Wave pressure as a function of distance from Primacord ignitor for vessel A. Initial pressure 0.1 mm Hg, initial temperature 70°F.

Fig. 78. Wave velocity as a function of distance from Primacord ignitor in the 2 ft diam x 40 ft long vessel. $H_2 + O_2$ composition, initial pressure 600 mm Hg, initial temperature 70°F.

Fig. 79. Wave pressure as a function of distance from Primacord ignitor in the 2 ft diam x 40 ft long vessel. $H_2 + O_2$ composition, initial pressure 600 mm Hg, initial temperature 70°F.

Fig. 80. Wave velocity as a function of distance from spark ignitor in the 2 ft diam x 40 ft long vessel. $H_2 + O_2$ composition, initial pressure 600 mm Hg, initial temperature 70°F.

Fig. 81. Wave pressure as a function of distance from spark ignitor in the 2 ft diam x 40 ft long vessel. $H_2 + O_2$ composition, initial pressure 600 mm Hg, initial temperature 70°F.

Fig. 82. Wave velocity as a function of distance from Primacord ignitor in the 2 ft diam x 40 ft long vessel. $H_2 + O_2$ composition, initial pressure 400 mm Hg, initial temperature 70°F.

Fig. 83. Wave pressure as a function of distance from Primacord ignitor in the 2 ft diam x 40 ft long vessel. $H_2 + O_2$ composition, initial pressure 400 mm Hg, initial temperature 70°F.

Fig. 84. Wave velocity as a function of distance from Primacord ignitor in the 2 ft diam x 40 ft long vessel. $H_2 + O_2$ composition, initial pressure 200 mm Hg, initial temperature 70°F.

Fig. 85. Wave pressure as a function of distance from Primacord ignitor in the 2 ft diam x 40 ft long vessel. $H_2 + O_2$ composition, initial pressure 200 mm Hg, initial temperature 70°F.

Fig. 86. Wave velocity as a function of distance from Primacord ignitor in the 2 ft diam x 40 ft long vessel. $H_2 + O_2$ composition, initial pressure 10 mm Hg, initial temperature 70°F.

Fig. 87. Wave pressure as a function of distance from Primacord ignitor in the 2 ft diam x 40 ft long vessel. $H_2 + O_2$ composition, initial pressure 10 mm Hg, initial temperature 70°F.

Fig. 88. Wave velocity as a function of distance from Primacord ignitor in the 2 ft diam x 40 ft long vessel. $H_2 + O_2$ composition, initial pressure 1.0 mm Hg, initial temperature 70°F.

Fig. 89. Wave pressure as a function of distance from Primacord ignitor in the 2 ft diam x 40 ft long vessel. $H_2 + O_2$ composition, initial pressure 1.0 mm Hg, initial temperature 70°F.

Fig. 90. Wave velocity as a function of distance from Primacord ignitor in 40 ft vessel. Data from 20 ft vessel is also included. $H_2 + O_2$ composition, initial pressure 1.0 mm Hg, initial temperature 70°F.

Fig. 91. Wave pressure as a function of distance from Primacord ignitor in 40 ft vessel. Data from 20 ft vessel is also included. $H_2 + O_2$ composition, initial pressure 1.0 mm Hg, initial temperature 70°F.

Fig. 92. Wave velocities measured at last position in vessel CD, during room temperature tests, versus initial pressure. Theoretical C-J velocities shown for comparison.

Fig. 93. Wave velocities measured at last position in vessels A and CD, for $H_2 + O_2$ mixtures and air during room temperature tests, versus initial pressure. Theoretical C-J velocities shown for comparison.

Fig. 94. Peak incident pressure at last position in vessels A and CD as a function of initial pressure for air at room temperature.

Fig. 95. Reflected pressure in vessels A and CD as a function of initial pressure for air at room temperature.

Fig. 96. Peak incident pressure at last position in vessel CD as a function of initial pressure for air at +200 and +70°F.

Fig. 97. Peak incident pressure at last position in vessel CD as a function of initial pressure for air at -50 and -180°F.

Fig. 98. Peak incident pressure at last position in vessels A and CD as a function of initial pressure for $H_2 + O_2$ mixture at room temperature.

Fig. 99. Reflected wave pressure at last position in vessels A and CD as a function of initial pressure for $H_2 + O_2$ mixture at room temperature.

Fig. 100. Peak incident pressure at last position in vessels A and CD as a function of initial pressure for $2H_2 + O_2$ mixture at room temperature.

Fig. 101. Reflected wave pressure at last position in vessels A and CD as a function of initial pressure for $2H_2 + O_2$ mixture at room temperature.

Fig. 102. Peak incident pressure at last position in vessels A and CD as a function of initial pressure for $3H_2 + O_2$ mixture at room temperature.

Fig. 103. Reflected wave pressure at last position in vessels A and CD as a function of initial pressure for $3H_2 + O_2$ mixture at room temperature.

Fig. 104. Wave velocity measured at last position in vessel CD versus initial pressure for hydrogen-oxygen mixtures at room temperature.

Fig. 105. Peak incident pressure at last position in vessel CD versus initial pressure for hydrogen-oxygen mixtures at room temperature.

Fig. 106. Wave velocity measured at last position in vessel CD versus initial pressure for $3H_2 + O_2$ mixtures at +200°F.

Fig. 107. Peak incident pressure at last position in vessel CD versus initial pressure for $3H_2 + O_2$ mixtures at +200°F.

Fig. 108. Wave velocity measured at last position in vessel CD versus initial pressure for $3H_2 + O_2$ mixtures at -50°F.

Fig. 109. Peak incident pressure at last position in vessel CD versus initial pressure for $3H_2 + O_2$ mixtures at -50°F.

Fig. 110. Wave velocity measured at last position in vessel CD versus initial pressure for hydrogen-oxygen mixtures at -180°F.

Fig. 111. Peak incident pressure at last position in vessel CD versus initial pressure for hydrogen-oxygen mixtures at -180°F.

Fig. 112. Wave velocity measured at last position in vessel CD for hydrogen-oxygen mixtures initially at 100 mm Hg versus initial temperature.

Fig. 113. Peak incident pressure measured at last position in vessel CD for hydrogen-oxygen mixtures initially at 100 mm Hg versus initial temperature.

Fig. 114. Wave velocity measured at last position in vessel CD for hydrogen-oxygen mixtures initially at 10 mm Hg versus initial temperature.

Fig. 115. Peak incident pressure measured at last position in vessel CD for hydrogen-oxygen mixtures initially at 10 mm Hg versus initial temperature.

Fig. 116. Wave velocity measured at last position in vessel CD for $3H_2 + O_2$ mixtures initially at 1.0 mm Hg versus initial temperature.

Fig. 117. Peak incident pressure measured at last position in vessel CD for $3H_2 + O_2$ mixtures initially at 1.0 mm Hg versus initial temperature.

Fig. 118. Wave velocity measured at last position in vessel CD as a function of volume per cent of hydrogen for mixtures initially at pressures of 100 and 10 mm Hg and room temperature. Theoretical C-J velocities included for comparison.

Fig. 119. Incident wave pressure measured at last position in vessel CD as a function of volume per cent of hydrogen for mixtures initially at pressures of 100 and 10 mm Hg and temperatures of 70 and -180°F. Theoretical C-J velocities included for comparison.

Fig. 120. Wave velocity measured at last position in vessel CD as a function of volume per cent of hydrogen for mixtures initially at pressures of 100 and 10 mm Hg and -180°F. Theoretical C-J velocities included for comparison.

Fig. 121. Incident wave pressure measured at last position in vessel CD as a function of volume per cent of hydrogen for mixtures initially at pressures 100 and 10 mm Hg and -180°F. Theoretical C-J velocities included for comparison.

Fig. 122. Streak Schlieren photograph of a steady detonation wave in $3H_2 + O_2$ mixture initially at 100 mm Hg and room temperature.

Fig. 123. Space-time diagram of detonation wave in vessel CD for $3H_2 + O_2$ mixture with Primacord ignition. Initial pressure 100 mm Hg, initial temperature 70°F. Space-time location of Fig. 122 shown as insert.

Fig. 124. Streak Schlieren photograph of initial flame acceleration in vessel CD for an $H_2 + O_2$ mixture with spark ignition. Initial pressure 100 mm Hg, initial temperature, 70°F. Distance measured from point of ignition. Flame front depicted by bright line curved diagonally up to the right. Similar traces behind front are indicative of flame structure.

Fig. 125. Space-time diagram of accelerating flame in vessel CD for an $H_2 + O_2$ mixture with spark ignition. Initial

pressure 100 mm Hg, initial temperature 70°F. Distance measured from point of ignition. Time-space location of photographs of Fig. 124 shown as inserts.

Fig. 126. Space-time diagram of accelerating flame in vessel CD for a $2H_2 + O_2$ mixture with spark ignition. Initial pressure 100 mm Hg, initial temperature 70°F.

Fig. 127. Space-time diagram of accelerating flame in vessel CD for a $3H_2 + O_2$ mixture with spark ignition. Initial pressure 100 mm Hg, initial temperature 70°F.

Fig. 128. Space-time diagram of Fig. 126 replotted with pressure records included to demonstrate build-up of pressure pulse.

Fig. 129. Graphical representation of the solution for heat of reaction and average flame propagation speed of Fig. 128. The curved lines emanating from the origin represent flame world-lines, Eq. (15), while the straight lines describe characteristics of the simple pressure wave, Eq. (16). The crosses, obtained from experiment, establish the value of K.

Fig. 130. Space-time wave diagram of accelerating flame in vessel CD. $H_2 + O_2$ mixture at 100 mm Hg initial pressure and room temperature. Spark ignition.

Fig. 131. Space-time wave diagram of accelerating flame in vessel CD. $H_2 + O_2$ mixture at 100 mm Hg initial pressure and room temperature. Hot plate ignition.

Fig. 132. Space-time wave diagram of accelerating flame in vessel A. $H_2 + O_2$ mixture at 100 mm Hg initial pressure and room temperature. Spark ignition.

Fig. 133. Space-time diagram of accelerating flame in vessel CD for $2H_2 + O_2$ mixture with spark ignition. Initial pressure 100 mm Hg, initial temperature 70°F. Space-time location of Schlieren photograph of Fig. 134 shown as insert.

Fig. 134. Streak Schlieren photograph of a flame-reflected shock interaction pattern in vessel CD for $2H_2 + O_2$ mixture initially at 100 mm Hg and 70°F. Spark ignition.

Fig. 135. Space-time diagram of a wave interaction pattern in 40 ft vessel for $H_2 + O_2$ mixture with spark ignition. Data from 20 ft vessel is also included. Initial pressure 100 mm Hg, initial temperature 70°F.

Fig. 136. Space-time diagram with superimposed pressure records of wave interaction pattern in the 40 ft vessel shown in Fig. 134.

Fig. 137. Space-time diagram with superimposed pressure record of wave interaction pattern in the 2 ft diam x 40 ft long vessel for $H_2 + O_2$ mixture with spark ignition. Initial pressure 200 mm Hg, initial temperature 70°F. Initiation of detonation behind reflected shock wave.

Fig. 138. Space-time diagram with superimposed pressure record of wave interaction pattern in the 2 ft diam x 40 ft long vessel for $H_2 + O_2$ mixture with spark ignition. Initial pressure 200 mm Hg, initial temperature 70°F. Initiation of detonation behind precursor shock wave.

Fig. 139. Space-time diagram with superimposed pressure record of wave interaction pattern in the 2 ft diam x 40 ft

long vessel for $H_2 + O_2$ mixture with spark ignition. Initial pressure 250 mm Hg, initial temperature 70°F. Initiation of detonation behind precursor shock wave.

Fig. 140. Space-time diagram with superimposed pressure record of wave interaction pattern in the 2 ft diam x 40 ft long vessel for $H_2 + O_2$ mixture with spark ignition. Initial pressure 300 mm Hg, initial temperature 70°F. Initiation of detonation behind precursor shock wave.

Fig. 141. Space-time diagram with superimposed pressure record of wave interaction pattern in the 2 ft diam x 40 ft long vessel for $2H_2 + O_2$ mixture with spark ignition. Initial pressure 100 mm Hg, initial temperature 70°F. Initiation of detonation behind reflected shock wave.

Fig. 142. Space-time diagram with superimposed pressure record of wave interaction pattern in the 2 ft diam x 40 ft long vessel for $3H_2 + O_2$ mixture with spark ignition. Initial pressure 200 mm Hg, initial temperature 70°F. Initiation of detonation behind reflected shock wave.

Fig. 143. Space-time diagram with superimposed pressure record of wave interaction pattern in the 2 ft diam x 40 ft long vessel for $3H_2 + O_2$ mixture with spark ignition. Initial pressure 250 mm Hg, initial temperature 70°F. Initiation of detonation behind reflected shock wave.

Fig. 144. Space-time diagram with superimposed pressure record of wave interaction pattern in the 2 ft diam x 40 ft long vessel for $3H_2 + O_2$ mixture with spark ignition. Initial pressure 300 mm Hg, initial temperature 70°F. Initiation of detonation behind reflected shock wave.

Fig. 145. Space-time diagram with superimposed pressure record of wave interaction pattern in the 2 ft diam x 40 ft long vessel for $3H_2 + O_2$ mixture with spark ignition. Initial pressure 300 mm Hg, initial temperature 70°F. Initiation of detonation behind precursor shock.

Fig. 146. Space-time diagram with superimposed pressure record of a wave interaction pattern in the 2 ft diam x 20 ft long vessel for $H_2 + O_2$ mixture with spark ignition. Initial pressure 100 mm Hg, initial temperature -180°F. Initiation of detonation behind precursor shock.

Fig. 147. Space-time diagram with superimposed pressure record of a wave interaction pattern in the 2 ft diam x 20 ft long vessel for $2H_2 + O_2$ mixture with spark ignition. Initial pressure 100 mm Hg, initial temperature -180°F. Initiation of detonation behind precursor shock.

Fig. 148. Space-time diagram with superimposed pressure record of a wave interaction pattern in the 2 ft diam x 20 ft long vessel for $3H_2 + O_2$ mixture with spark ignition. Initial pressure 100 mm Hg, initial temperature -180°F. Initiation of detonation behind precursor shock.

Fig. 149. Space-time diagram with superimposed pressure record of a wave interaction pattern in the 2 ft diam x 20 ft long vessel for $3H_2 + O_2$ mixture with spark ignition. Initial pressure 100 mm Hg, initial temperature -260°F.

Fig. 150. Space-time diagram with superimposed pressure record of a wave interaction pattern in the 2 ft diam x 20 ft long vessel for $3H_2 + O_2$ mixture with spark ignition. Initial pressure 100 mm Hg, initial temperature -50°F.

Fig. 151. Product of oxygen concentration and ignition delay time plotted as a function of inverse temperature. Band in lower left-hand corner represents data of references 10 and 11.

Legend:

1. Detonation Vessels B and CD
2. Detonation Vessel A
3. Schlieren Apparatus
4. Area for Schlieren Traverse
5. Vacuum Equipment
6. LN Storage
7. Gas Mixing and Storage
8. Instrumentation and Controls
9. Safety Barricades

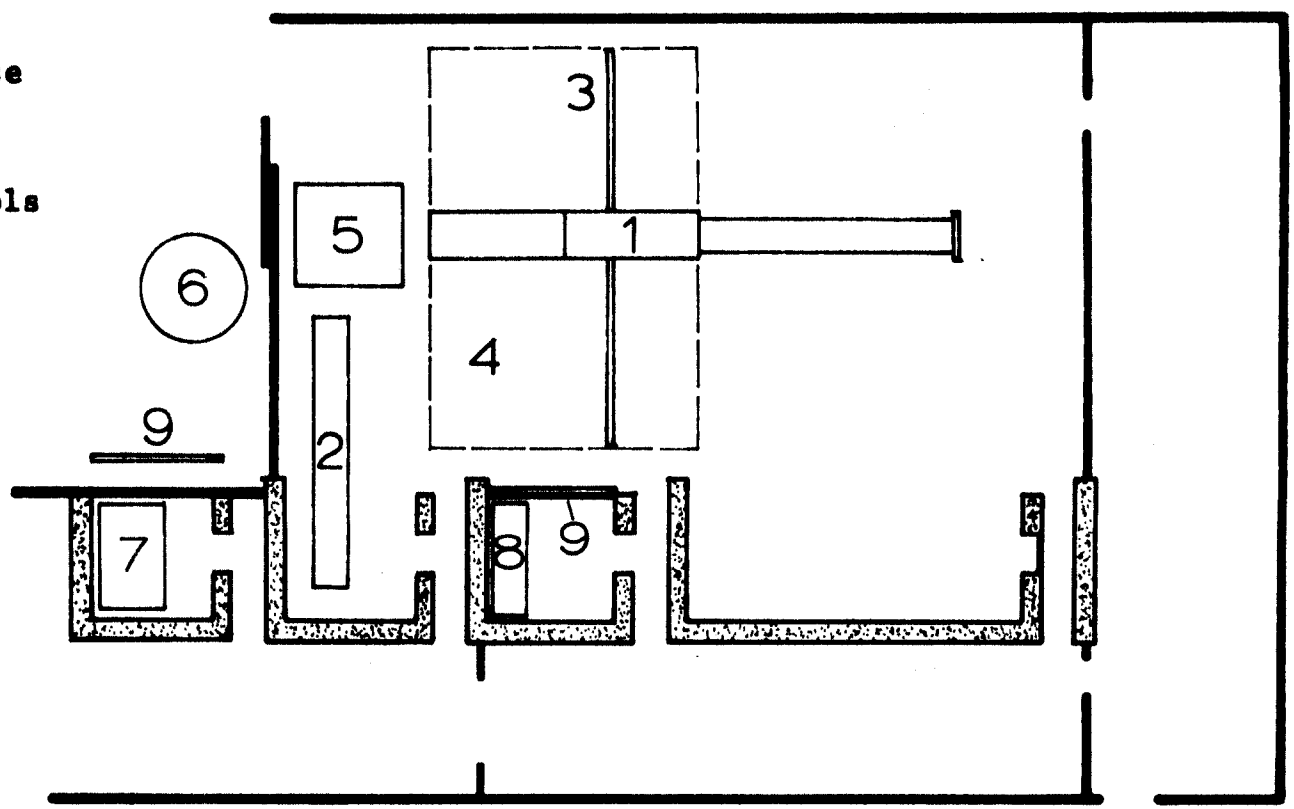

Fig. 1 Laboratory Floor Plan

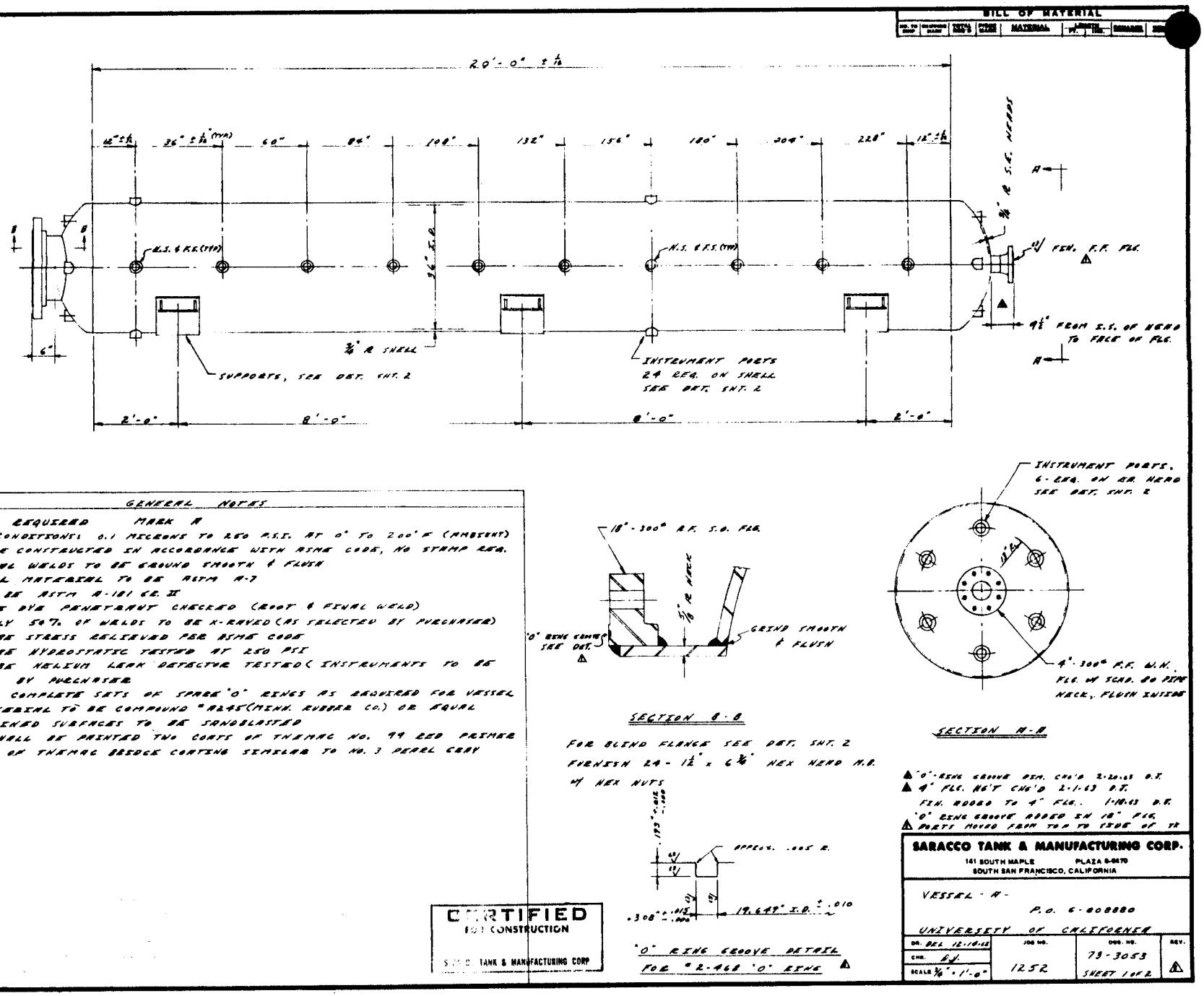

Fig. 2 Design of Vessel A

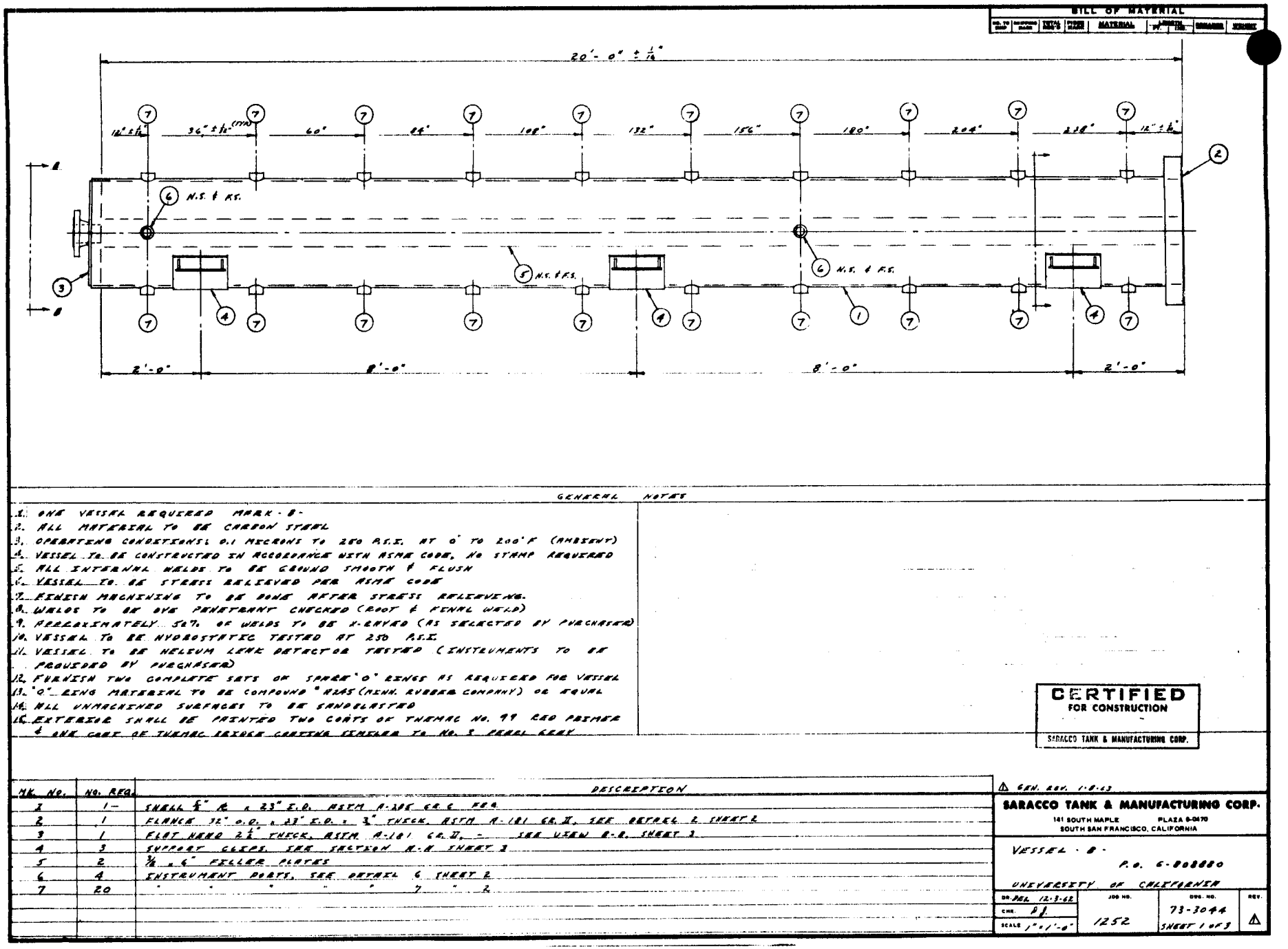

GENERAL NOTES

1. ONE VESSEL REQUIRED MARK - B -
2. ALL MATERIAL TO BE CARBON STEEL
3. OPERATING CONDITIONS: 0.1 MICRONS TO 250 P.S.I. AT 0° TO 200° F (AMBIENT)
4. VESSEL TO BE CONSTRUCTED IN ACCORDANCE WITH ASME CODE, NO STAMP REQUIRED
5. ALL INTERNAL WELDS TO BE GROUND SMOOTH & FLUSH
6. VESSEL TO BE STRESS RELIEVED PER ASME CODE
7. FINISH MACHINING TO BE DONE AFTER STRESS RELIEVING.
8. WELDS TO BE DYE PENETRANT CHECKED (ROOT & FINAL WELD)
9. APPROXIMATELY 50% OF WELDS TO BE X-RAYED (AS SELECTED BY PURCHASER)
10. VESSEL TO BE HYDROSTATIC TESTED AT 250 P.S.I.
11. VESSEL TO BE HELIUM LEAK DETECTOR TESTED (INSTRUMENTS TO BE PROVIDED BY PURCHASER)
12. FURNISH TWO COMPLETE SETS OF SPARE "O" RINGS AS REQUIRED FOR VESSEL
13. "O" RING MATERIAL TO BE COMPOUND "N285 (MINN. RUBBER COMPANY) OR EQUAL
14. ALL UNMACHINED SURFACES TO BE SANDBLASTED
15. EXTERIOR SHALL BE PAINTED TWO COATS OF THEMEC NO. 99 RED PRIMER & ONE COAT OF THEMEC ENAMEL COATING FINISHED TO NO. 2 PEARL GRAY

CERTIFIED
FOR CONSTRUCTION
SARACCO TANK & MANUFACTURING CORP.

MK. NO.	NO. REQ.	DESCRIPTION
1	1 —	SHELL ½" R. x 23" I.D. ASTM A-285 GR. C FOR.
2	1	FLANGE 32" O.D. x 23" I.D. x 3" THICK. ASTM A-181 GR. II. SEE DETAIL 2 SHEET 2
3	1	FLAT HEAD 2½" THICK. ASTM A-181 GR. II, — SEE VIEW B-B. SHEET 3
4	3	SUPPORT CLEATS. SEE SECTION A-A SHEET 3
5	2	⅜ x 4" FILLER PLATES
6	4	INSTRUMENT BOSSES, SEE DETAIL 6 SHEET 2
7	20	" " " " " 7 " 2

⚠ GEN. REV. 1-9-63

SARACCO TANK & MANUFACTURING CORP.
141 SOUTH MAPLE PLAZA 8-0470
SOUTH SAN FRANCISCO, CALIFORNIA

VESSEL - B -
P.O. G-808880
UNIVERSITY OF CALIFORNIA

DR. REL 12-3-62	JOB NO.	DWG. NO.	REV.
CHK. BJ.	1252	73-3044	⚠
SCALE 1"=1'-0"		SHEET 1 OF 3	

Fig. 3 Design of Vessel B

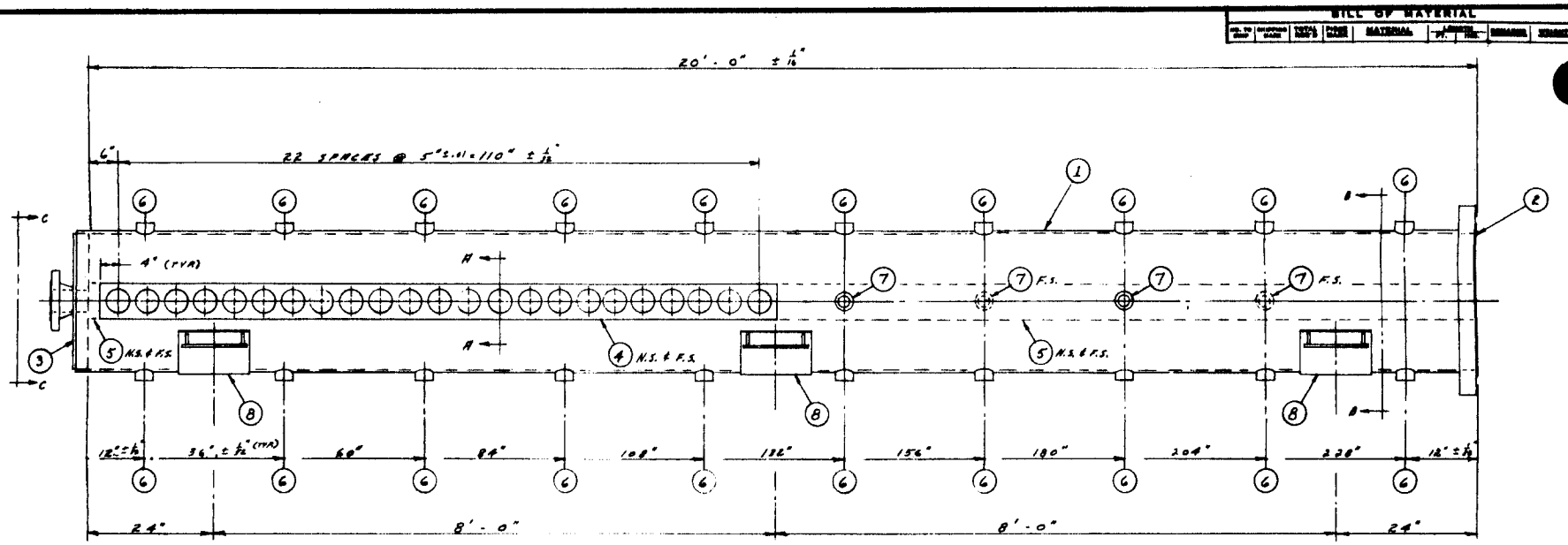

GENERAL NOTES

1. ONE VESSEL REQUIRED MARK C-D
2. ALL MATERIAL TO BE TYPE 304 SS UNLESS SPECIFIED OTHERWISE
3. OPERATING CONDITIONS; 0.1 MICRONS TO 250 P.S.I. AT -100° F TO +200° F
4. VESSEL TO BE CONSTRUCTED IN ACCORDANCE WITH ASME CODE, NO STAMP REQUIRED
5. ALL INTERNAL WELDS TO BE GROUND SMOOTH & FLUSH
6. VESSEL TO BE STRESS RELIEVED PER ASME CODE
7. FINISH MACHINING TO BE DONE AFTER STRESS RELIEVING
8. APPROXIMATELY 50% OF WELDS TO BE X-RAYED (AS SELECTED BY PURCHASER)
9. VESSEL TO BE HYDROSTATIC TESTED AT 250 P.S.I.
10. VESSEL TO BE HELIUM LEAK DETECTOR TESTED (INSTRUMENTS TO BE PROVIDED BY PURCHASER)
11. FURNISH TWO COMPLETE SETS OF SPARE 'O'-RINGS AS REQUIRED FOR VESSEL
12. "O" RING MATERIAL TO BE COMPOUND "N-145 (MINN. RUBBER COMPANY) OR EQUAL
13. WELDS TO BE DYE PENETRANT CHECKED (ROOT & FINAL WELD)
14. ALL UNMACHINED SURFACES TO BE SANDBLASTED

CERTIFIED FOR CONSTRUCTION
SARACCO TANK & MANUFACTURING CORP.

MK. NO.	NO. REQ.	DESCRIPTION
1	1	SHELL ½" Rt. x 23" I.D., ASTM A-240 T-304 STAINLESS STEEL
2	1	FLANGE 32" O.D. x 23" I.D. x 3" THICK, ASTM A-182 F-304 SEE DETAIL 2 SHEET 3
3	1	FLAT HEAD 2½" THICK ASTM A-182 F-304 SEE VIEW C-C SHEET 3
4	2	SECNT PORT BLOCKS, 5" x 6" x 11⅞", SEE SECTION A-A, SHEET 2
5	2	⅜ x 6" FILLER PLATES, ASTM A-240 T-304 SS
6	20	INSTRUMENT PORTS, SEE DETAIL 6 SHEET 2
7	4	" " " 7 " 2
8	3	SUPPORT CLIPS, SEE SECTION B-B, SHEET 4
9	1	BLIND FLANGE, ASTM A-182 F-304, SEE DETAIL SHEET 3
10	46	SECNT PORT FLANGES, SEE DETAIL SHEET 4

⚠ GEN. REV. 1-8-63 D.J.

SARACCO TANK & MANUFACTURING CORP.
141 SOUTH MAPLE PLAZA 6-0670
SOUTH SAN FRANCISCO, CALIFORNIA

VESSEL C-D
P.O. G-808880
UNIVERSITY OF CALIFORNIA

DR. BAL 11-29-62	JOB NO.	DWG. NO.	REV.
CHK. D.J.	1252	73-3037	⚠
SCALE 1" = 1'-0"		SHEET 1 OF 4	

Fig. 4 Diagram of Vessel CD

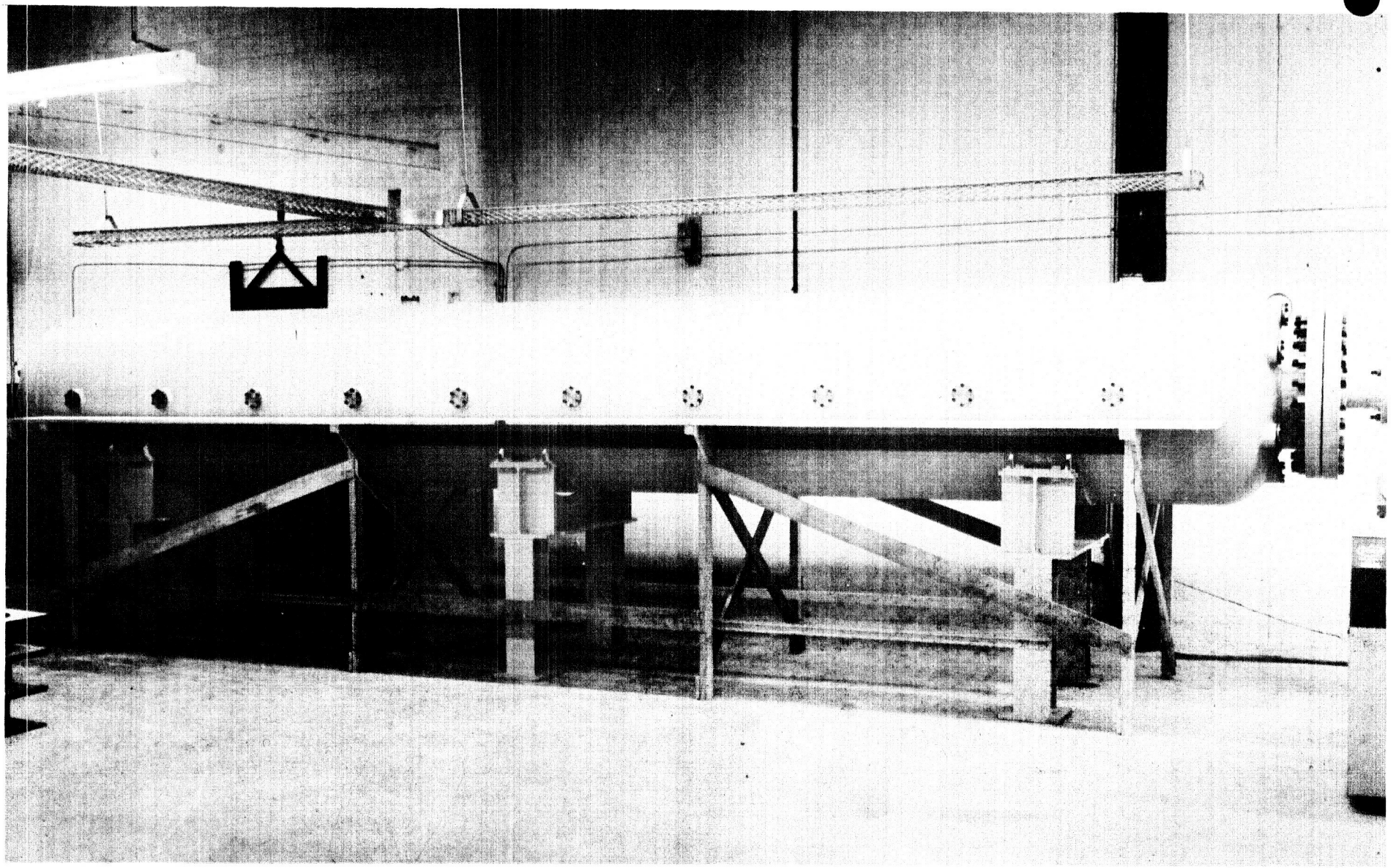

Fig. 5 Vessel A, 3 ft. x 20 ft. long carbon steel

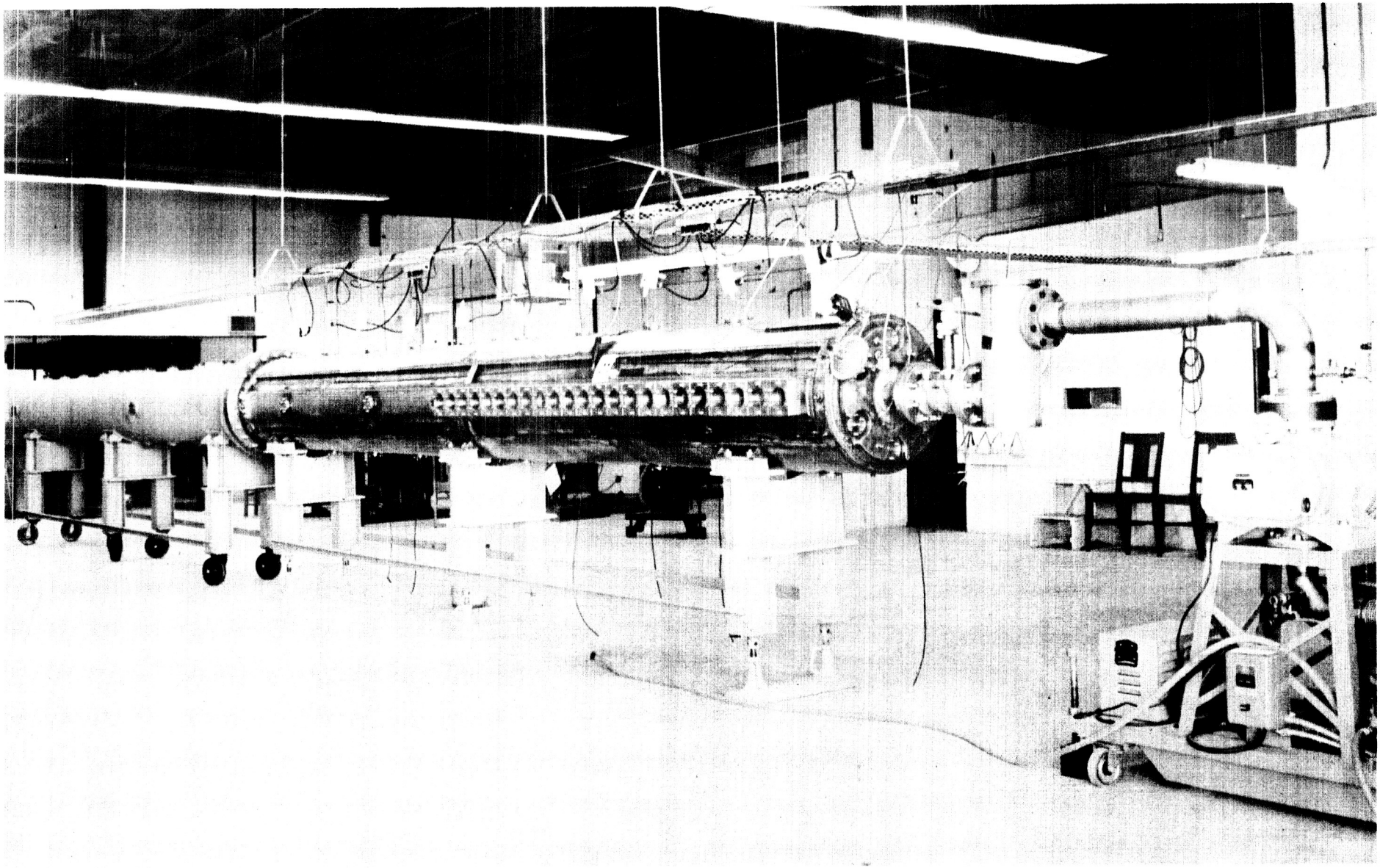

Fig. 6 Vessel B, 2 ft. dia. x 20 ft. long carbon steel; and Vessel CD, 2 ft. dia. x 20 ft. long stainless steel

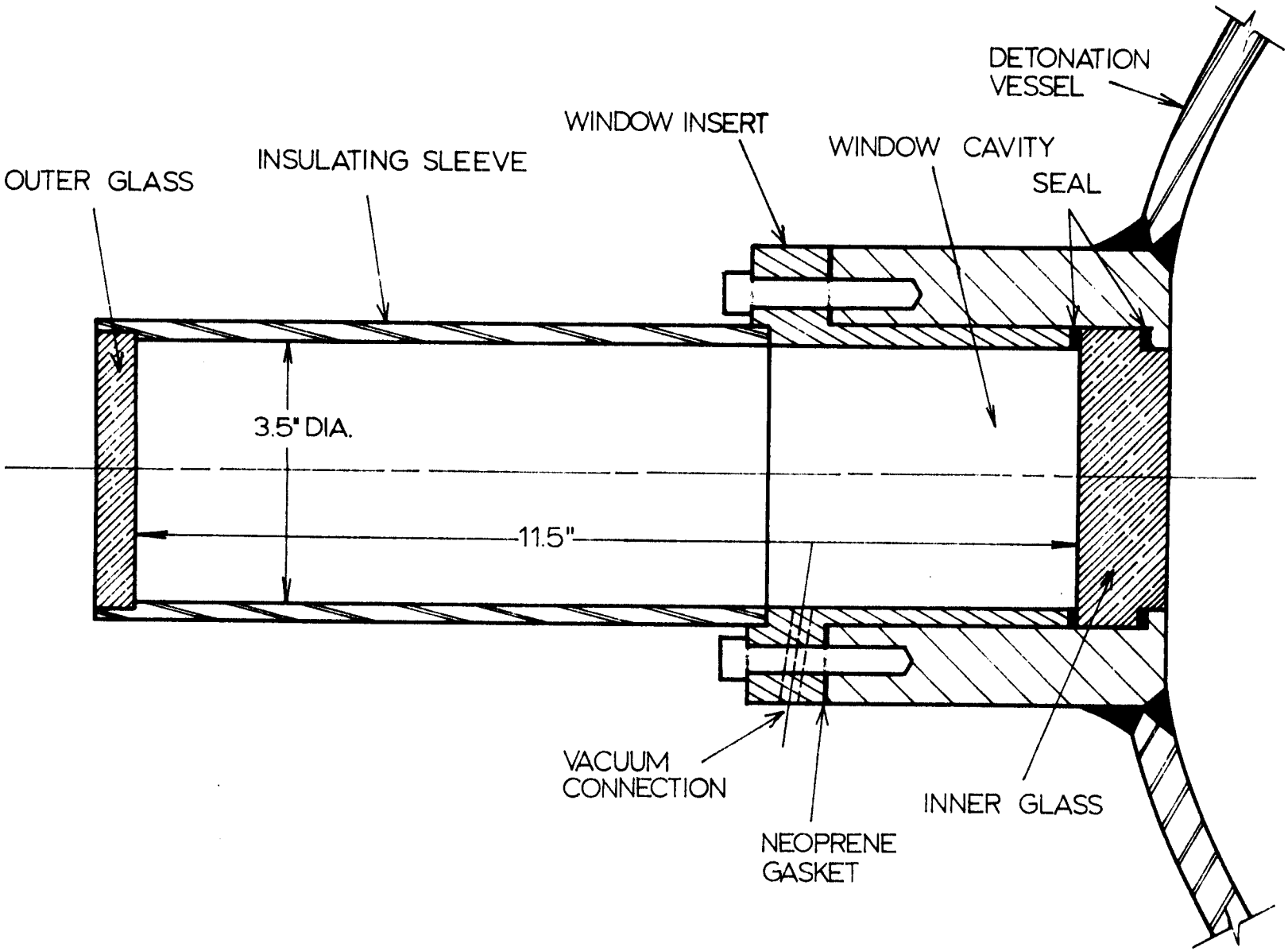

Fig. 7 Sectional view of schlieren observation ports in Vessel CD

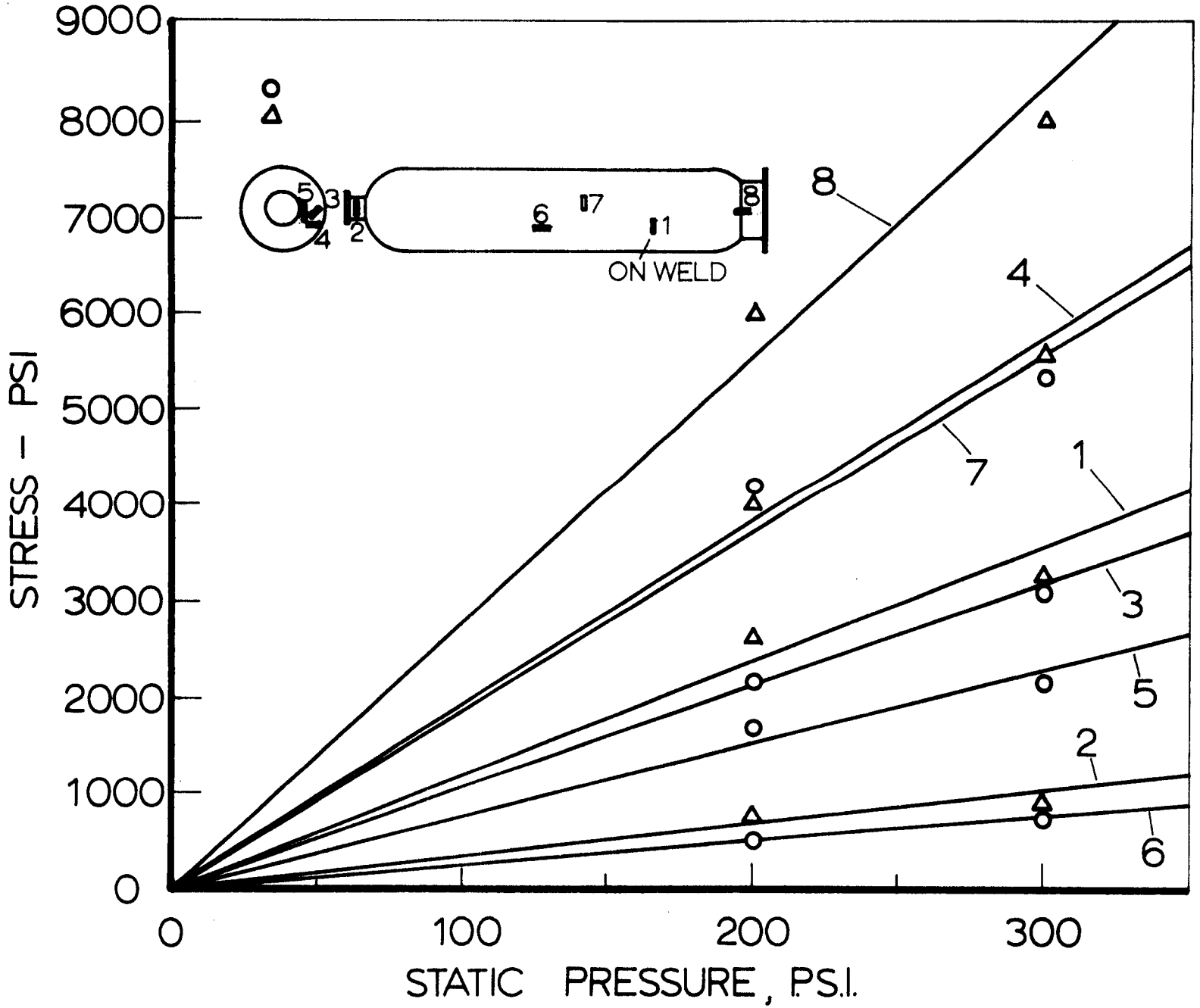

Fig. 8 Vessel A - hydrostatic test results

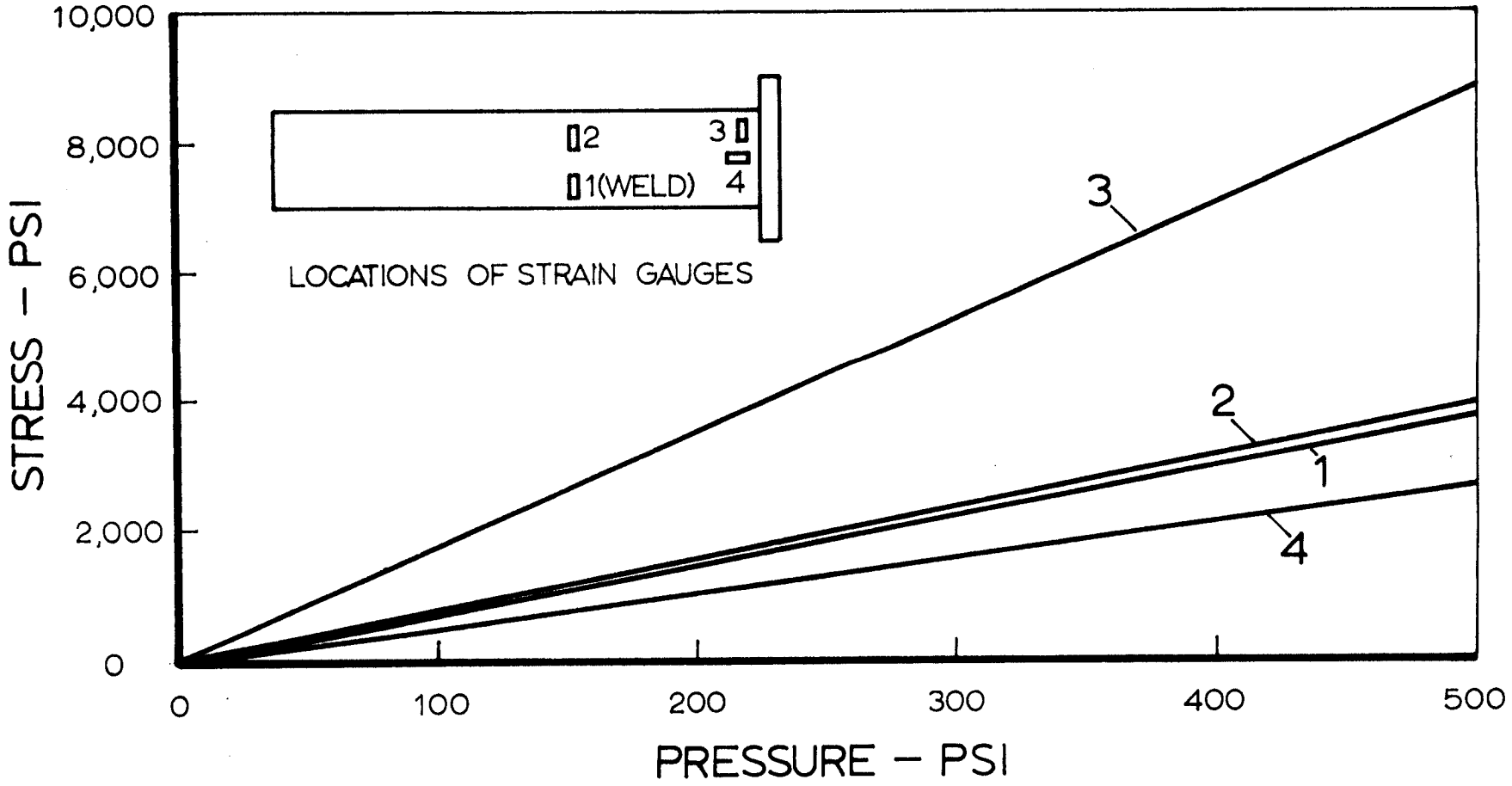

Fig. 9 Vessel B - hydrostatic test results

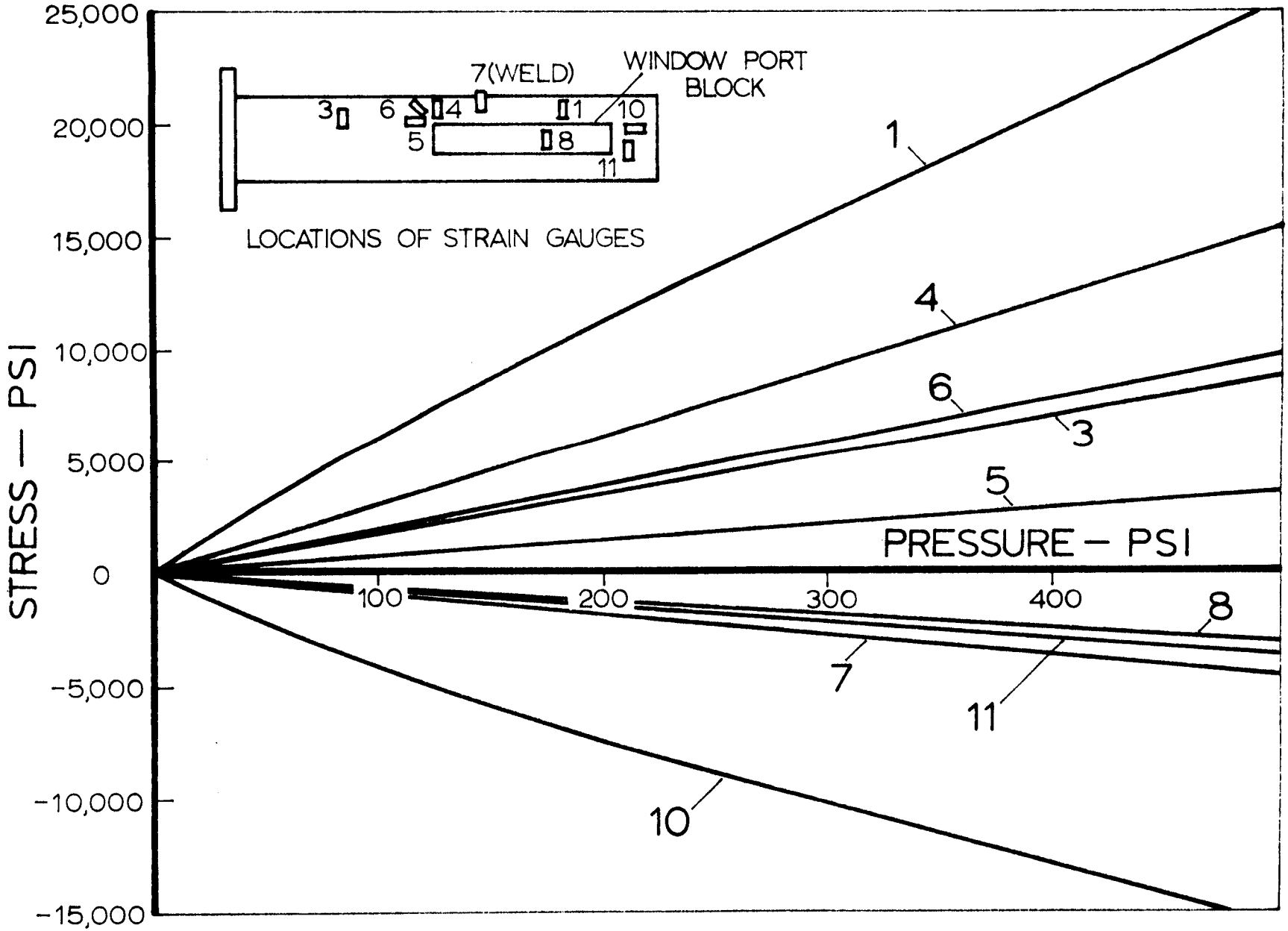

Fig. 10 Vessel CD - hydrostatic test results

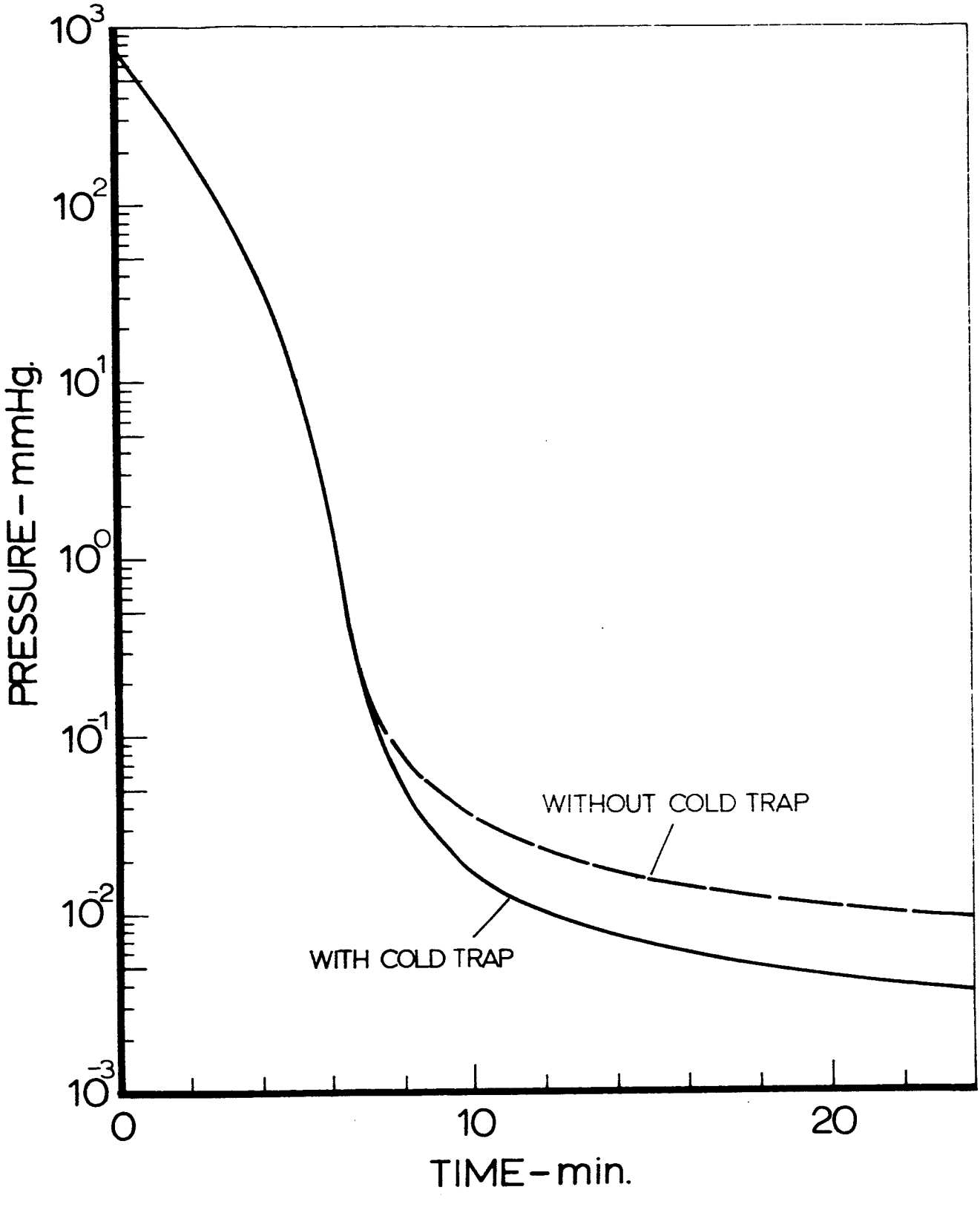

Fig. 11 Pumpdown characteristics of Vessel A

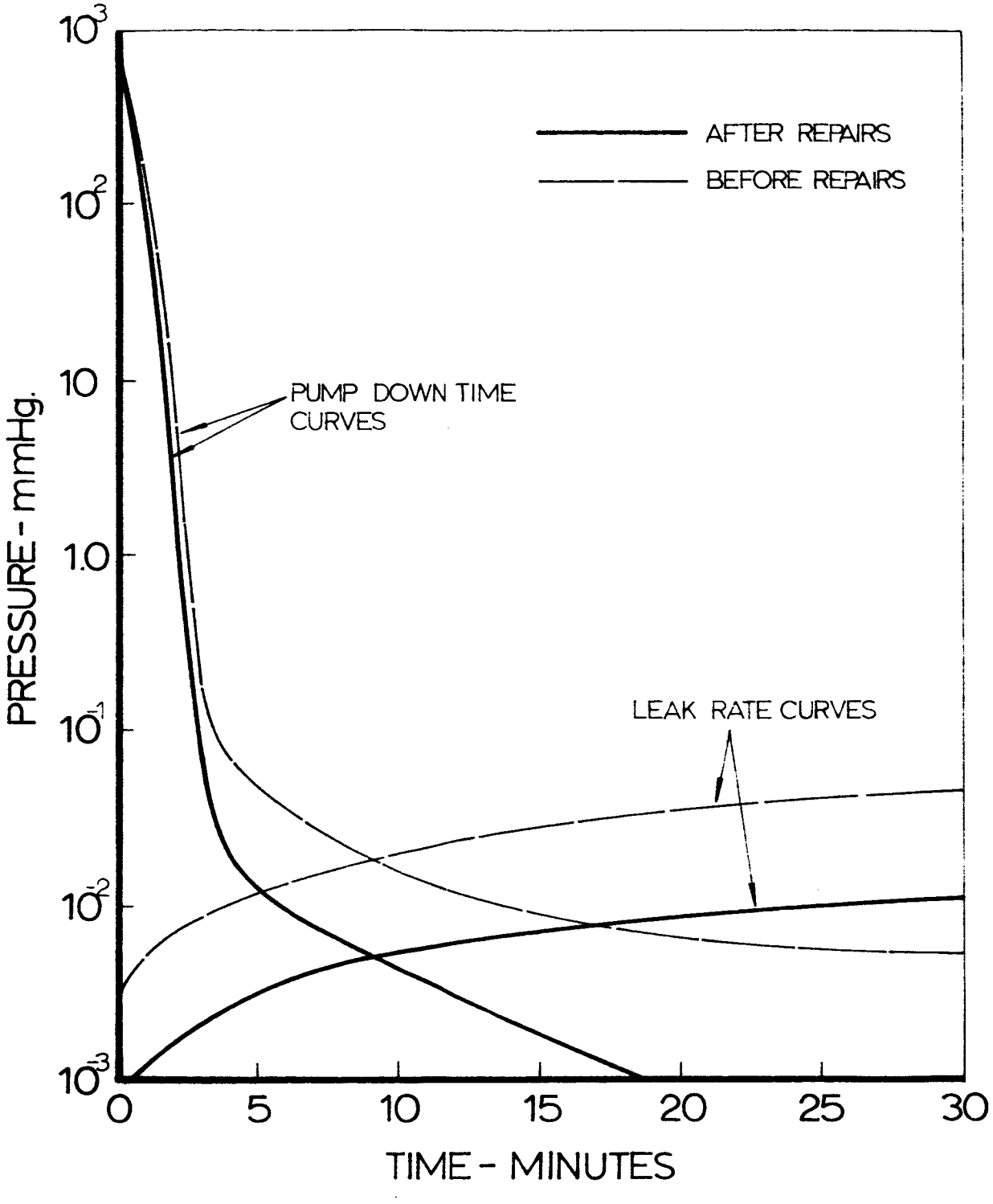

Fig. 12 Vacuum test results of Vessel CD before and after repairs.

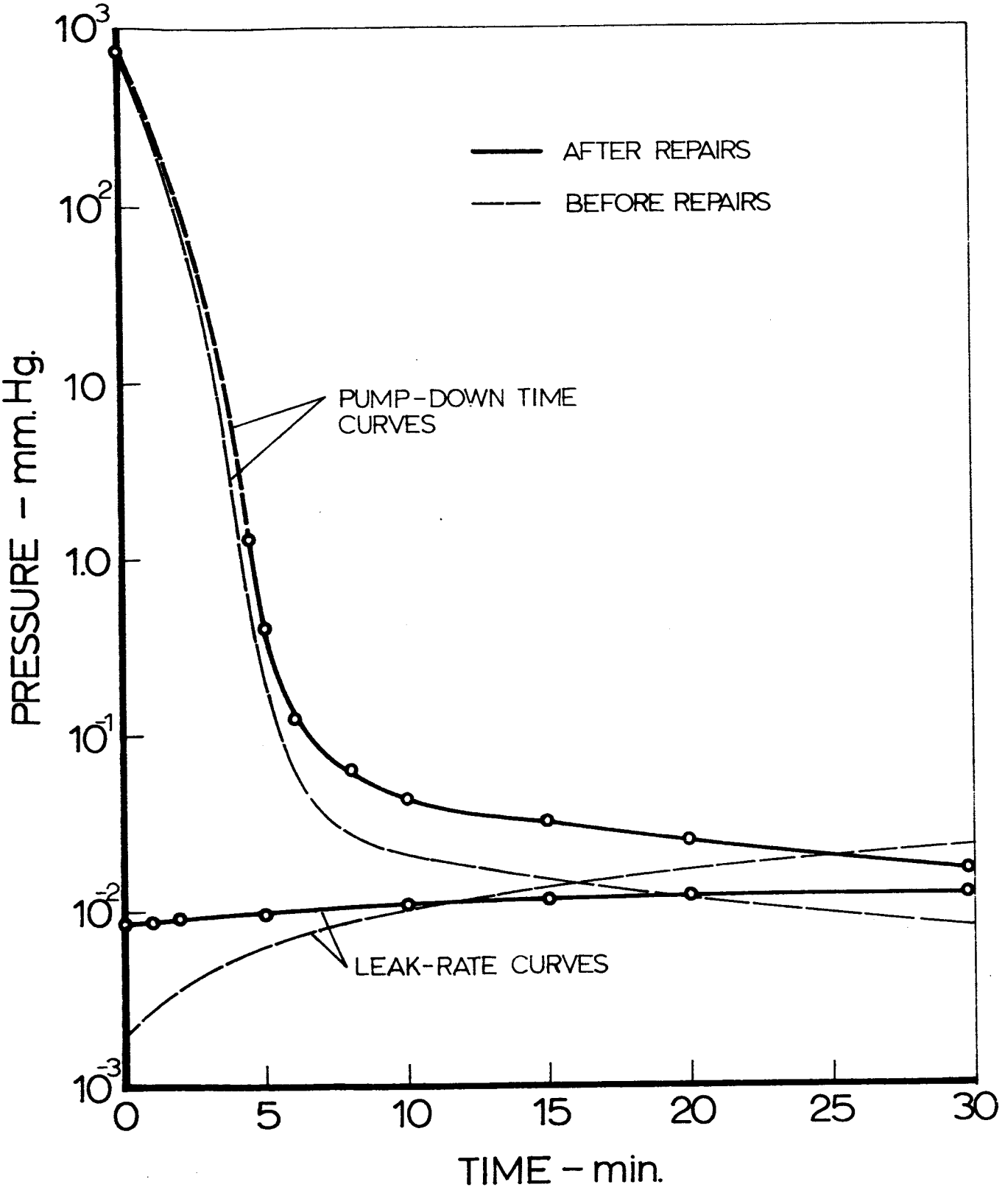

Fig. 13 Vacuum test results of Vessels C-D and B connected together, before and after final repairs

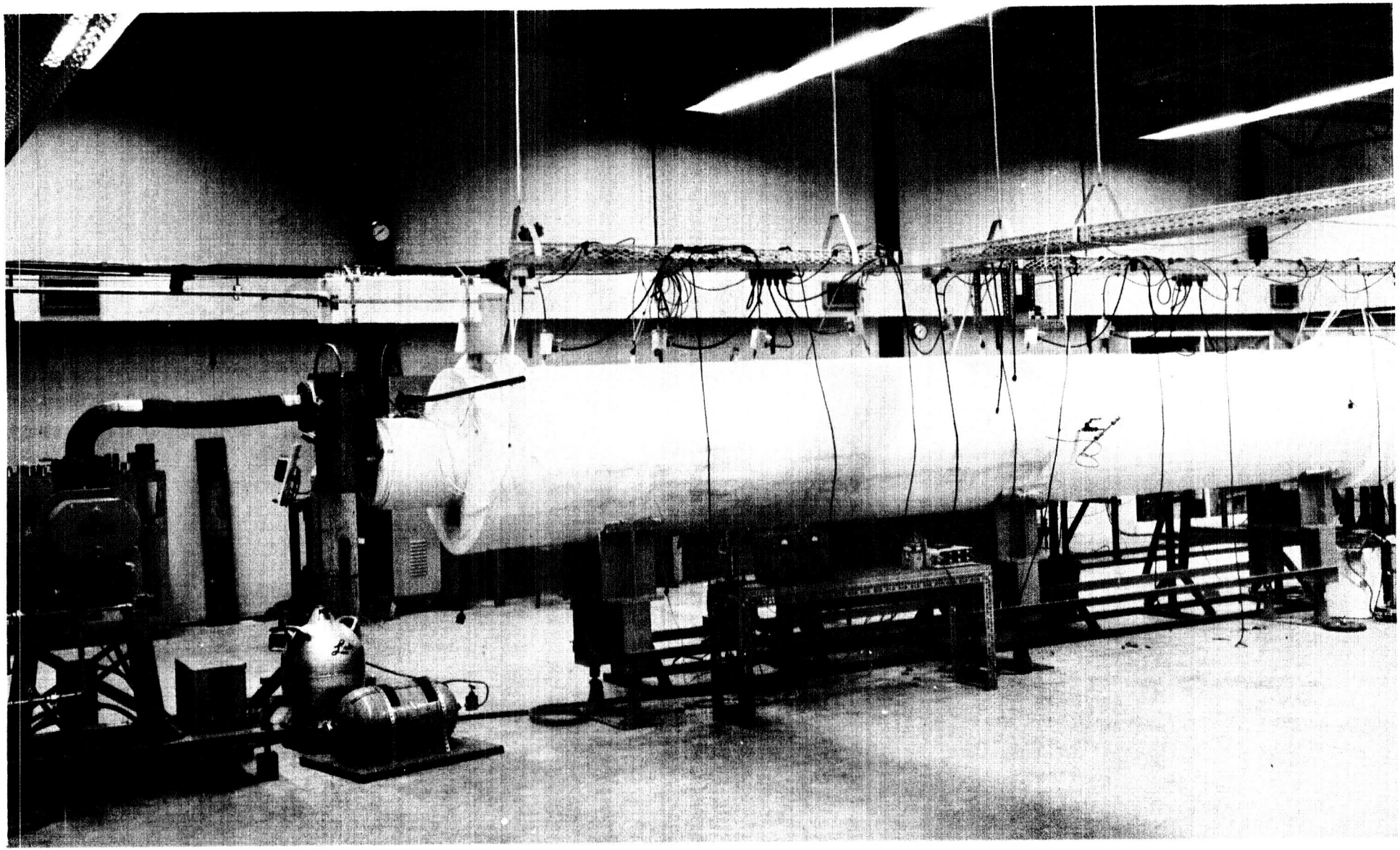

Fig. 14 Vessel CD with Insulation

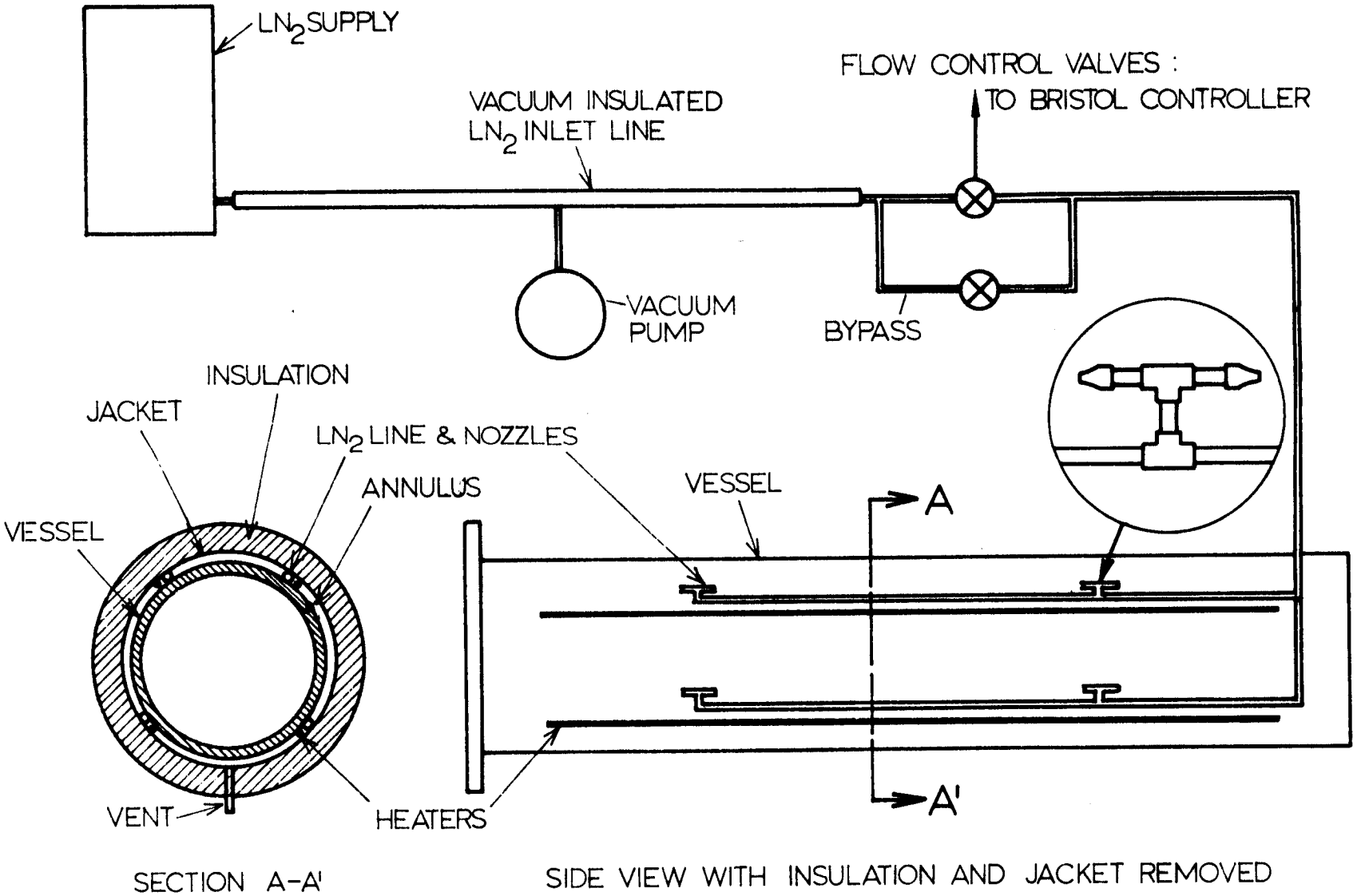

Fig. 15 Schematic of temperature control system on Vessel CD

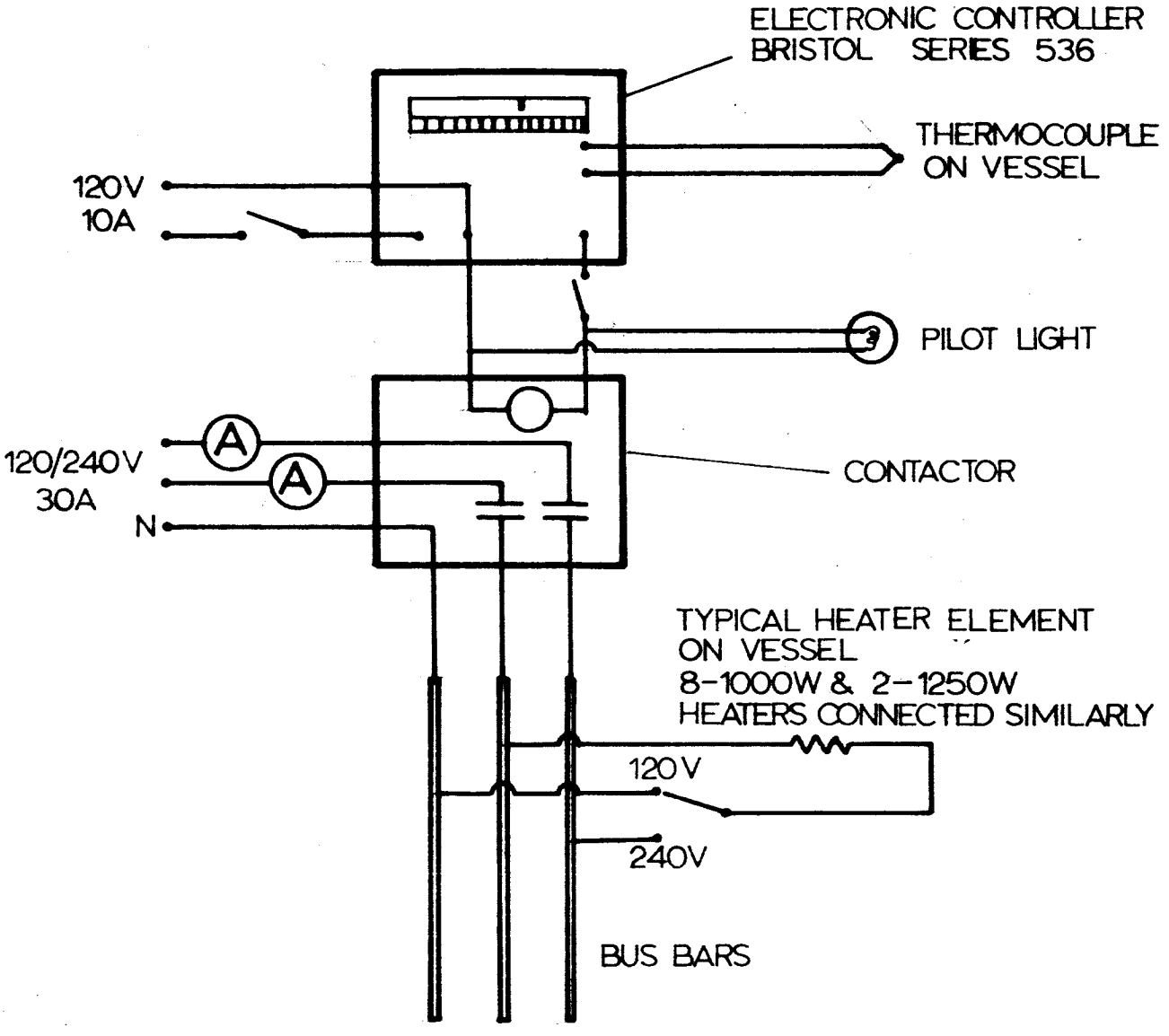

FIGURE 16

CONTROL ARRANGEMENT OF

ELECTRIC HEATERS INSTALLED ON VESSEL CD

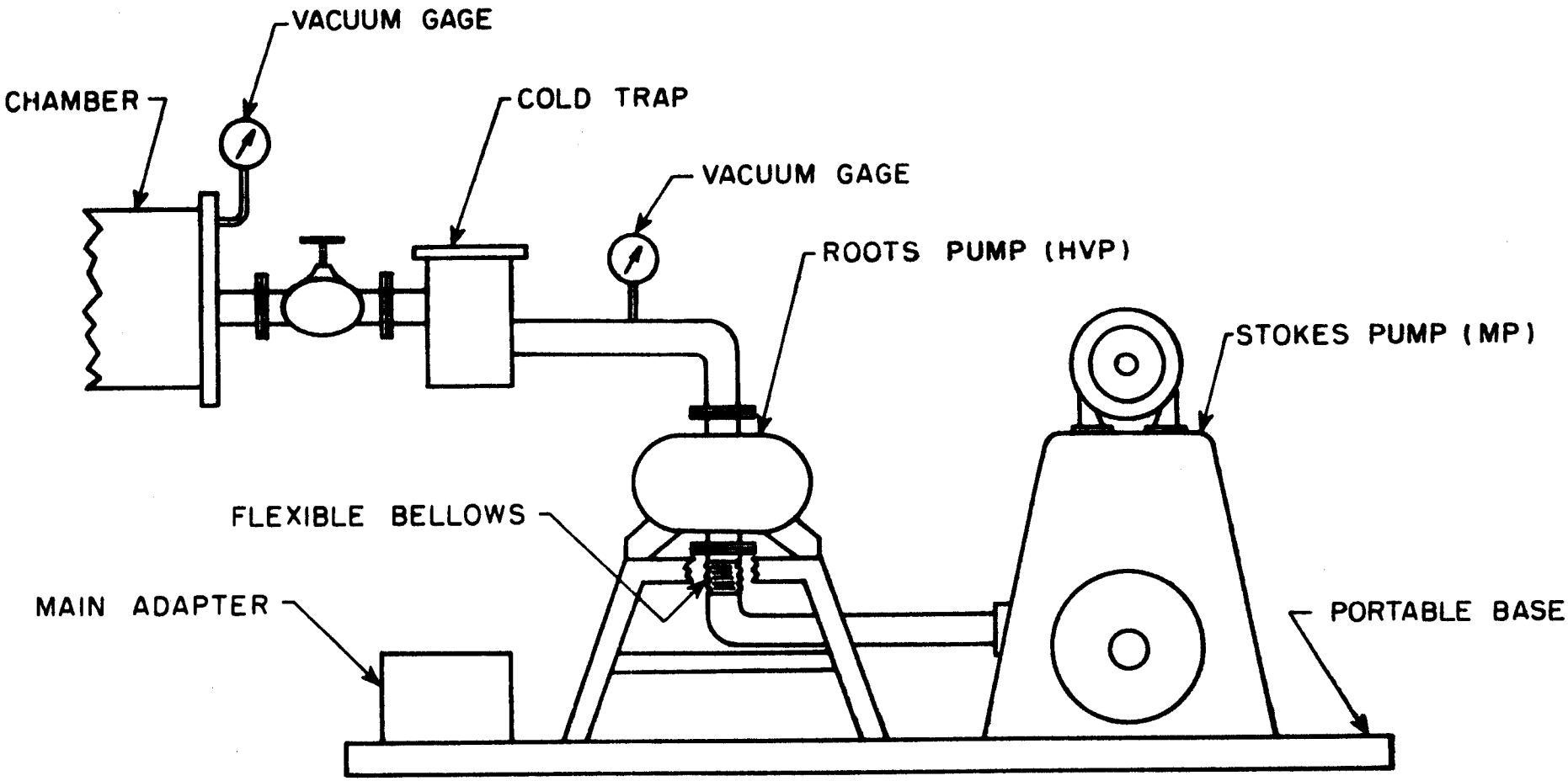

Fig.17 Assembly of Vacuum Pump System

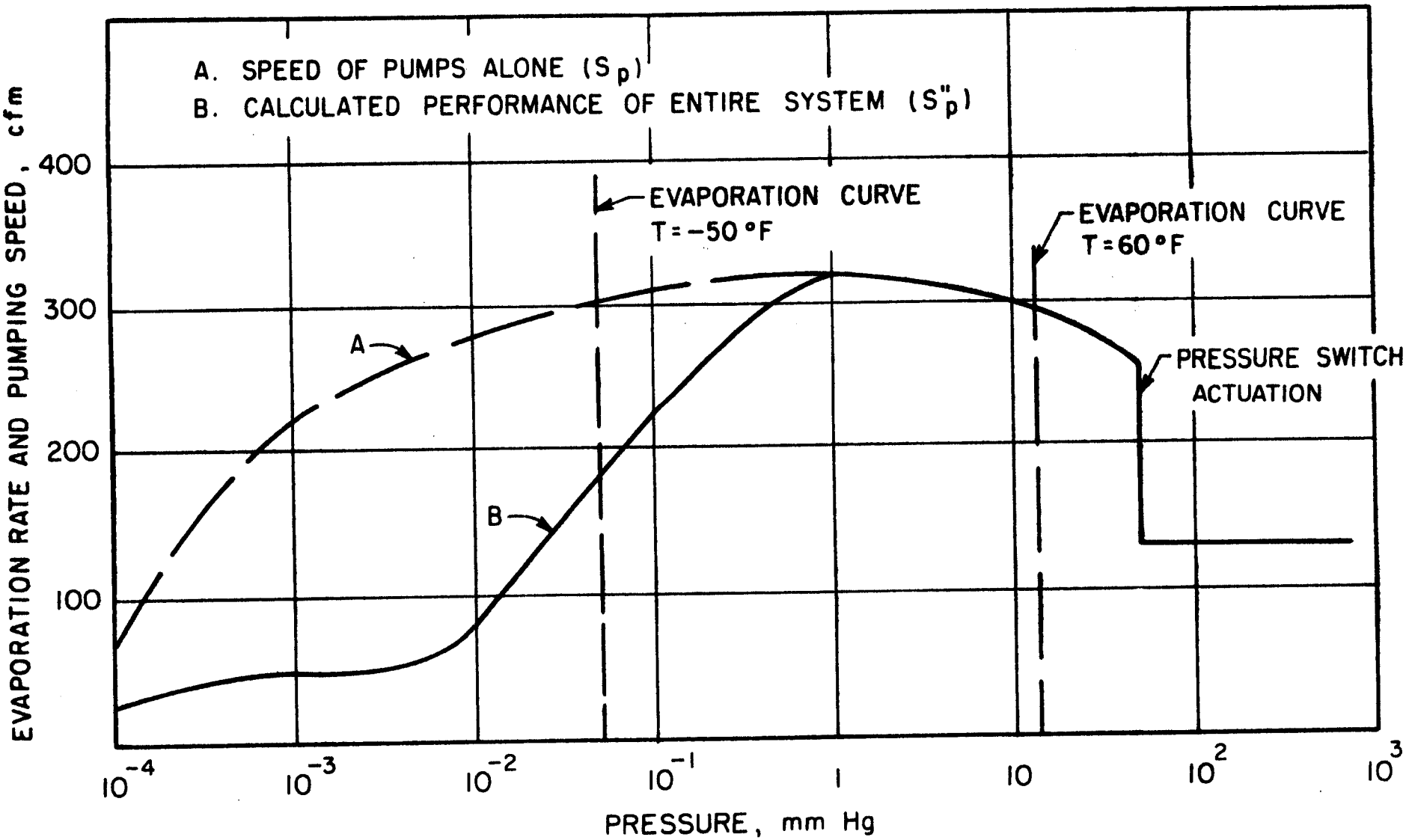

Fig. 18 Vacuum Pump System Performance Curves

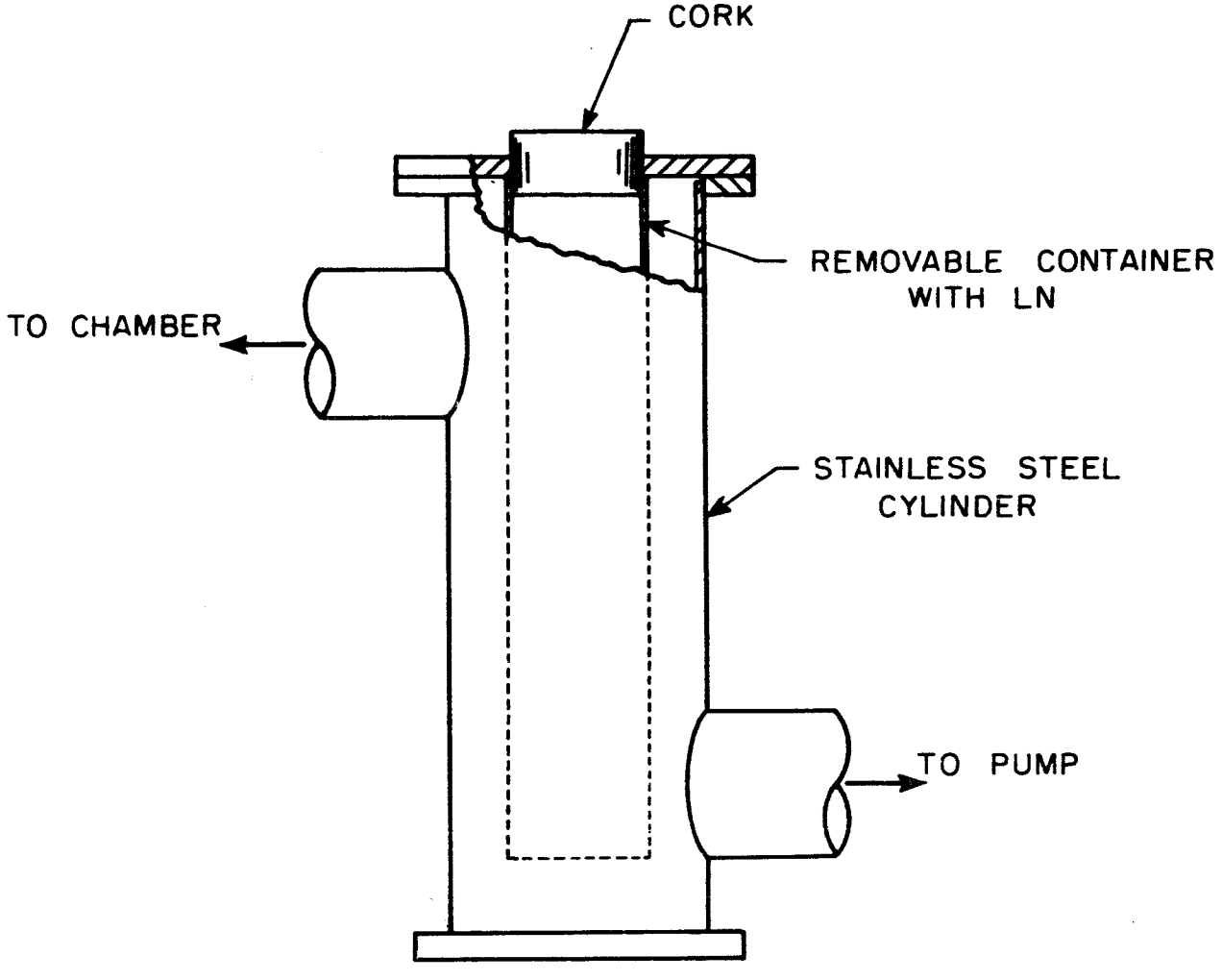

Fig.19 Cold trap construction

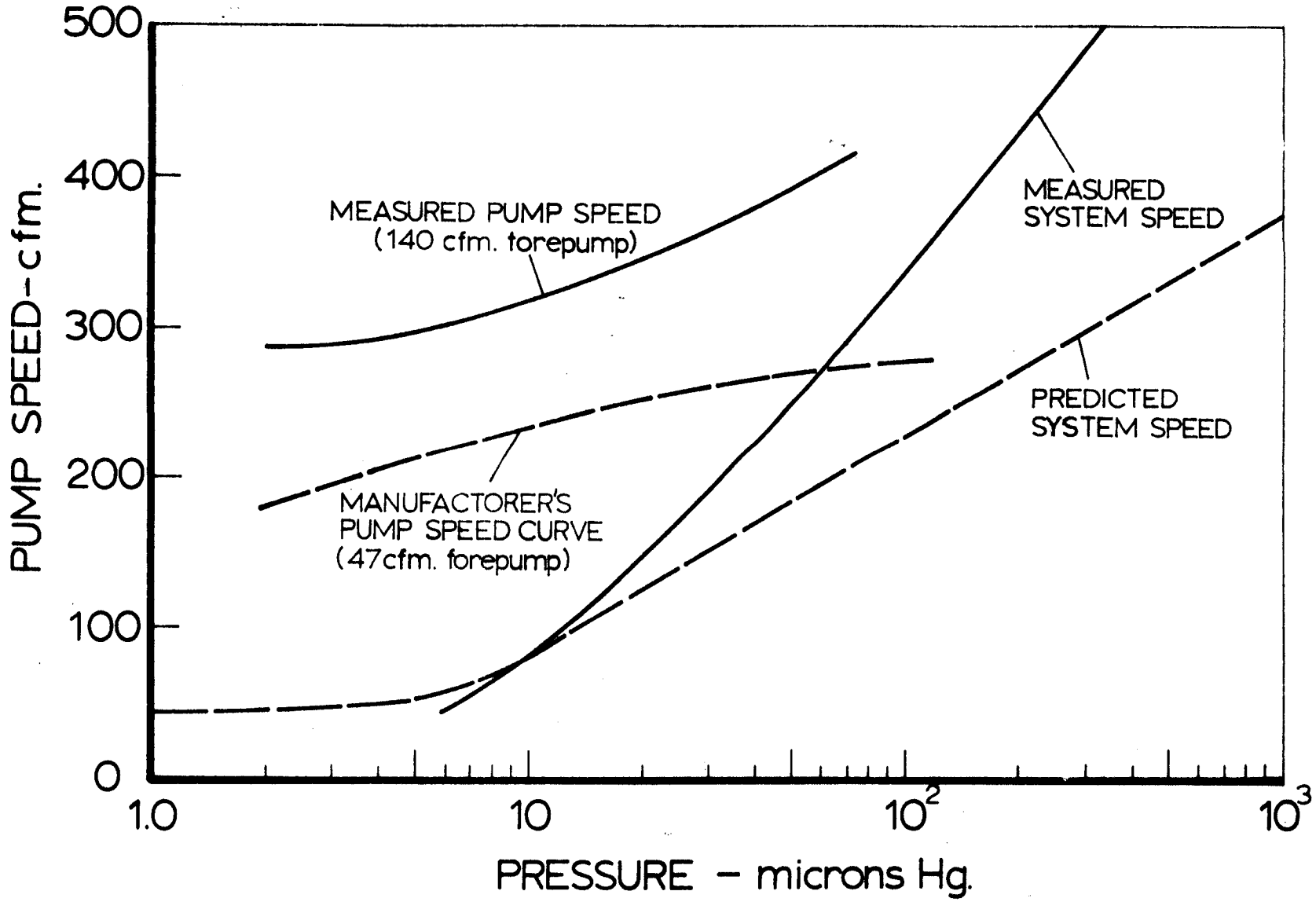

FIGURE 20

PERFORMANCE CHARACTERISTICS OF VACUUM PUMP AND ENTIRE SYSTEM INCLUDING VESSEL A

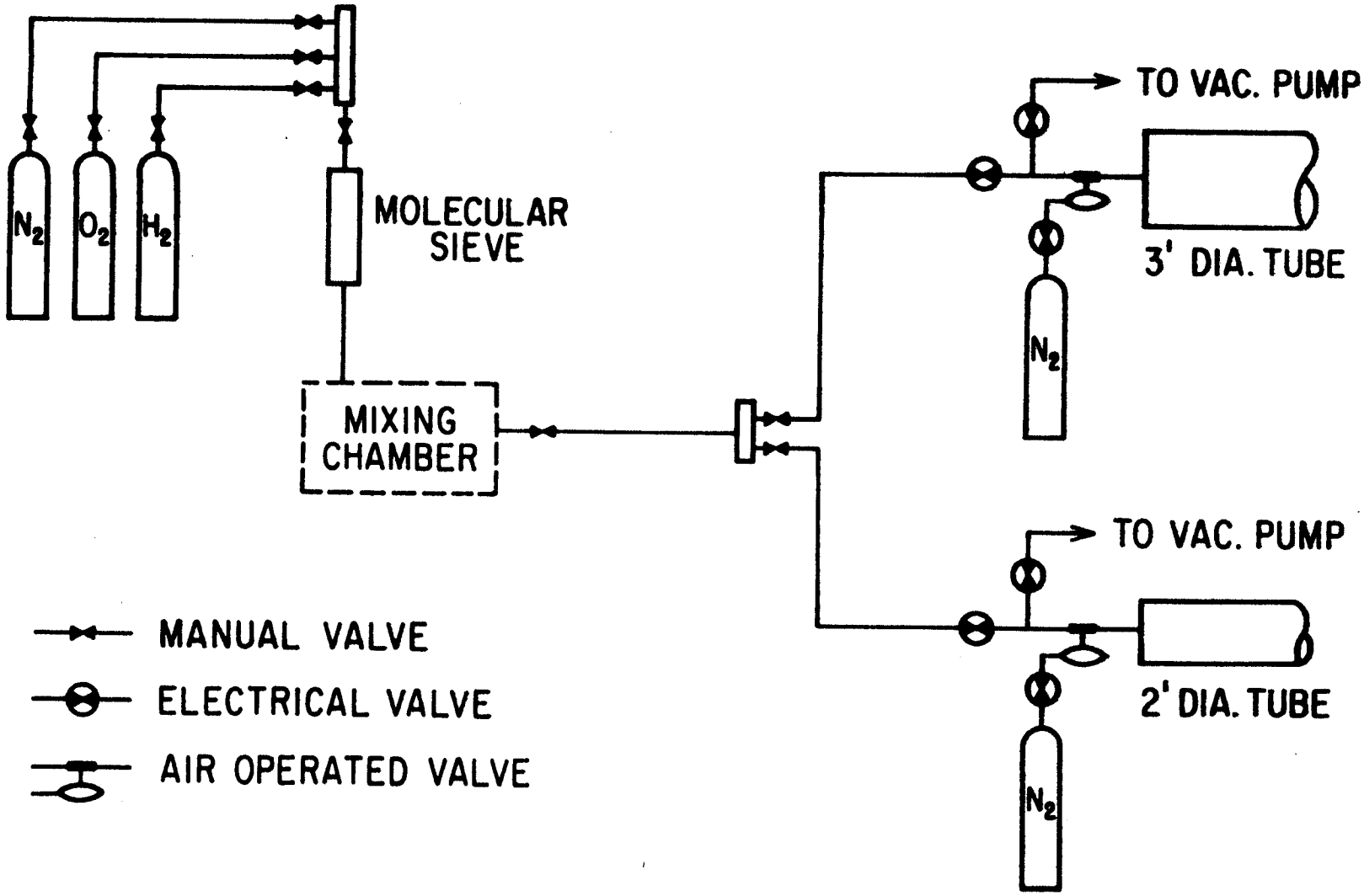

Fig.21 Schematic of Premixed Gas Handling System

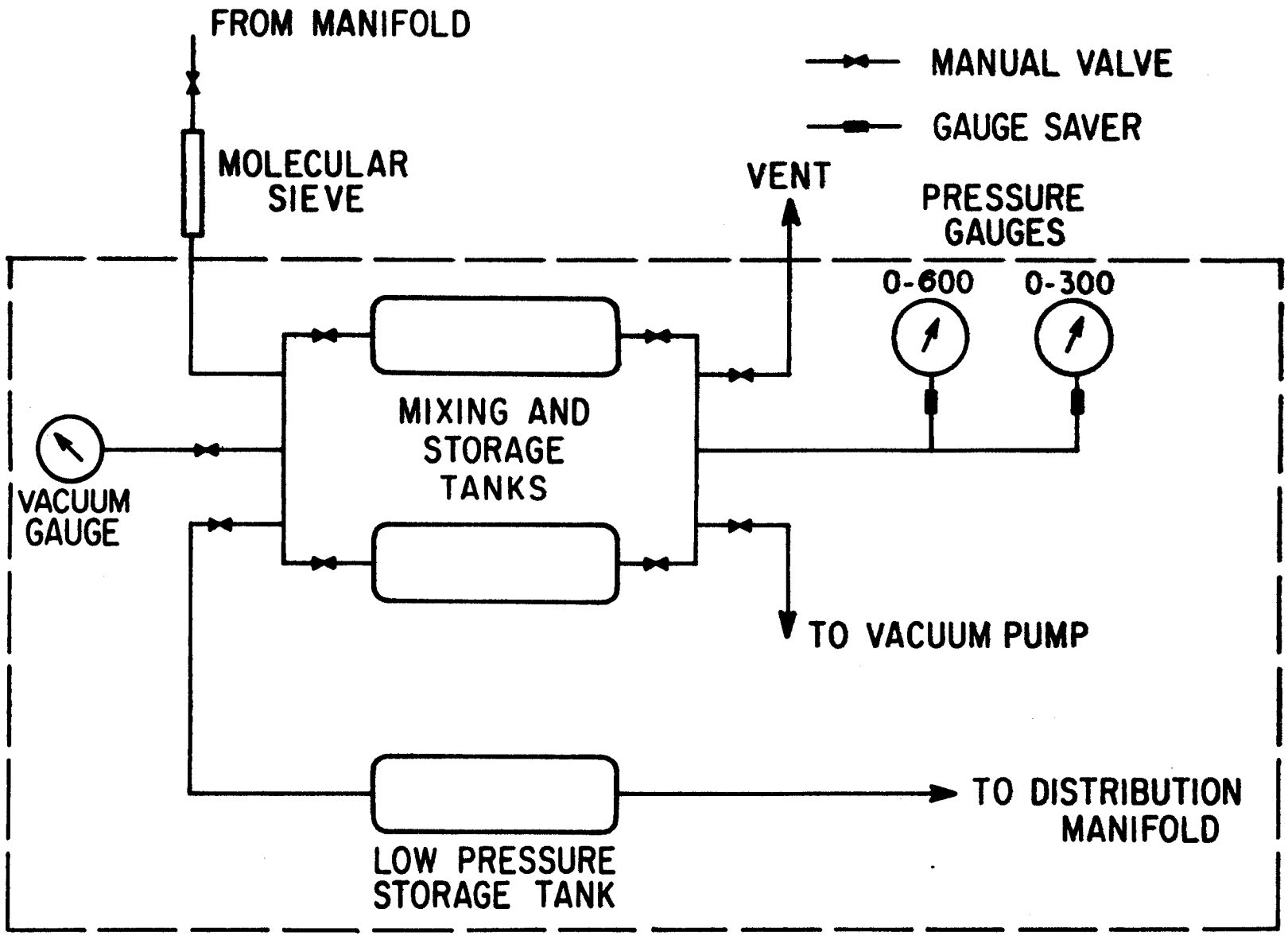

Fig. 22 Schematic of Mixing Chamber

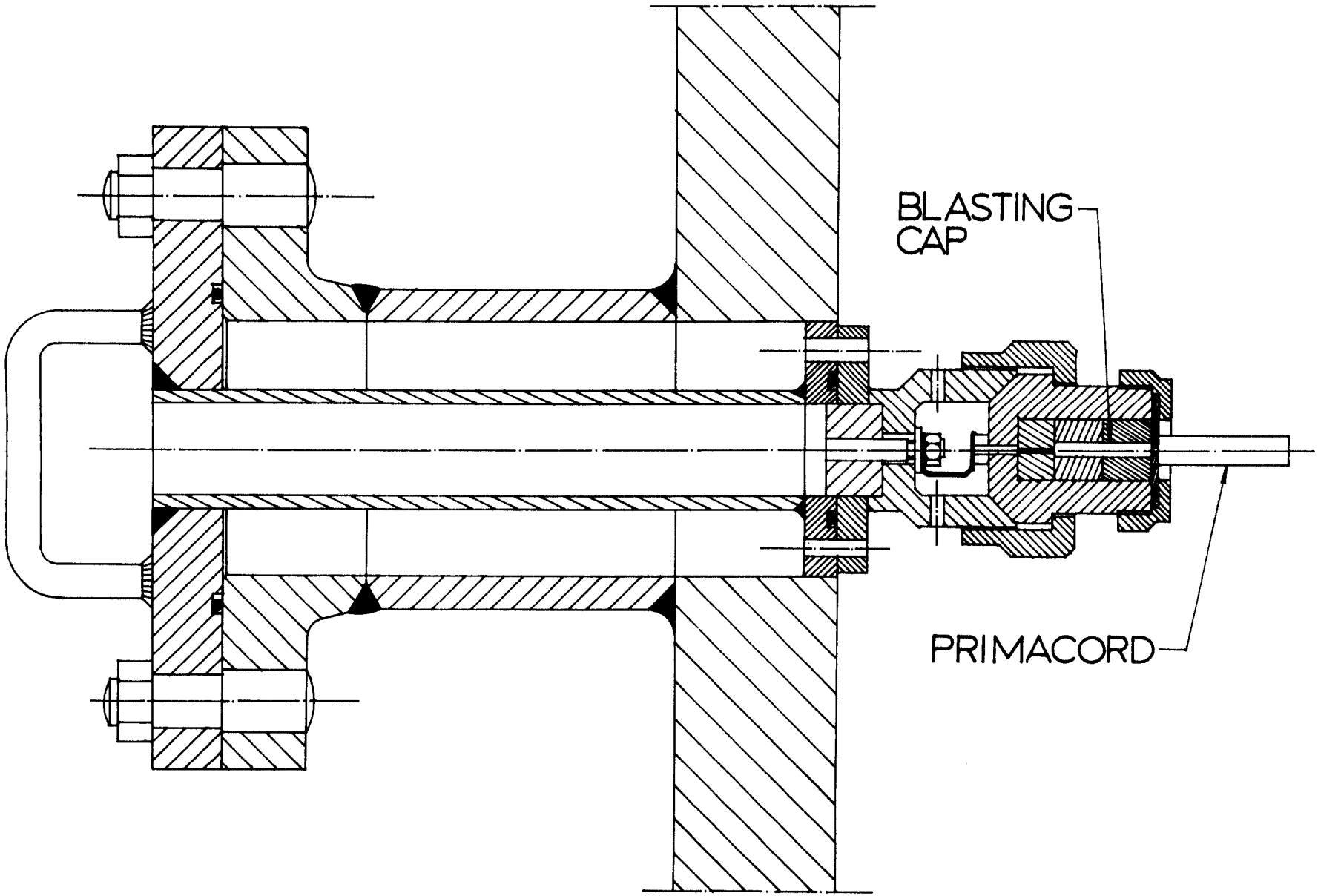

Fig. 23 Primacord ignition holder assembly

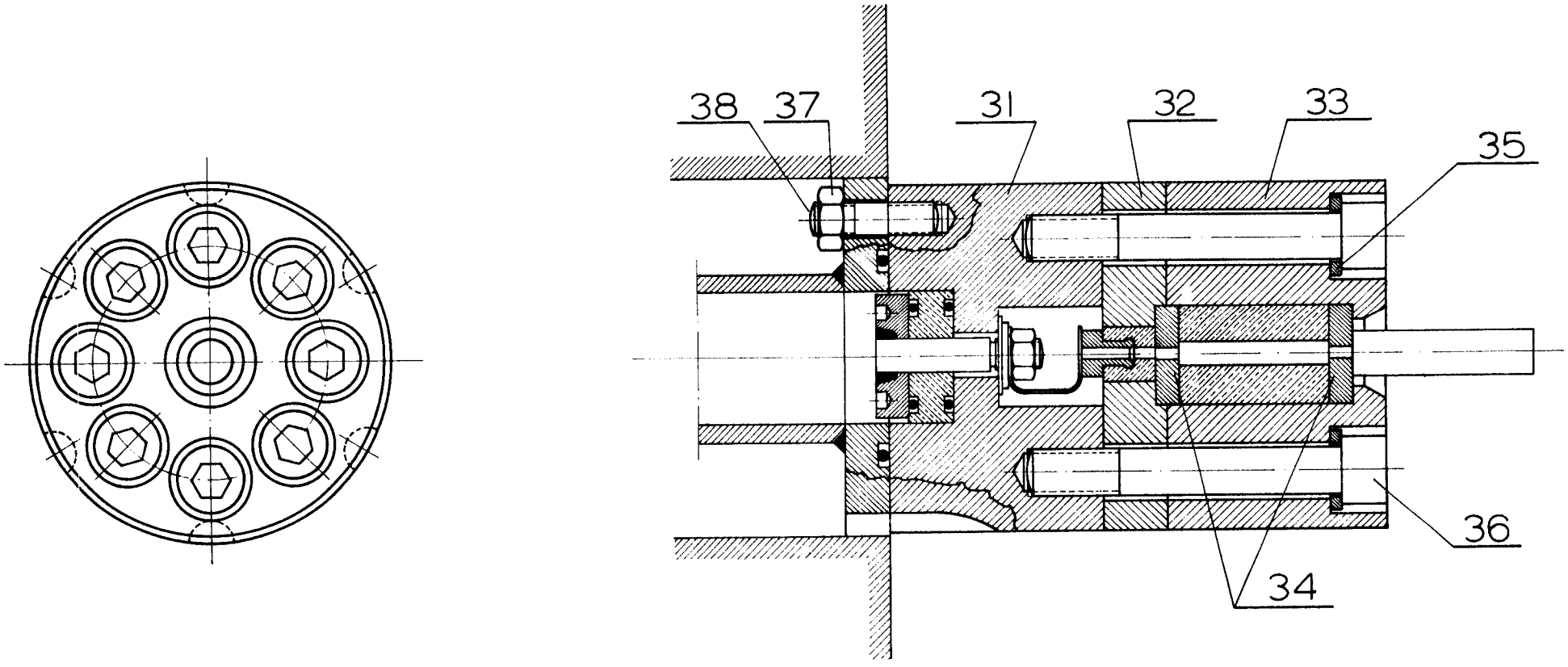

Fig. 24 Modified Ignition Holder Assembly

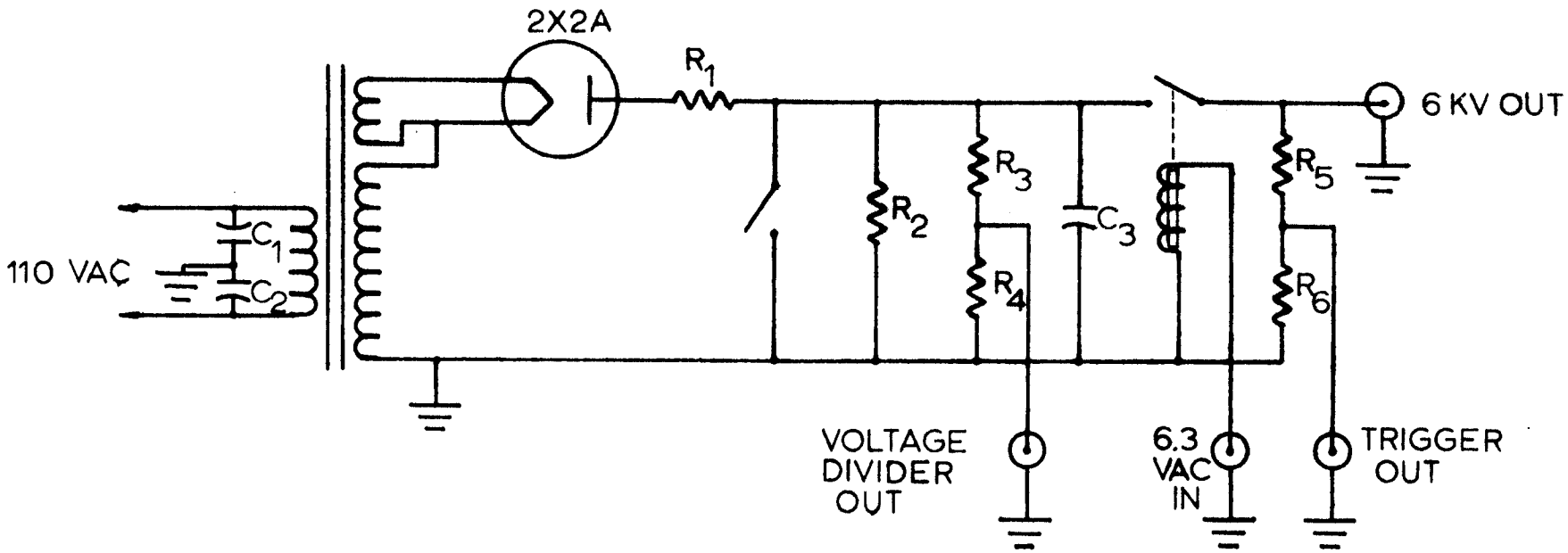

R_1 - 3.3 MegΩ R_3 - 40 MegΩ R_5 - 10 KΩ C_1 - .1uf 400V C_3 - 2uf 15KV

R_2 - 14 MegΩ R_4 - 12 MegΩ R_6 - 100Ω C_2 - .1uf 400V

Fig 25 Circuit Diagram for Spark Ignition System

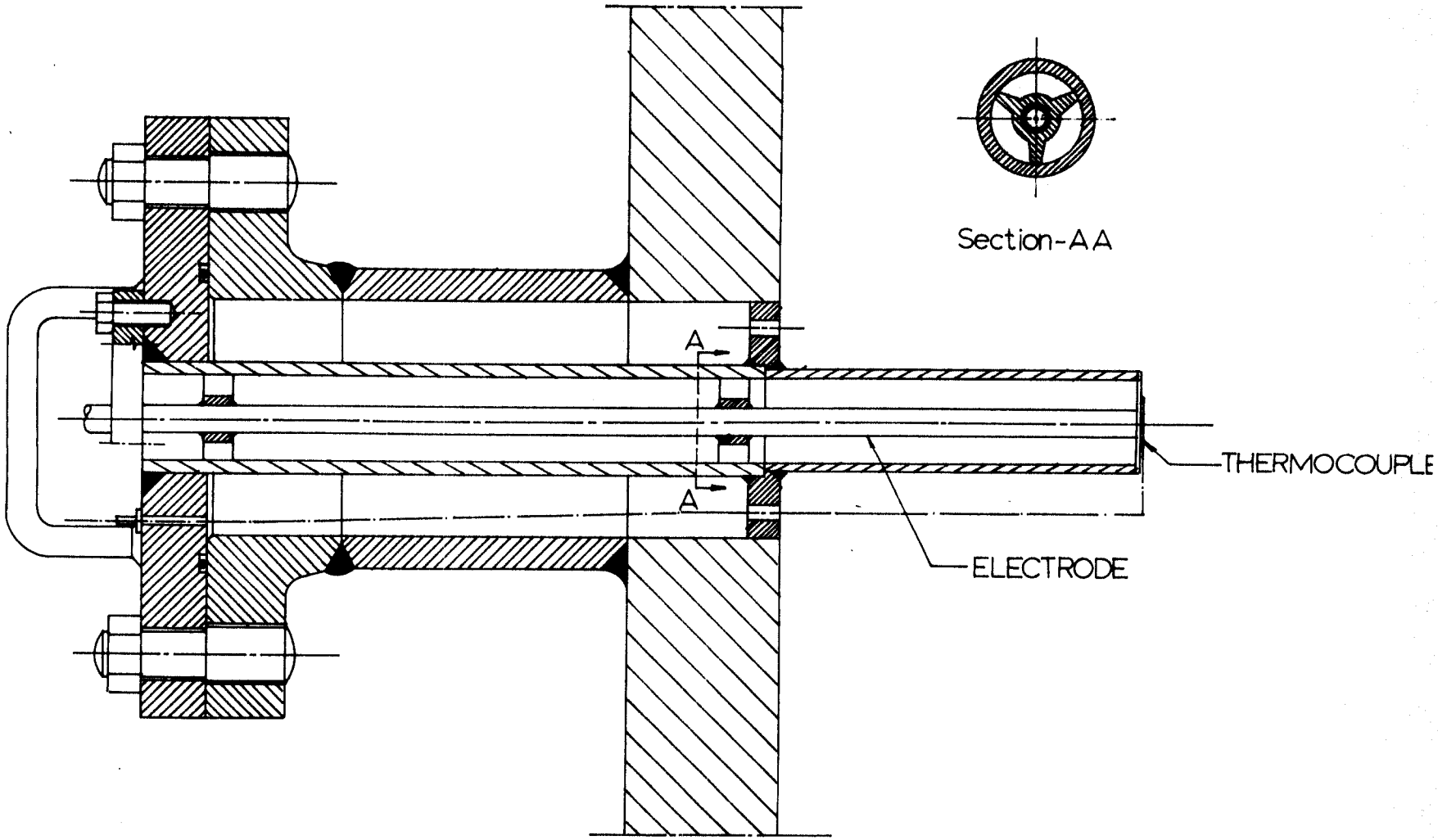

Fig. 26 Hot plate ignitor

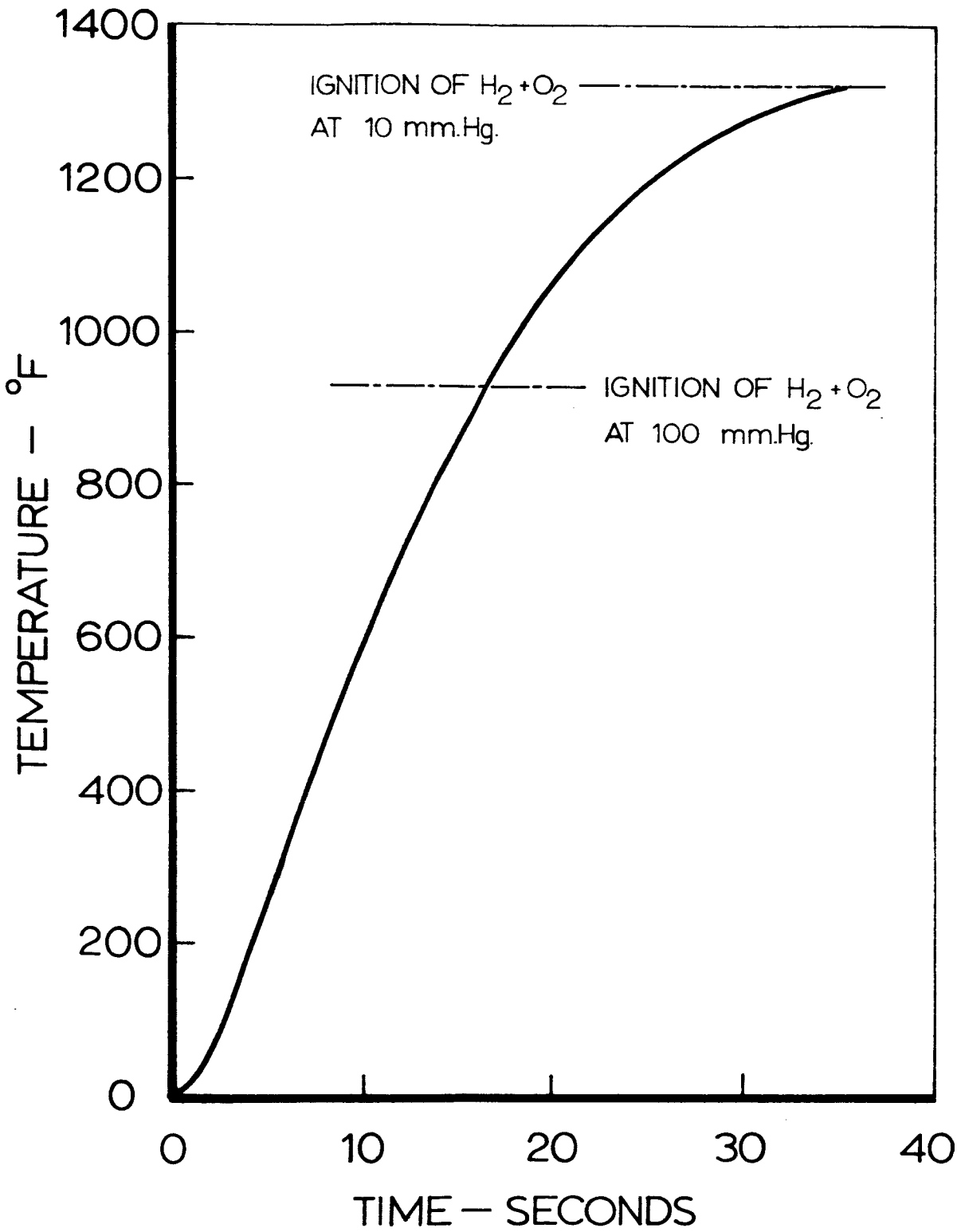

Fig. 27 Temperature history of hot plate ignitor

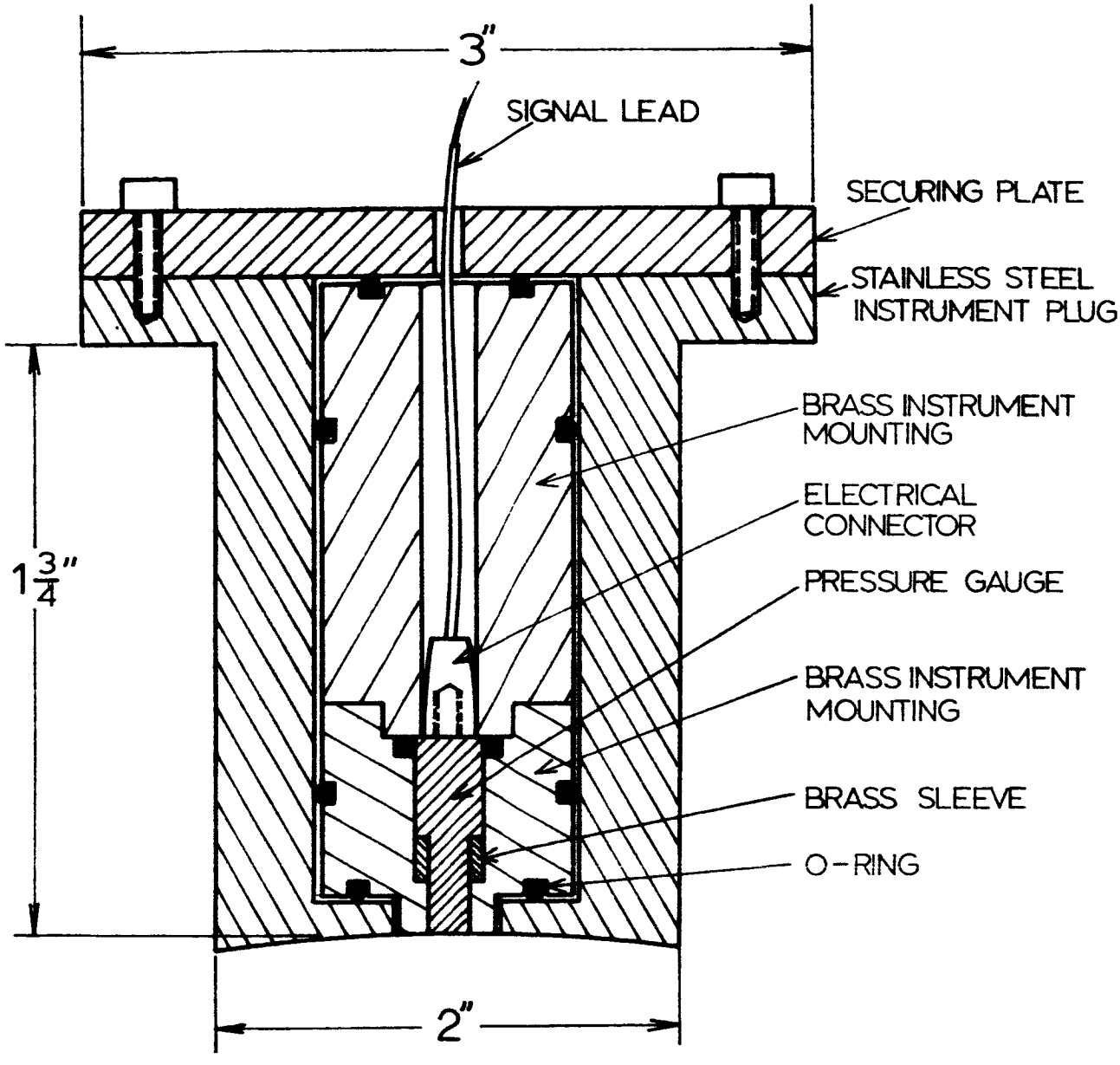

Fig.28 Pressure Gauge and Housing (Section View)

(O-rings provide vacuum seal and serve to isolate gauge from direct contact with housing)

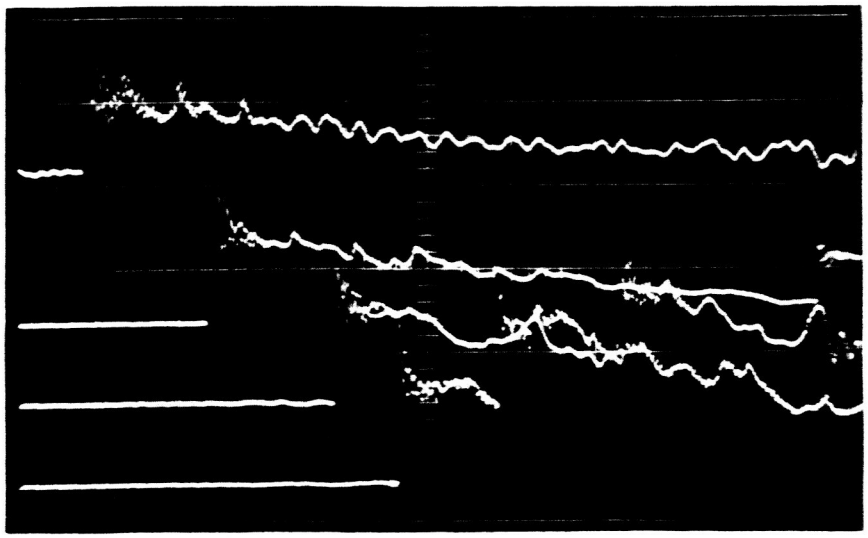

Fig. 29 Typical oscilloscope record of output of pressure transducers located, from top to bottom, at positions 3, 5, 7 and 9. Vertical scale: 20 psi/div., horizontal scale: 300 μsec/div. Test conditions: $2H_2+O_2$ composition, 100 mmHg initial pressure, room temperature, Primacord ignition, Vessel CD.

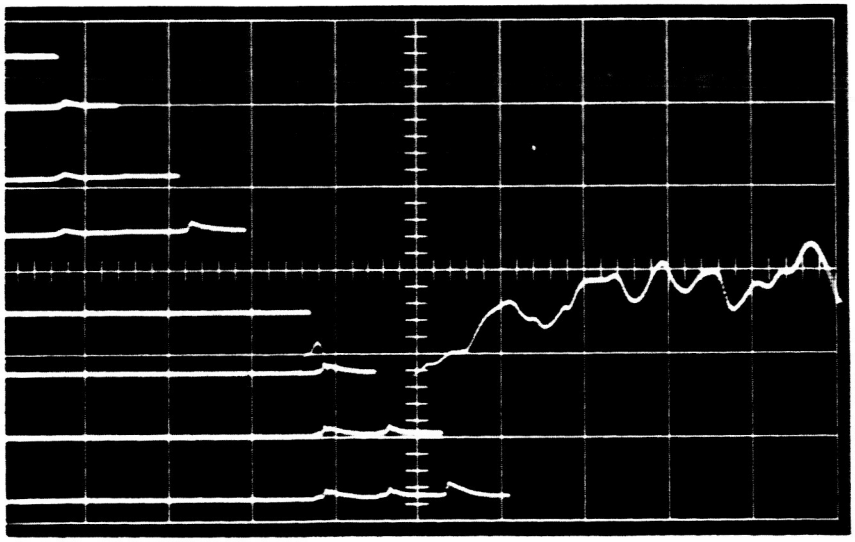

Fig. 30 Typical oscilloscope record of ionization signals. Vertical scale: 1 volt/div., horizontal scale: 300 μsec/div. First ionization probe located at position 3. Test conditions: $2H_2+O_2$ composition, 100 mmHg initial pressure, room temperature, Primacord ignition, Vessel CD.

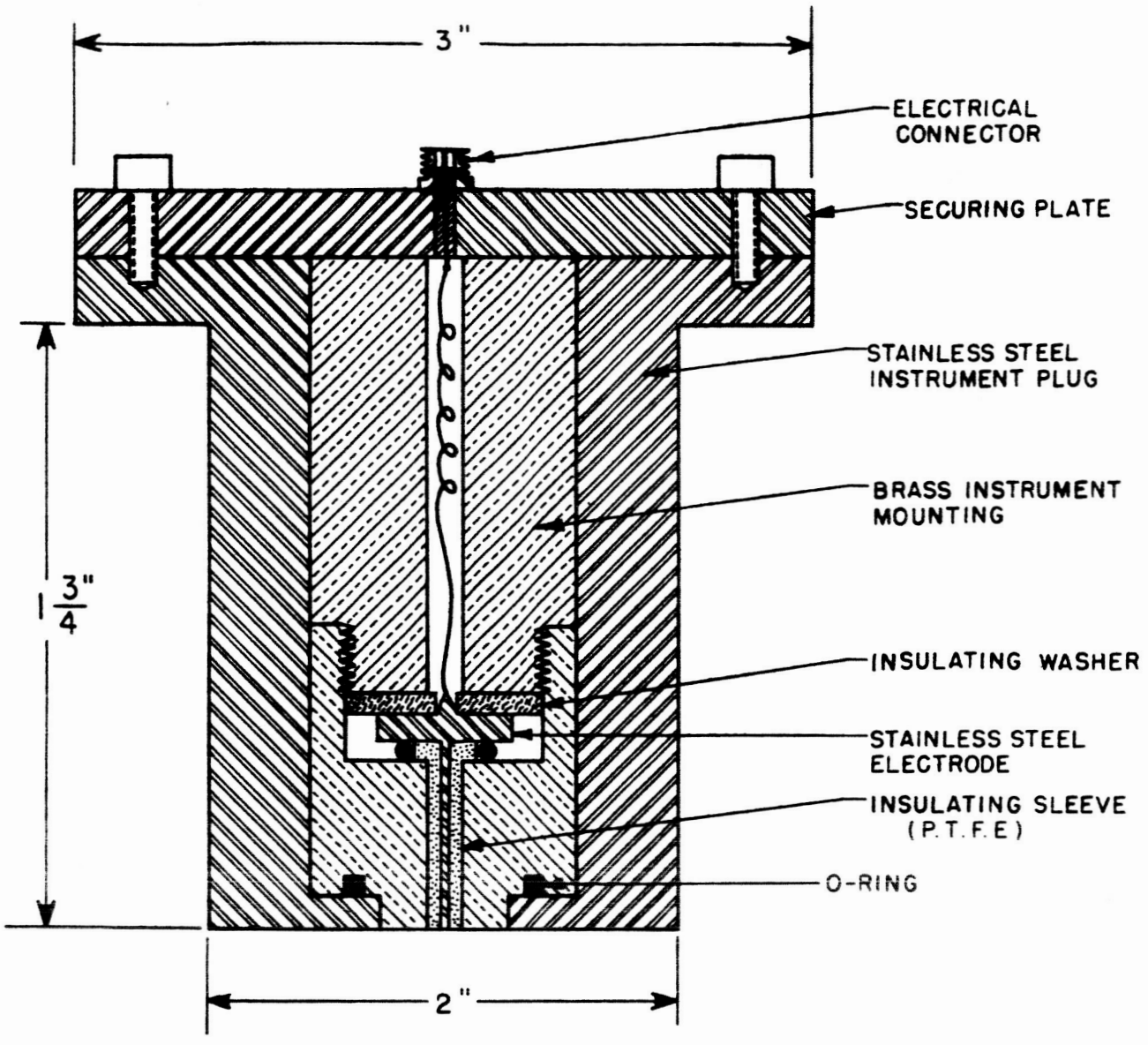

Fig. 31 Ionization Gauge and Housing

(Section View)

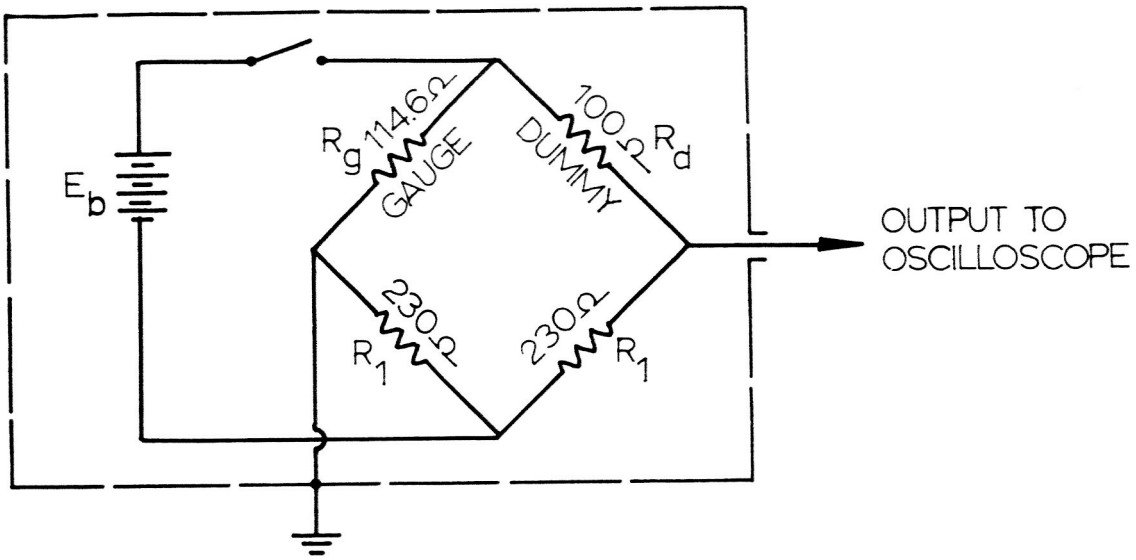

Fig. 32 Strain gauge circuit for Vessel A

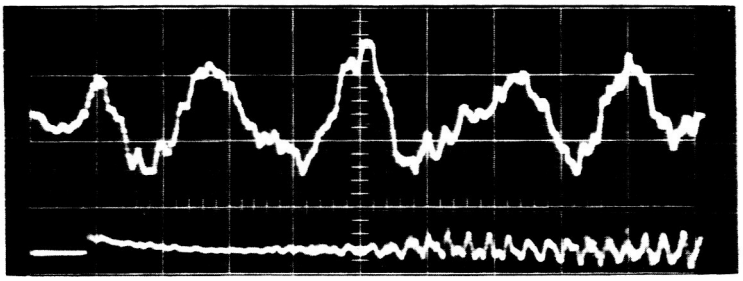

Fig. 33 Typical oscillograph of dynamic response of strain gauge attached to Vessel A. Vertical scale in arbitrary units, horizontal scale: 2 msec/div. from left to right. Upper trace is strain gauge record, lower trace is response of pressure transducer located at position 10.

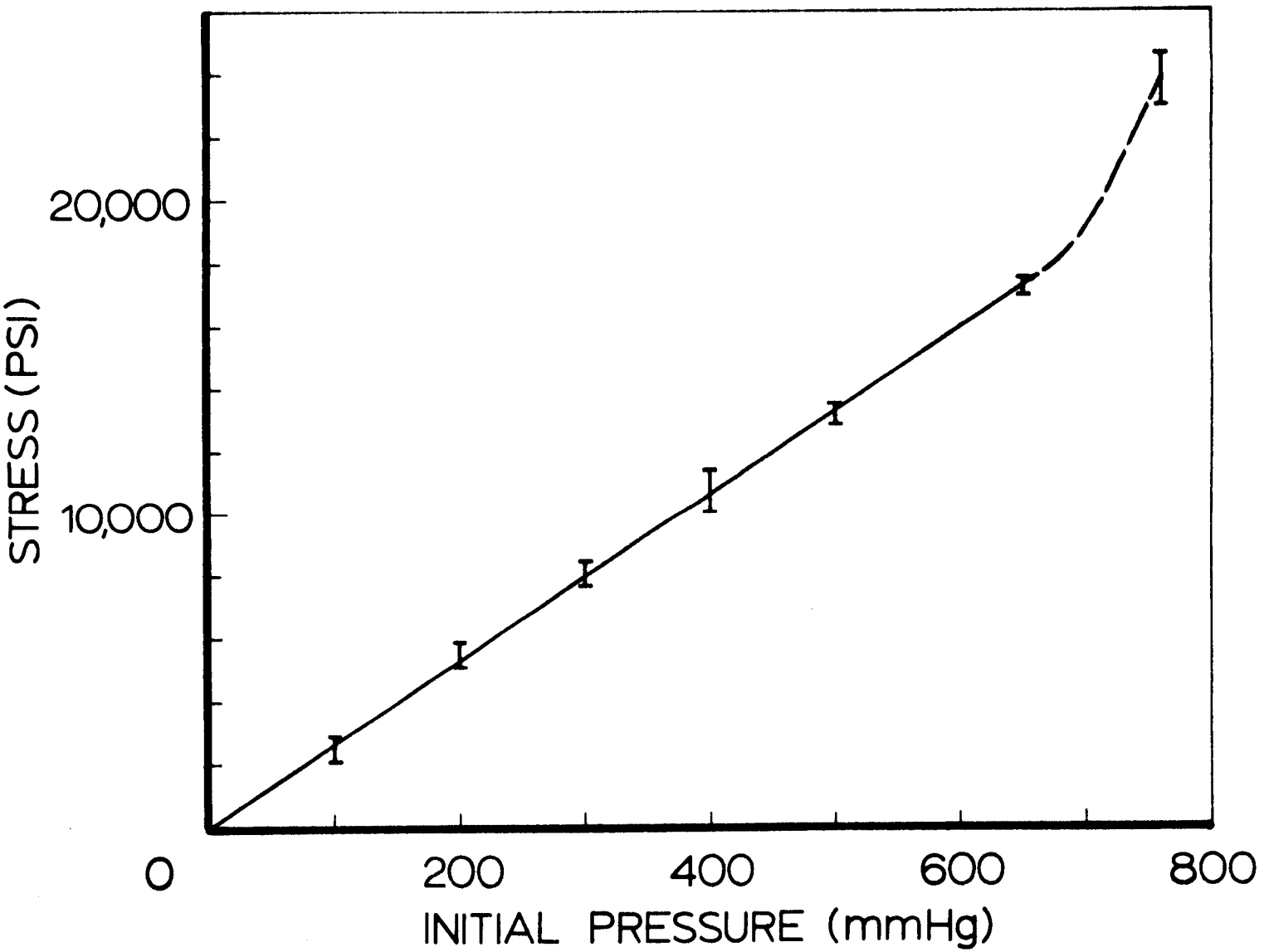

Fig. 34 Measured peak dynamic stress versus initial pressure for Vessel A

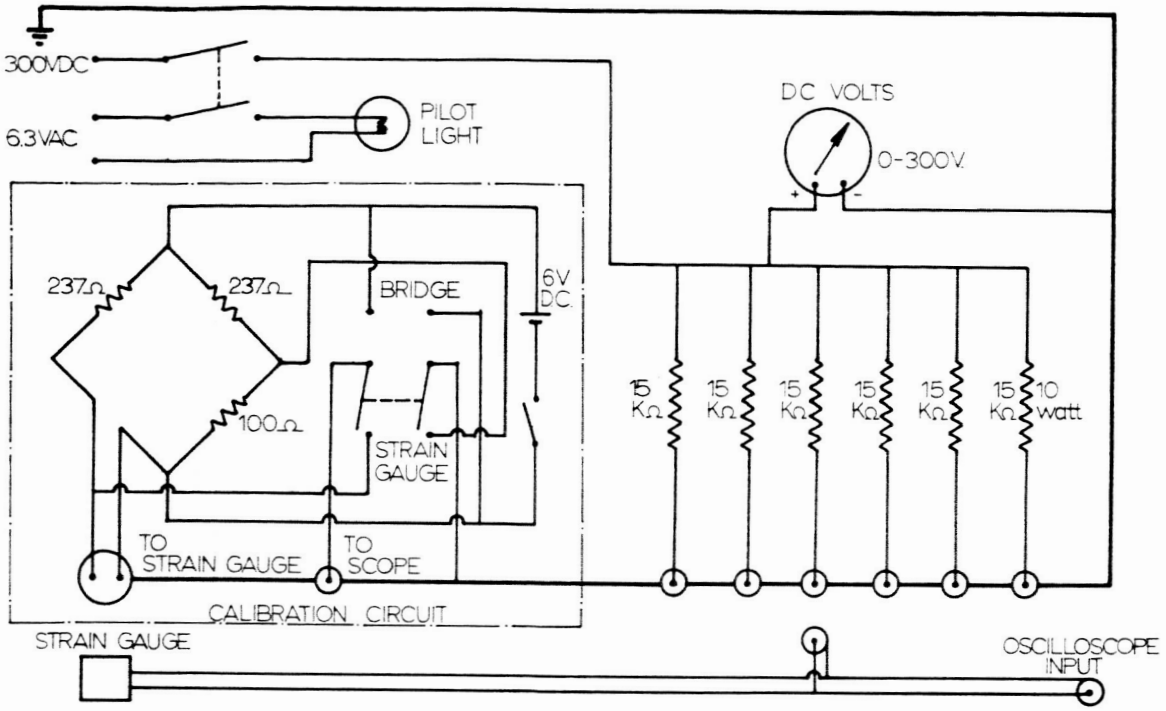

Fig.35 Strain Gauge Circuit

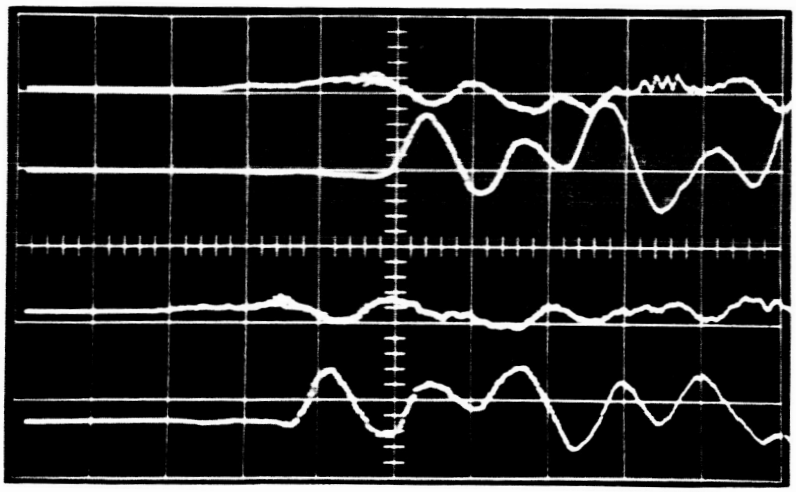

Fig.36 Typical oscillograph of dynamic response of strain gauge attached to Vessel CD. Vertical scales noted below; horizontal scale: 300 μsec/div., from left to right. For strain gauge locations see Fig. 40. The traces are, from top to bottom, for the following strain gauge locations and orientations:

1. Point B - axial, 59.76 μin/in/cm
2. Point B - circumferential, 62.31 μin/in/cm
3. Point A - axial, 58.64 μin/in/cm
4. Point A - circumferential, 58.62 μin/in/cm

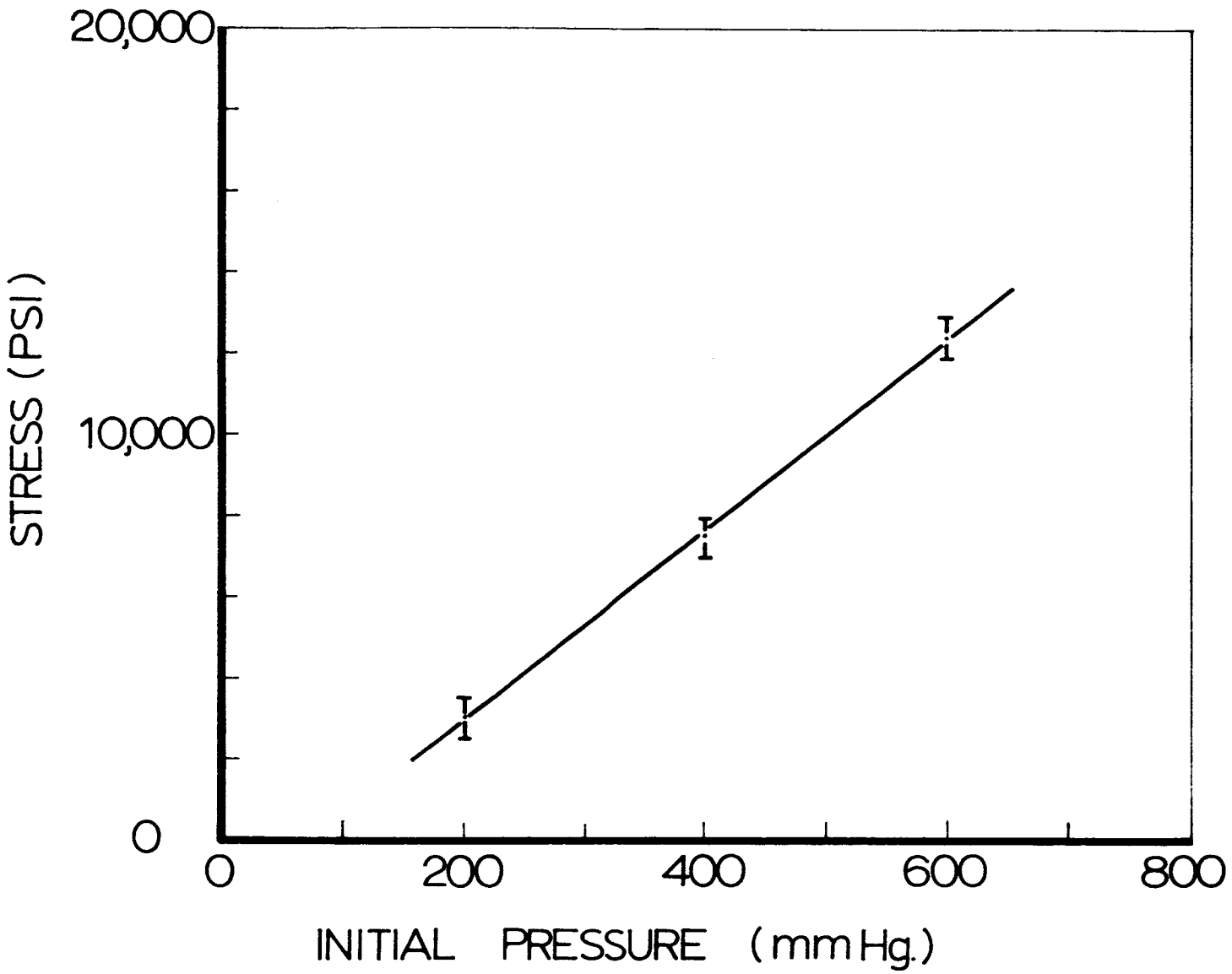

Fig. 37 Measured peak dynamic stress versus initial pressure for vessel CD.

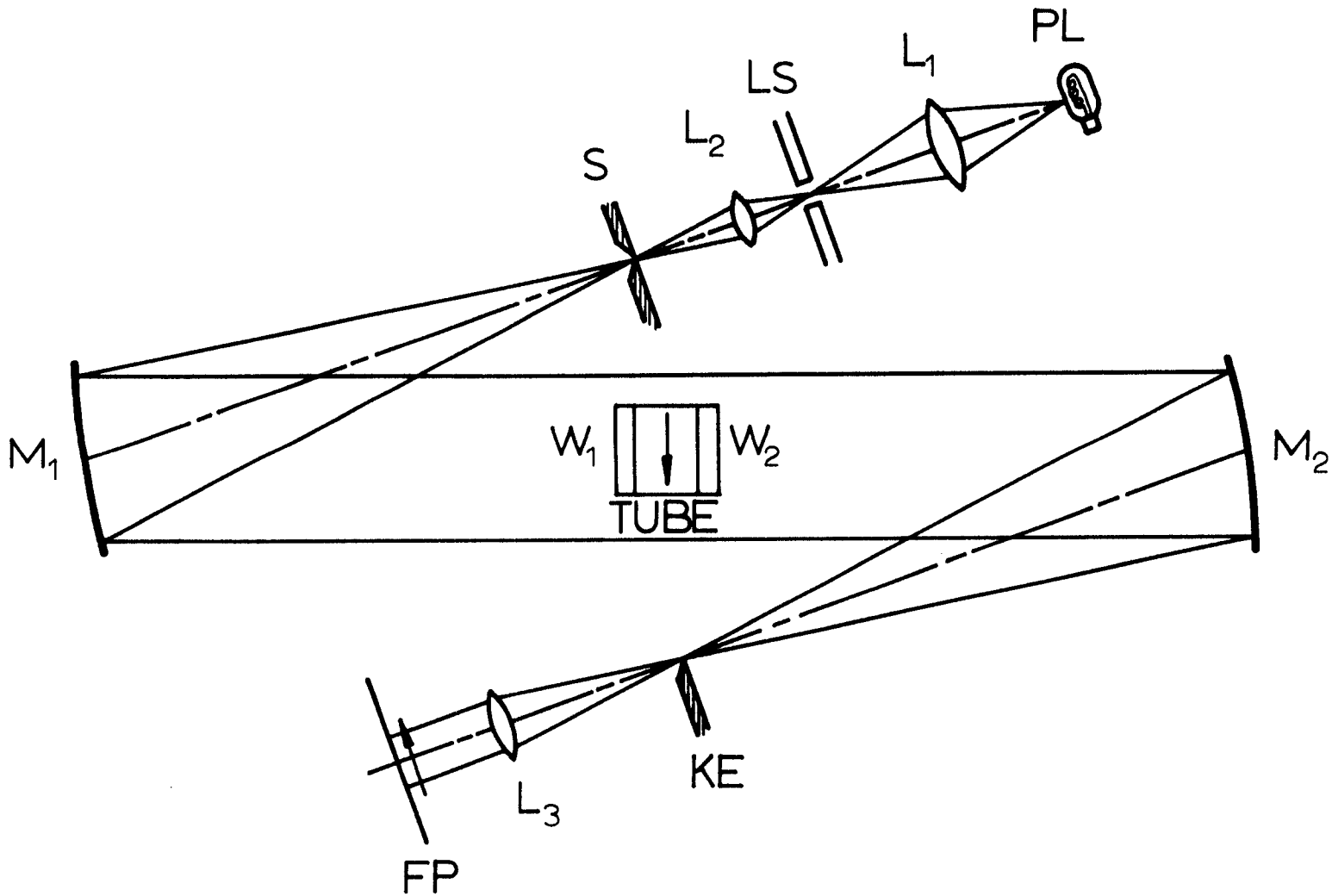

Fig. 38 Schematic of schlieren system

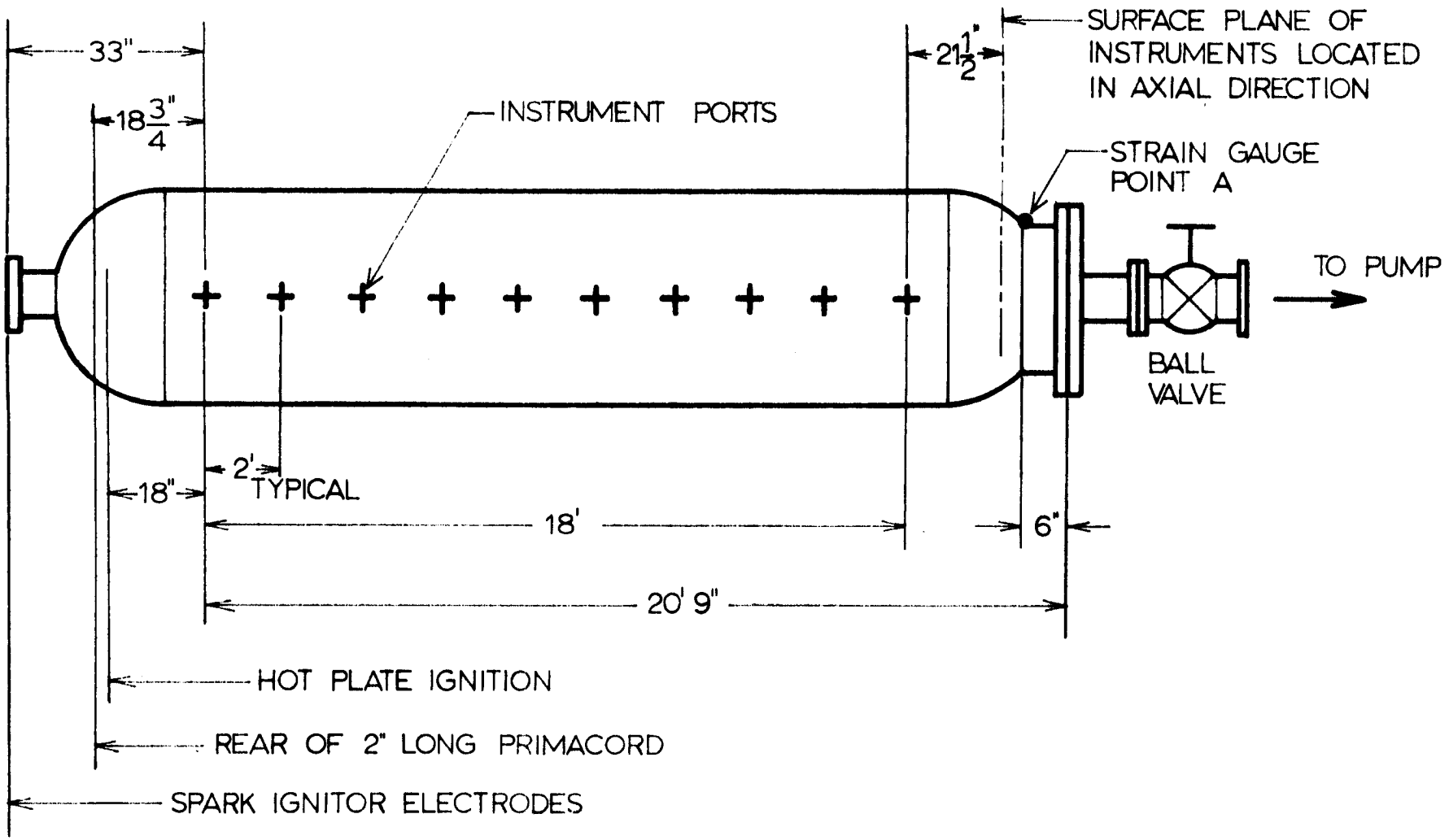

Fig. 39 Layout of 3 ft. dia. vessel showing location of instruments

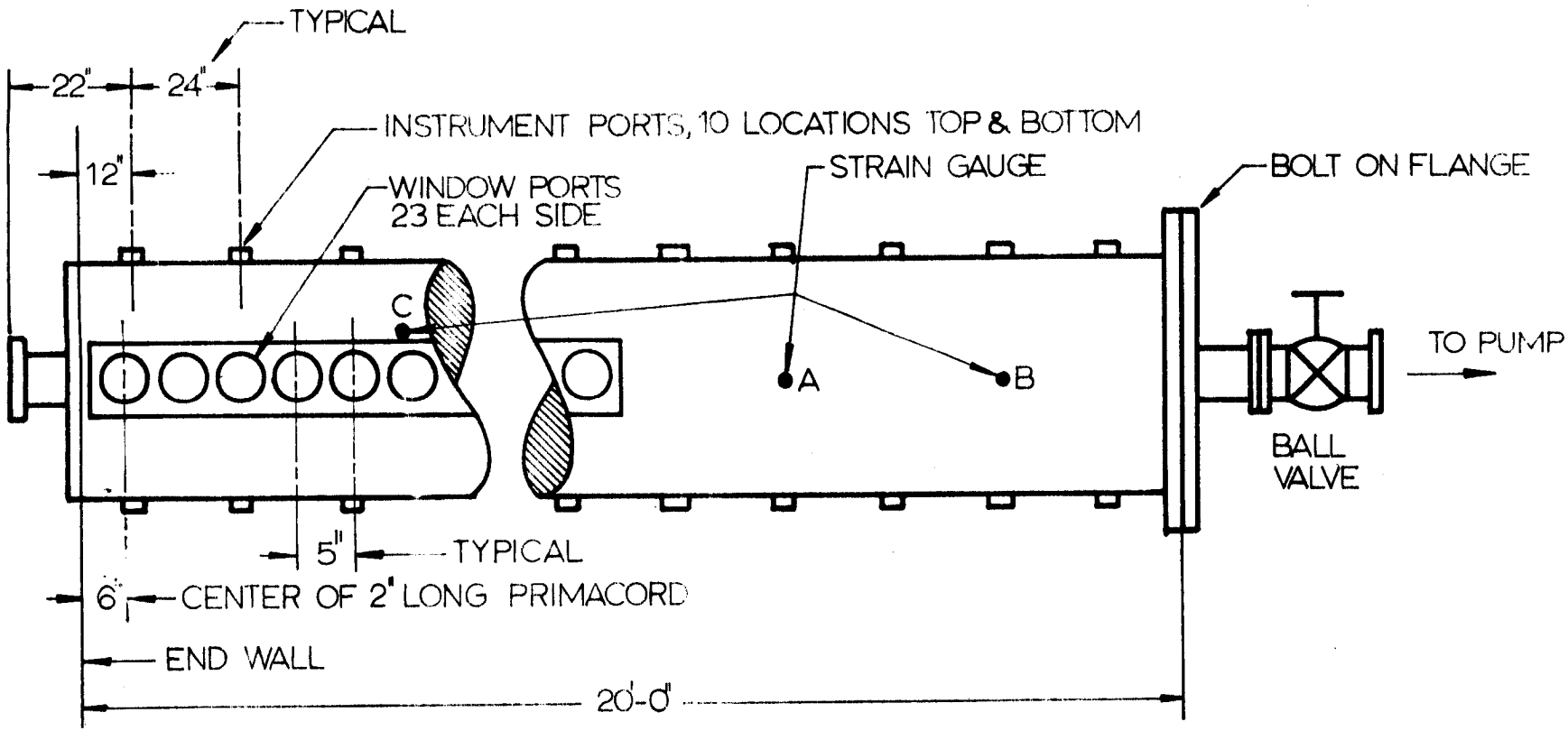

Fig. 40 Layout of Vessel CD showing locations of instruments and important dimensions

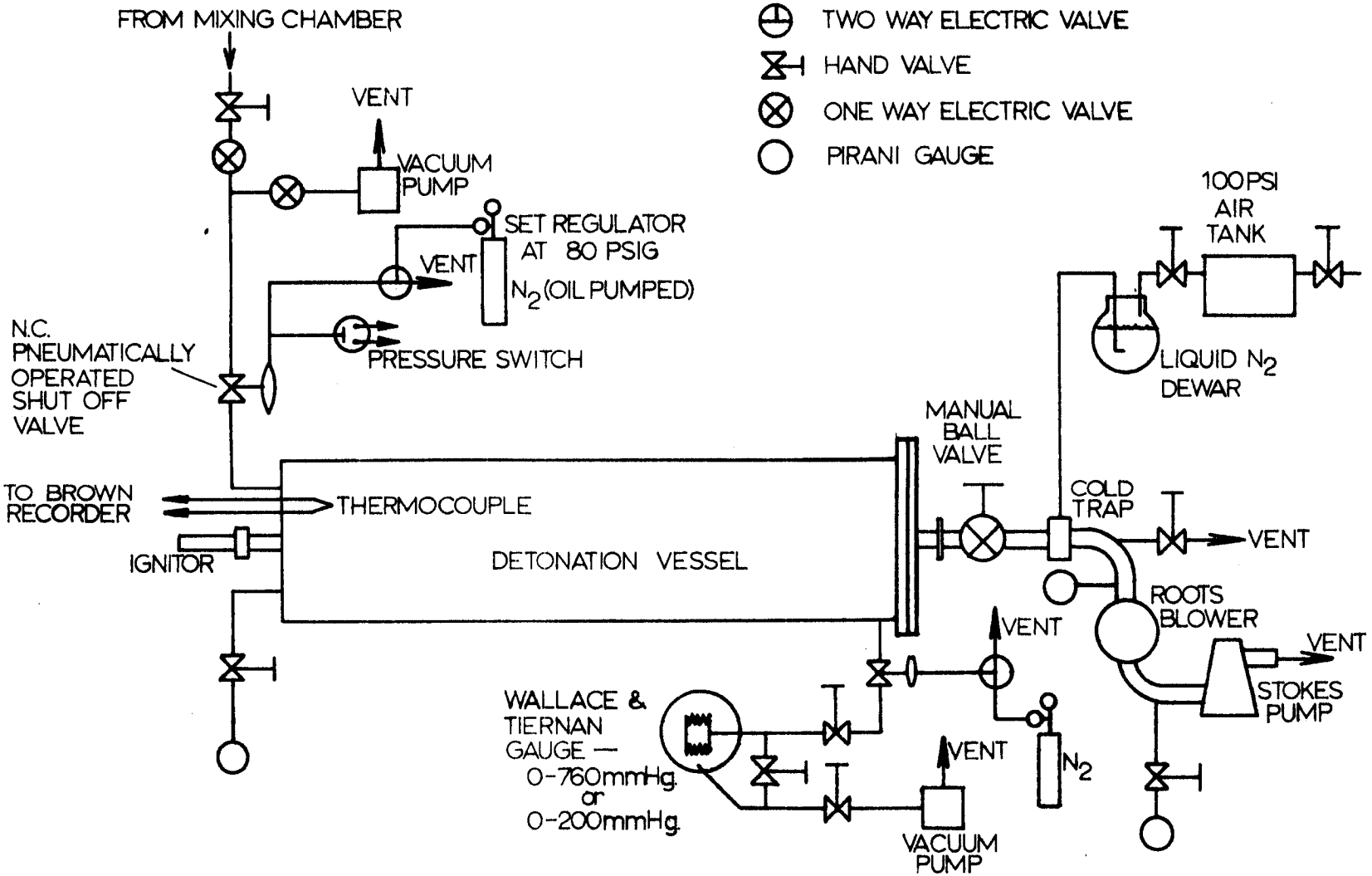

Fig. 41 Schematic diagram of Vessel CD and accessory equipment

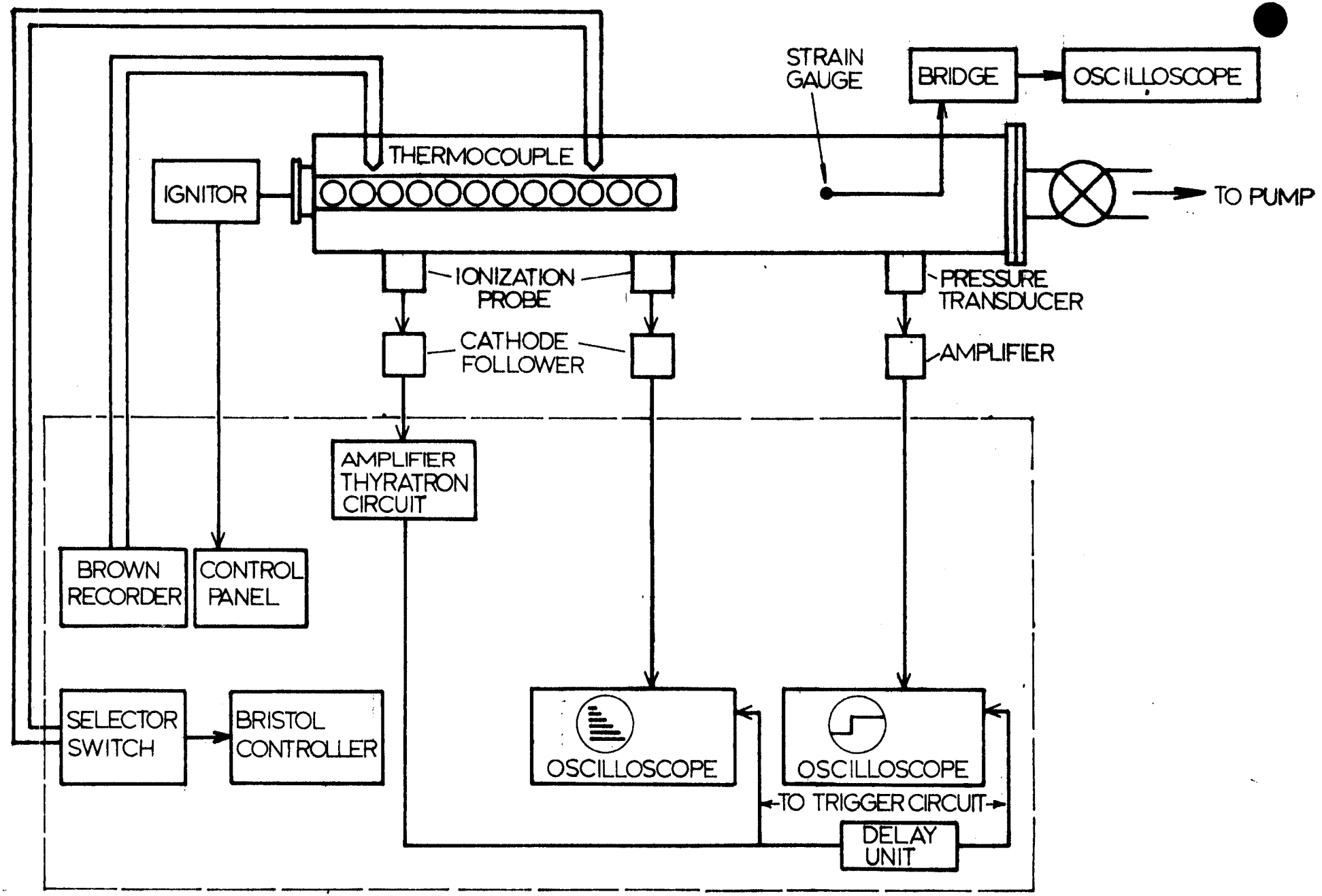

Fig.42 Block Diagram of Instrumentation

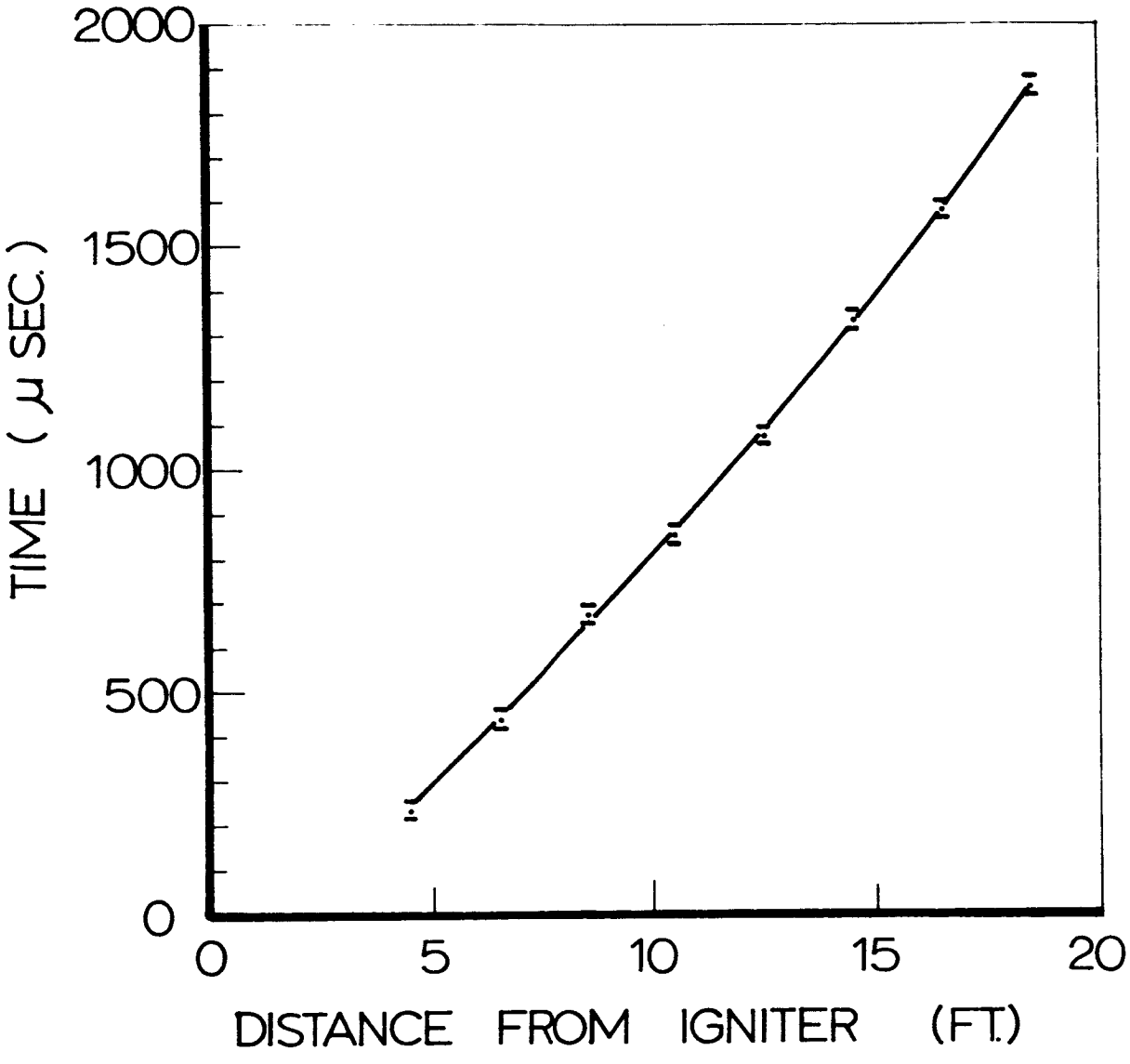

Fig. 43 Flame world line in space-time plane.

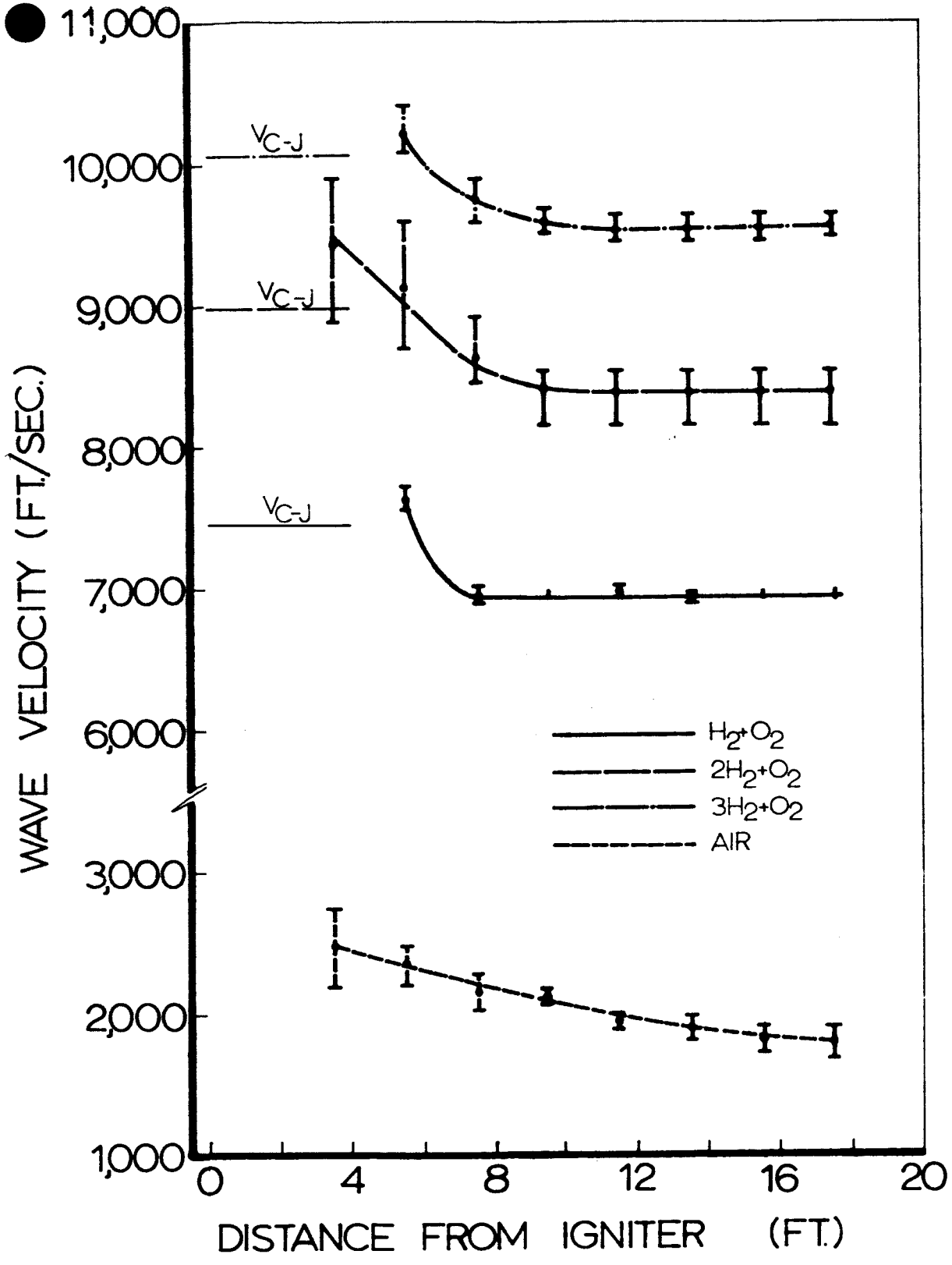

Fig.44 Wave velocity as a function of distance from Primacord igniter in Vessel CD. Mixture initially at 100 mm Hg and room temperature. Position of ordinate corresponds to end-wall.

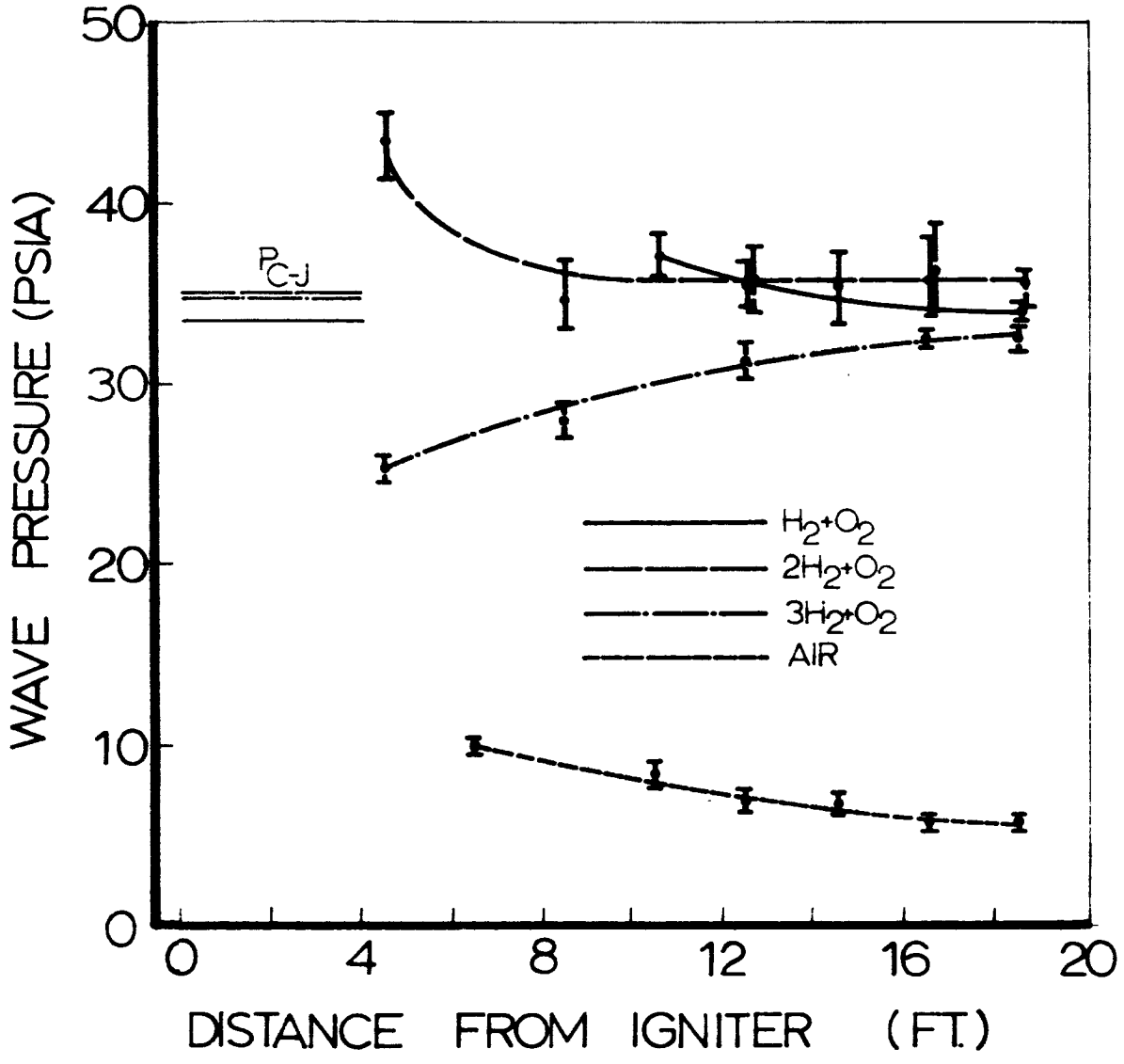

Fig.45 Wave pressure as a function of distance from Primacord igniter in Vessel CD. Mixture initially at 100 mm Hg and room temperature. Position of ordinate corresponds to end-wall.

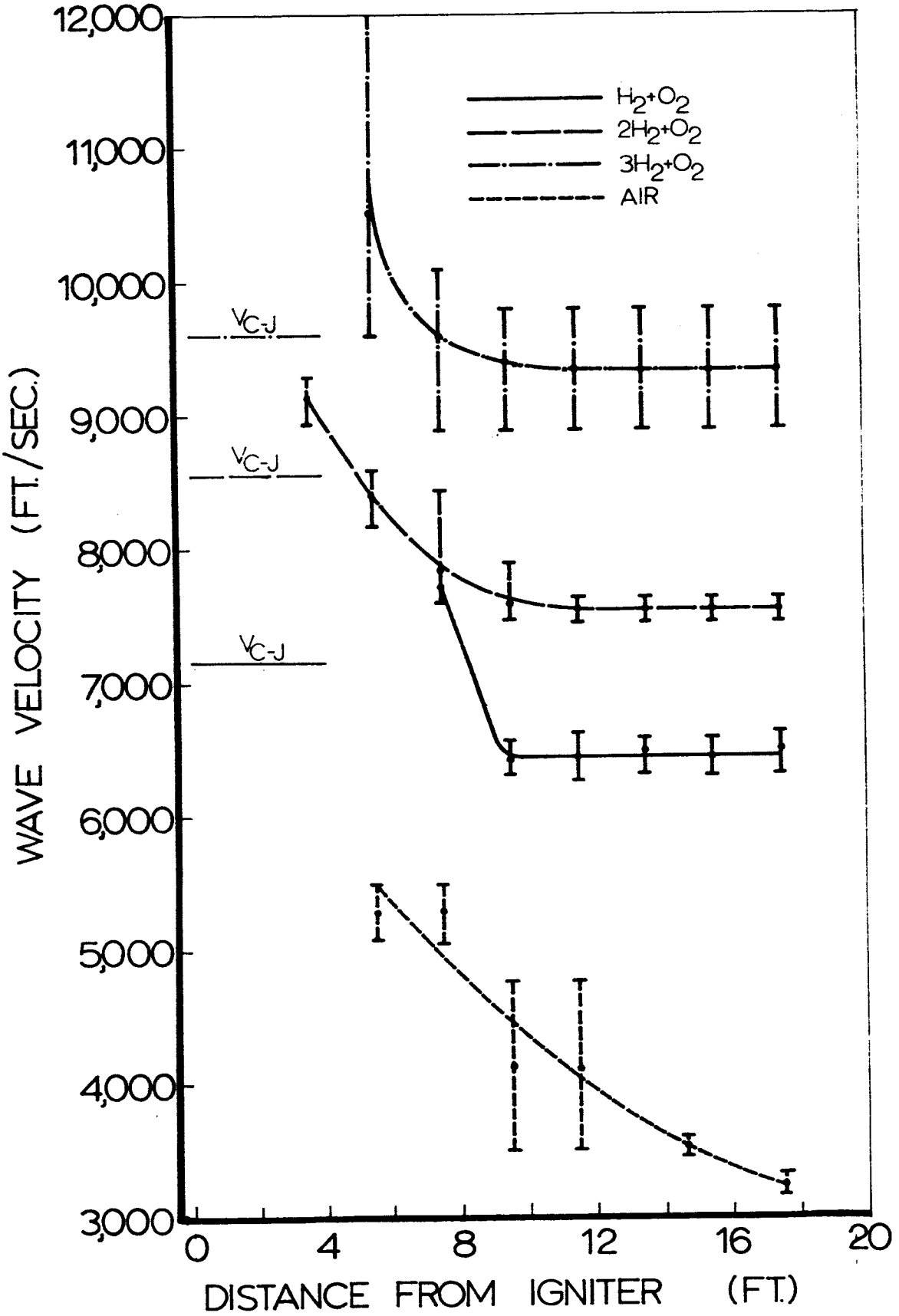

Fig. 46 Wave velocity as a function of distance from Primacord igniter in Vessel CD. Mixture initially at 10 mm Hg pressure and room temperature. Position of ordinate corresponds to end-wall.

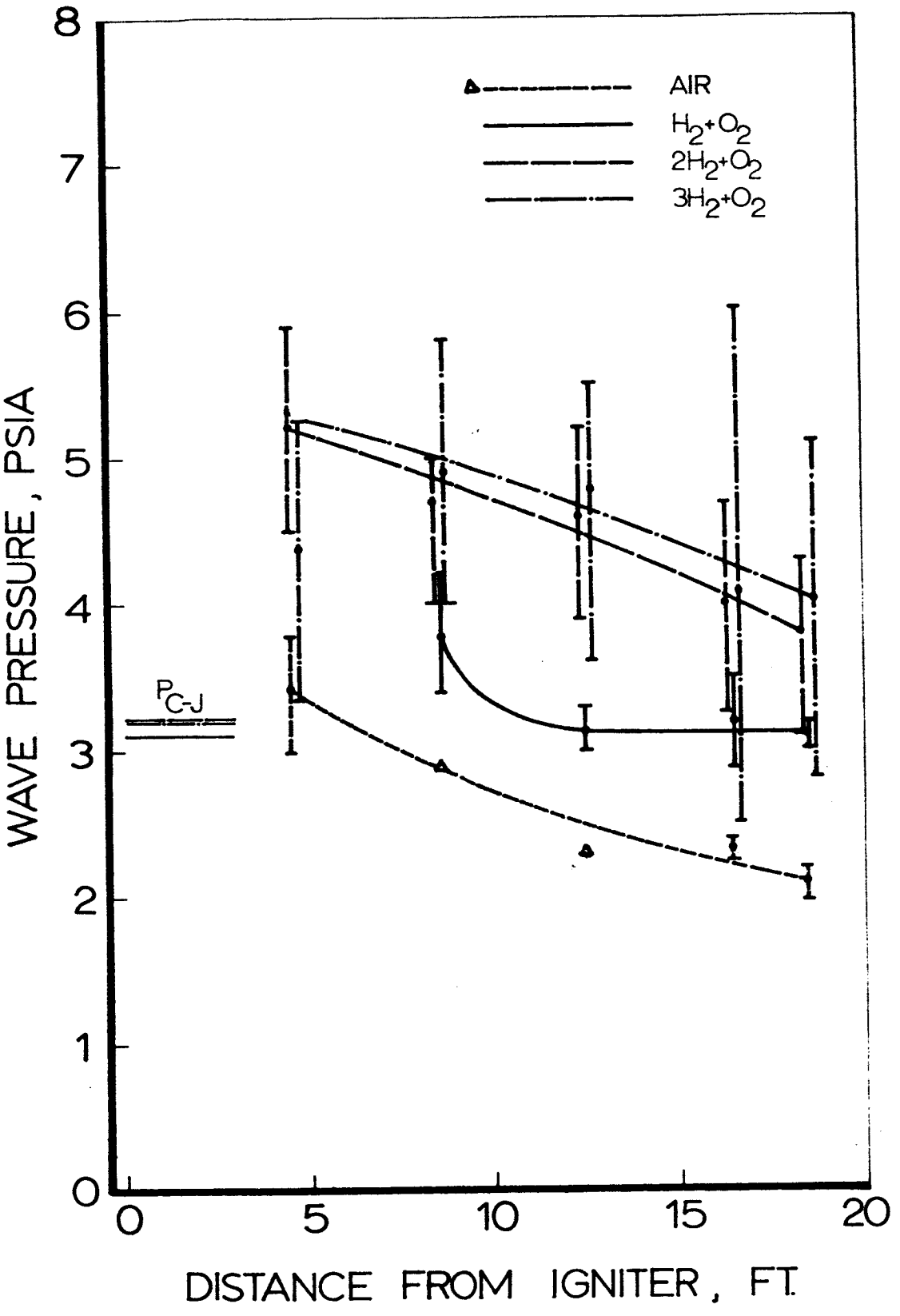

Fig.47 Wave pressure as a function of distance from Primacord igniter in Vessel CD. Mixture initially at 10 mm Hg pressure and room temperature. Position of ordinate corresponds to end-wall.

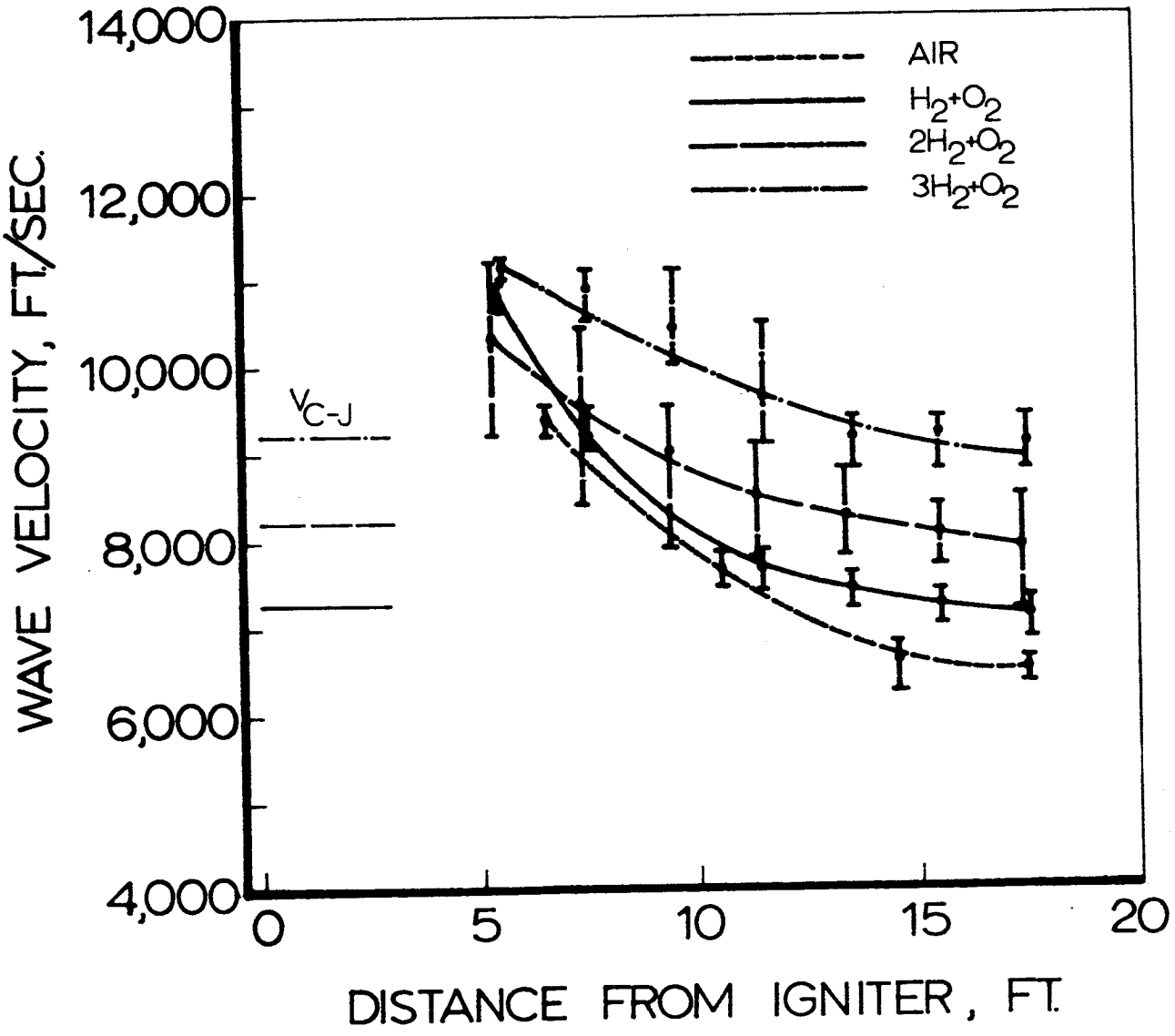

Fig. 48 Wave velocity as a function of distance from Primacord igniter in Vessel CD. Mixture initially at 1 mm Hg ($2H_2+O_2$, $3H_2+O_2$) and 1.5 mm Hg (H_2+O_2, air) pressures and room temperature. Position of ordinate corresponds to end-wall.

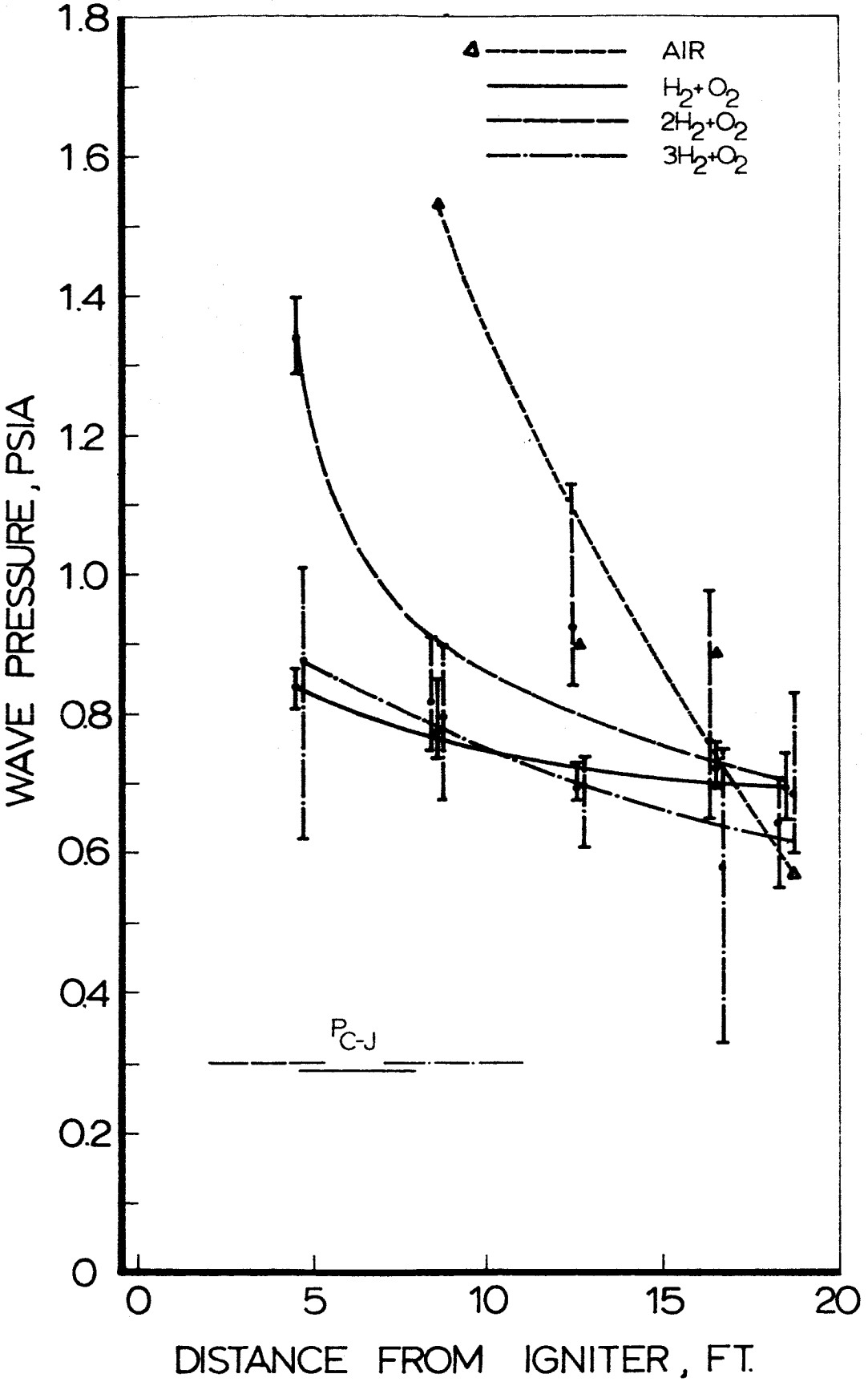

Fig.49 Wave pressure as a function of distance from Primacord igniter in Vessel CD. Mixture initially at 1 mm Hg ($2H_2+O_2$, $3H_2$ O_2) and 1.5 mm Hg ($_2+O_2$, Air) pressures and room ^{2} temperature. Position of ordinate corresponds to end-wall.

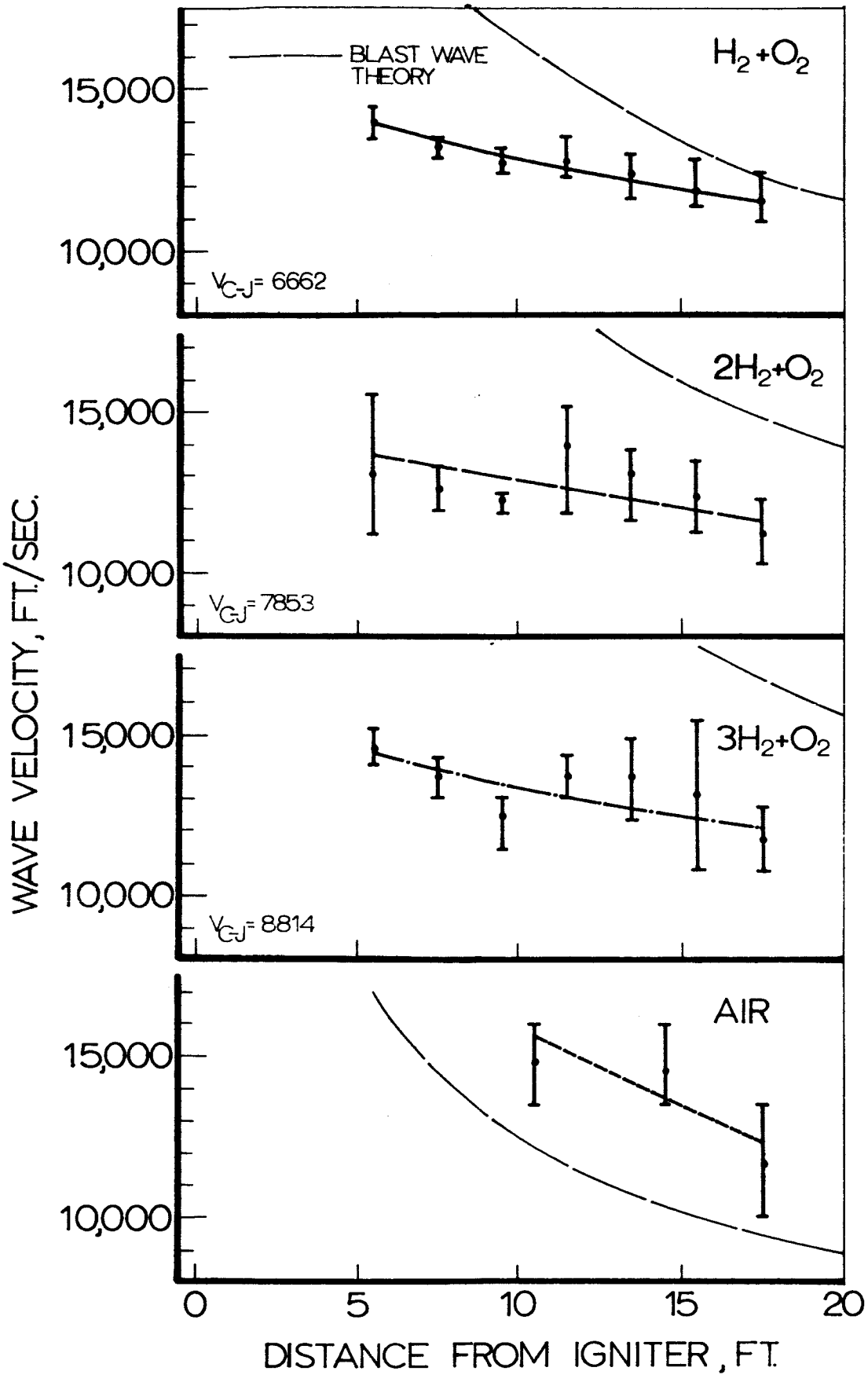

Fig.50 Wave velocity as a function of distance from Primacord igniter in Vessel CD. Mixture initially at 0.1 mm Hg pressure and room temperature. Position of ordinate corresponds to end-wall.

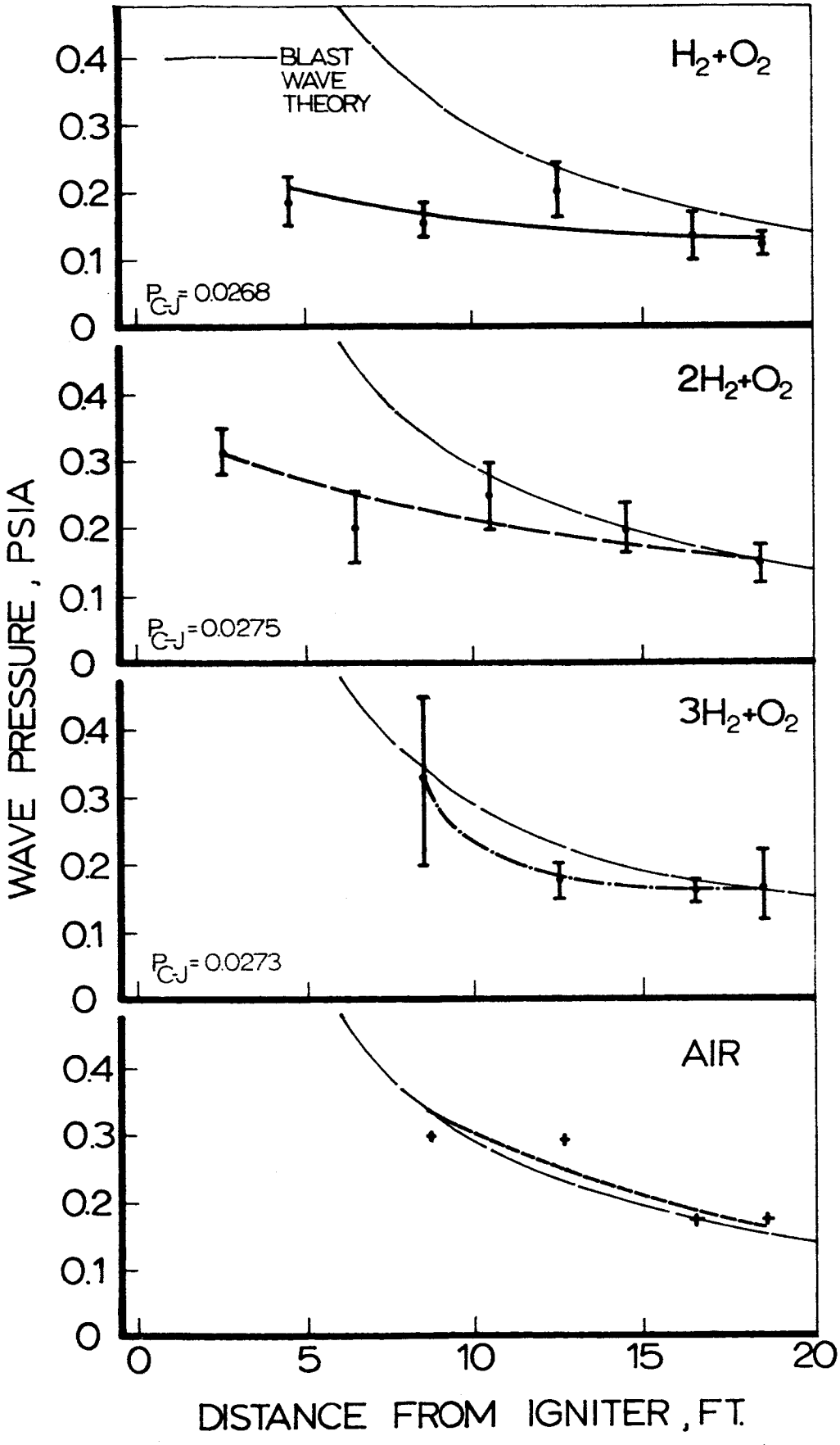

Fig. 51 Wave pressure as a function of distance from Primacord igniter in Vessel CD. Mixture initially at 0.1 mm Hg pressure and room temperature. Position of ordinate corresponds to end-wall.

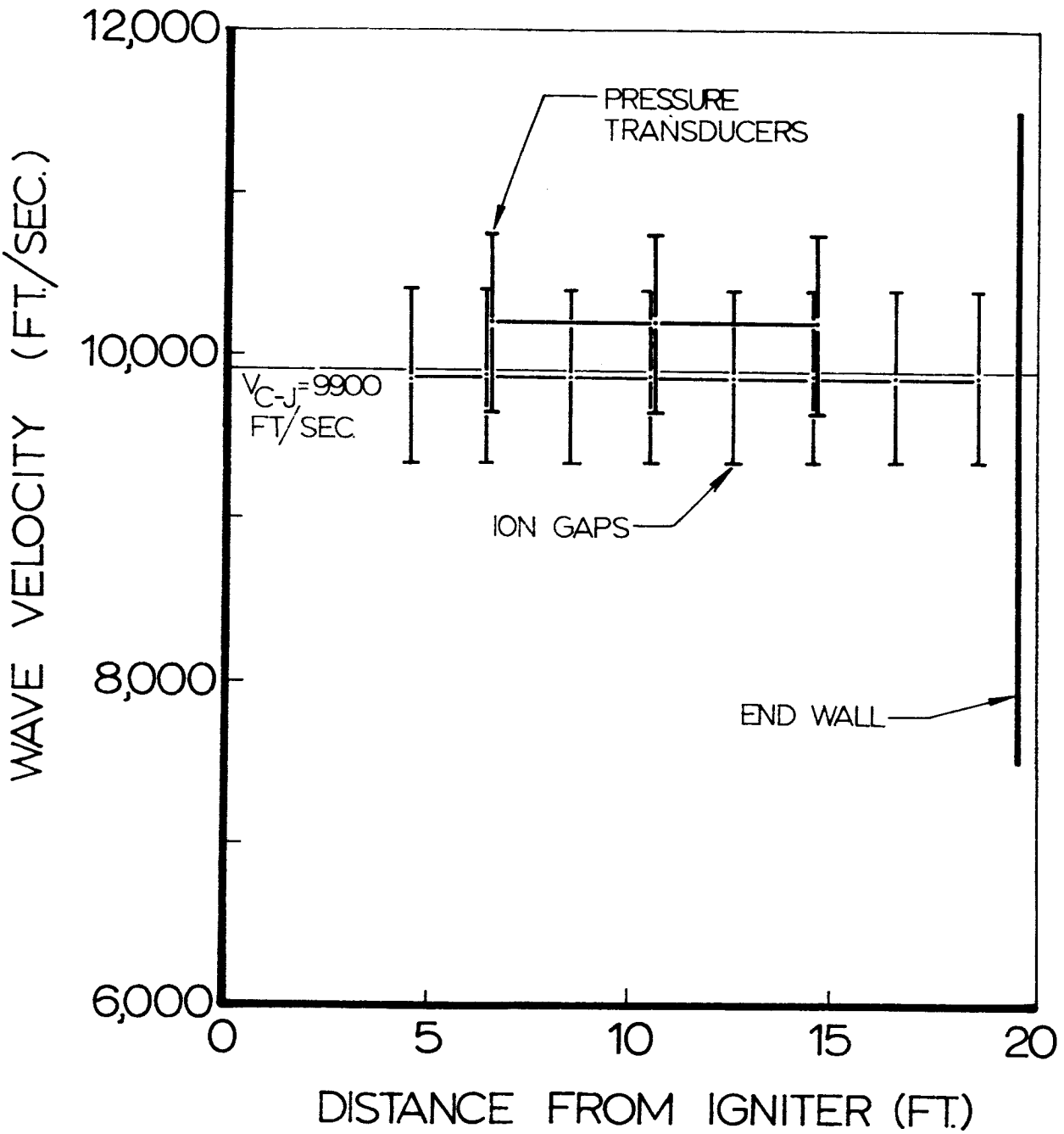

Fig. 52 Wave velocity as function of distance from Primacord ignitor in the 2 ft. dia. x 20 ft. long vessel. $3H_2+O_2$ composition, initial pressure 100 mm Hg, initial temperature +200 °F.

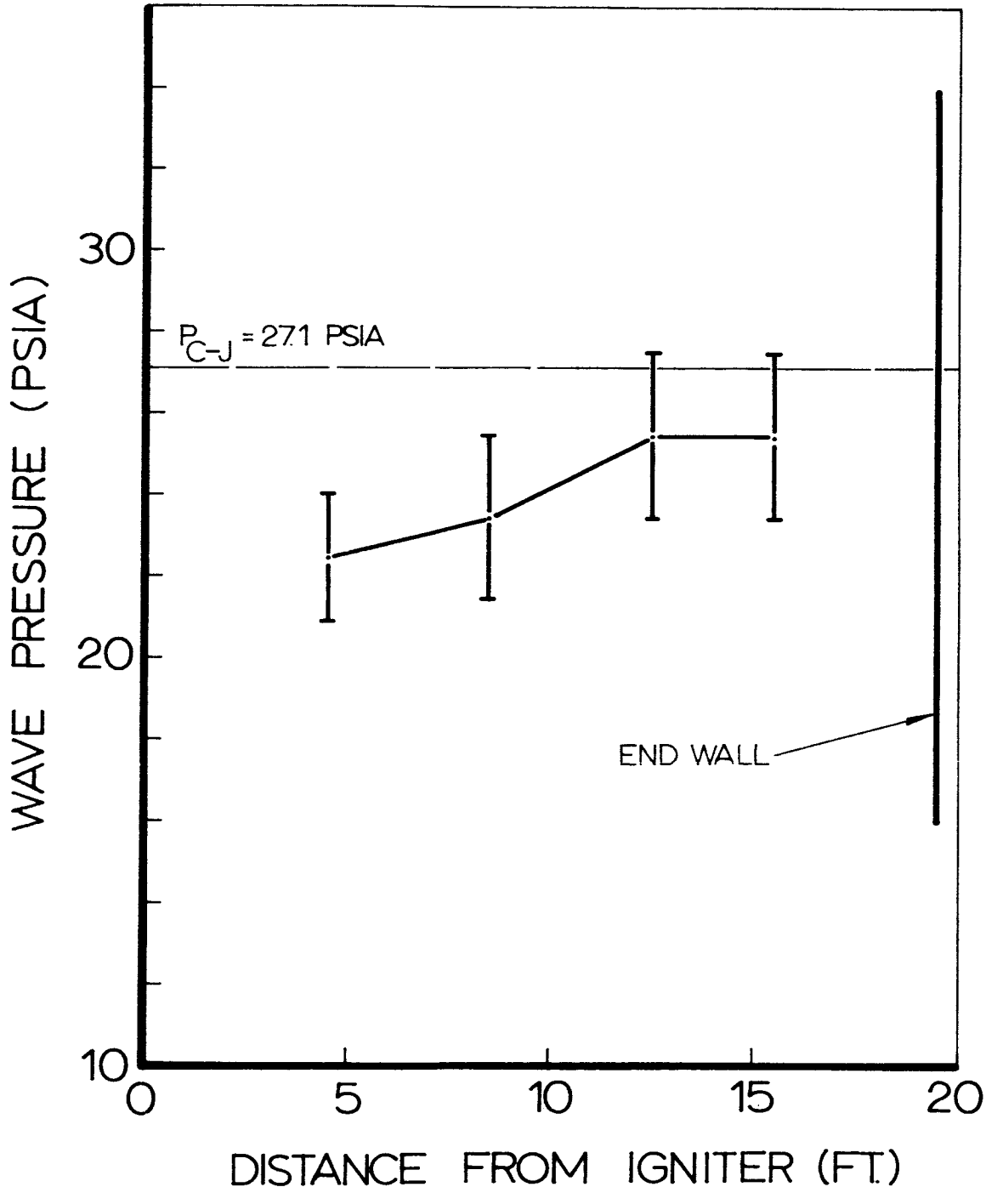

Fig.53 Peak-wave pressure as function of distance from Primacord ignitor in the 2 ft. dia. x 20 ft. long vessel. $3H_2+O_2$ composition, initial pressure 100 mmHg, initial temperature +200 °F.

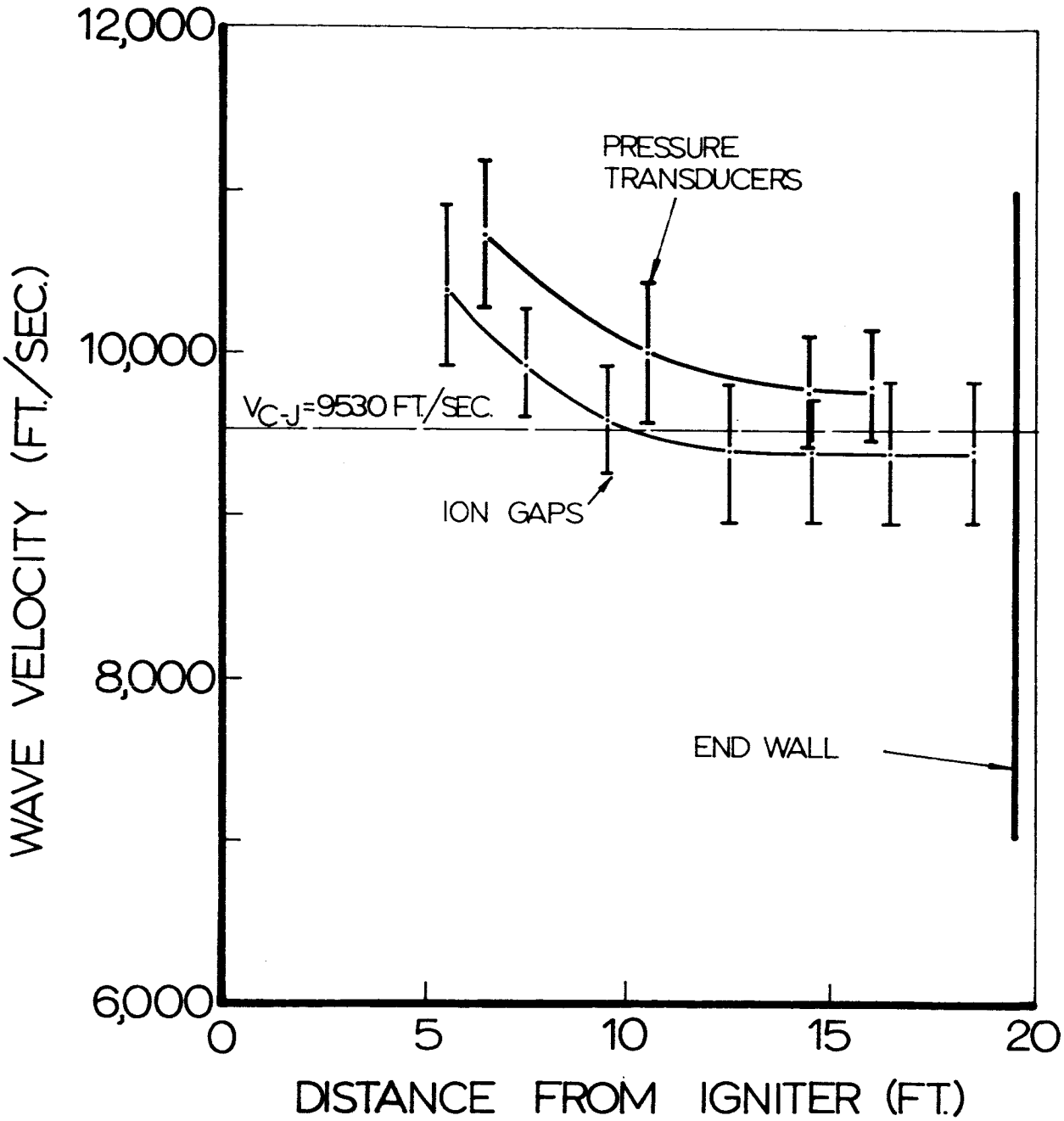

Fig. 54 Wave velocity as function of distance from Primacord ignitor in the 2 ft. dia. x 20 ft. long vessel. $3H_2+0_2$ composition, initial pressure 10 mmHg, initial temperature +200 °F.

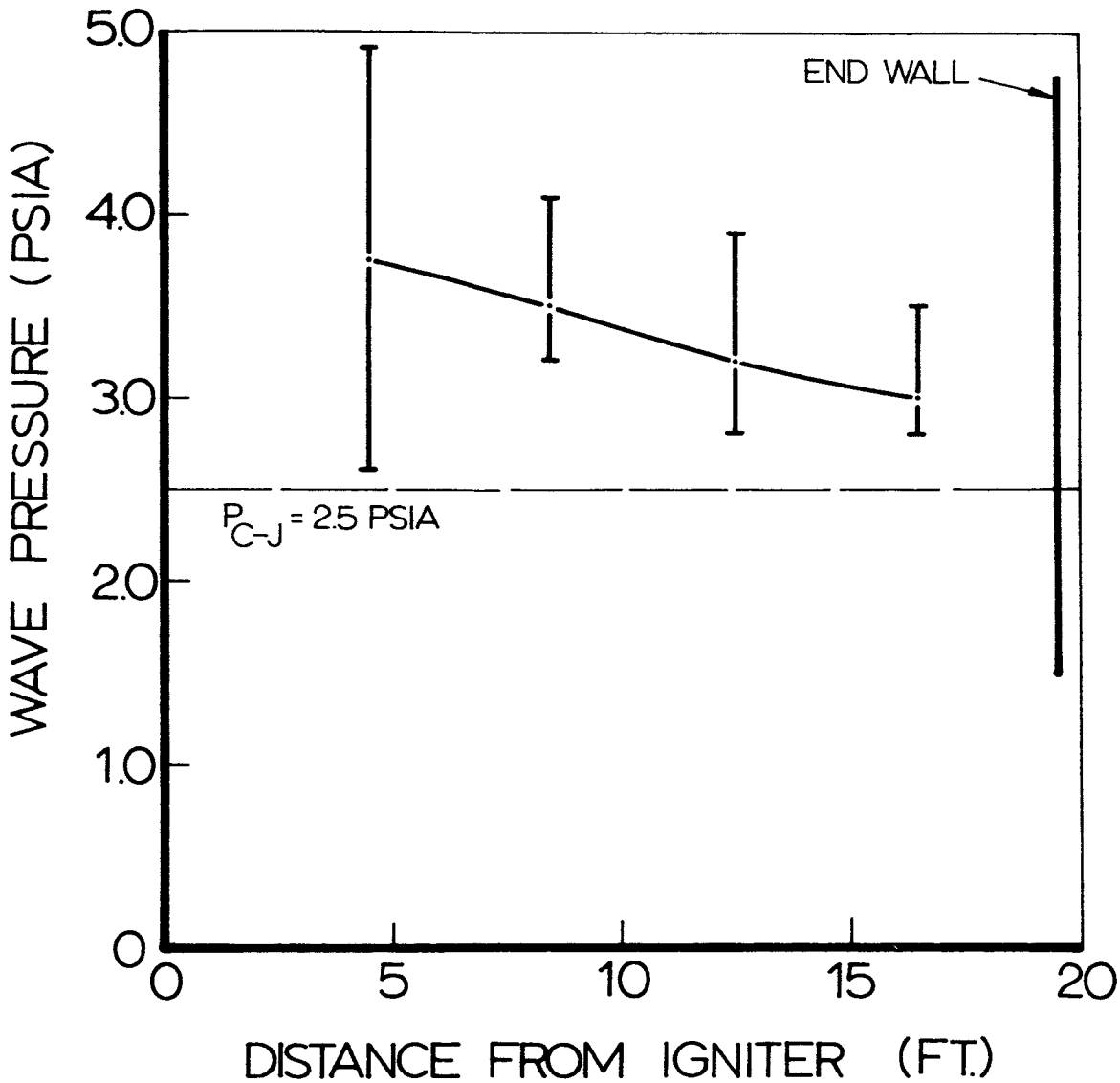

Fig. 55 Peak-wave pressure as function of distance from Primacord ignitor in the 2 ft. dia. x 20 ft. long vessel. $3H_2+0_2$ composition, initial pressure 10 mmHg, initial temperature +200 °F.

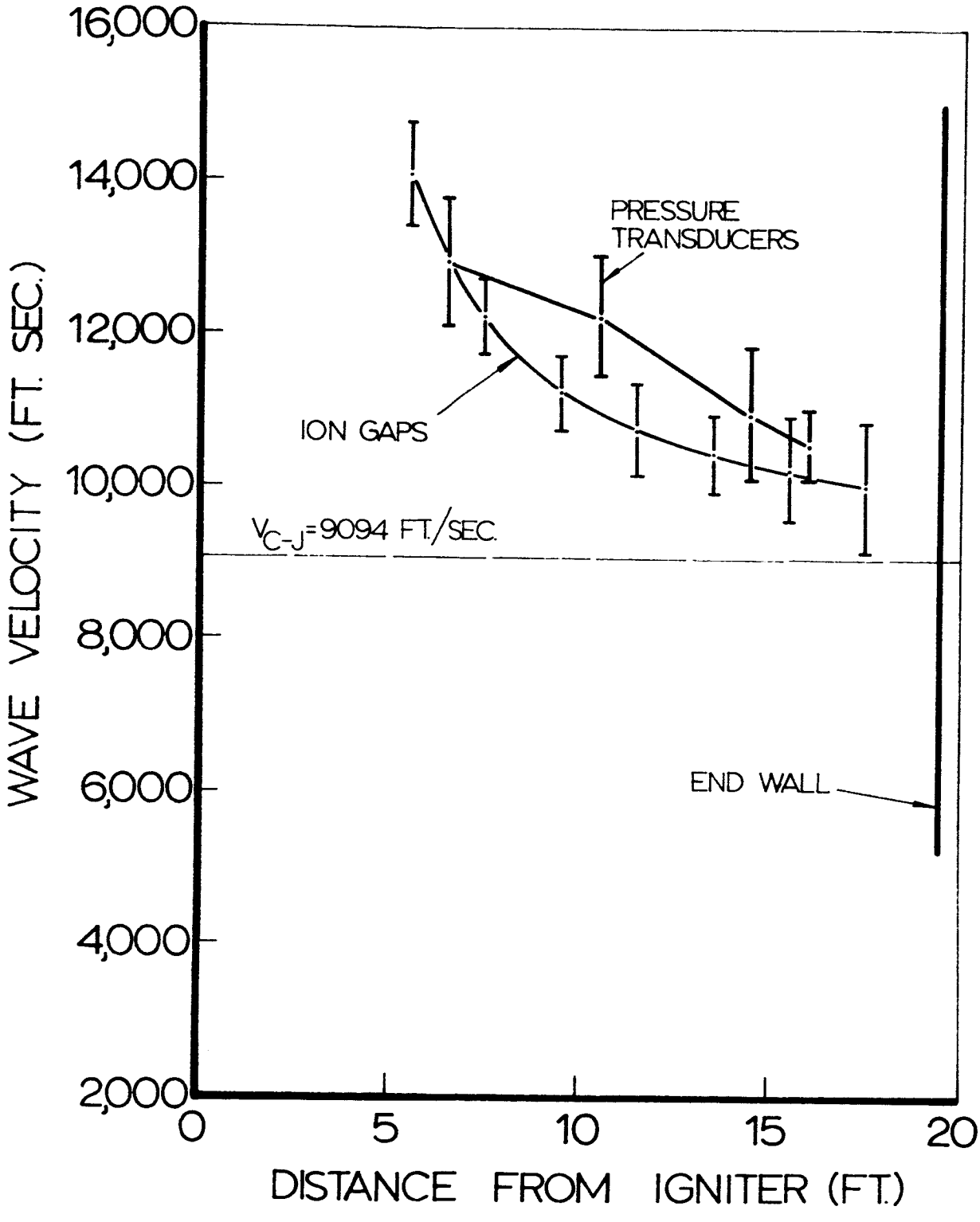

Fig. 56 Wave velocity as function of distance from Primacord ignitor in the 2 ft. dia. x 20 ft. long vessel. $3H_2+O_2$ composition, initial pressure 1.0 mmHg, initial temperature +200 °F.

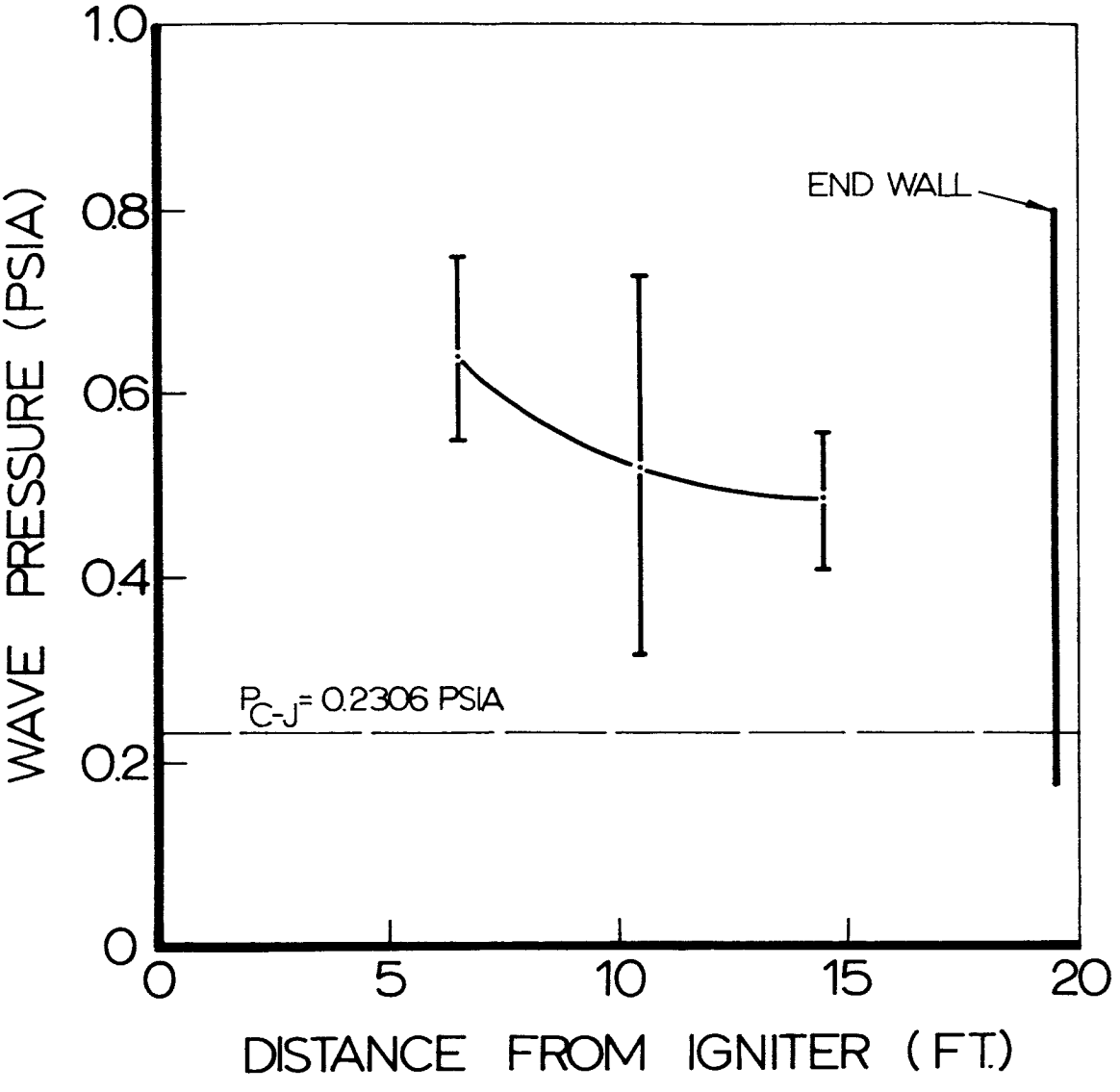

Fig. 57 Peak-wave pressure as function of distance from Primacord ignitor in the 2 ft. dia. x 20 ft. long vessel. $3H_2+0_2$ composition, initial pressure 1.0 mmHg, initial temperature +200 °F.

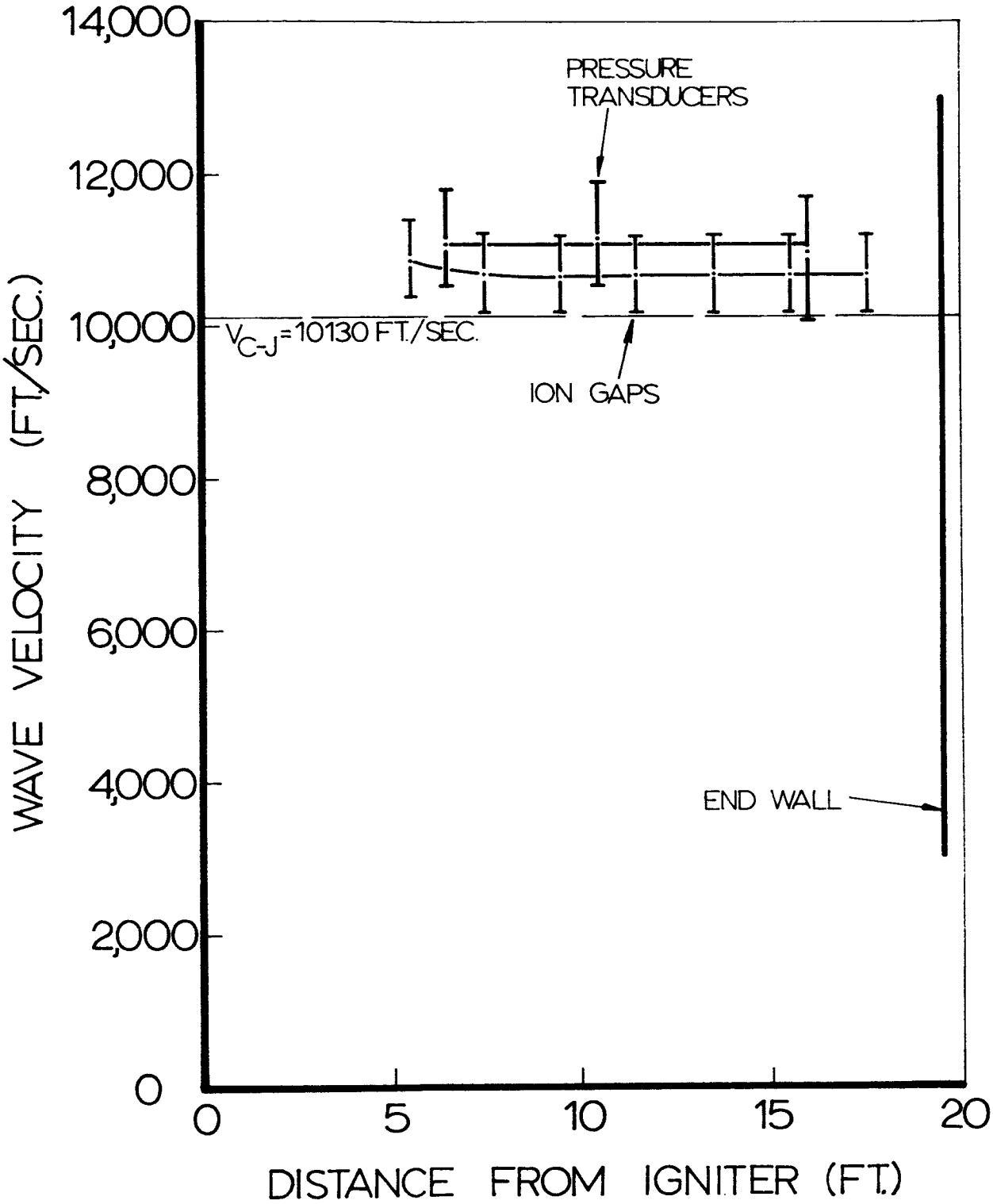

Fig. 58 Wave velocity as function of distance from Primacord ignitor in the 2 ft. dia. x 20 ft. long vessel. $3H_2+O_2$ composition, initial pressure 100 mm Hg, initial temperature -50°F.

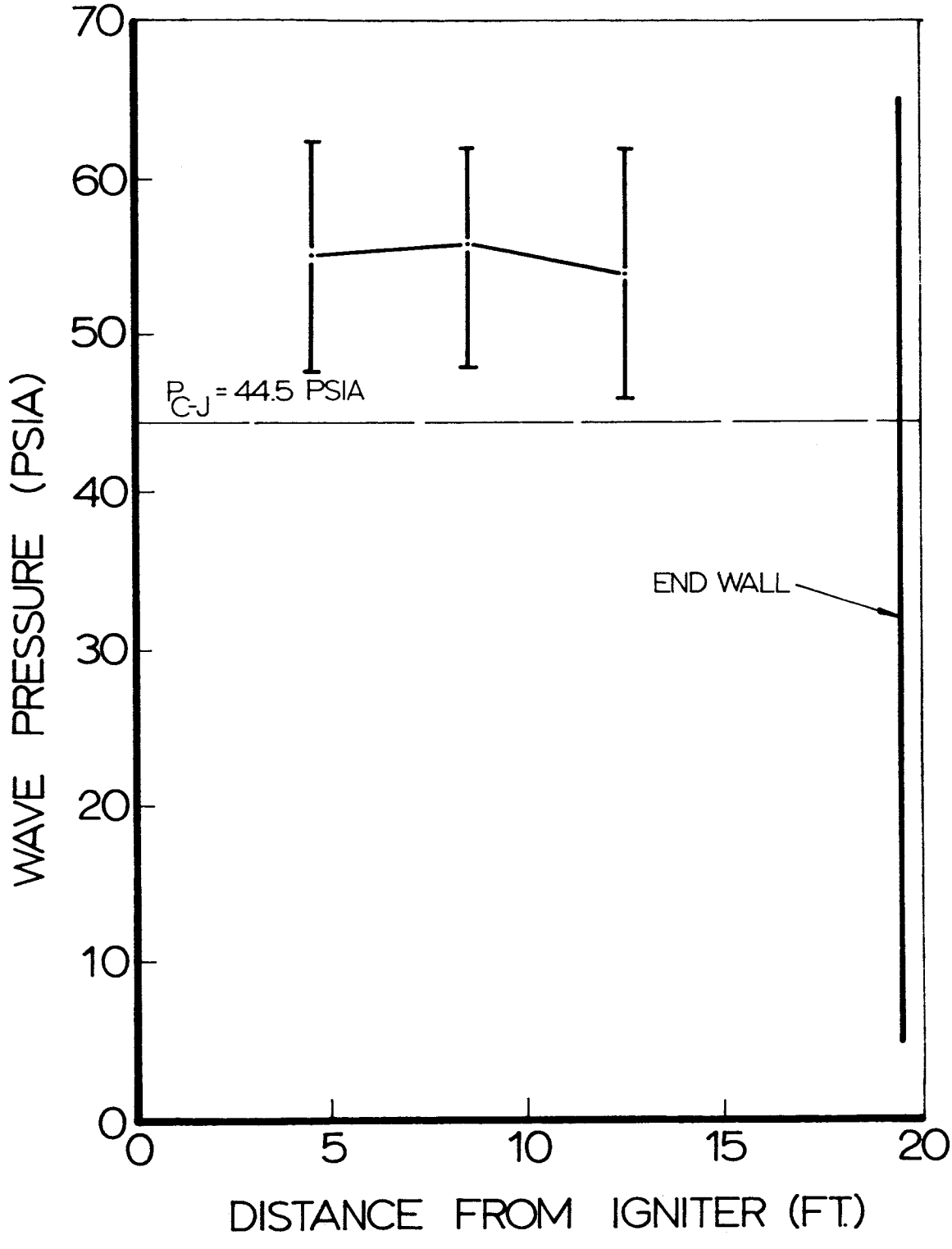

Fig. 59 Peak-wave pressure as function of distance from Primacord ignitor in the 2 ft. dia. x 20 ft. long vessel. $3H_2+O_2$ composition, initial pressure 100 mm Hg, initial temperature -50°F.

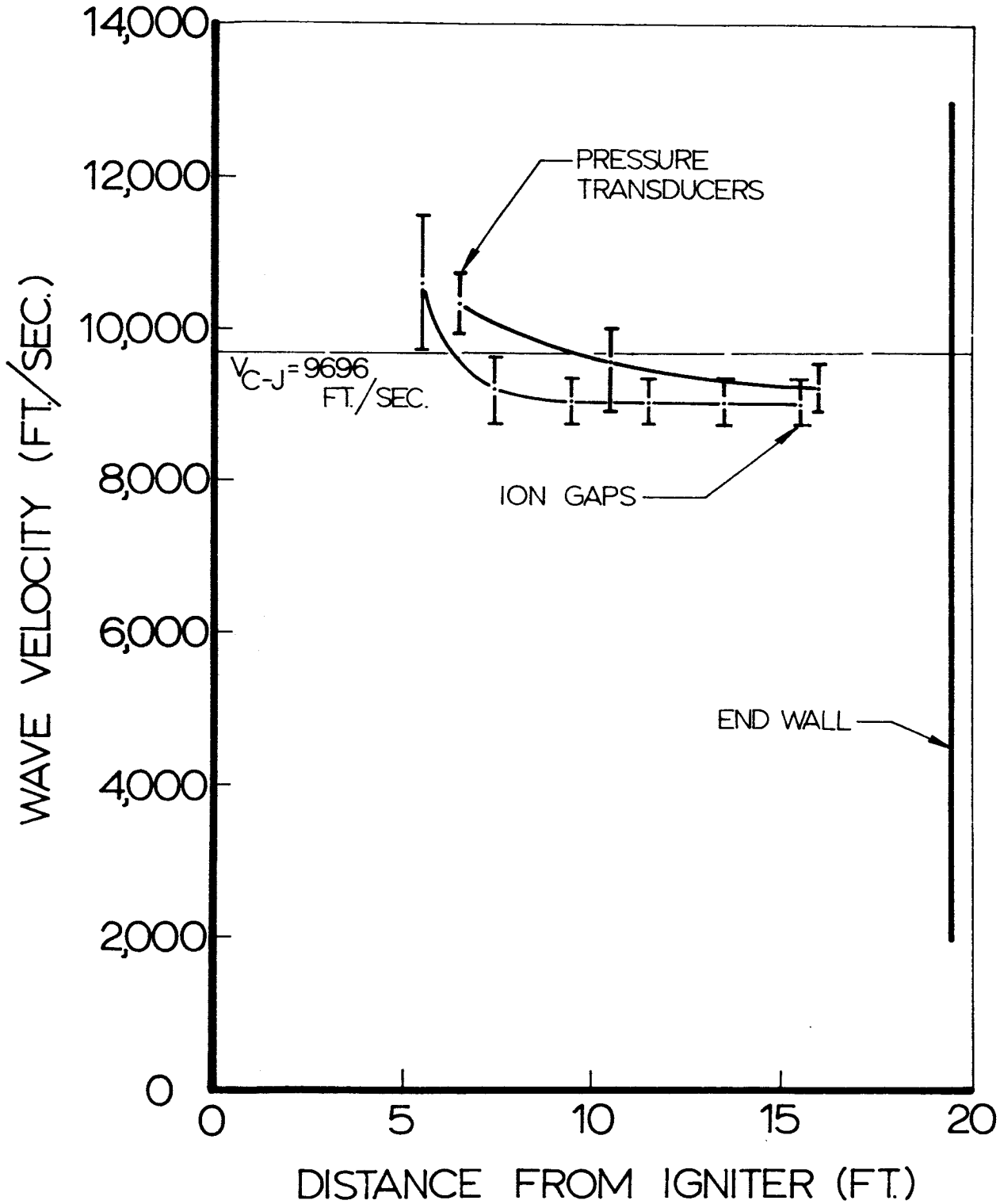

Fig. 60 Wave velocity as function of distance from Primacord ignitor in the 2 ft. dia. x 20 ft. long vessel. $3H_2+O_2$ composition, initial pressure 10 mm Hg, initial temperature -50°F.

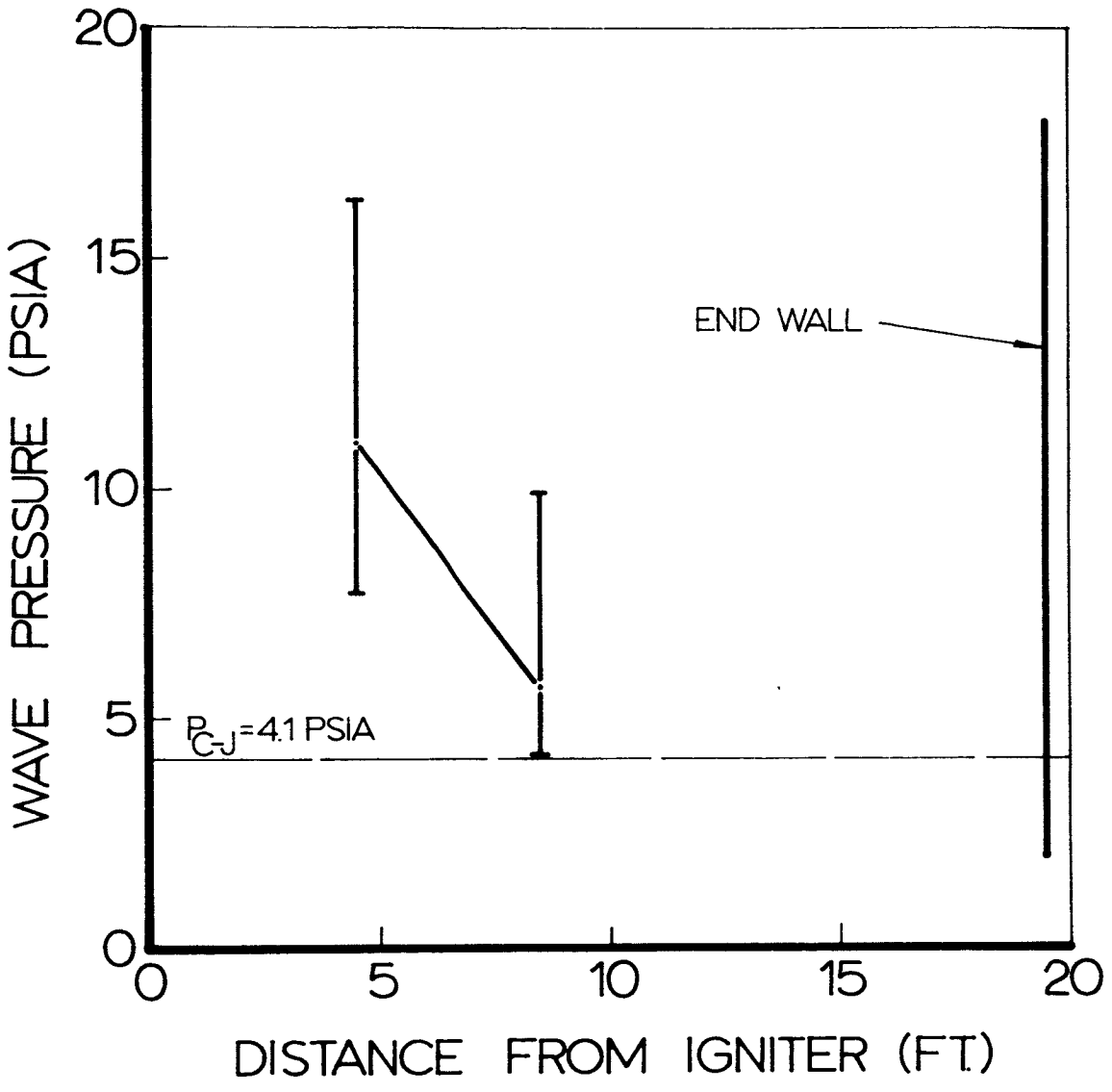

Fig. 61 Peak-wave pressure as function of distance from Primacord ignitor in the 2 ft. dia. x 20 ft. long vessel. $3H_2+0_2$ composition, initial pressure 10 mmHg, initial temperature -50°F.

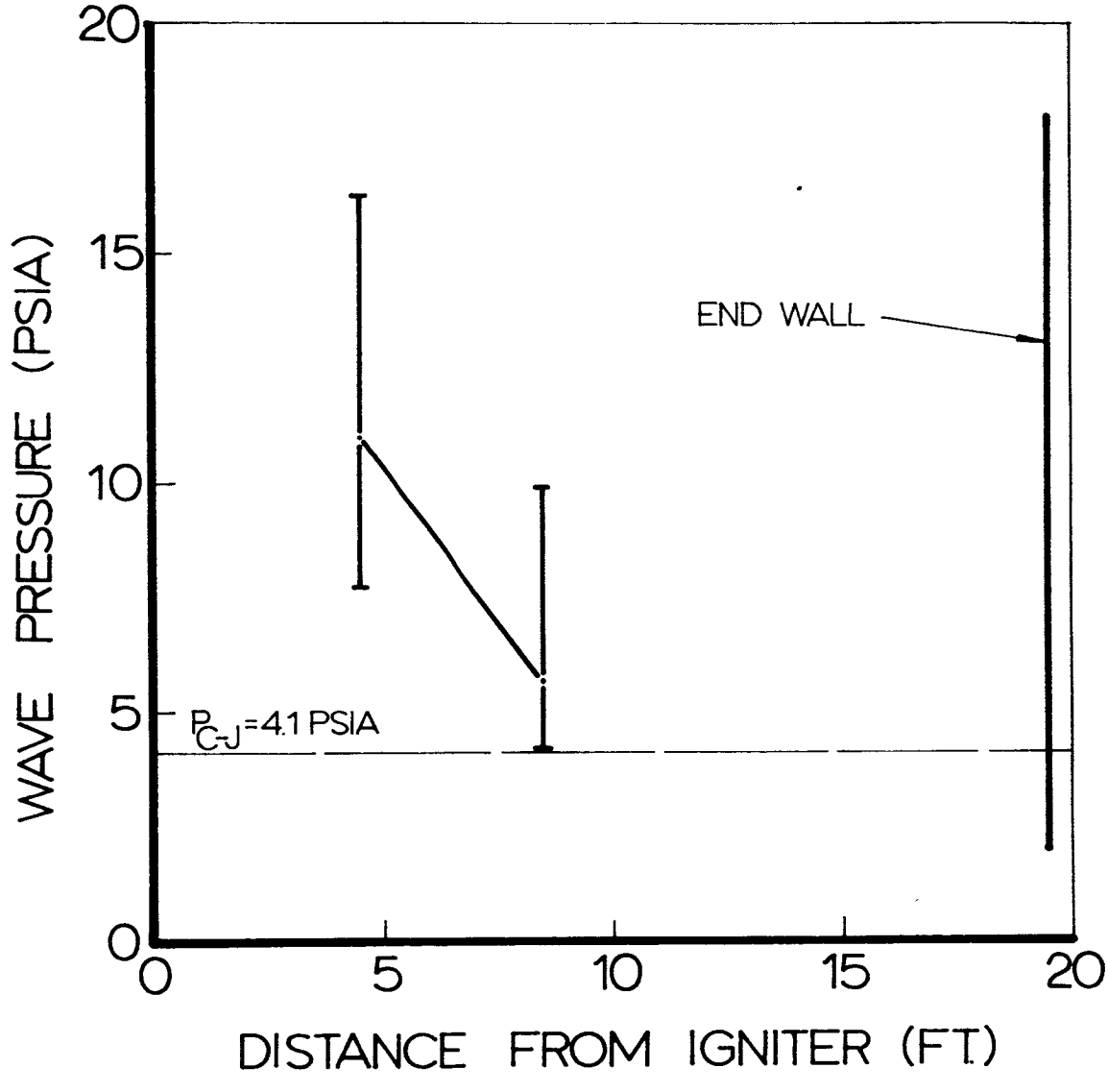

Fig. 61 Peak-wave pressure as function of distance from Primacord ignitor in the 2 ft. dia. x 20 ft. long vessel. $3H_2+0_2$ composition, initial pressure 10 mmHg, initial temperature -50°F.

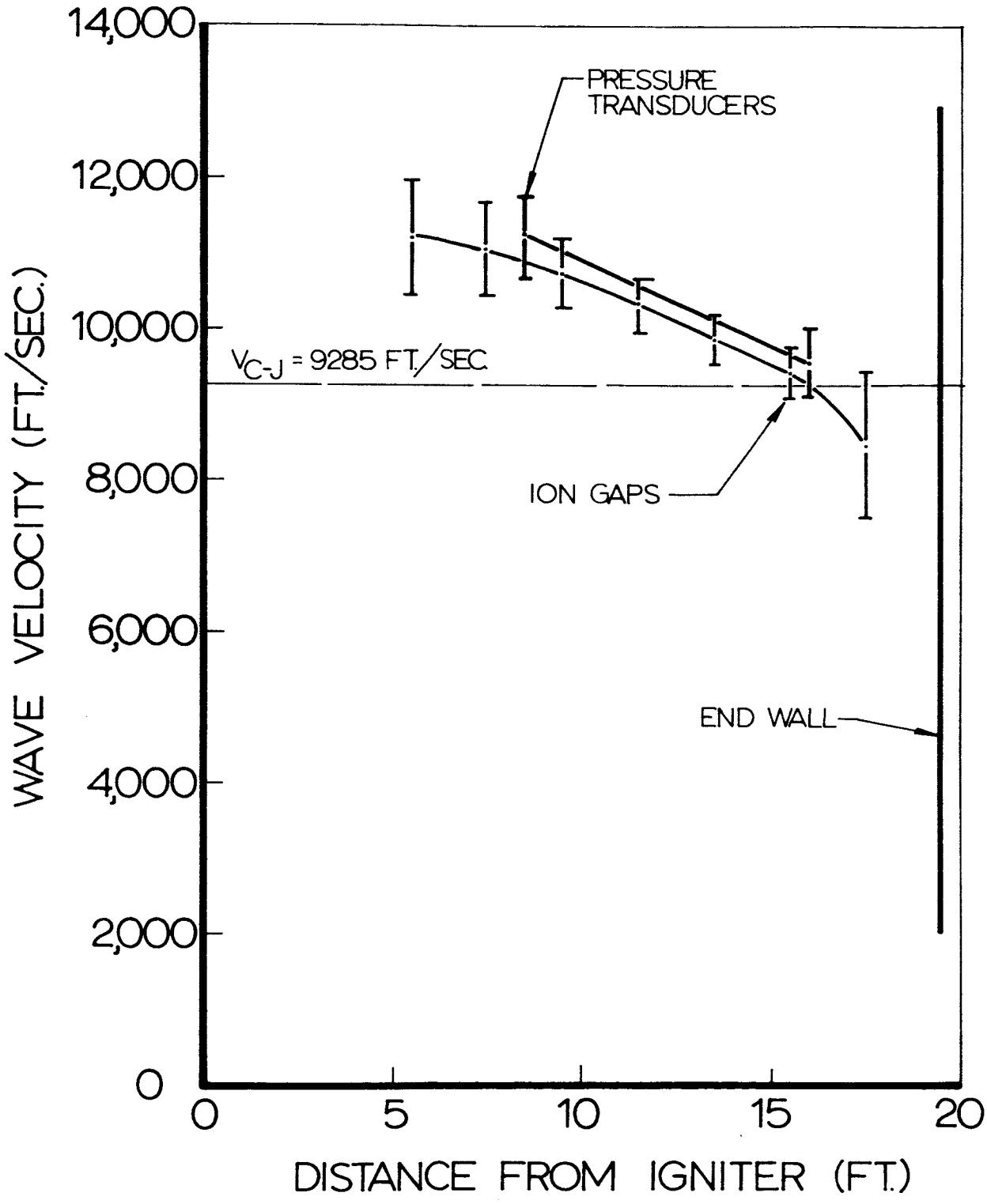

Fig.62 Wave velocity as function of distance from Primacord ignitor in the 2 ft. dia. x 20 ft. long vessel. $3H_2+0_2$ composition, initial pressure 1.0 mm Hg, initial temperature -50°F.

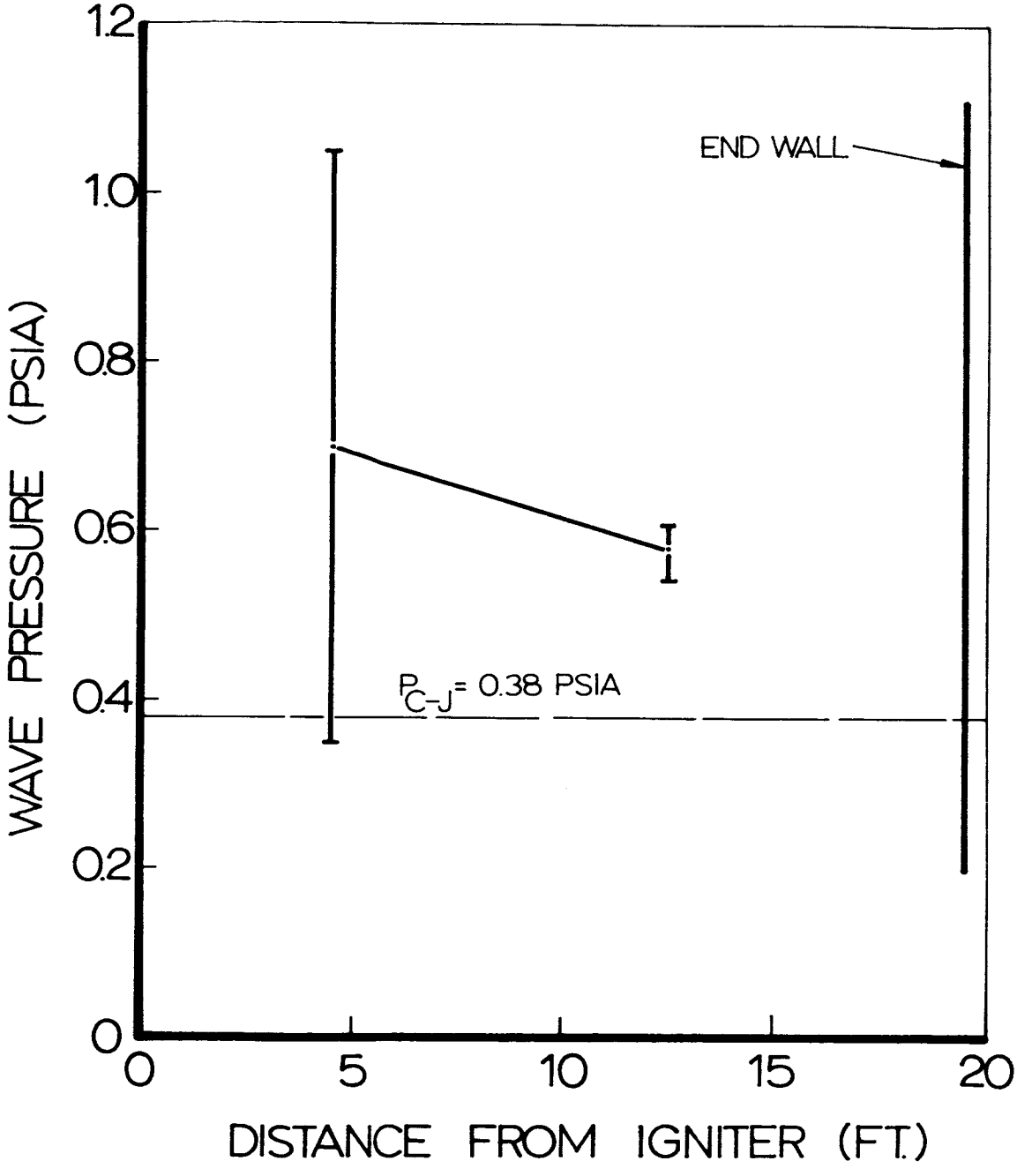

Fig.63 Peak-wave pressure as function of distance from Primacord ignitor in the 2 ft. dia. x 20 ft. long vessel. $3H_2+O_2$ composition, initial pressure 1.0 mmHg, initial temperature -50 °F.

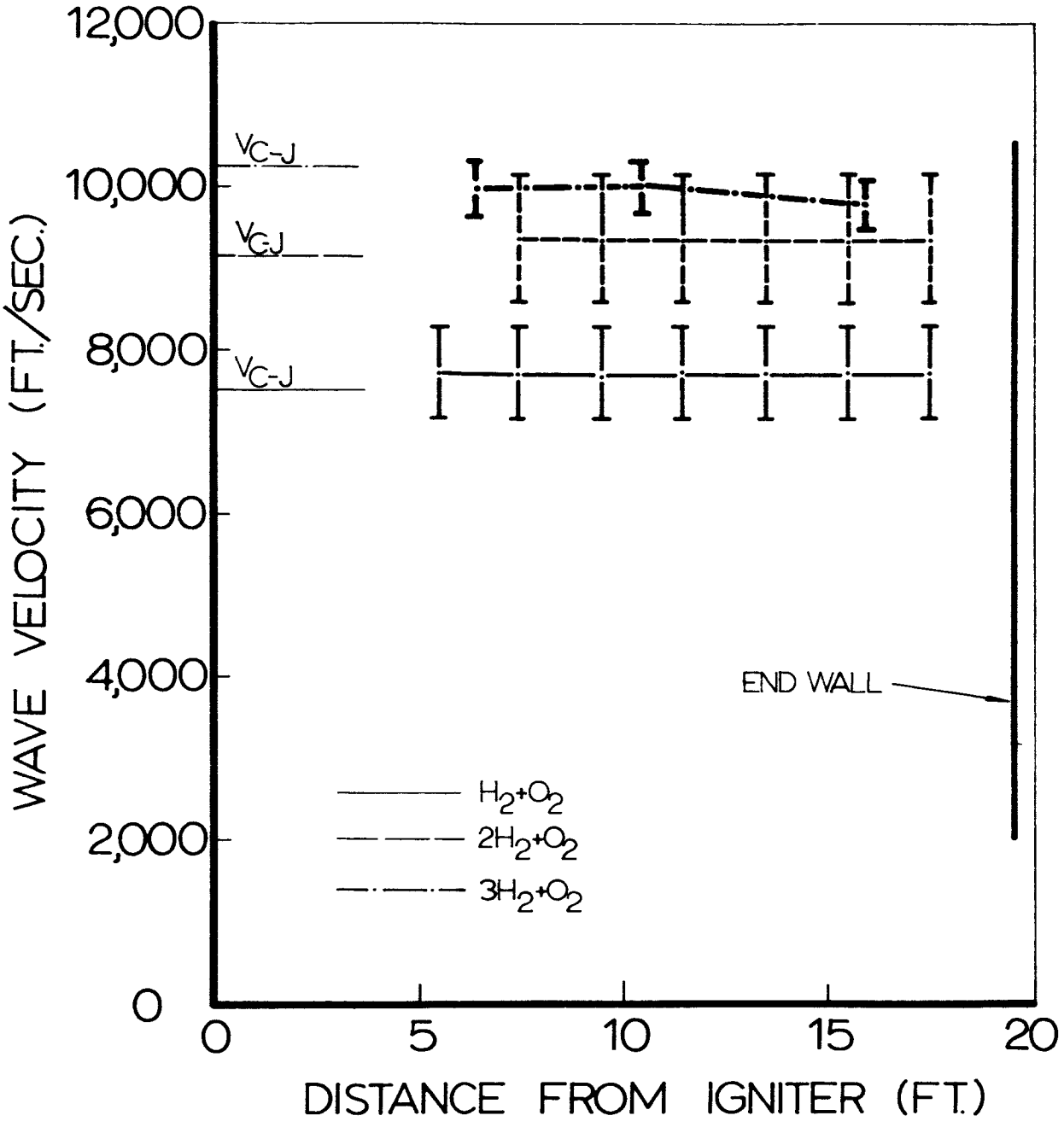

Fig. 64 Wave velocity as function of distance from spark ignitor in the 2 ft. dia. x 20 ft. long vessel. Initial pressure 100 mmHg, initial temperature -180°F.

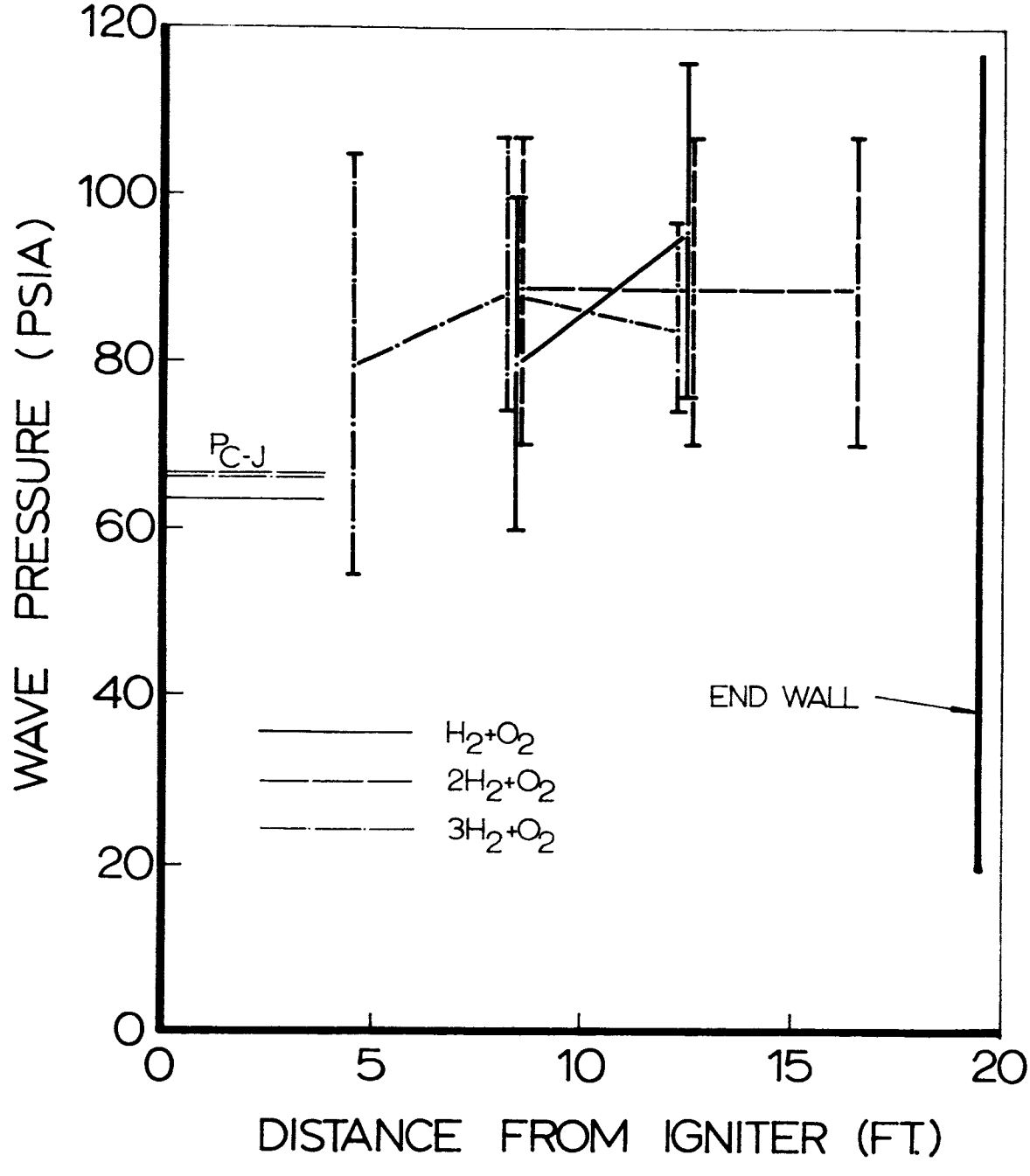

Fig. 65 Peak wave pressure as function of distance from spark ignitor in the 2 ft. dia. x 20 ft. long vessel. Initial pressure 100 mmHg, initial temperature -180°F.

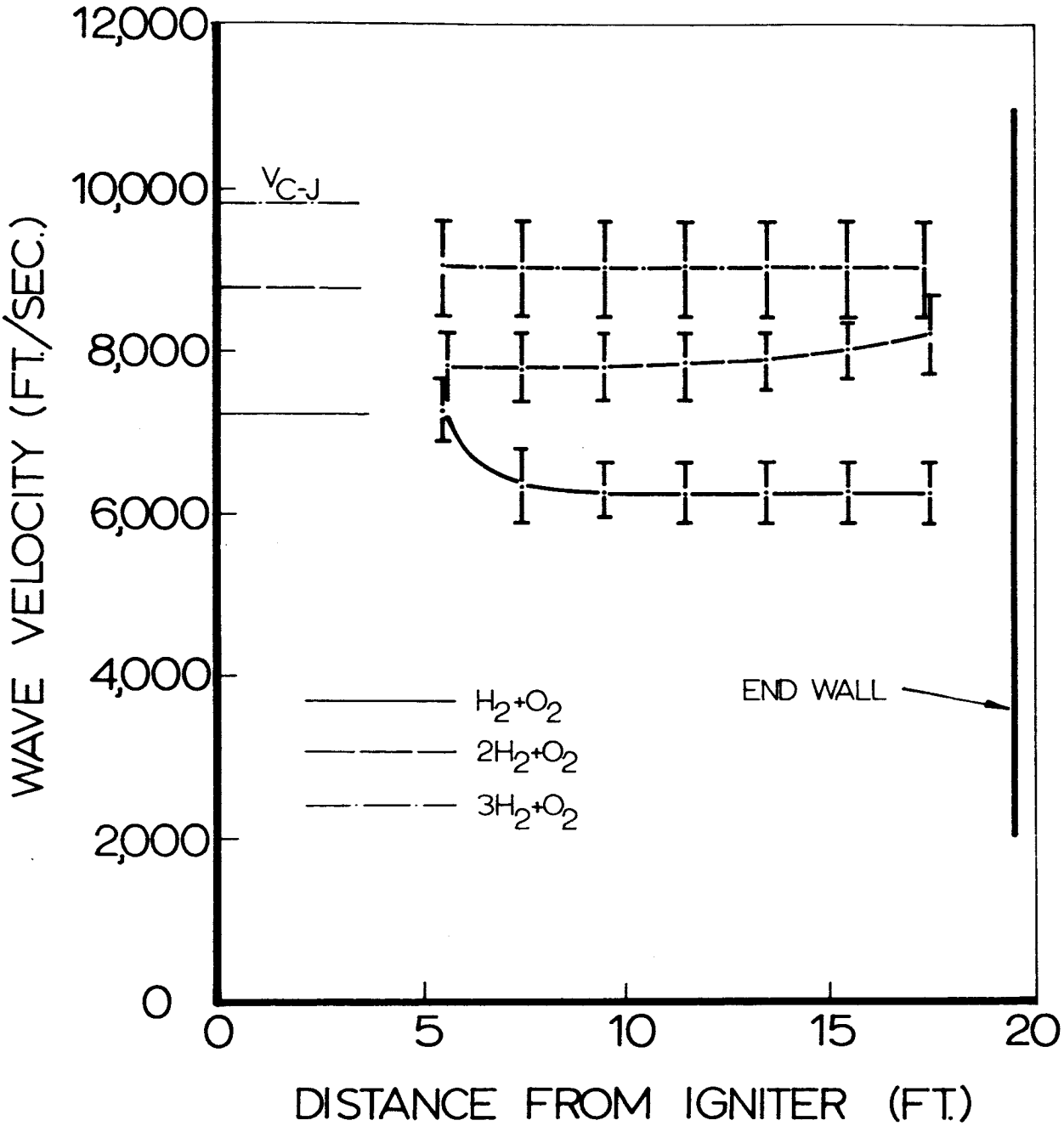

Fig.66 Wave velocity as function of distance from Primacord ignitor in the 2 ft. dia. x 20 ft. long vessel. Initial pressure 10 mmHg, initial temperature -180°F.

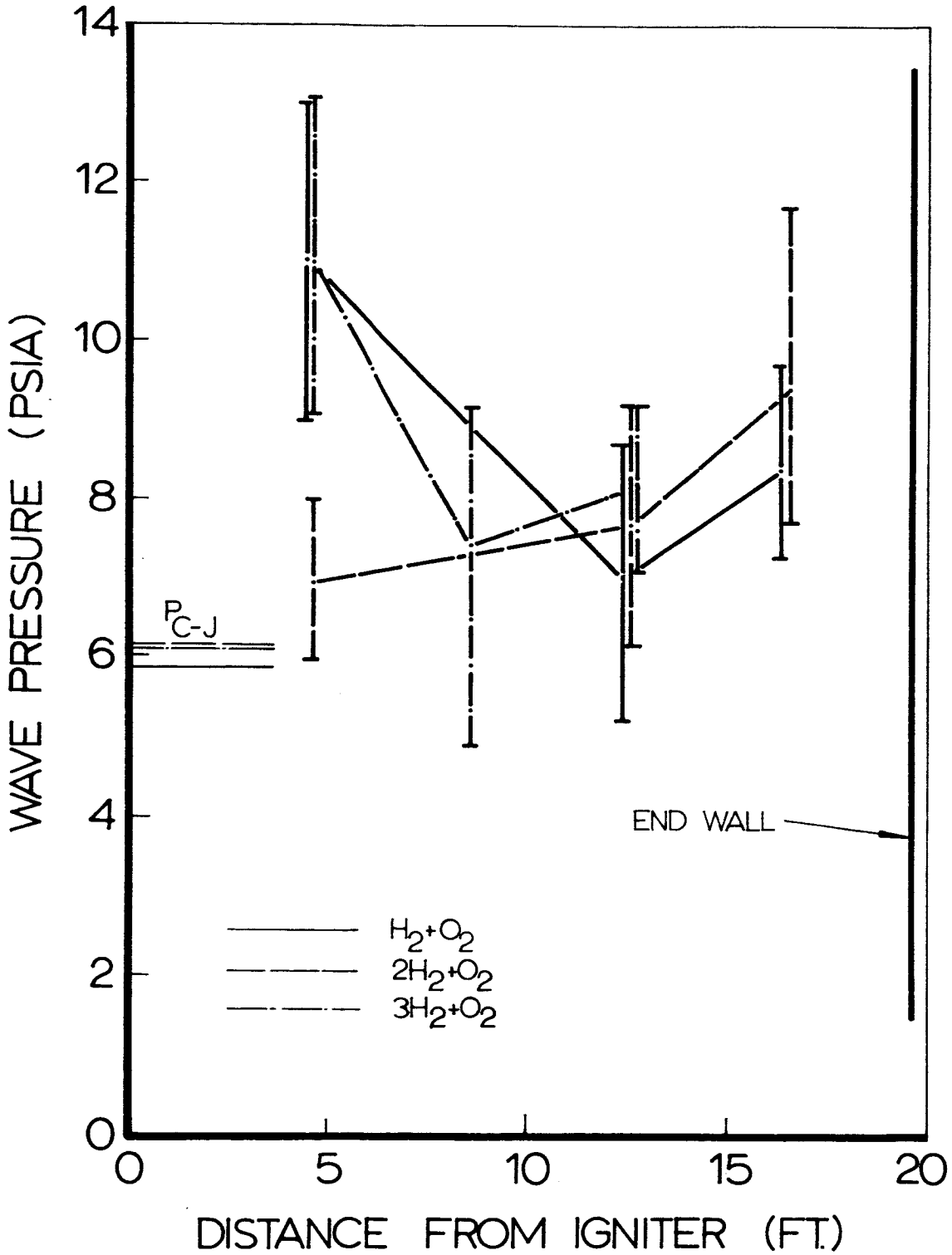

Fig. 67 Peak-wave pressure as function of distance from Primacord ignitor in the 2 ft. dia. x 20 ft. long vessel. Initial pressure 10 mm Hg, initial temperature -180°F.

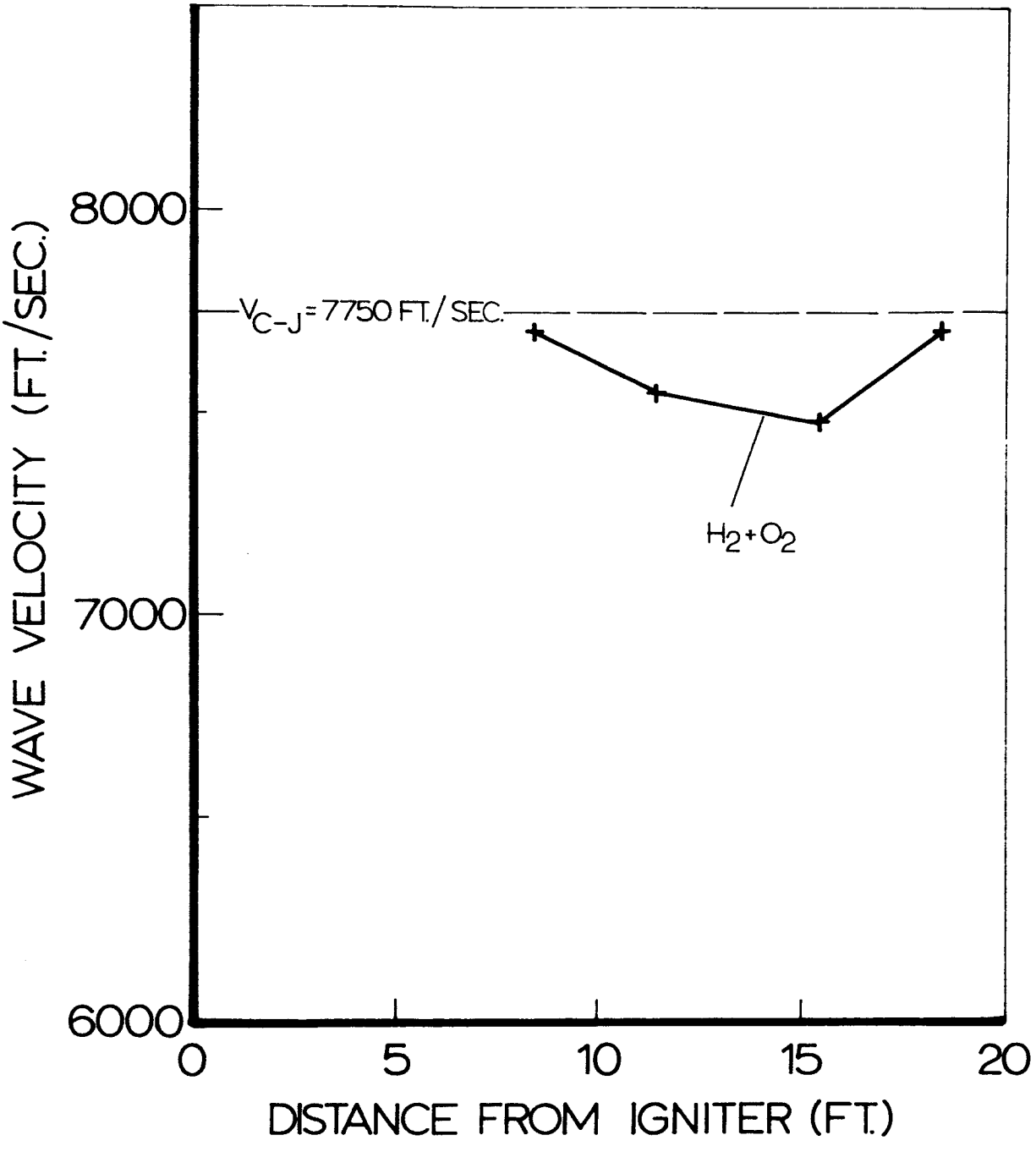

Fig. 68 Wave velocity as a function of distance from Primacord ignitor for Vessel A. Initial pressure 760 mmHg, initial temperature 68 °F.

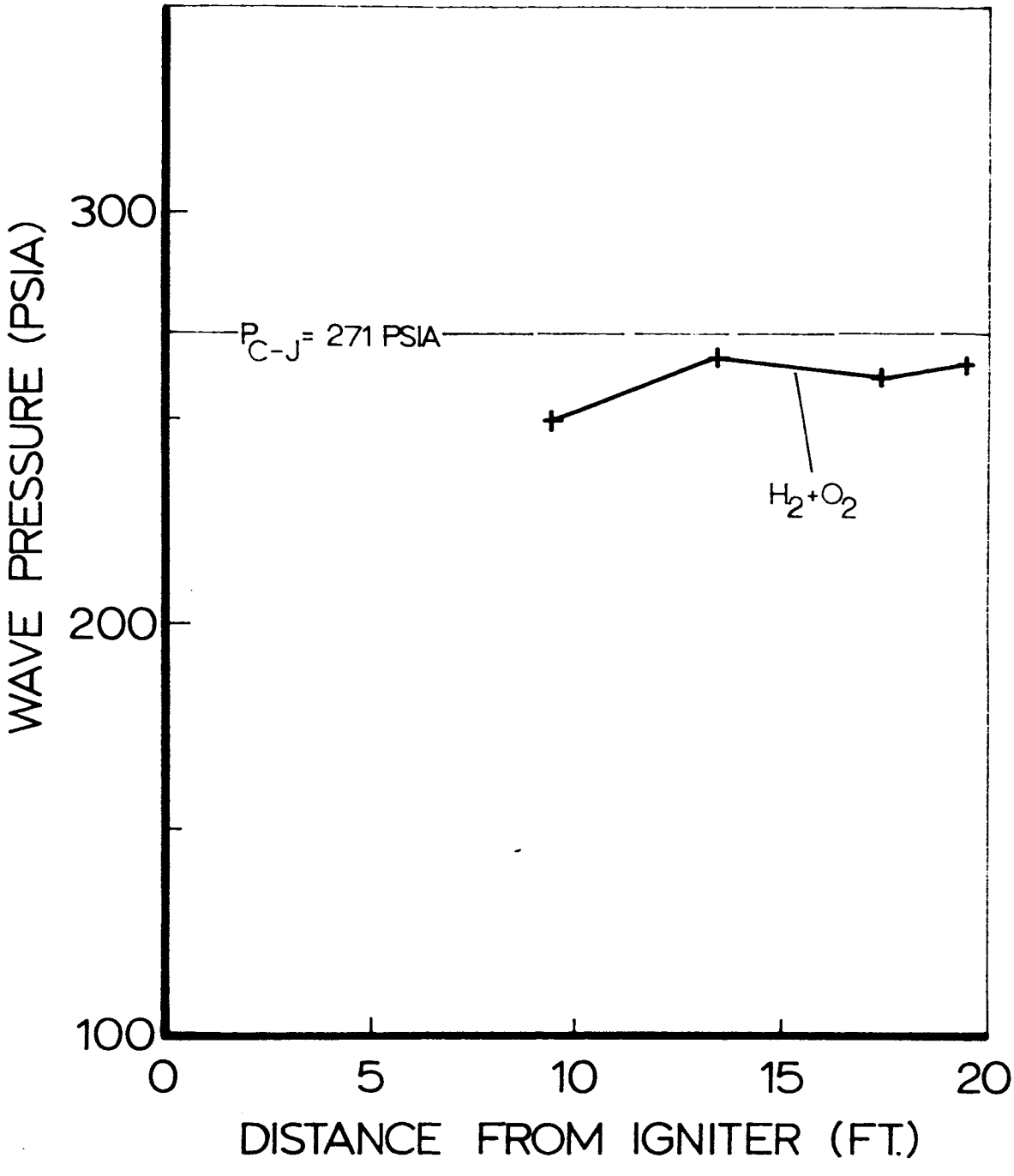

Fig. 69 Wave pressure as a function of distance from Primacord ignitor for Vessel A. Initial pressure 760 mmHg, initial temperature 68°F.

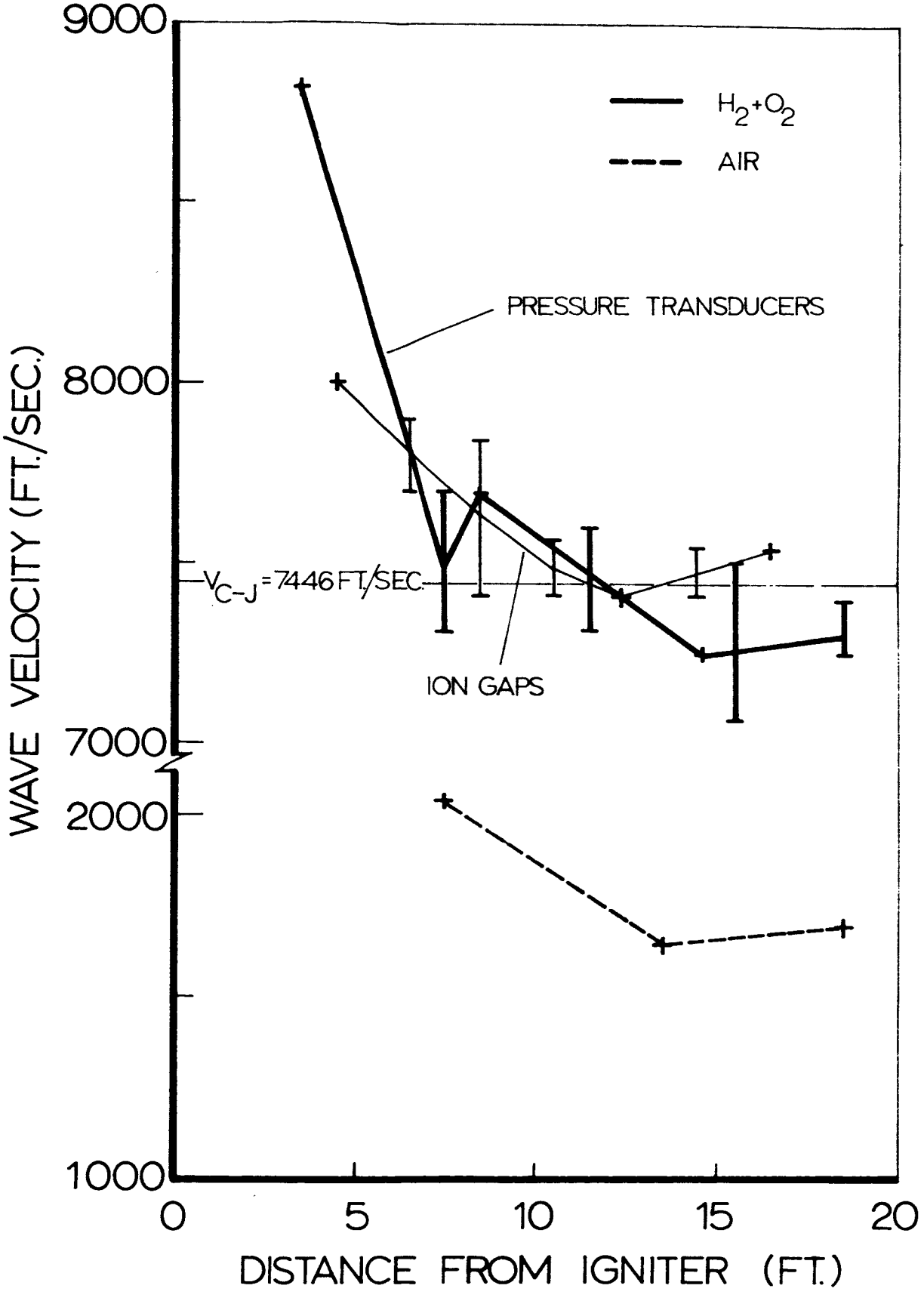

Fig. 70 Wave velocity as a function of distance from Primacord ignitor for Vessel A. Initial pressure 100 mmHg, initial temperature 73°F.

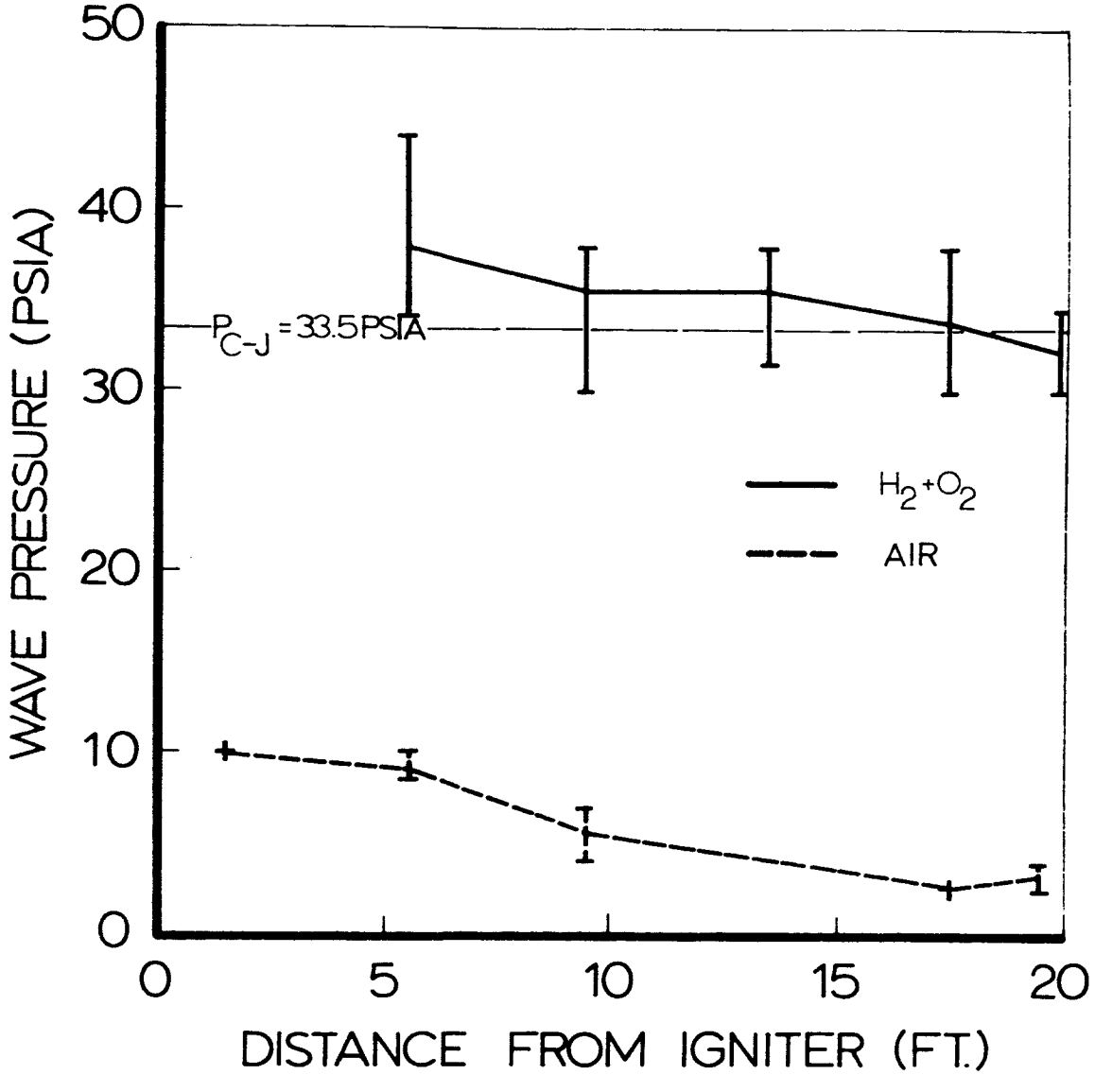

Fig. 71 Wave pressure as a function of distance from Primacord ignitor in Vessel A. Initial pressure 100 mmHg, initial temperature 73°F.

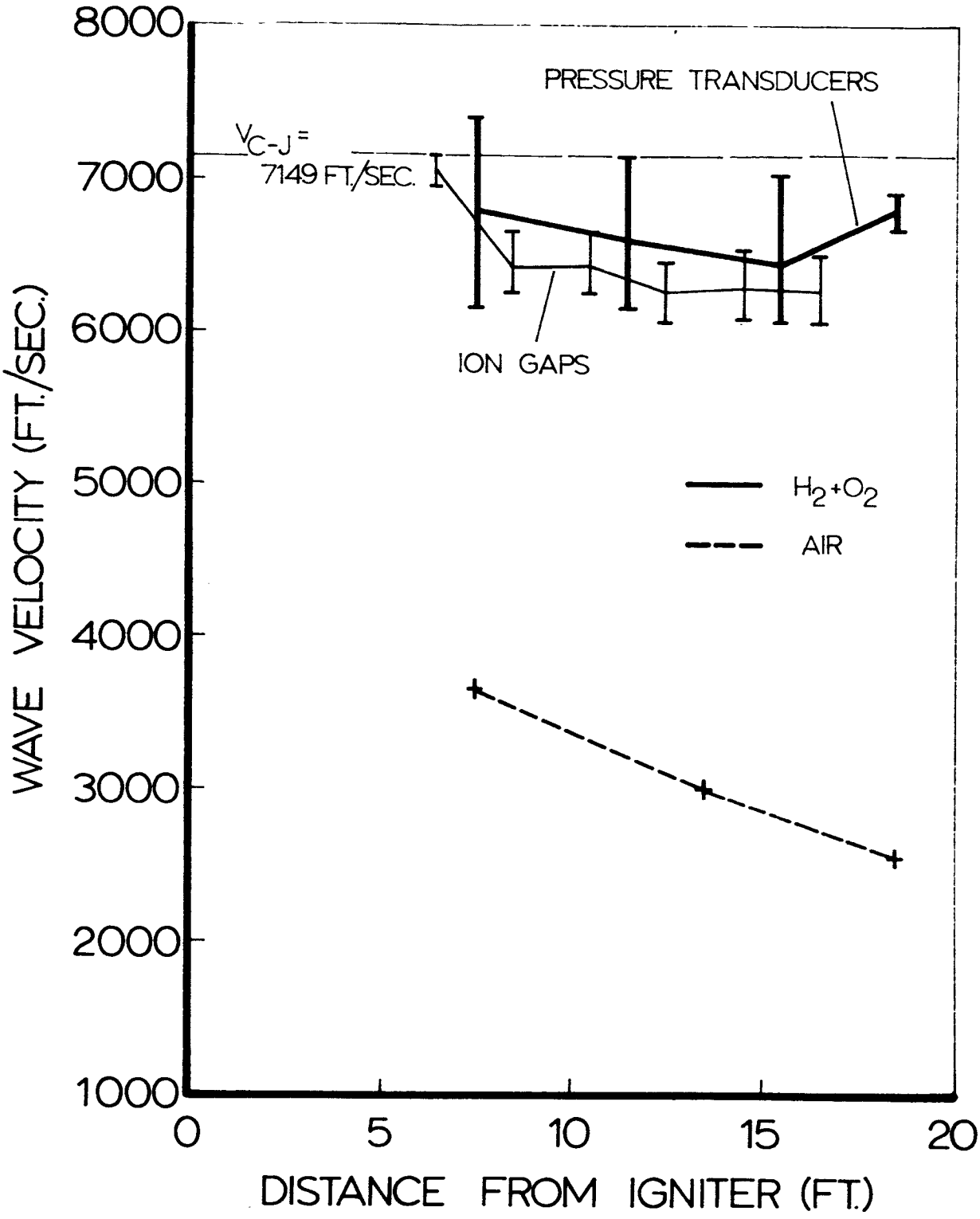

Fig. 72 Wave velocity as a function of distance from Primacord ignitor for Vessel A. Initial pressure 10 mmHg, initial temperature 73°F.

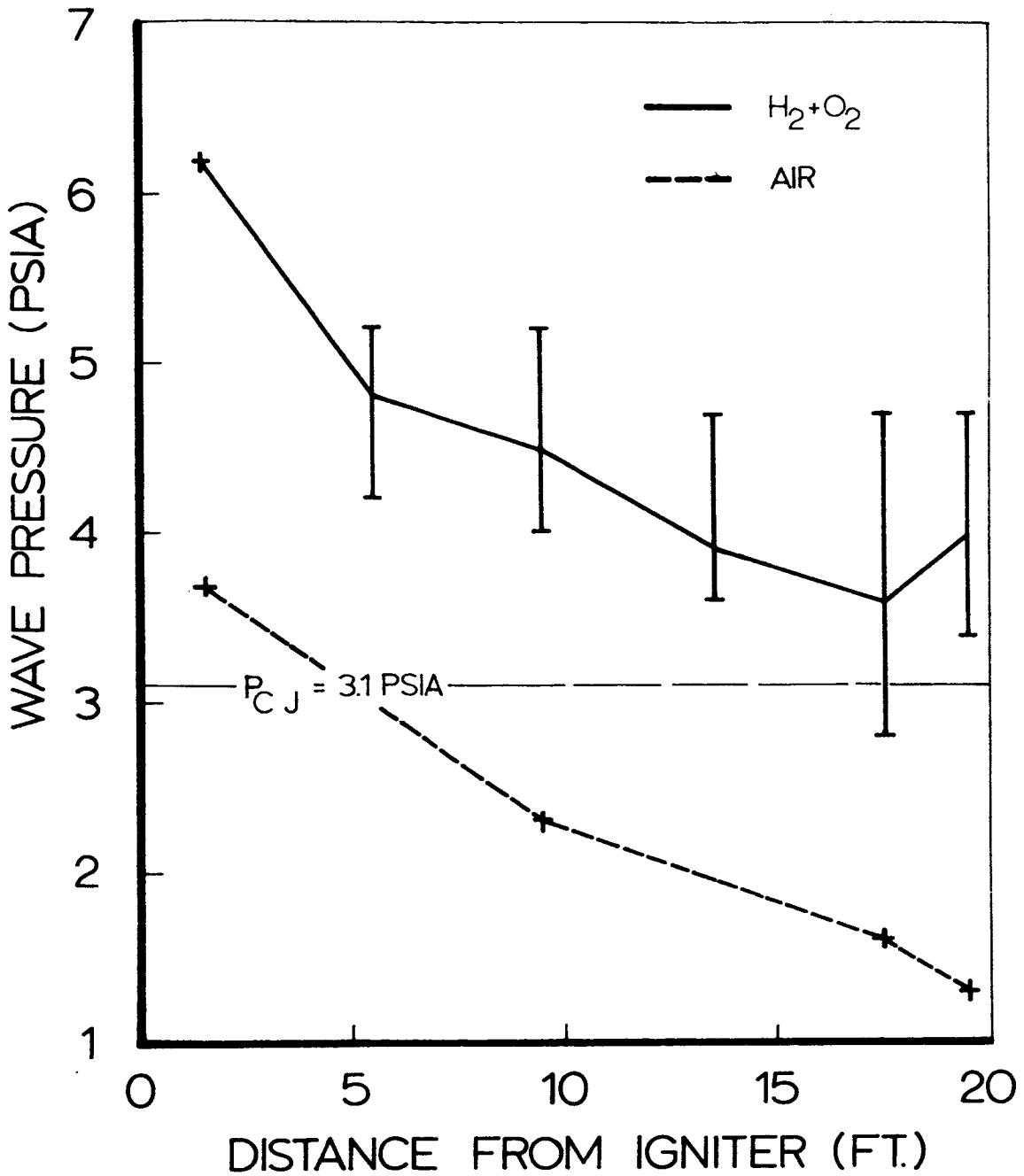

Fig. 73 Wave pressure as a function of distance from Primacord ignitor for Vessel A. Initial pressure 10 mmHg, initial temperature 73°F.

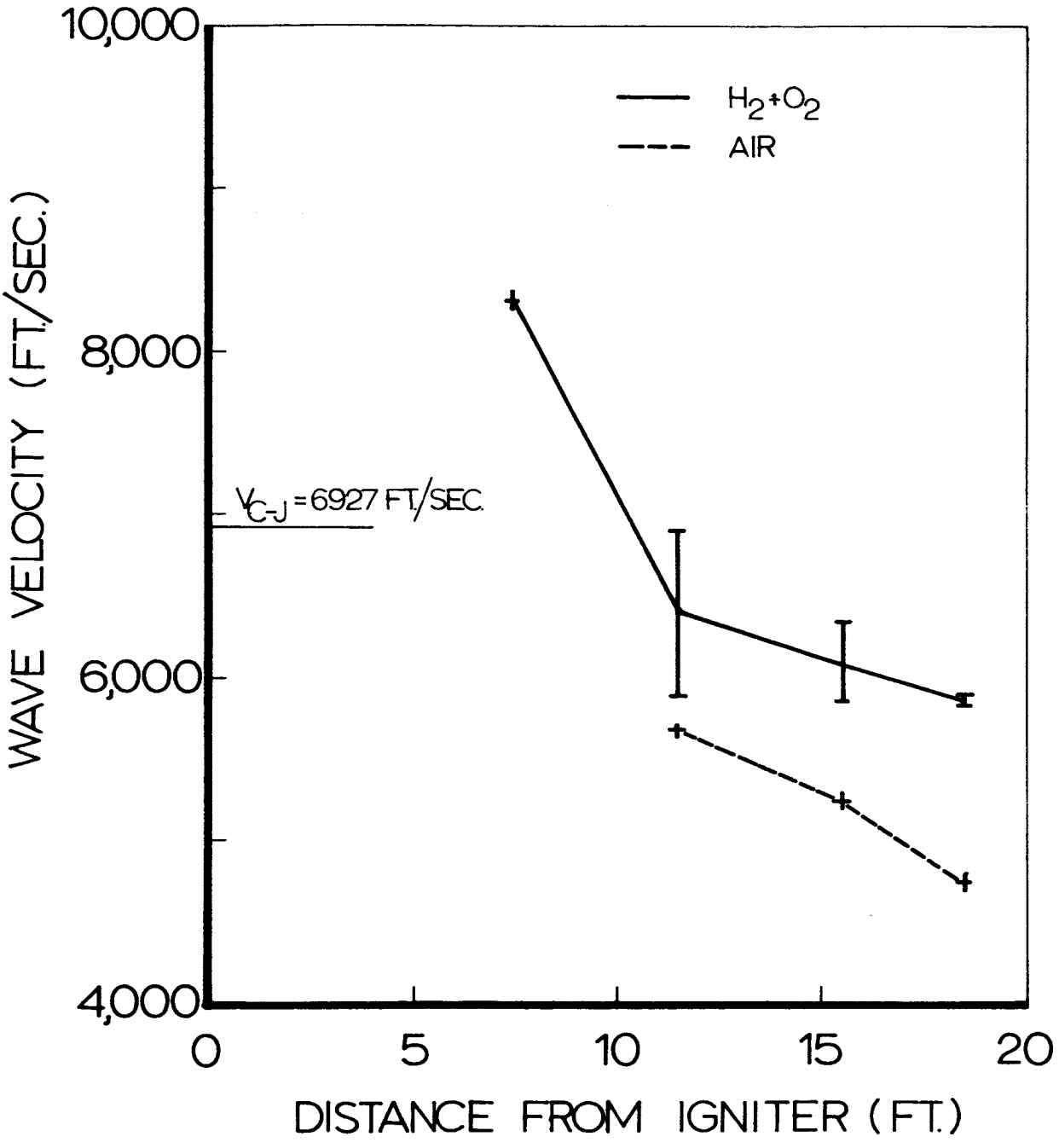

Fig.74 Wave velocity as a function of distance from Primacord ignitor for vessel A. Initial pressure 1 mmHg, initial temperature 72°F.

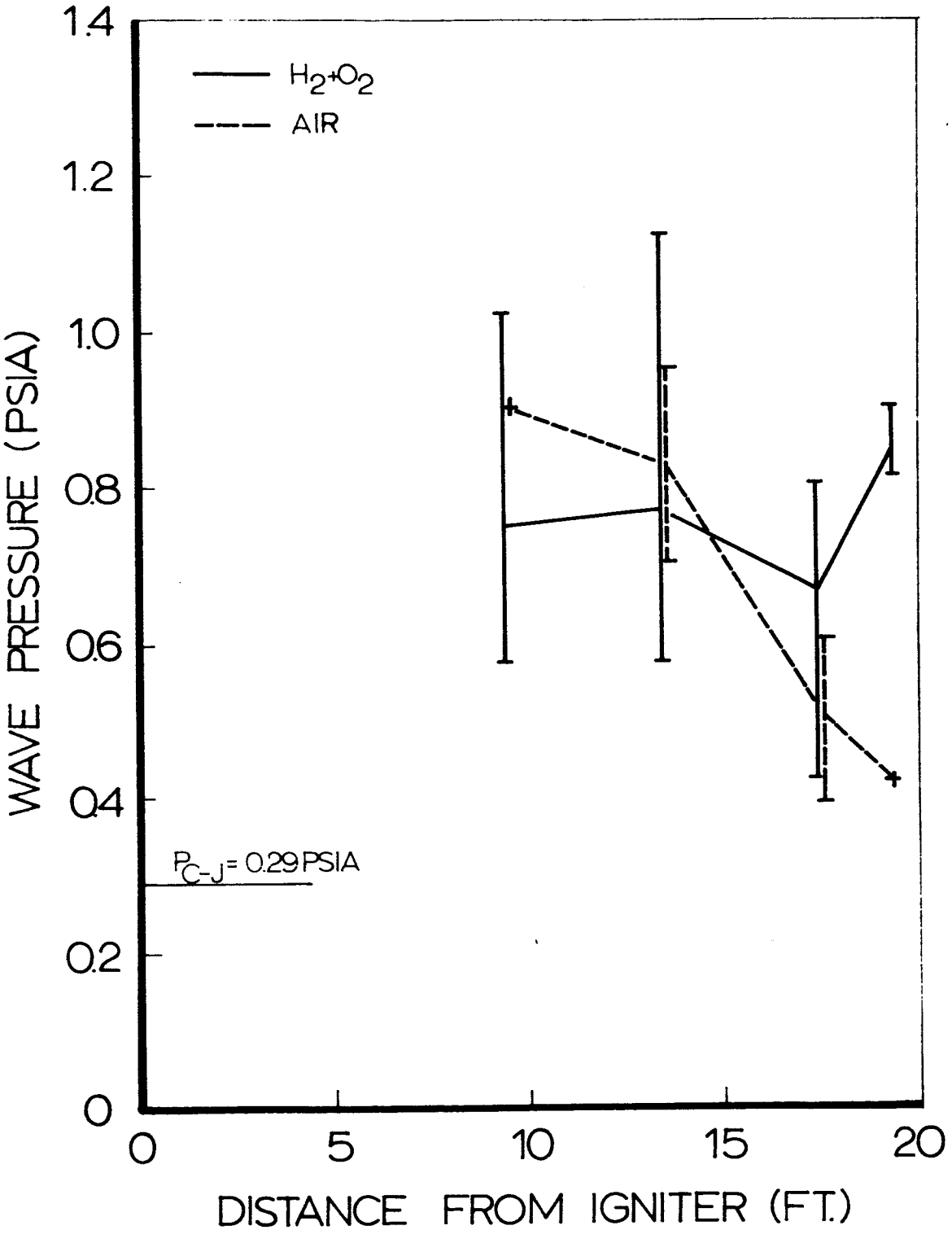

Fig. 75 Wave pressure as a function of distance from Primacord ignitor for Vessel A. Initial pressure 1.0 mmHg, initial temperature 72°F.

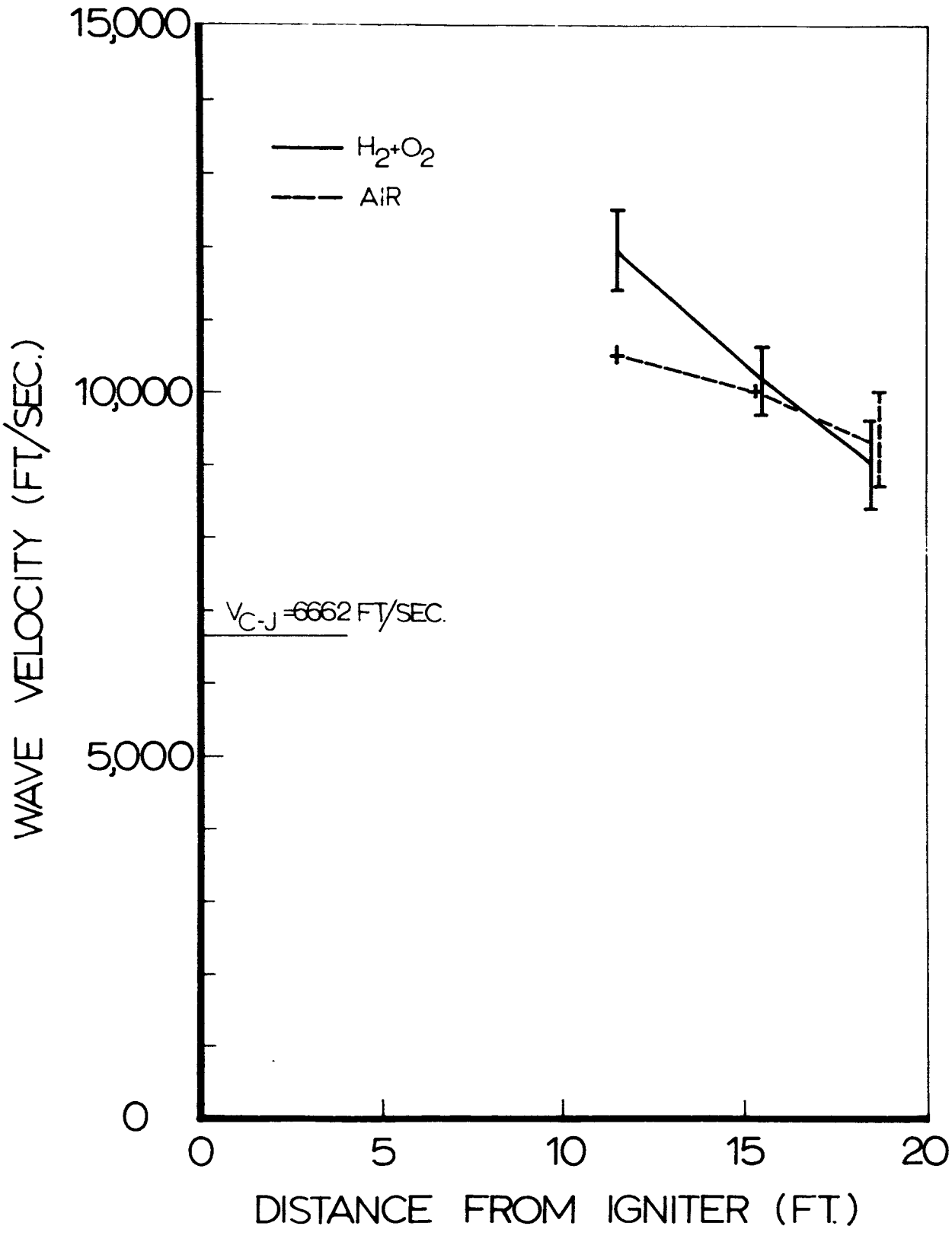

Fig. 76 Wave velocity as a function of distance from Primacord ignitor for vessel A. Initial pressure 0.1mmHg, initial temperature 70°F.

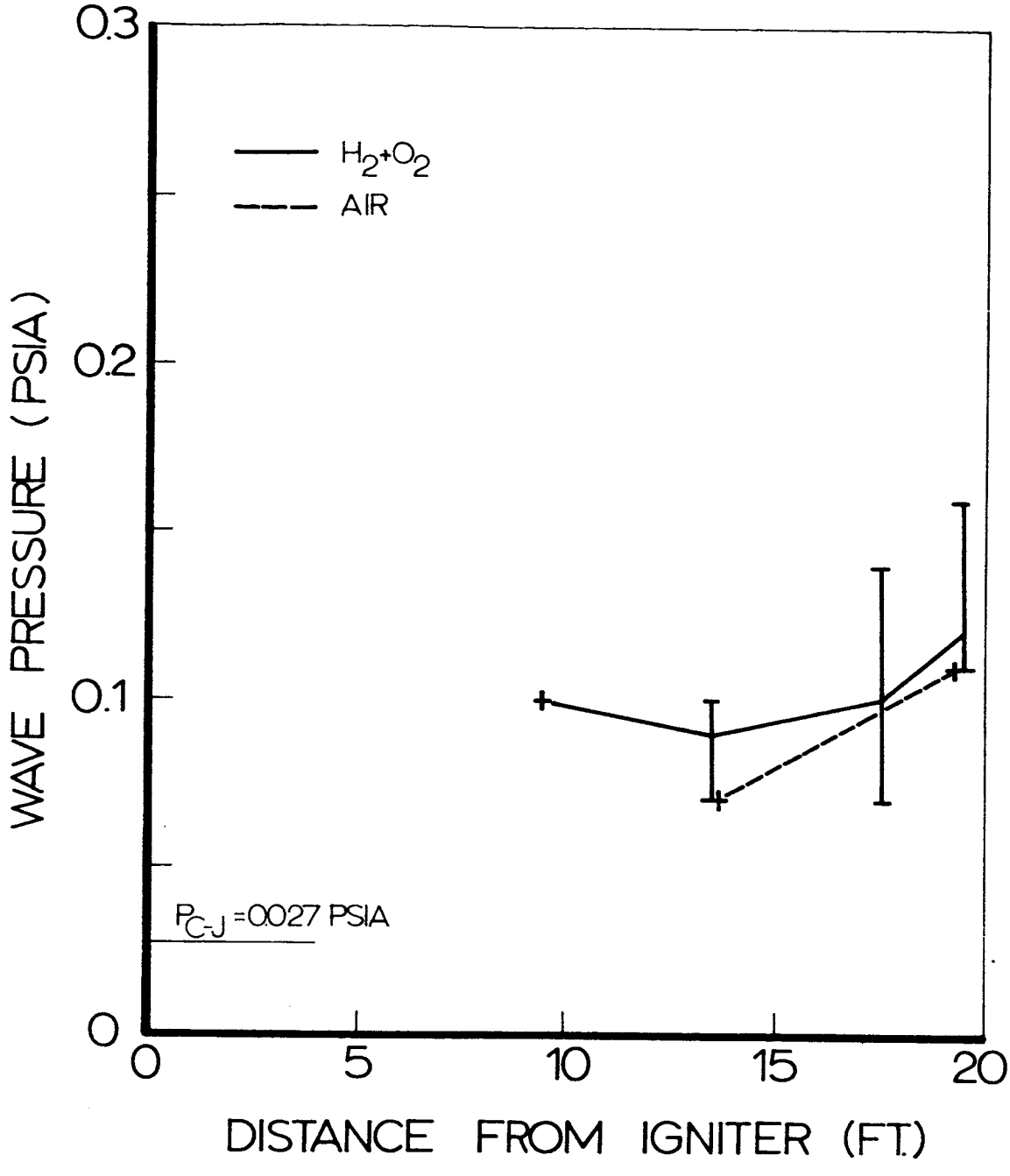

Fig.77 Peak wave pressure as a function of distance from Primacord ignitor for vessel A. Initial pressure 0.1 mmHg, initial temperature 70°F.

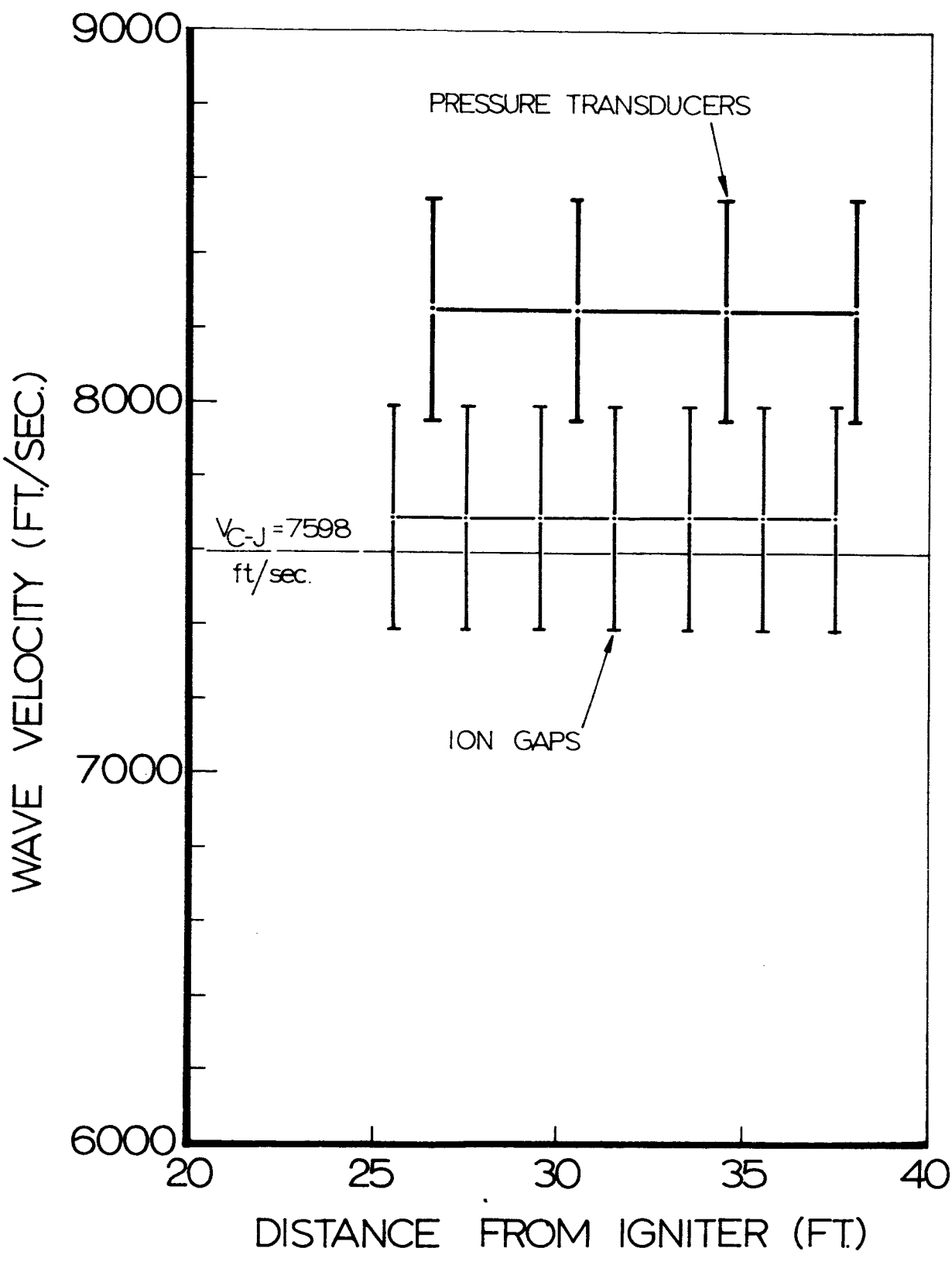

Fig. 78 Wave velocity as a function of distance from Primacord ignitor in the 2 ft. dia. x 40 ft. long Vessel. H_2+0_2 composition, initial pressure 600 mmHg, initial temperature 70°F.

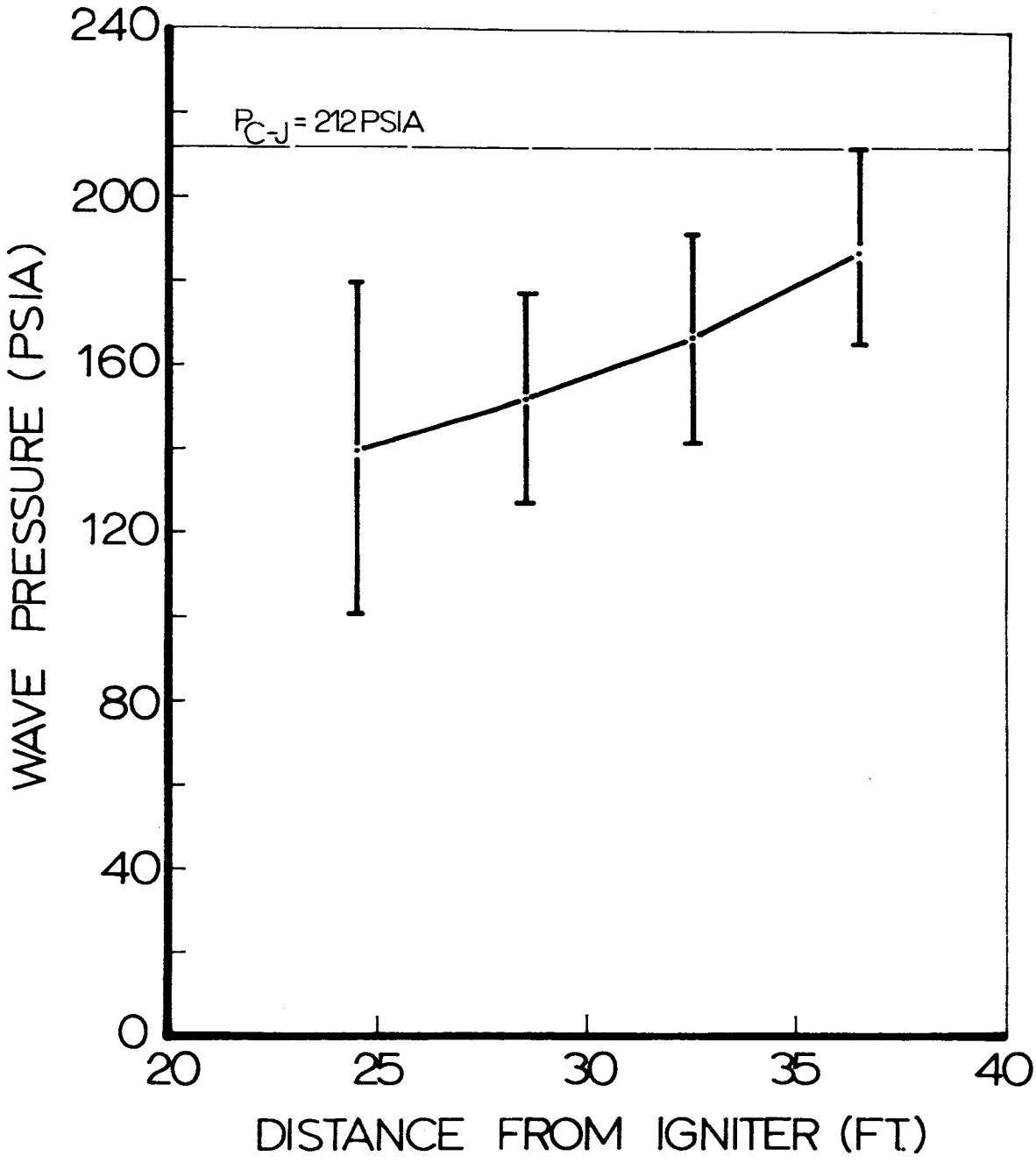

Fig. 79 Peak wave pressure as function of distance from Primacord ignitor in the 2 ft. dia. x 40 ft. long vessel. $H_2 + O_2$ composition, initial pressure 600 mm Hg, initial temperature 70°F.

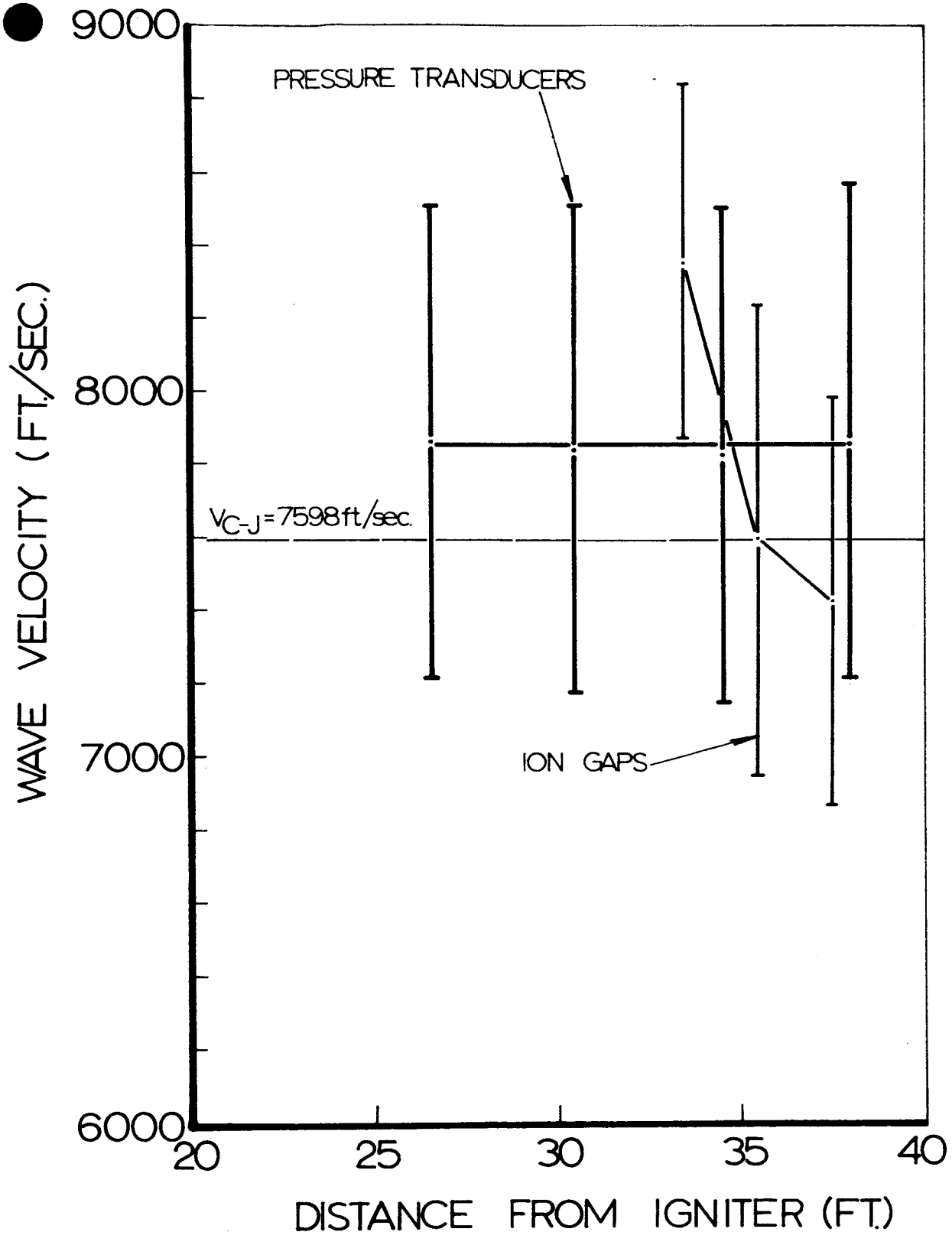

Fig. 80 Wave velocity as a function of distance from spark ignitor in the 2 ft. dia. x 40 ft. long vessel. H_2+O_2 composition, initial pressure 600 mmHg, initial temperature 70°F.

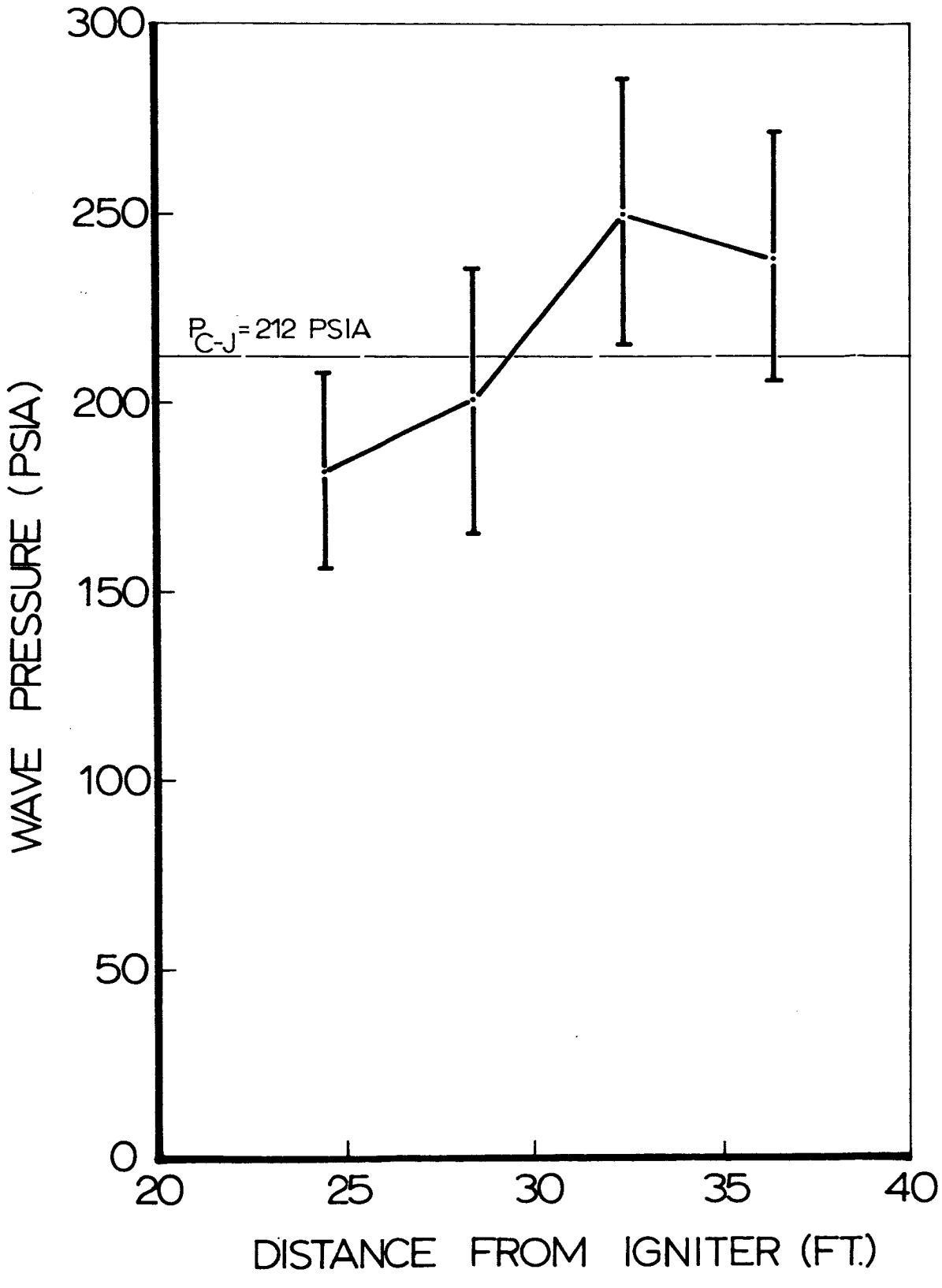

Fig. 81 Peak wave pressure as function of distance from spark ignitor in the 2 ft. dia. x 40 ft. long vessel. $H_2 + O_2$ composition, initial pressure 600 mm Hg, initial temperature 70°F.

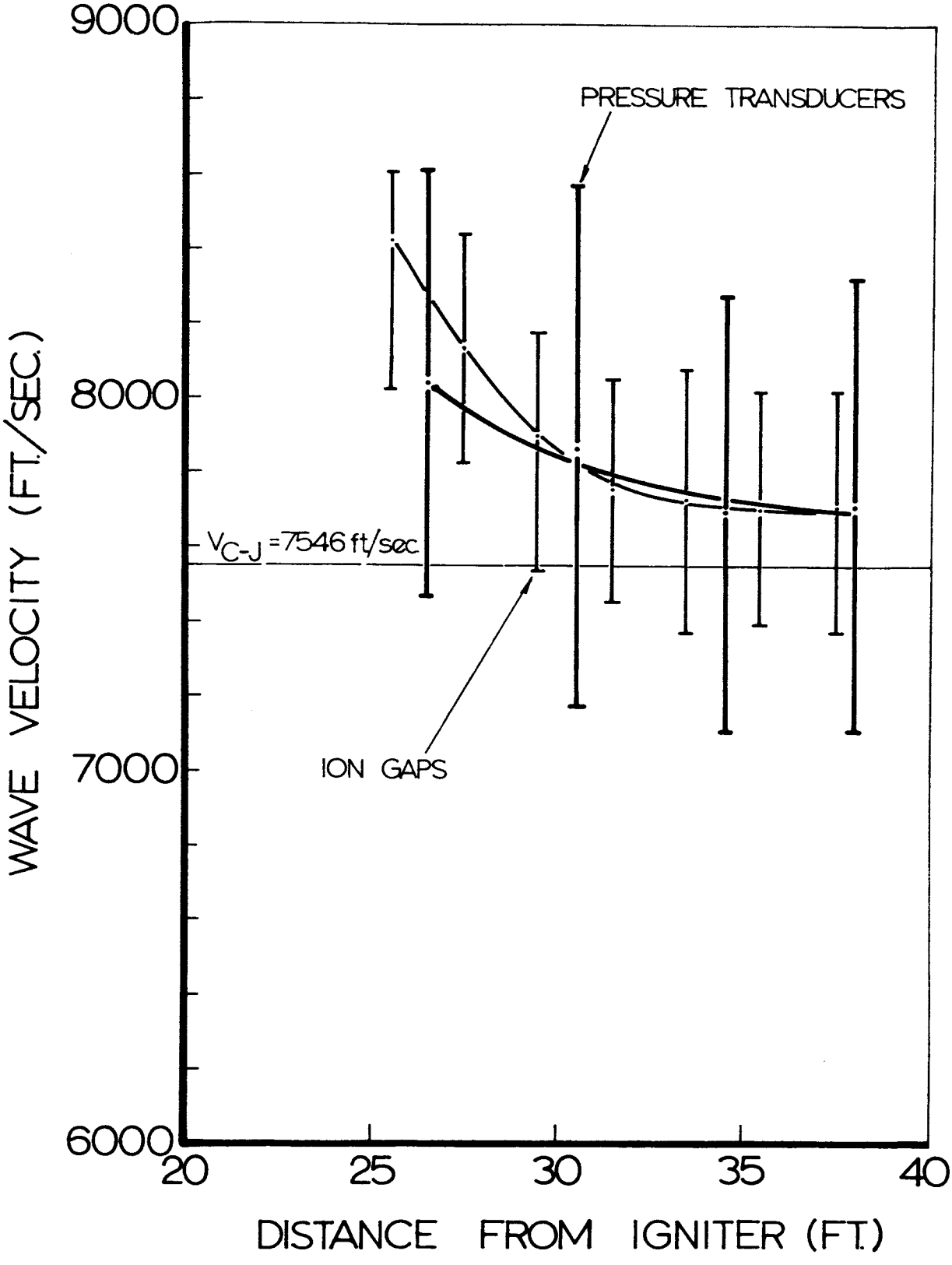

Fig. 82 Wave velocity as function of distance from Primacord ignitor in the 2 ft. dia. x 40 ft. long vessel. $H_2 + O_2$ composition, initial pressure 400 mm Hg, initial temperature 70°F.

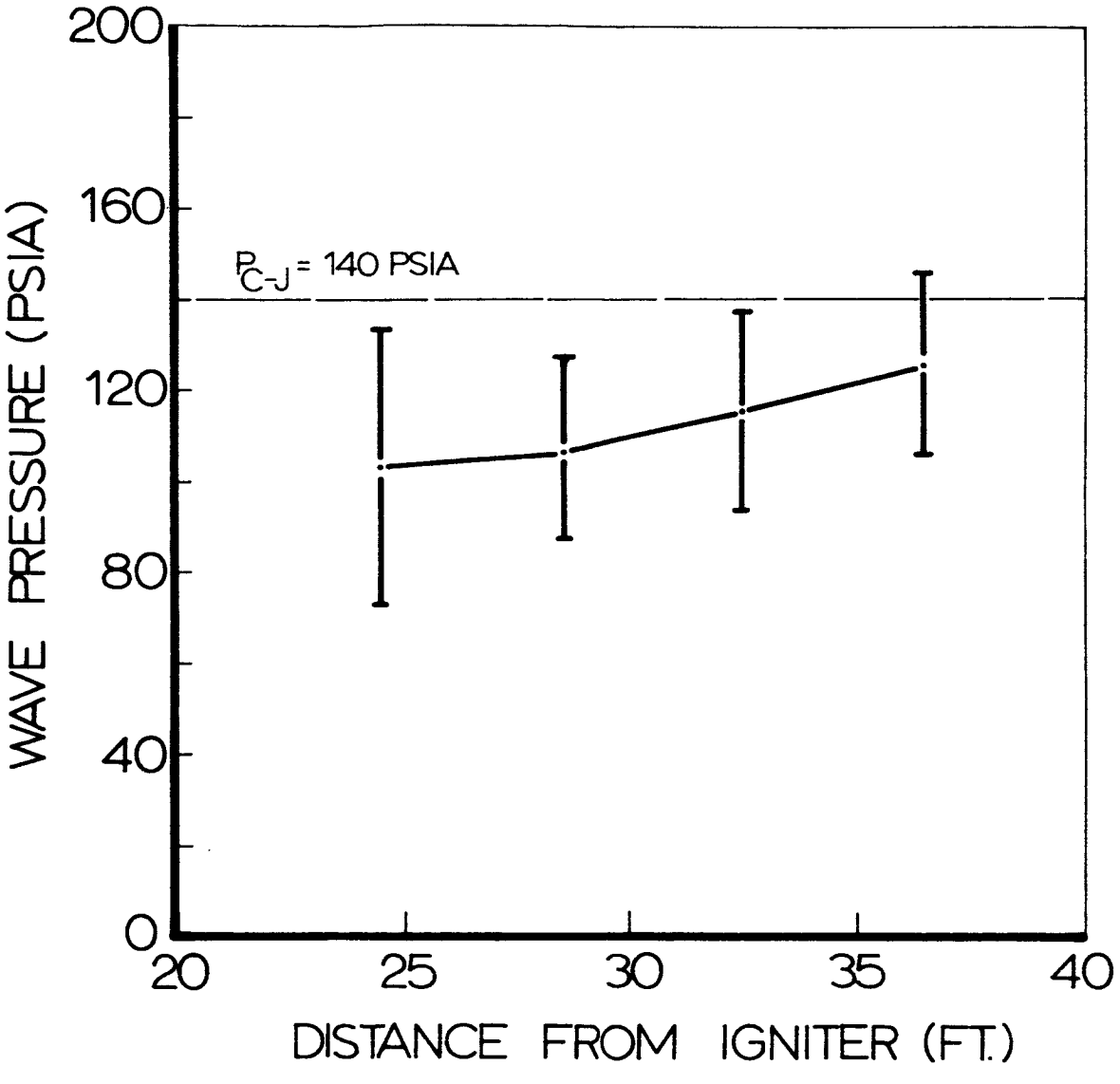

Fig. 83 Peak wave pressure as function of distance from Primacord ignitor in the 2 ft. dia. x 40 ft. long vessel, $H_2 + O_2$ composition, initial pressure 400 mm Hg, initial temperature 70°F.

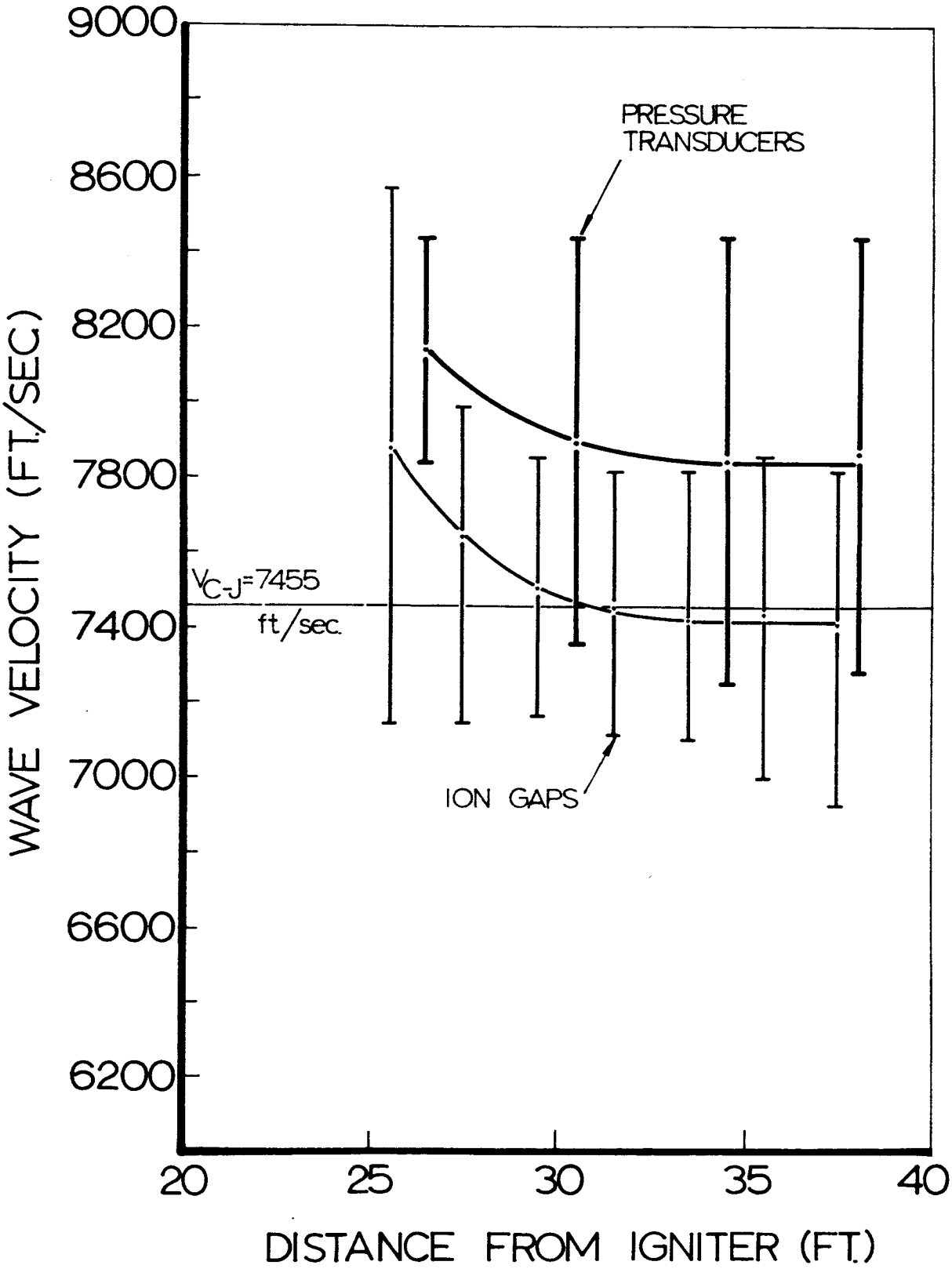

Fig. 84. Wave velocity as function of distance from Primacord ignitor in the 2 ft. dia. x 40 ft. long vessel. $H_2 + O_2$ composition, initial pressure 200 mm Hg, initial temperature 70° F.

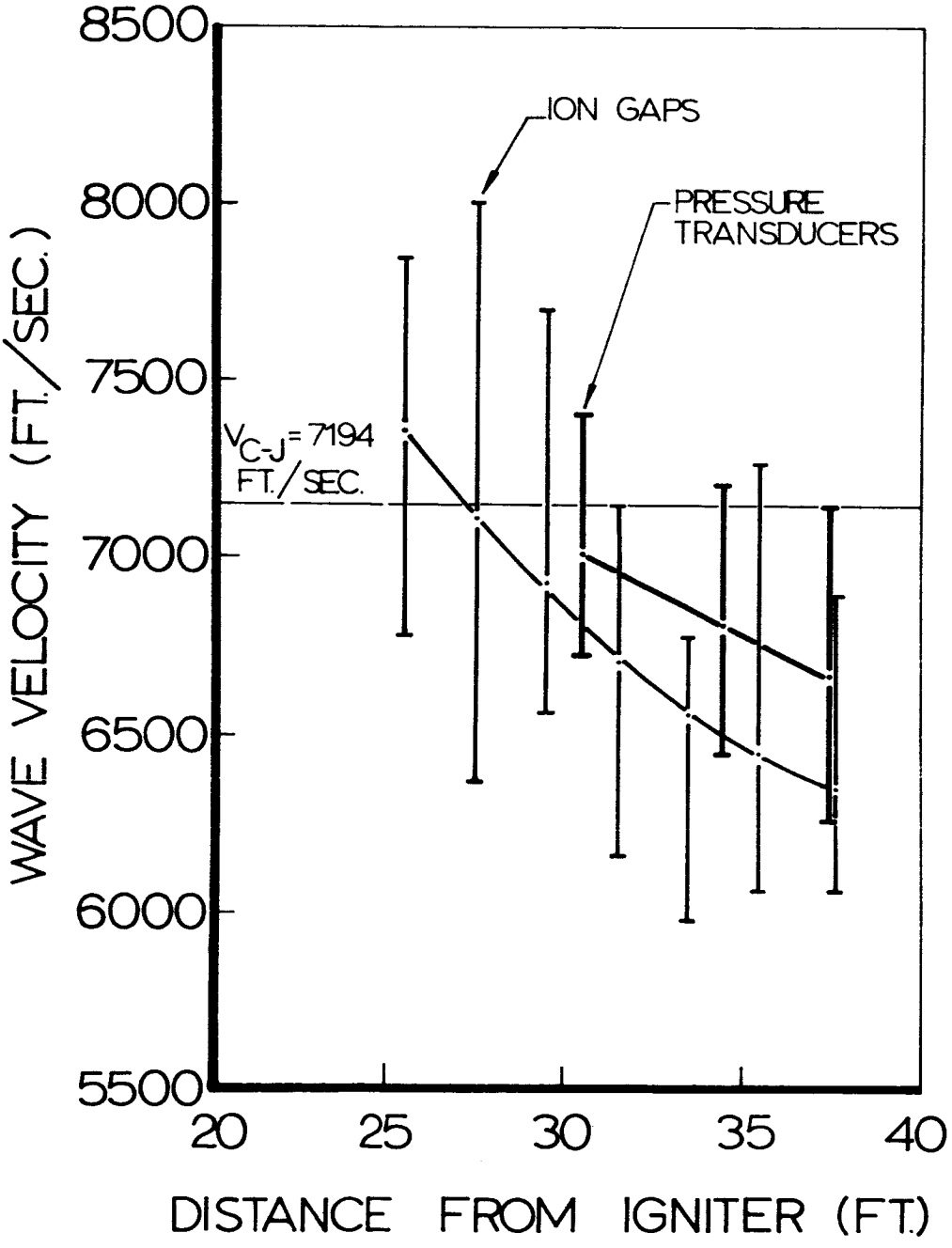

Fig.86 Wave velocity as function of distance from Primacord ignitor in the 40 ft. vessel. H_2+O_2 composition, initial pressure 10 mmHg, initial temperature 70°F.

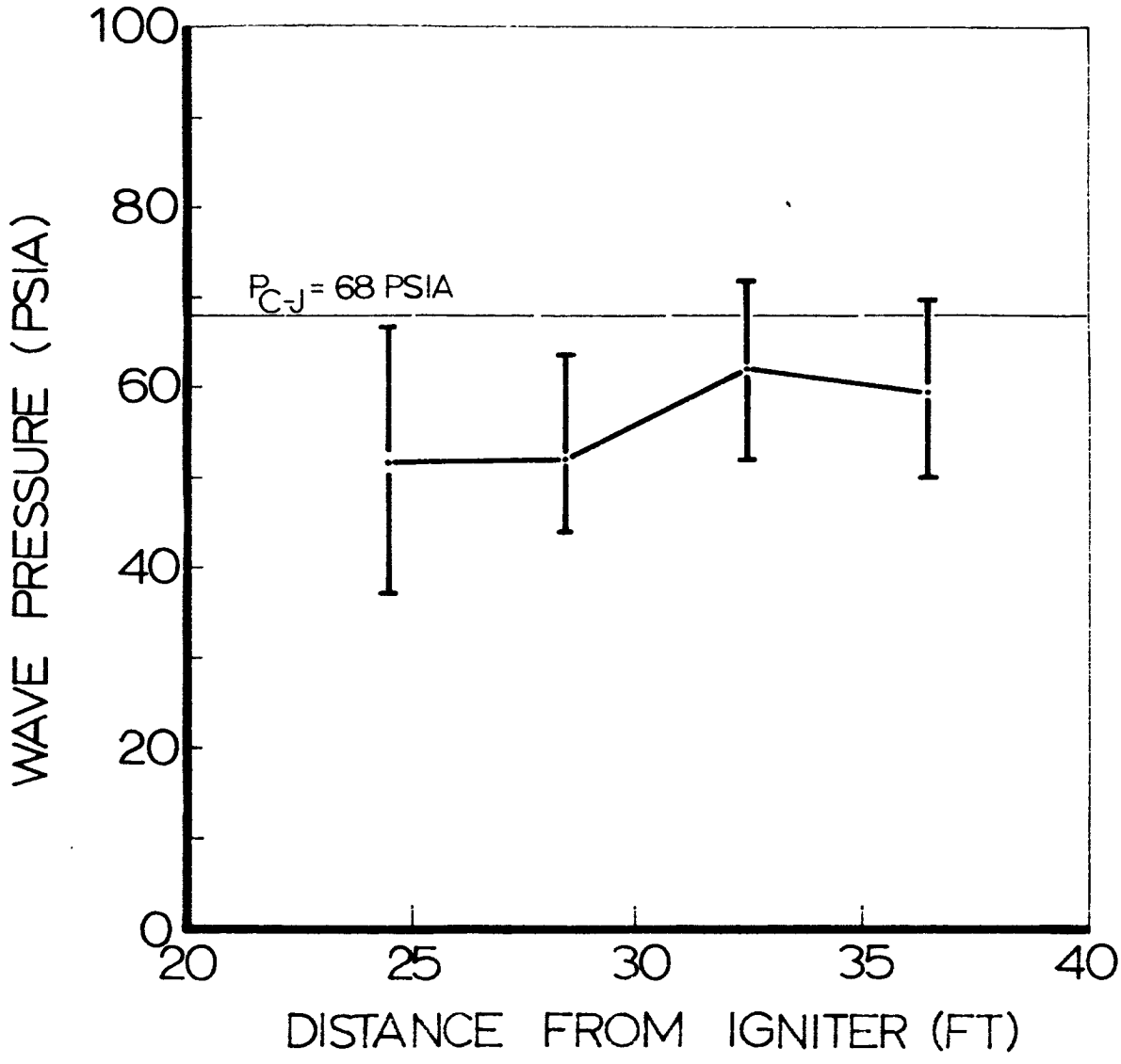

Fig.85 Peak wave pressure as function of distance fromPrimacord ignitor in the 2 ft. dia. x 40 ft. long vessel. $H_2 + O_2$ composition, initial pressure 200 mm Hg, initial temperature 70°F.

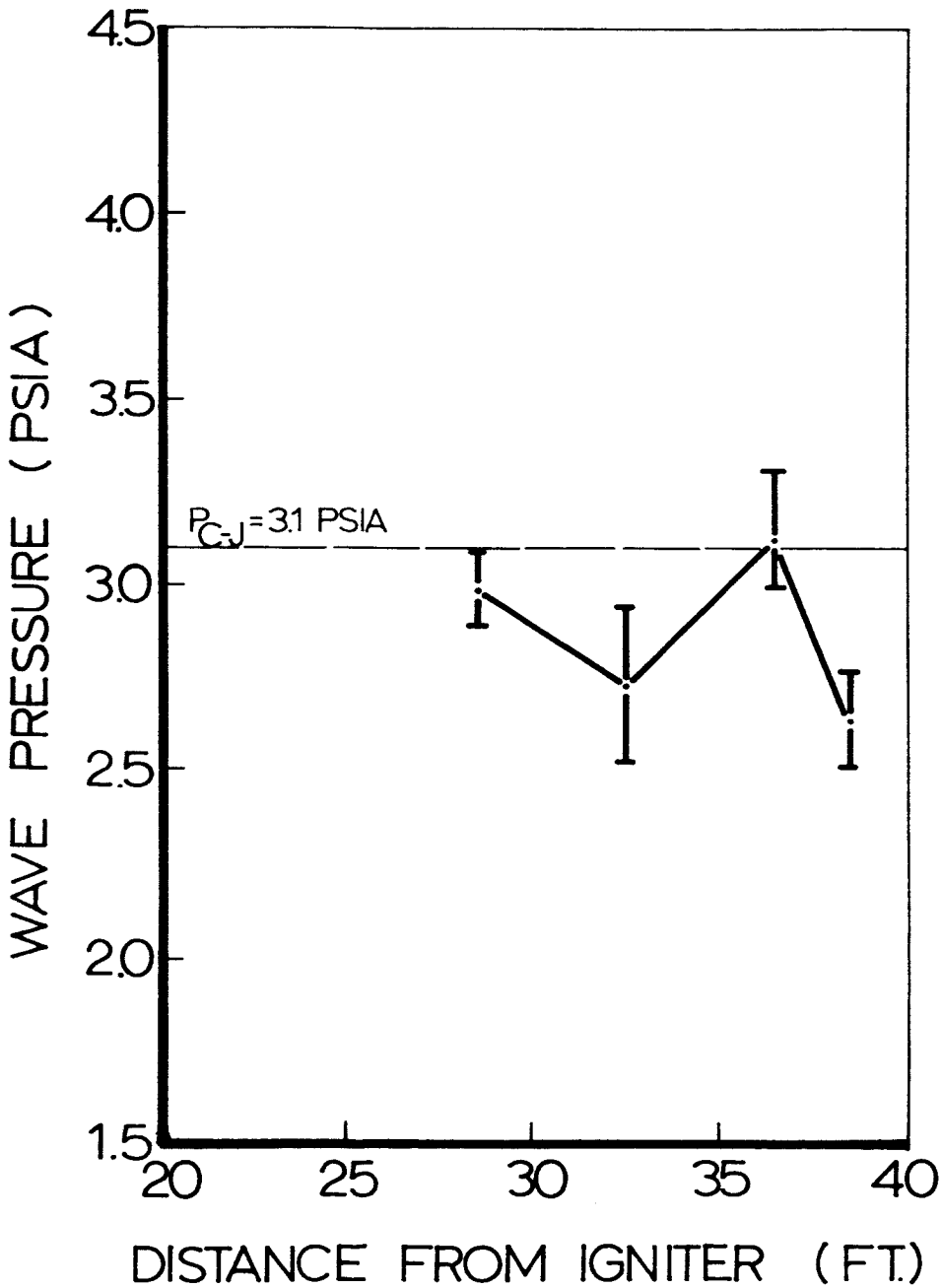

Fig. 87 Peak wave pressure as function of distance from Primacord ignitor in the 40 ft. vessel. H_2+O_2 composition, initial pressure 10 mm Hg, initial temperature 70° F.

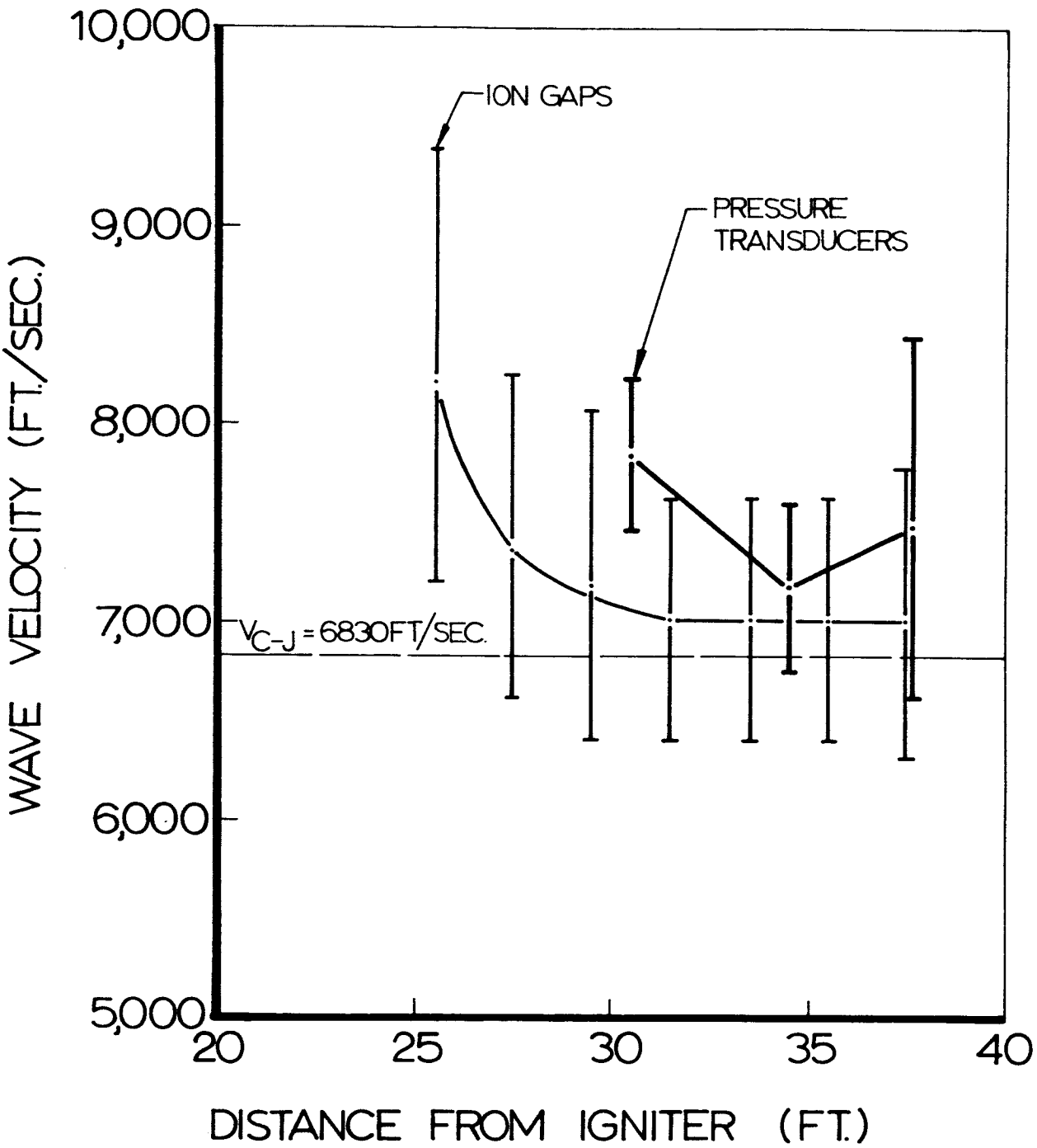

Fig. 88 Wave velocity as function of distance from Primacord ignitor in the 40 ft. vessel. H_2+O_2 composition, initial pressure 1.0 mmHg, initial temperature 70 °F.

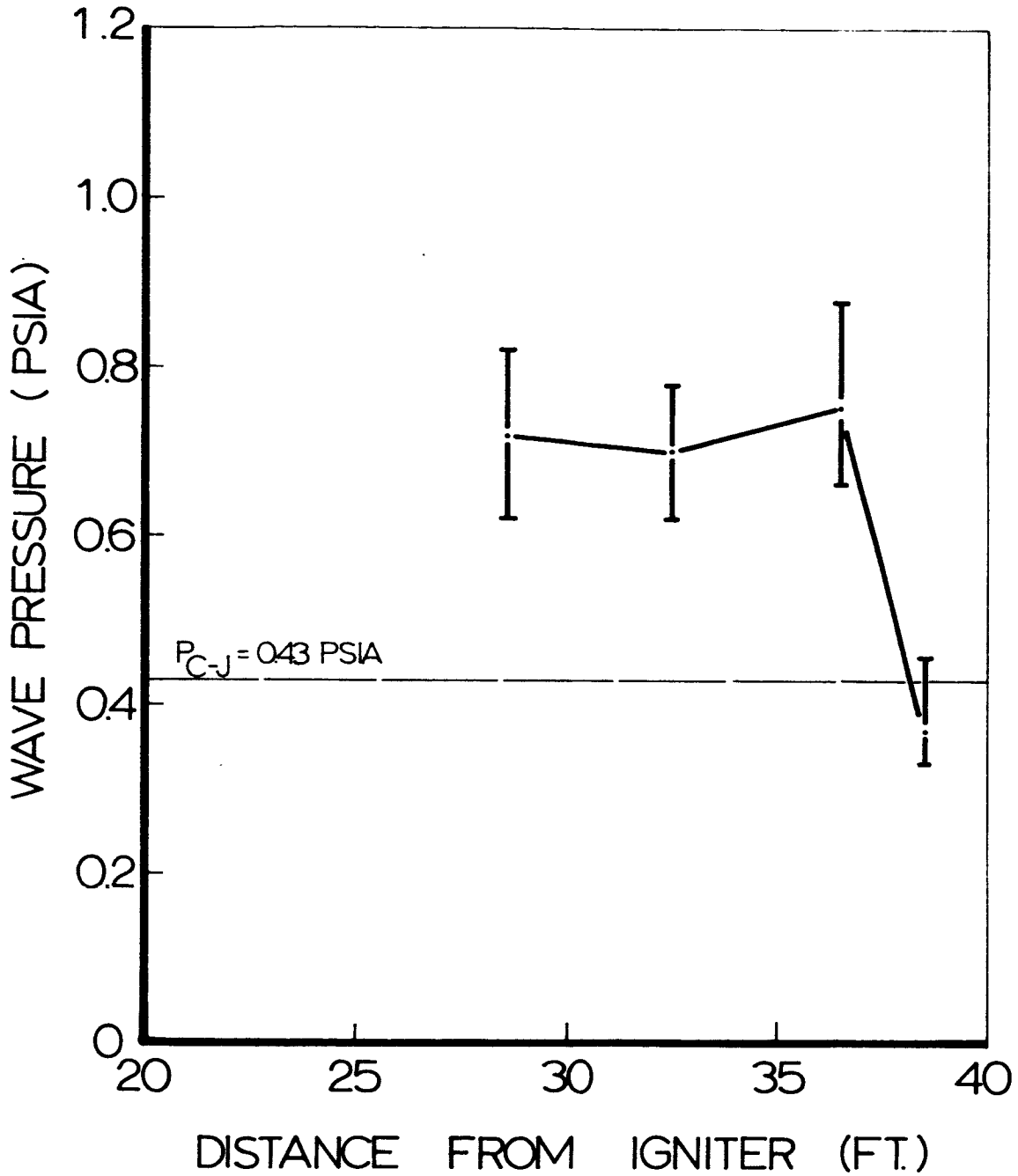

Fig. 89 Peak wave pressure as function of distance from Primacord ignitor in the 40 ft. vessel. H_2+O_2 composition, initial pressure 1.0 mmHg, initial temperature 70°F.

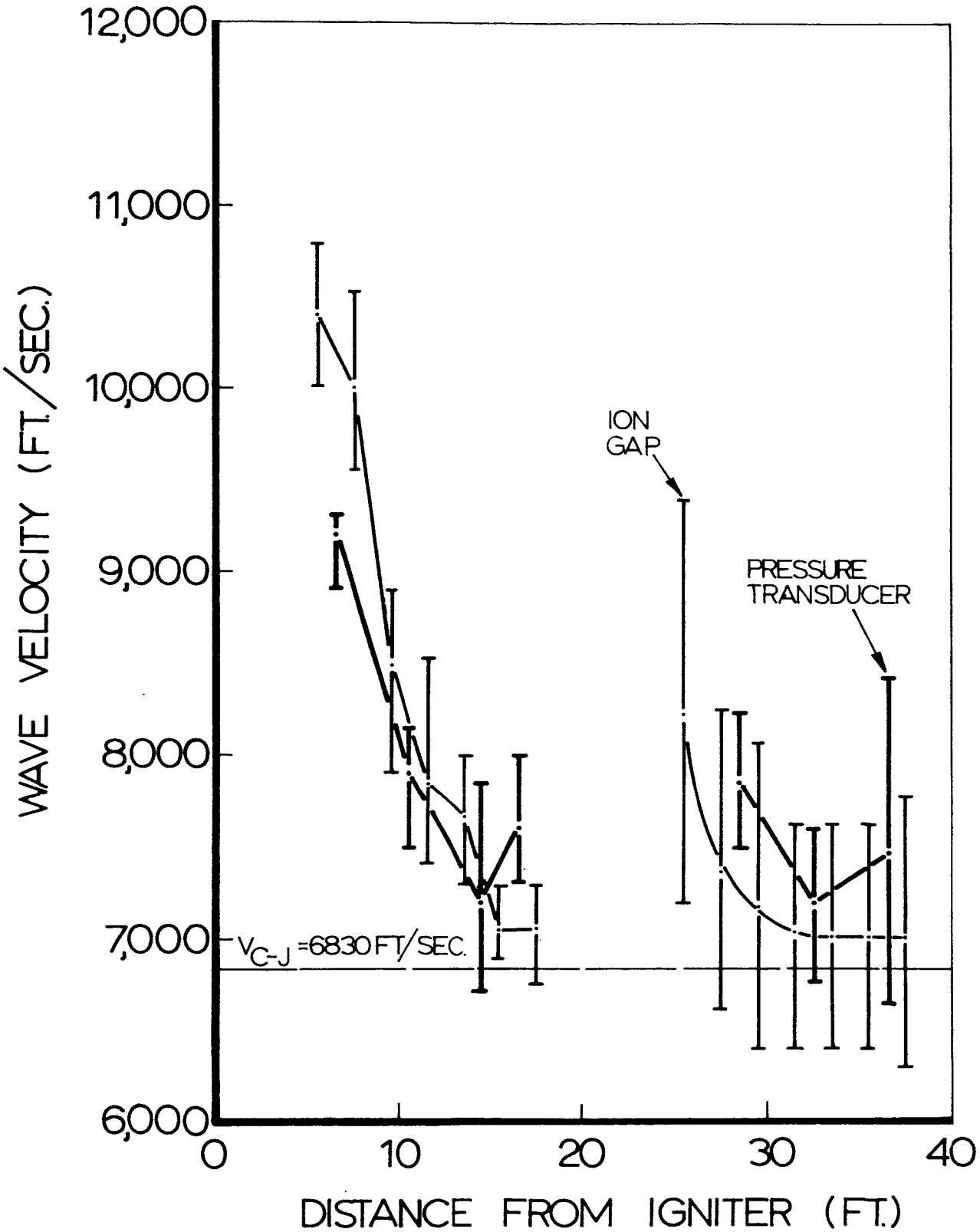

Fig. 90 Wave velocity as function of distance from Primacord ignitor in 40 ft. vessel. Data from 20 ft. vessel is also included. H_2+O_2 composition, initial pressure 1.0 mm Hg, initial temperature 70°F.

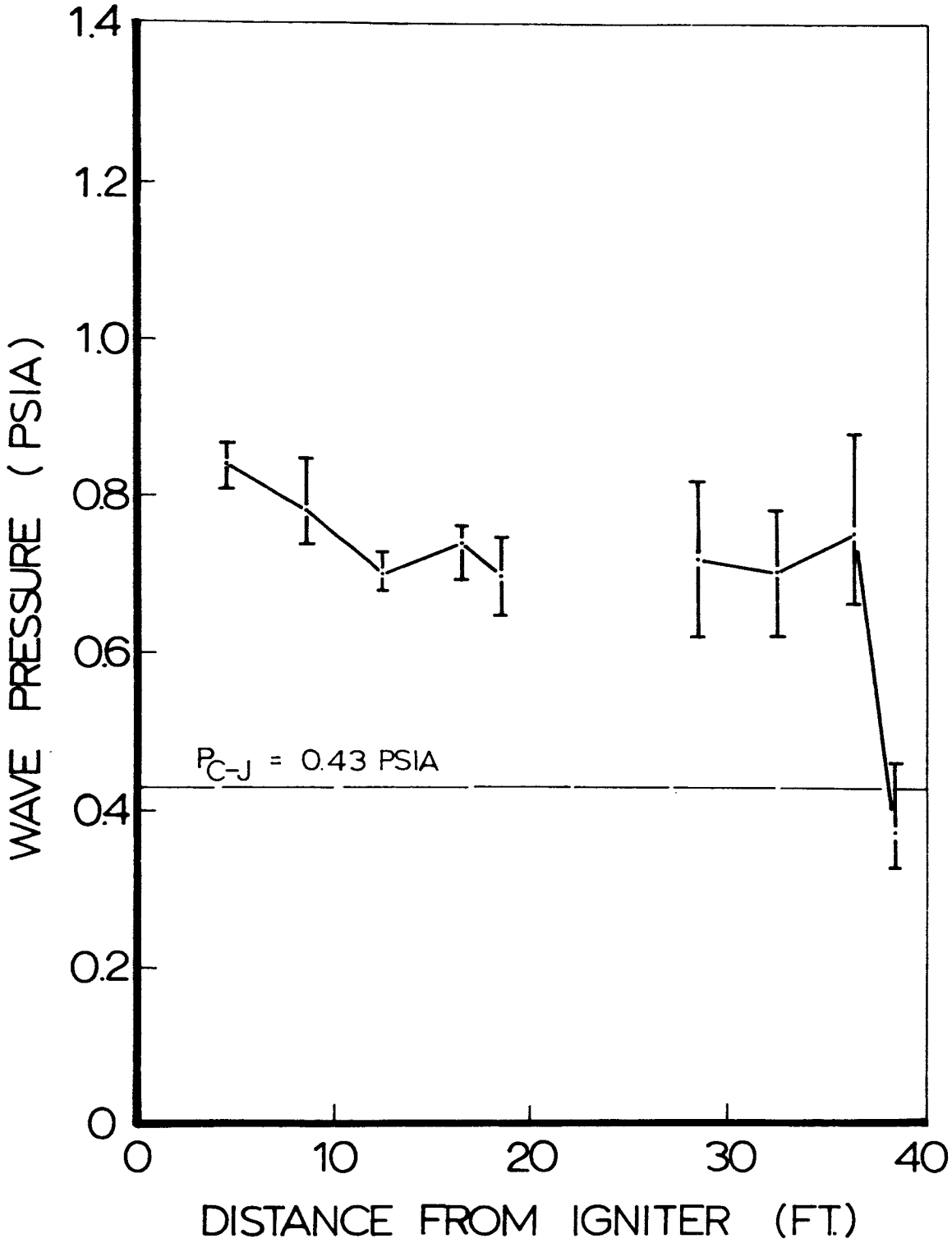

Fig. 91 Peak wave pressure as function of distance from Primacord ignitor in 40 ft. vessel. Data from 20 ft. vessel is also included. H_2+0_2 composition, initial pressure 1.0 mmHg, initial temperature 70°F.

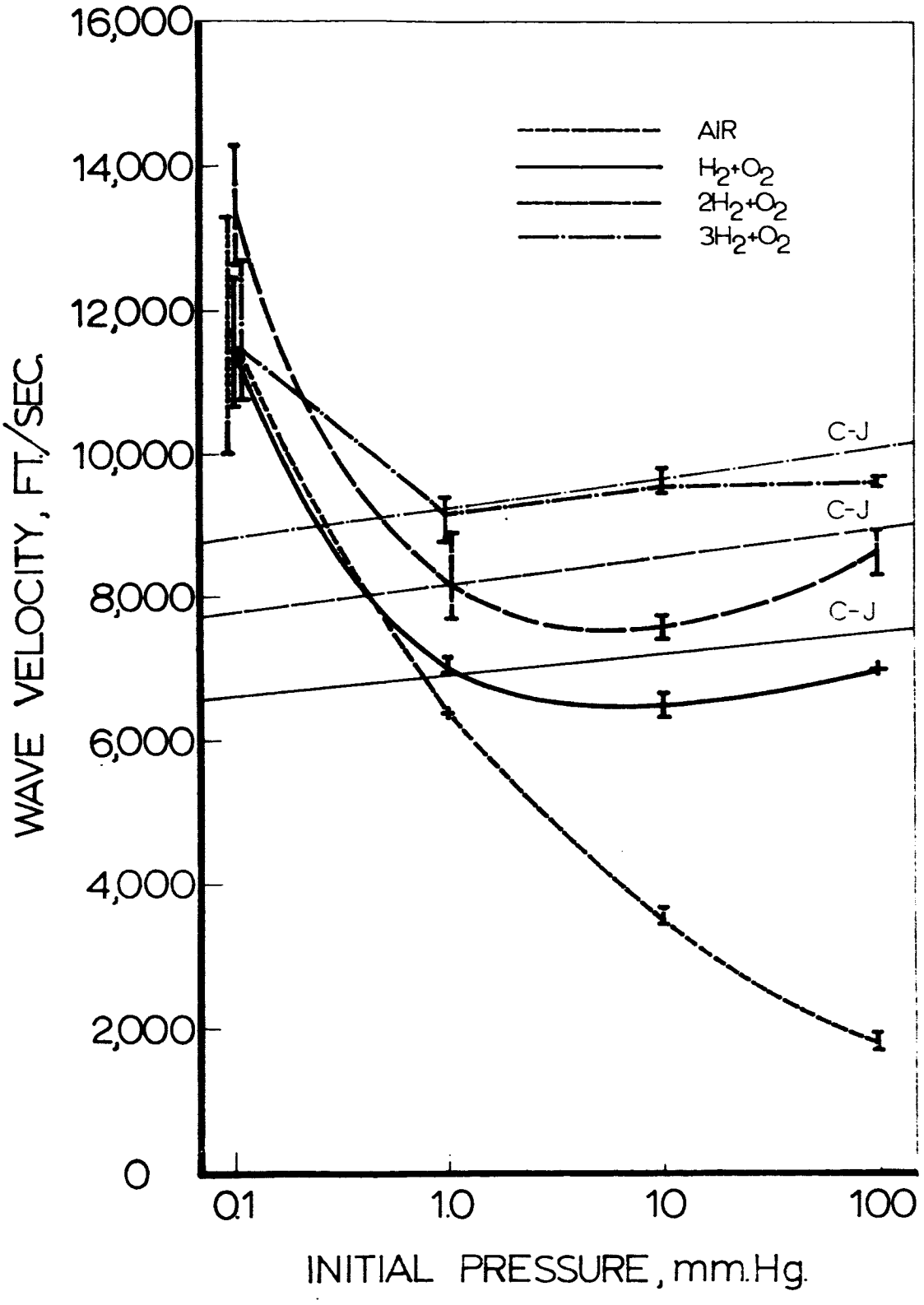

Fig. 92 Wave velocities measured at last position in Vessel CD, during room temperature tests, versus initial pressure. Theoretical C-J velocities shown from comparison.

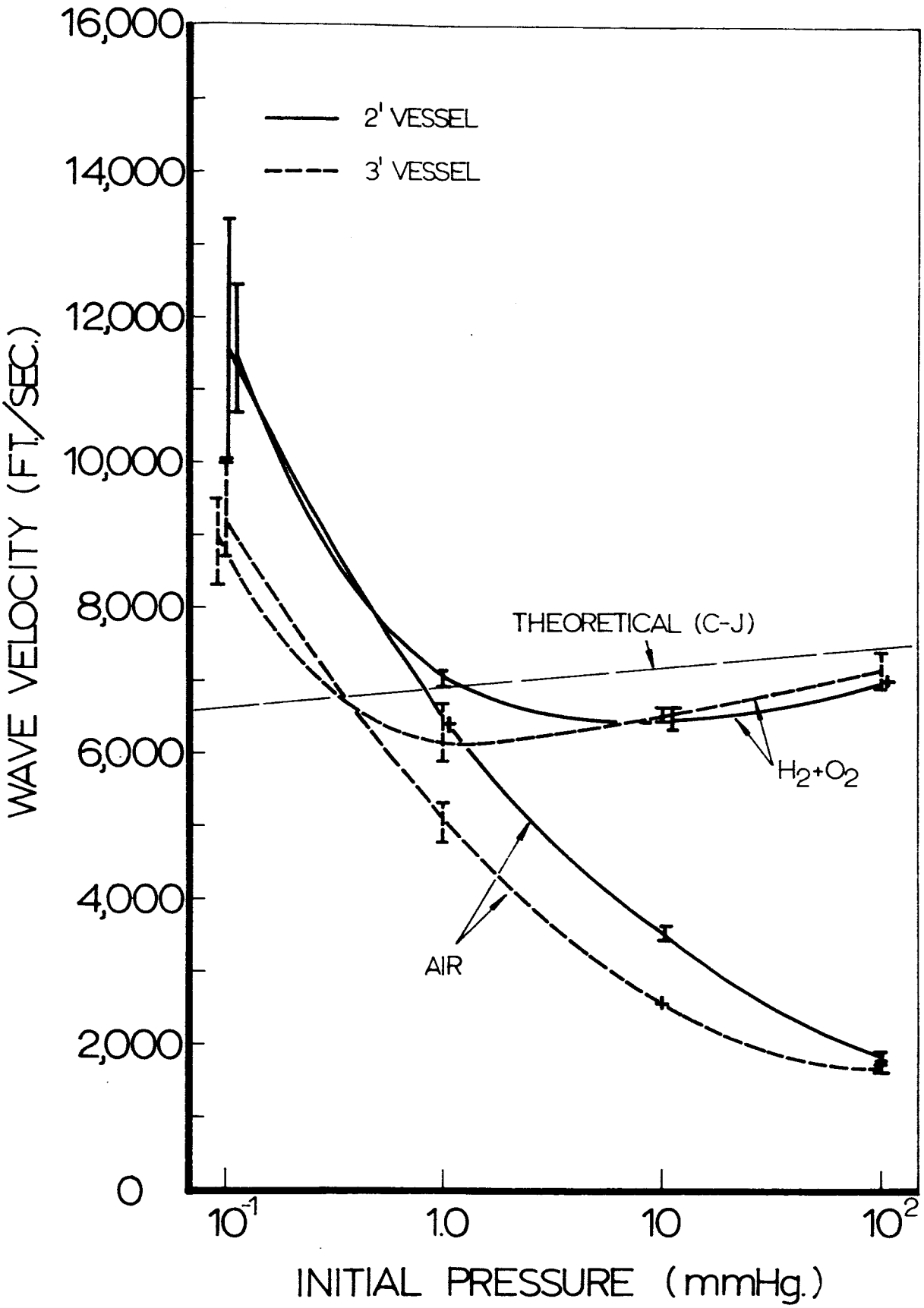

Fig. 93 Wave velocities measured at last position in vessels A and CD, for H_2+O_2 mixtures and air during room temperature tests, versus initial pressure. Theoretical C-J velocities shown for comparison.

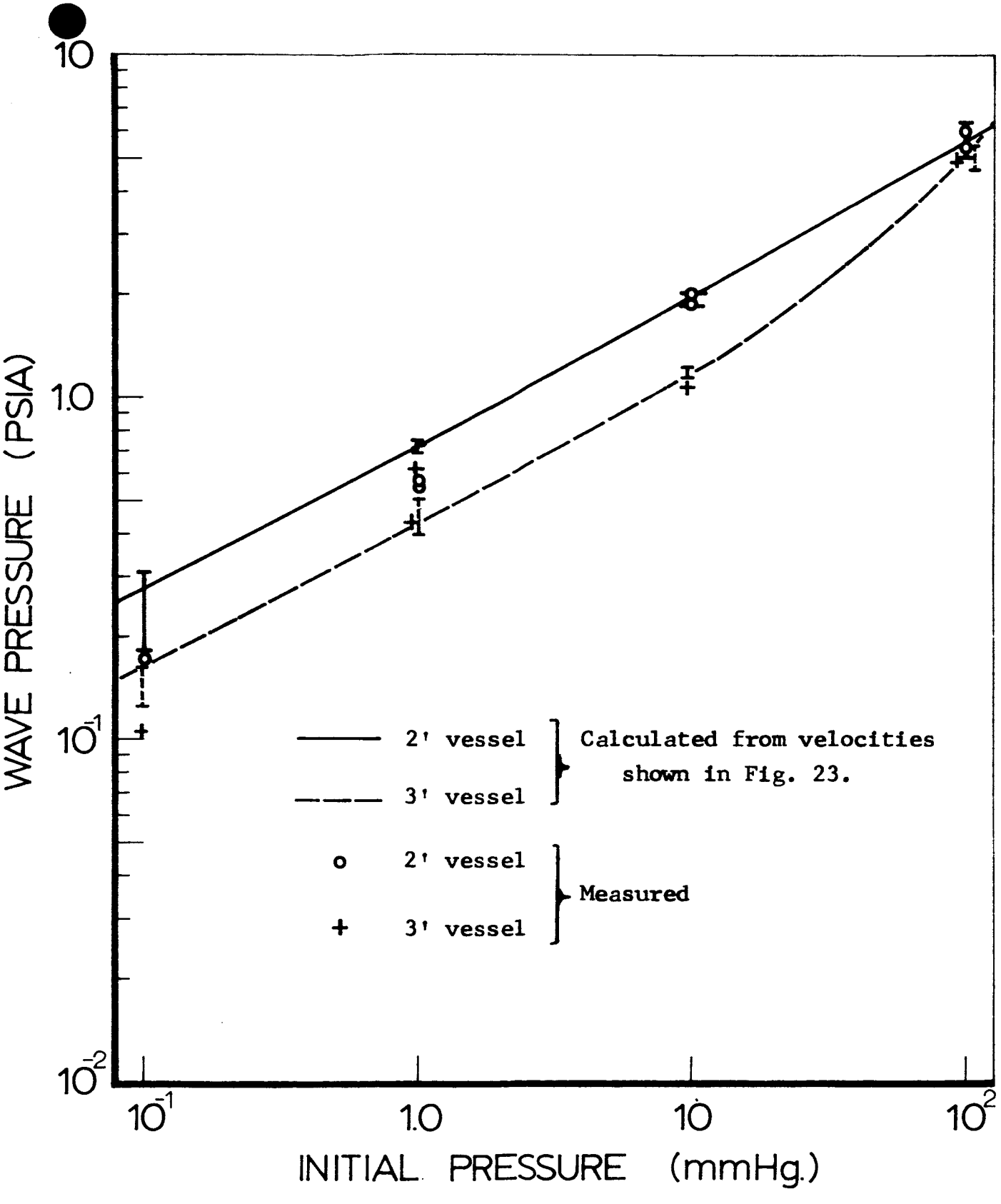

Fig. 94 Peak incident pressure at last position in Vessels A and CD as a function of initial pressure for air at room temperature.

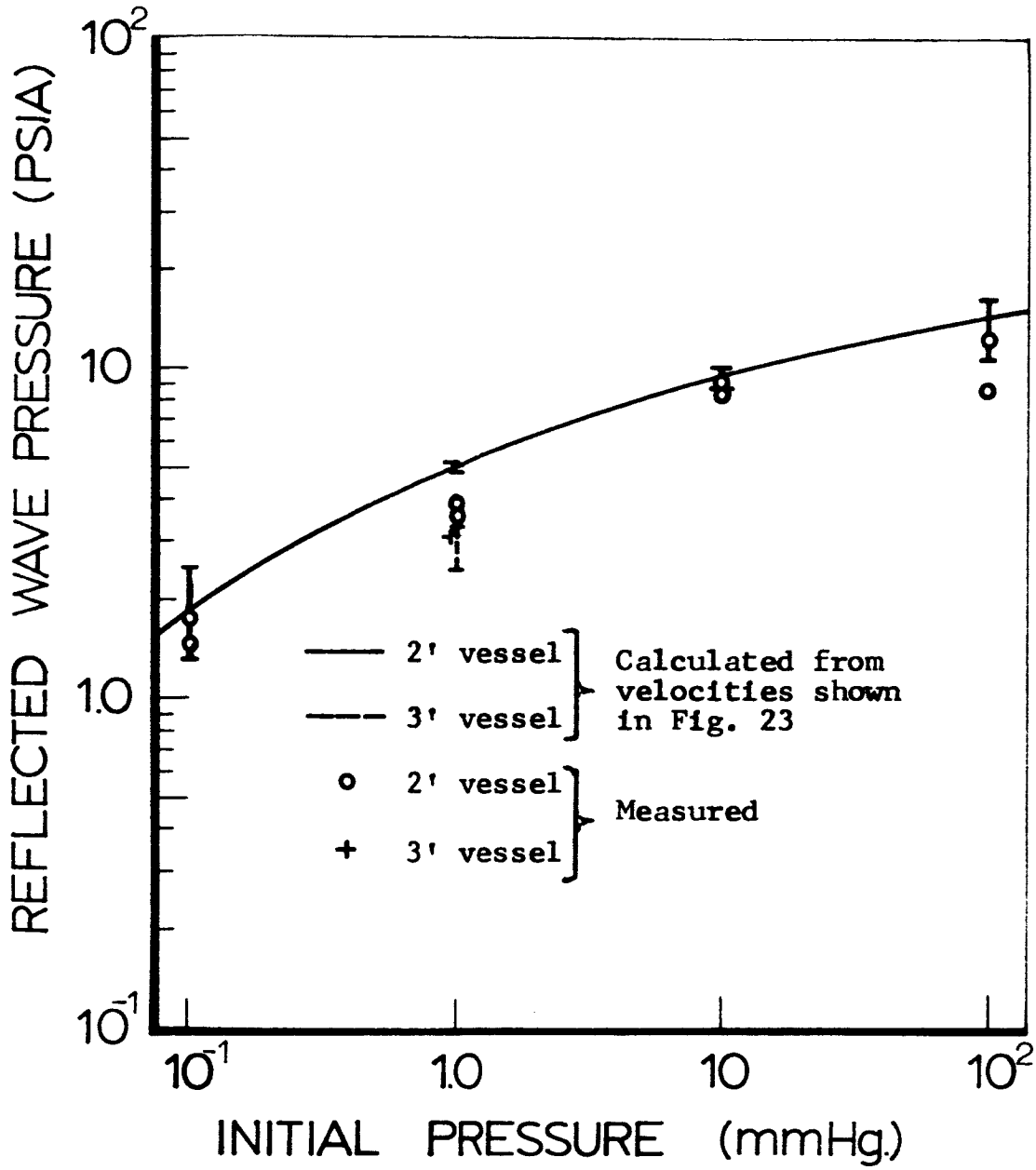

Fig. 95 Reflected pressure in Vessels A anc CD as a function of initial pressure for air at room temperature.

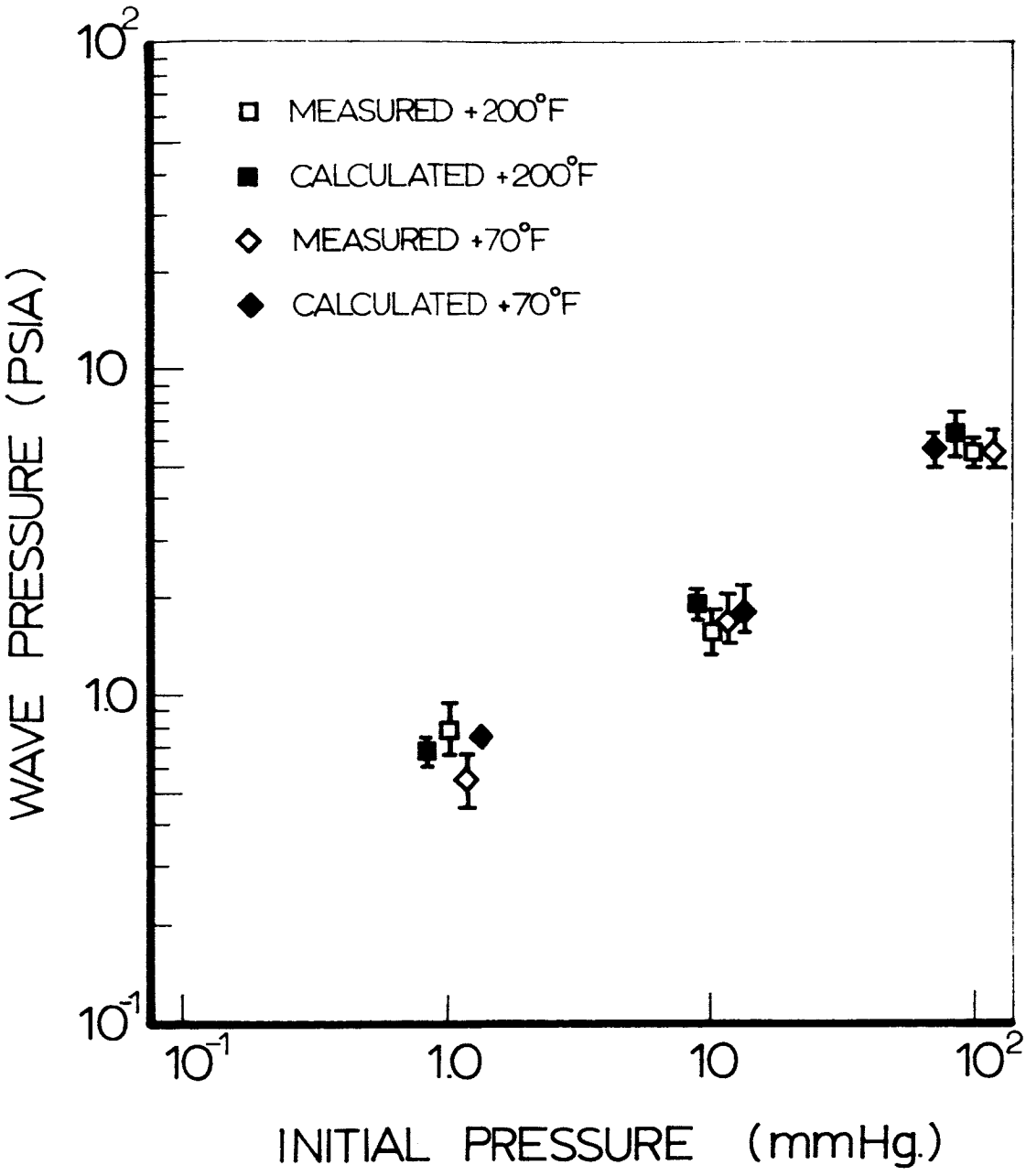

Fig. 96 Peak incident pressure at last position in Vessel CD as a function of initial pressure for air at +200 and +70°F.

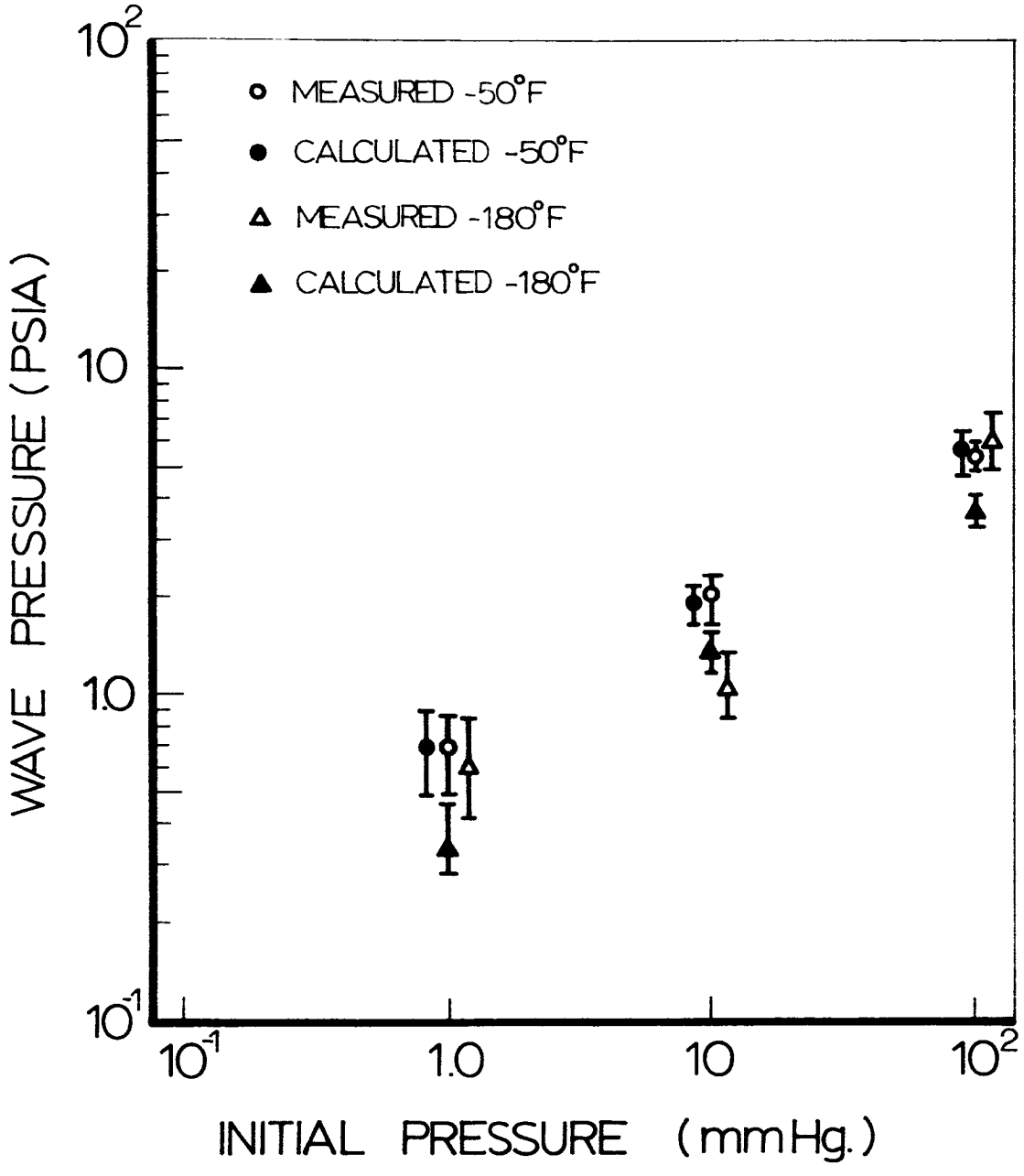

Fig. 97 Peak incident pressure at last position in Vessel CD as a function of initial pressure for air at -50 and -180°F.

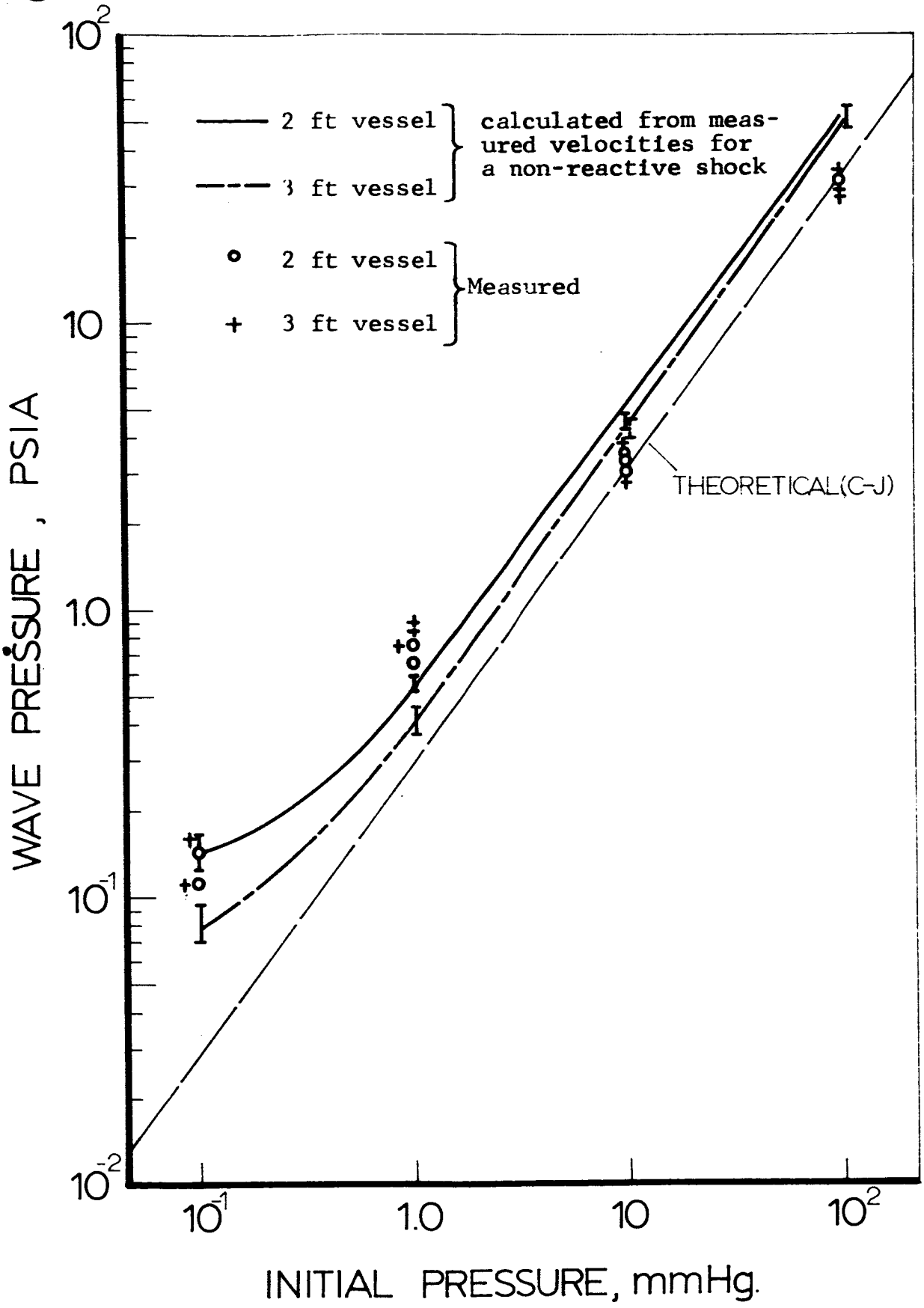

Fig. 98 Peak incident pressure at last position in Vessels A and CD as a function of initial pressure for H_2+O_2 mixture at room temperature.

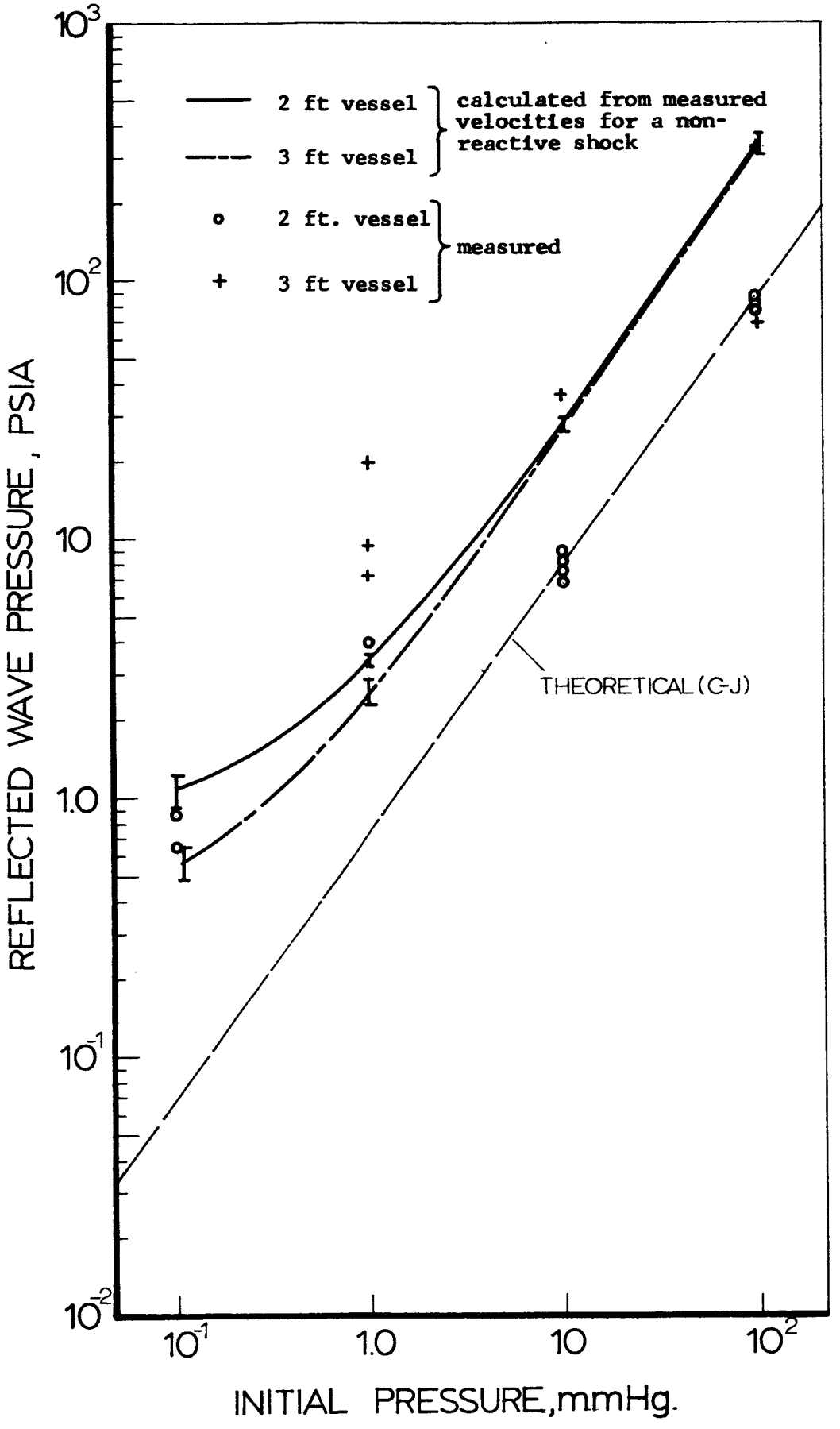

Fig. 99 Reflected wave pressure at last position in Vessels A and CD as a function of initial pressure for H_2+O_2 mixture at room temperature.

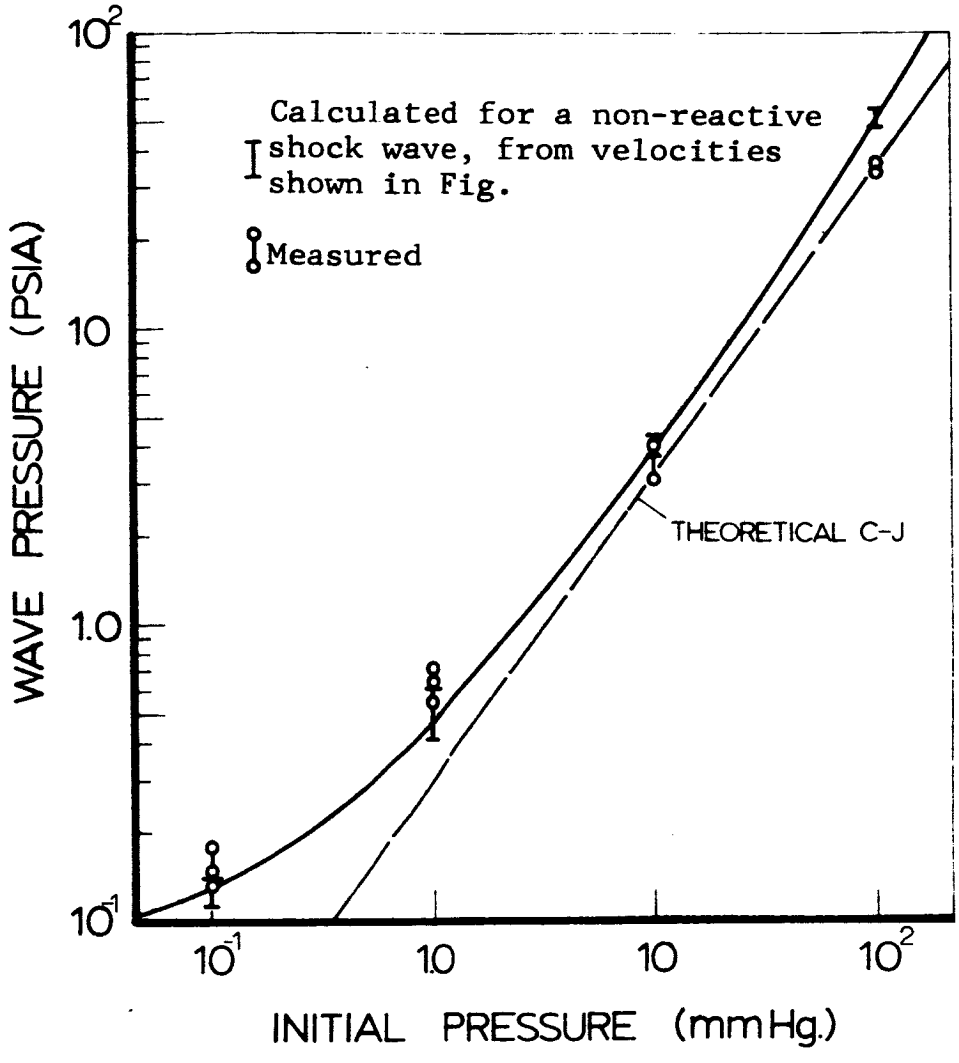

Fig. 100 Peak incident pressure at last position in Vessels A and CD as a function of initial pressure for $2H_2+0_2$ mixture at room temperature.

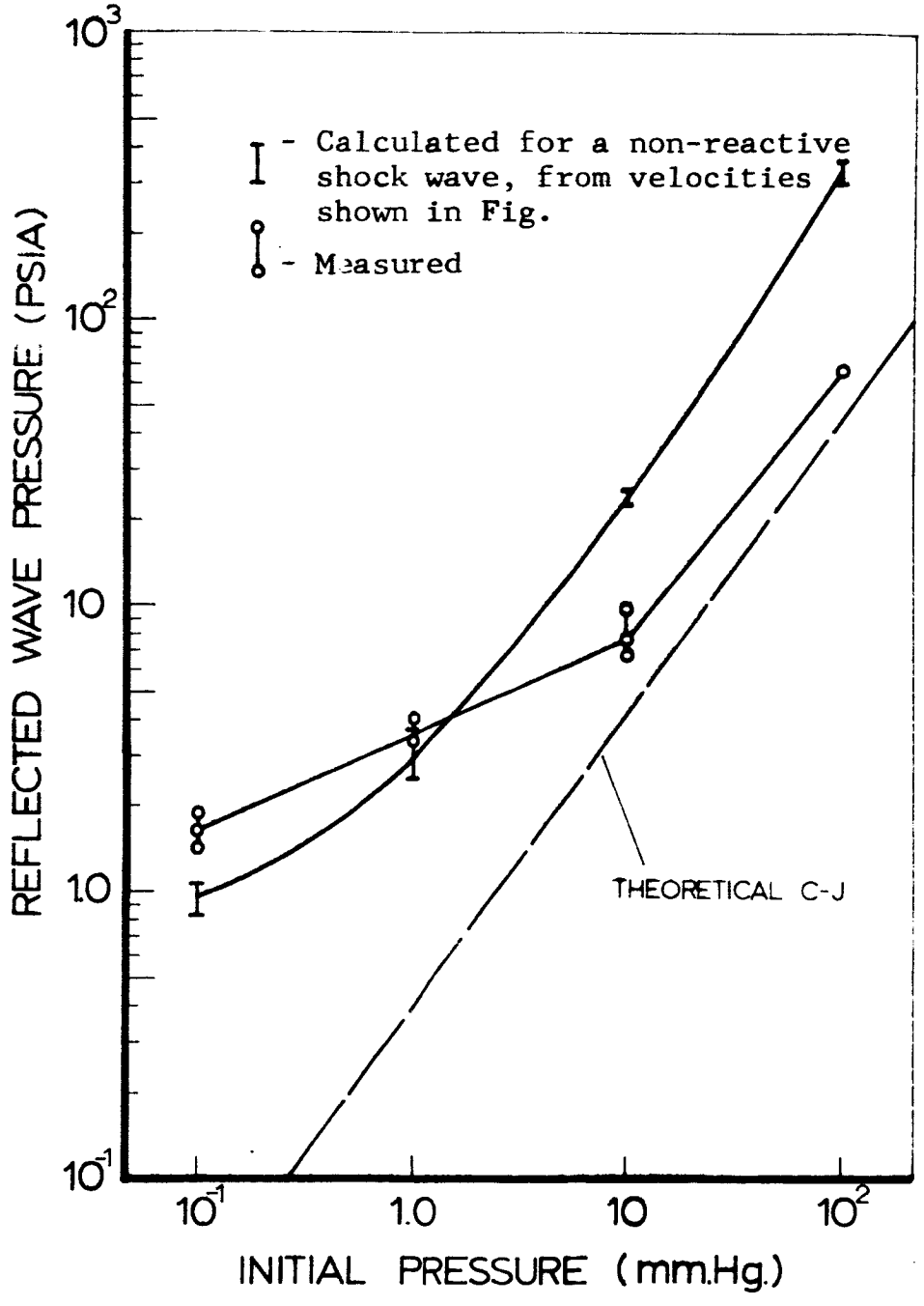

Fig. 101 Reflected wave pressure at last position in Vessels A and CD as a function of initial pressure for $2H_2+0_2$ mixture at room temperature.

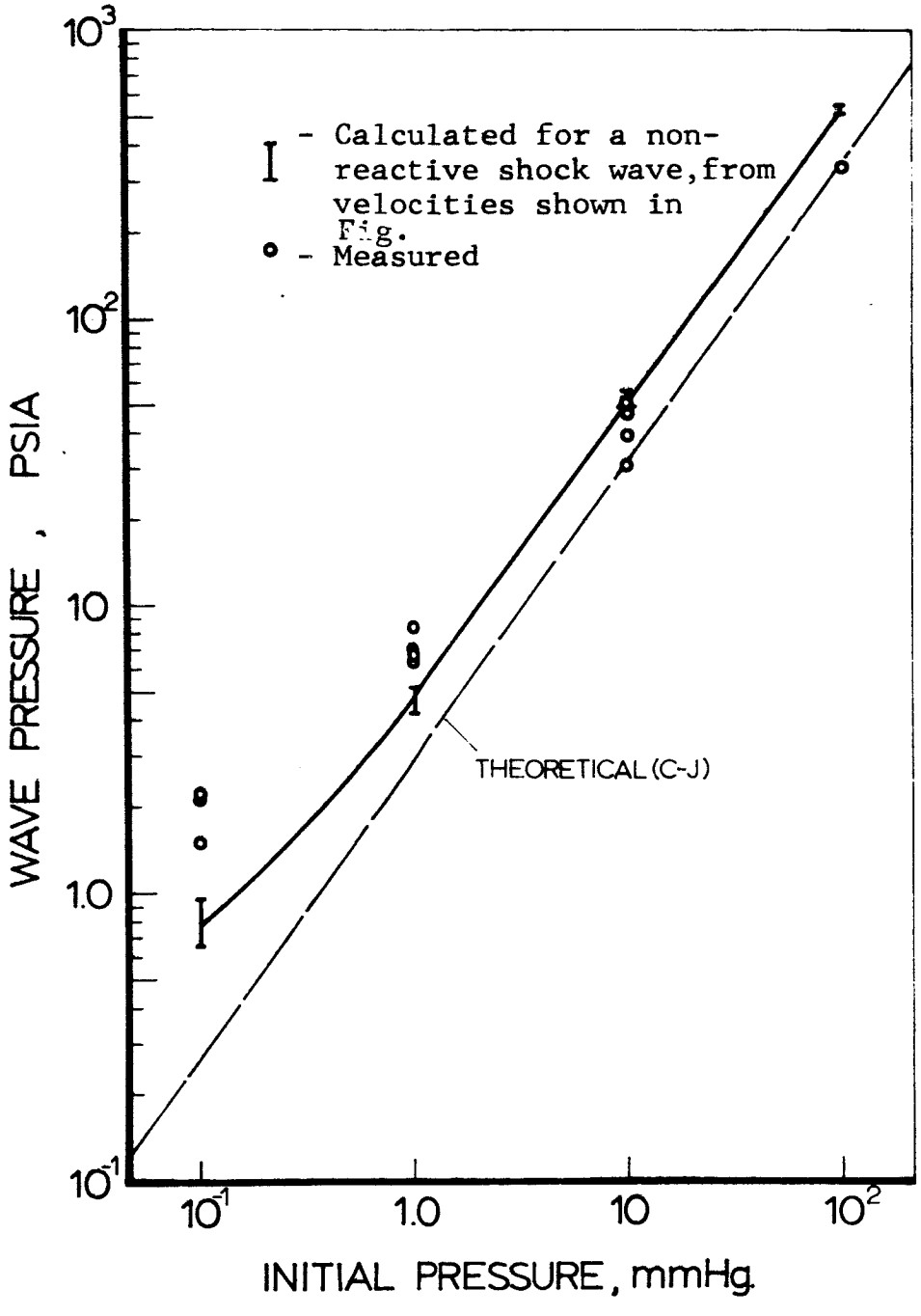

Fig. 102 Peak incident pressure at last position in Vessels A and CD as a function of initial pressure for $3H_2+O_2$ mixture at room temperature.

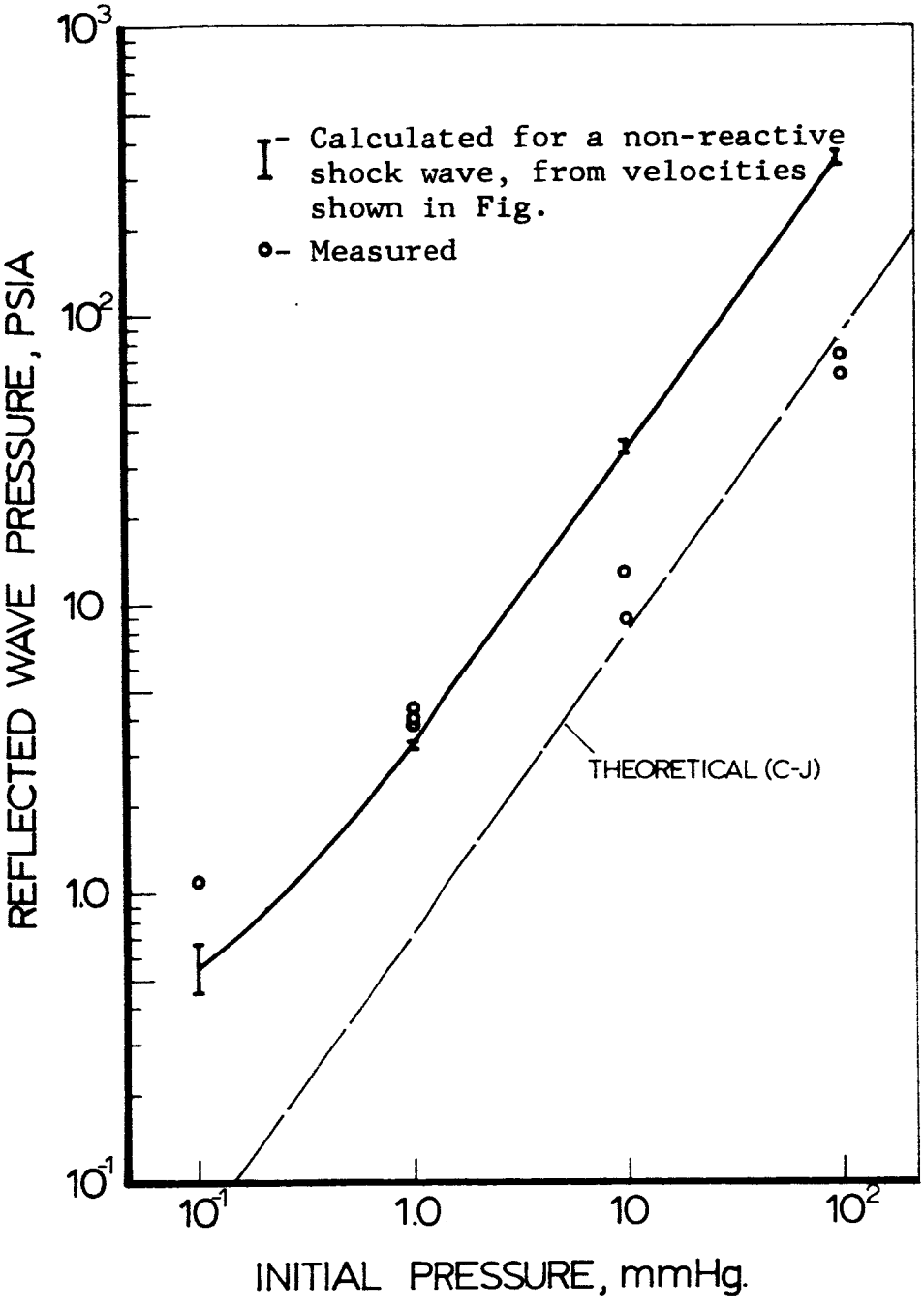

Fig. 103 Reflected wave pressure at last position in Vessels A and CD as a function of initial pressure for $3H_2+0_2$ mixture at room temperature.

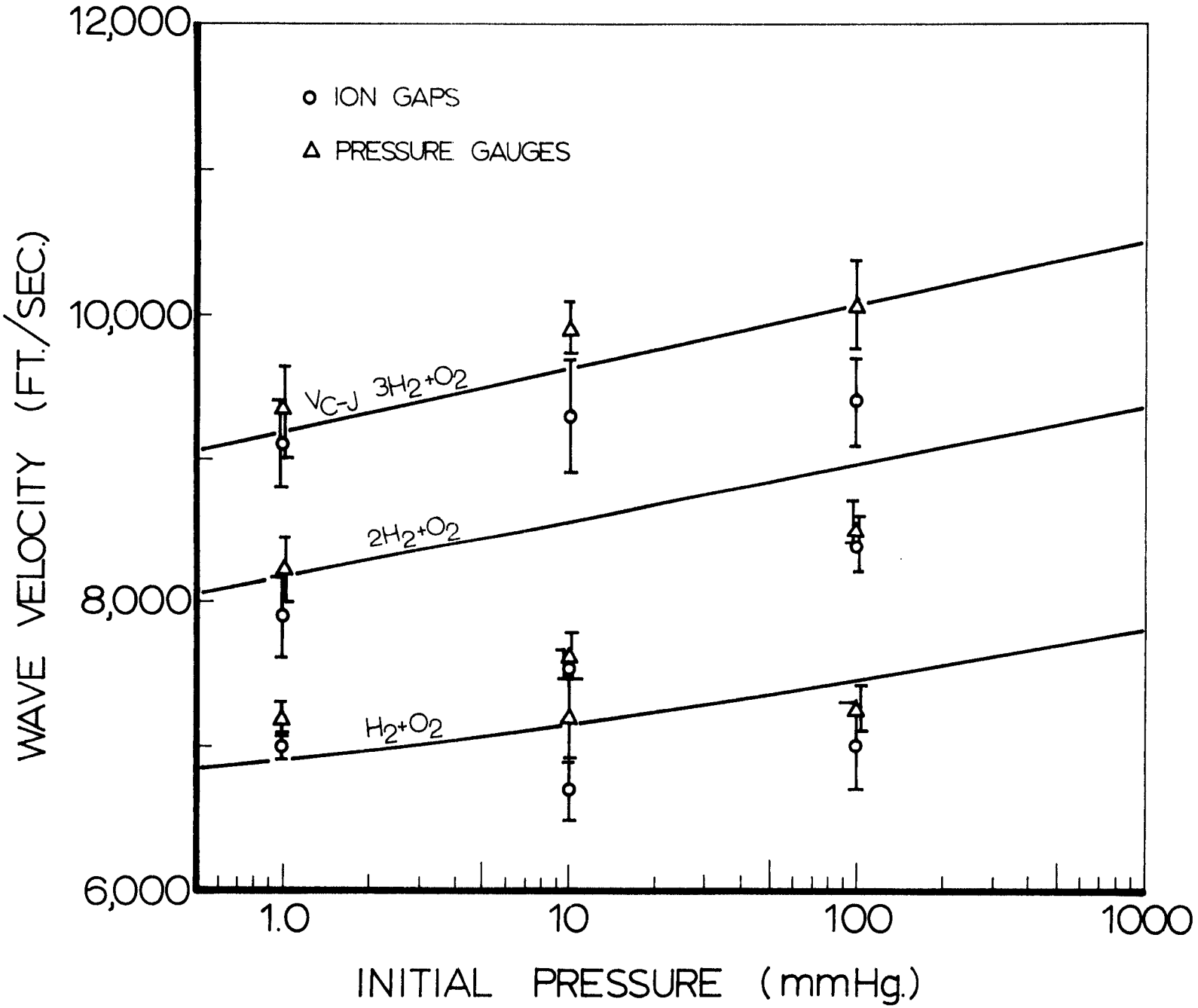

Fig. 104 Wave velocity measured at last position in Vessel CD versus initial pressure for hydrogen-oxygen mixtures at room temperature

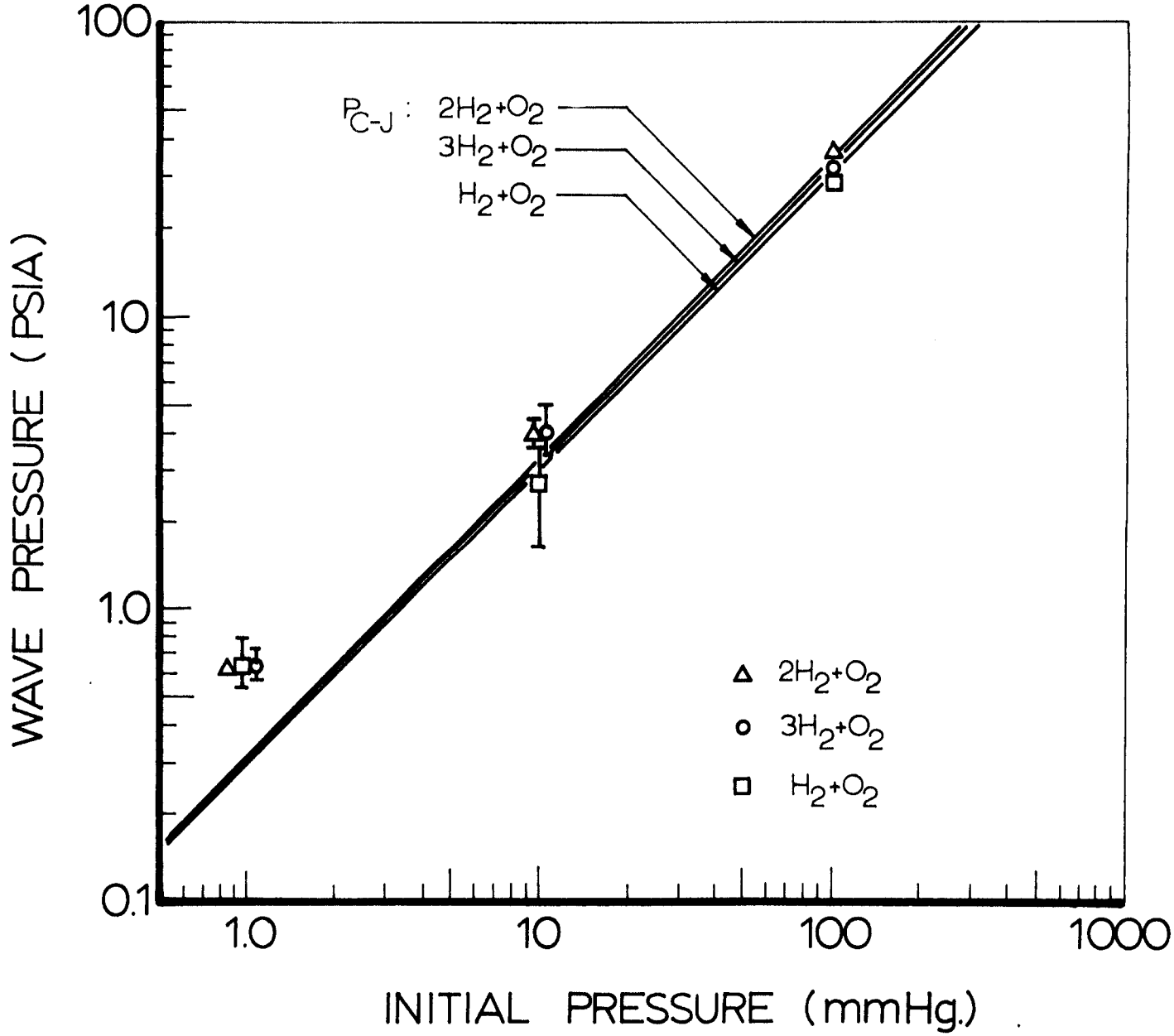

Fig. 105 Peak incident pressure at last position in Vessel CD versus initial pressure for hydrogen-oxygen mixtures at room temperature.

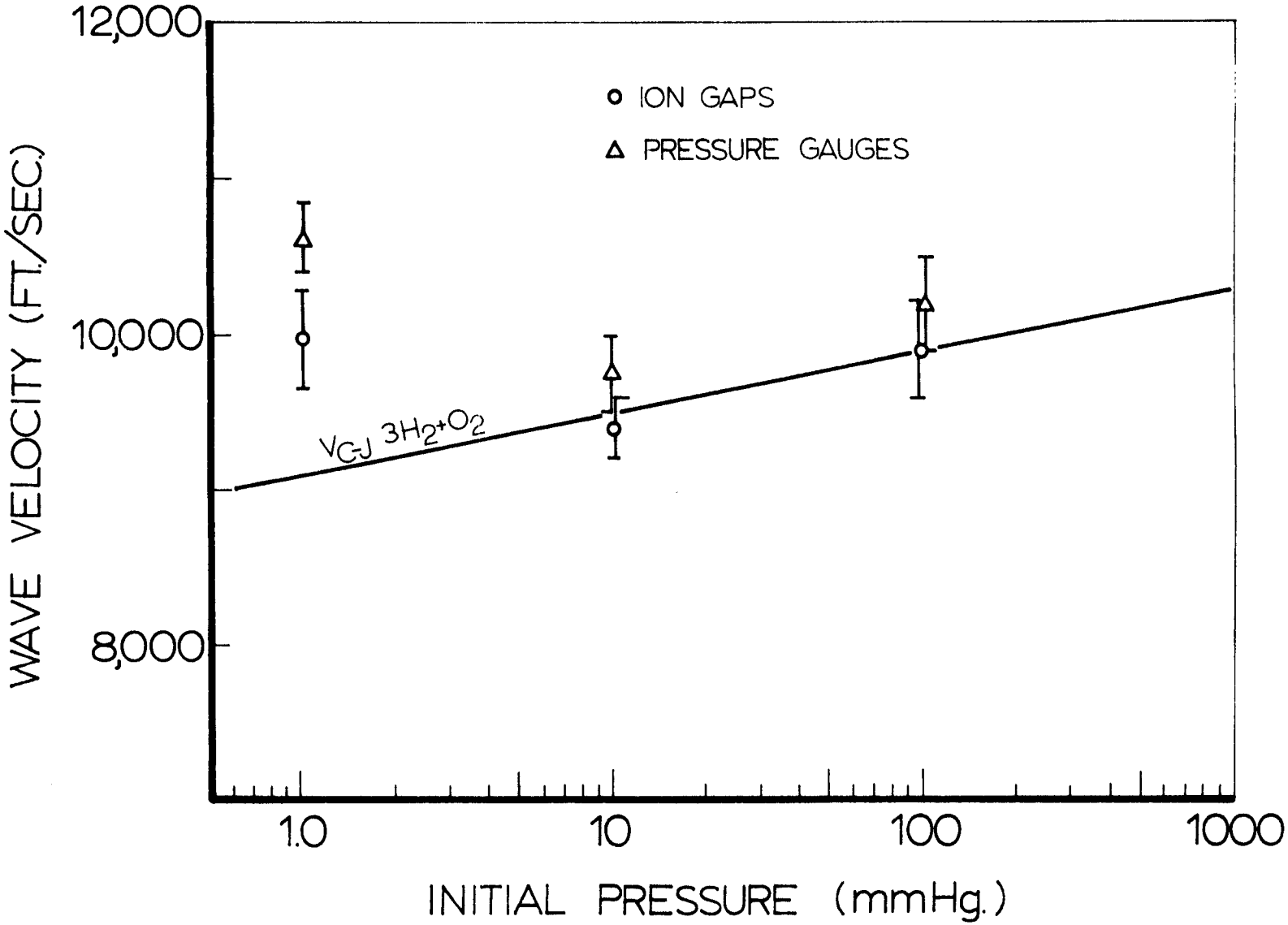

Fig. 106 Wave velocity measured at last position in Vessel CD versus initial pressure for $3H_2+O_2$ mixtures at +200 °F.

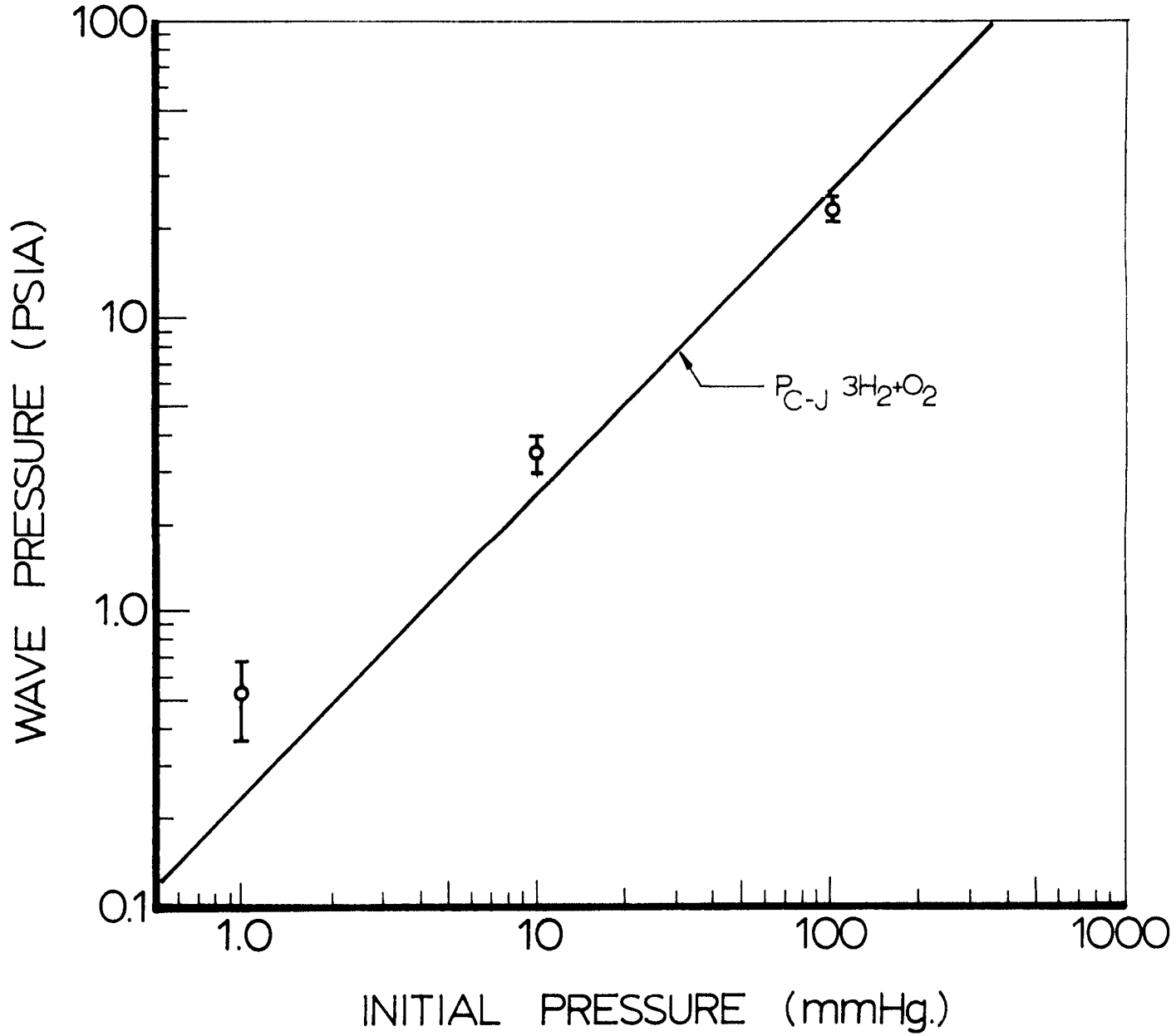

Fig. 107 Peak incident pressure at last position in Vessel CD versus initial pressure for $3H_2$ O_2 mixtures at +200 °F.

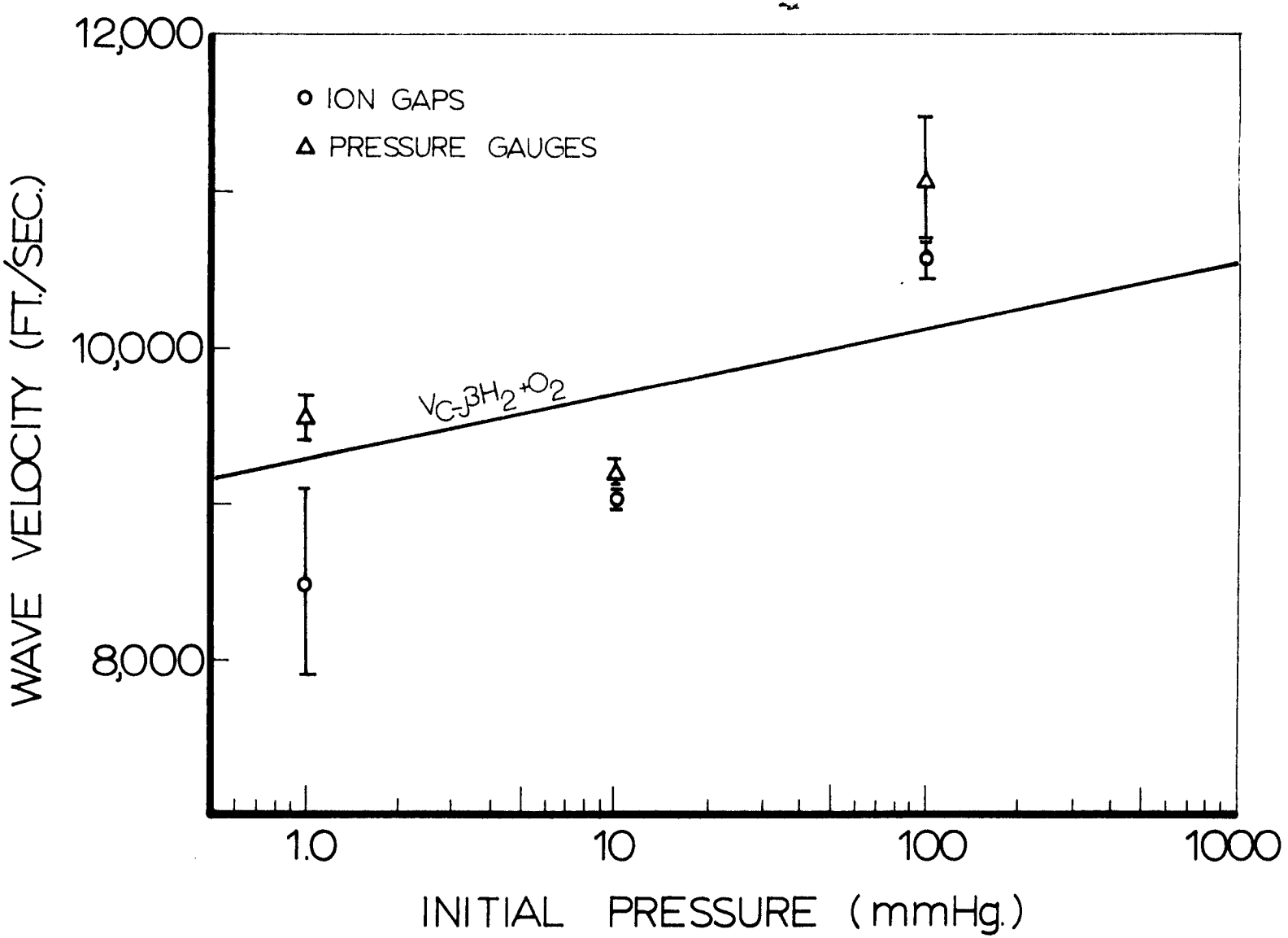

Fig. 108 Wave velocity measured at last position in Vessel CD versus initial pressure for $3H_2+O_2$ mixtures at -50°F.

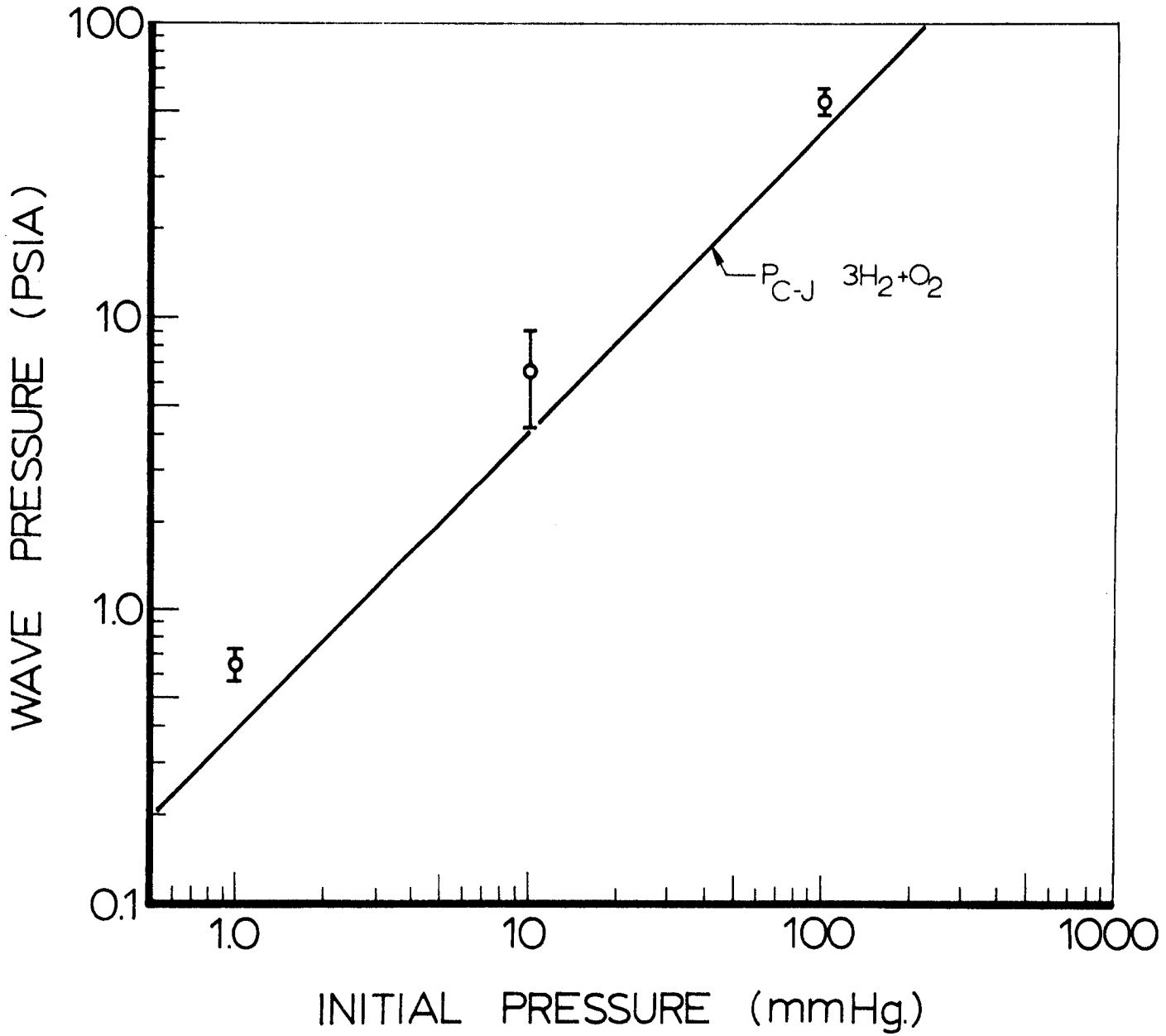

Fig. 109 Peak incident pressure at last position in Vessel CD versus initial pressure for $3H_2+O_2$ mixtures at -50°F.

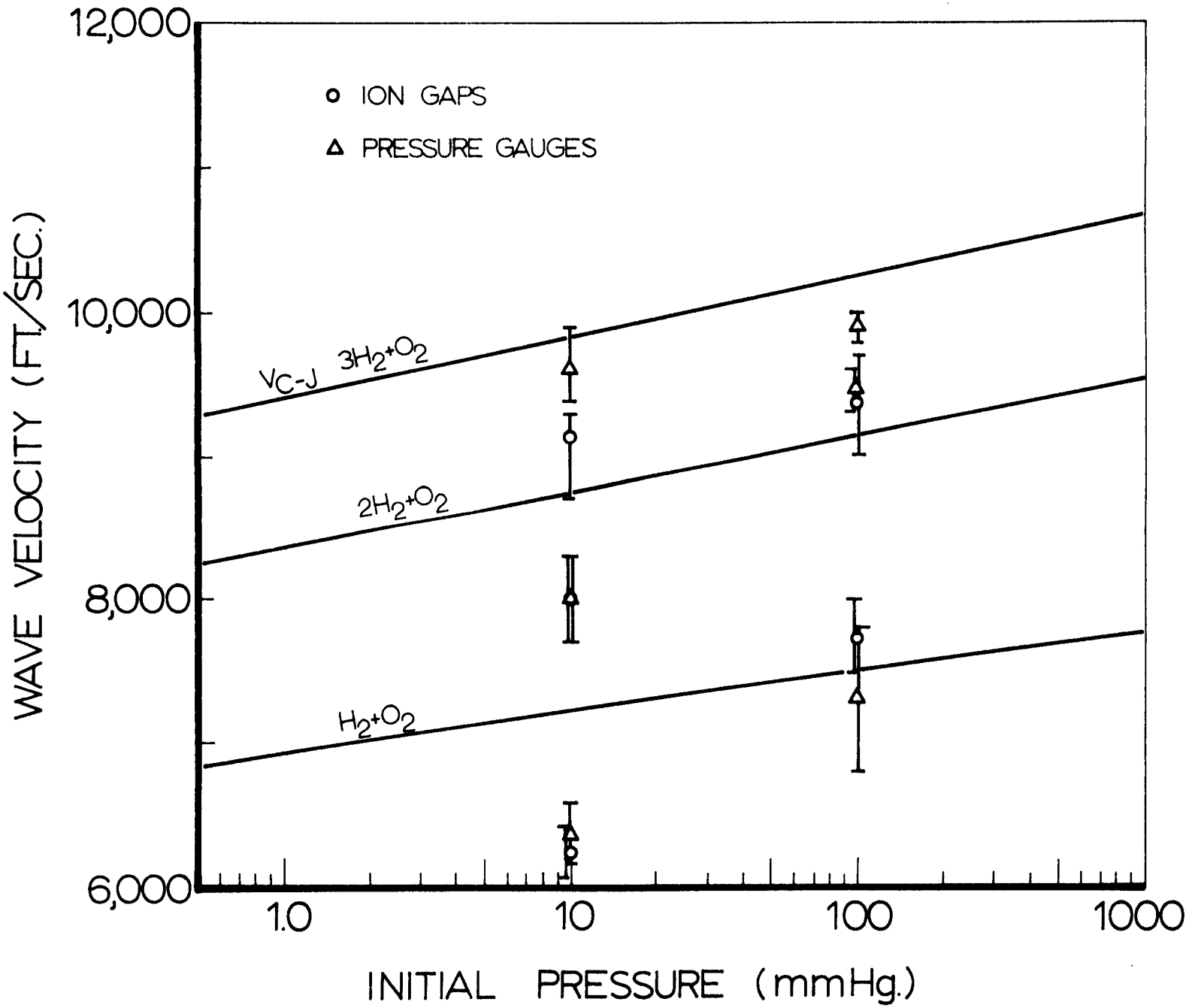

Fig. 110 Wave velocity measured at last position in Vessel CD versus initial pressure for hydrogen-oxygen mixtures at -180°F.

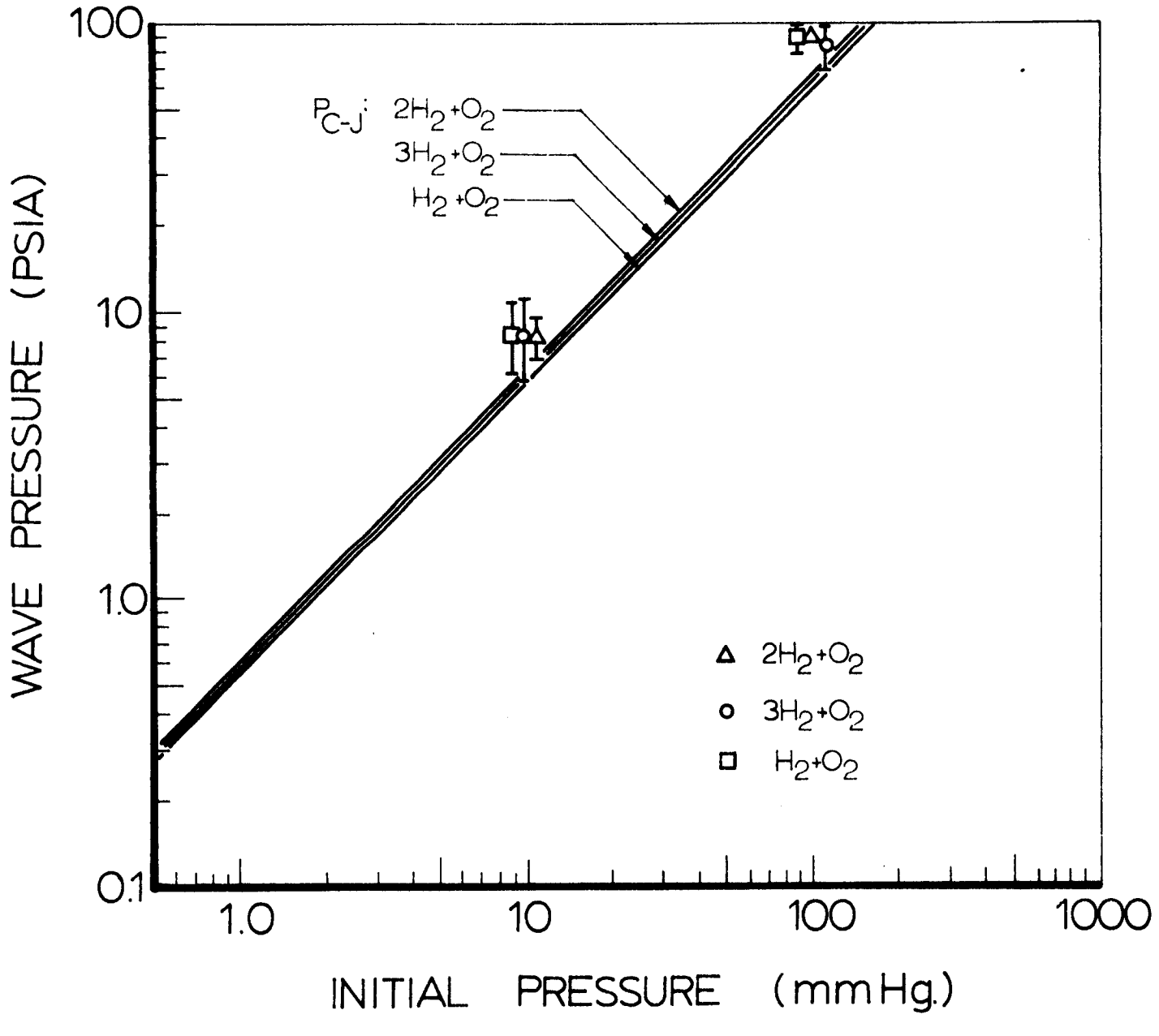

Fig. 111 Peak incident pressure at last position in Vessel CD versus initial pressure for hydrogen-oxygen mixtures at -180°F.

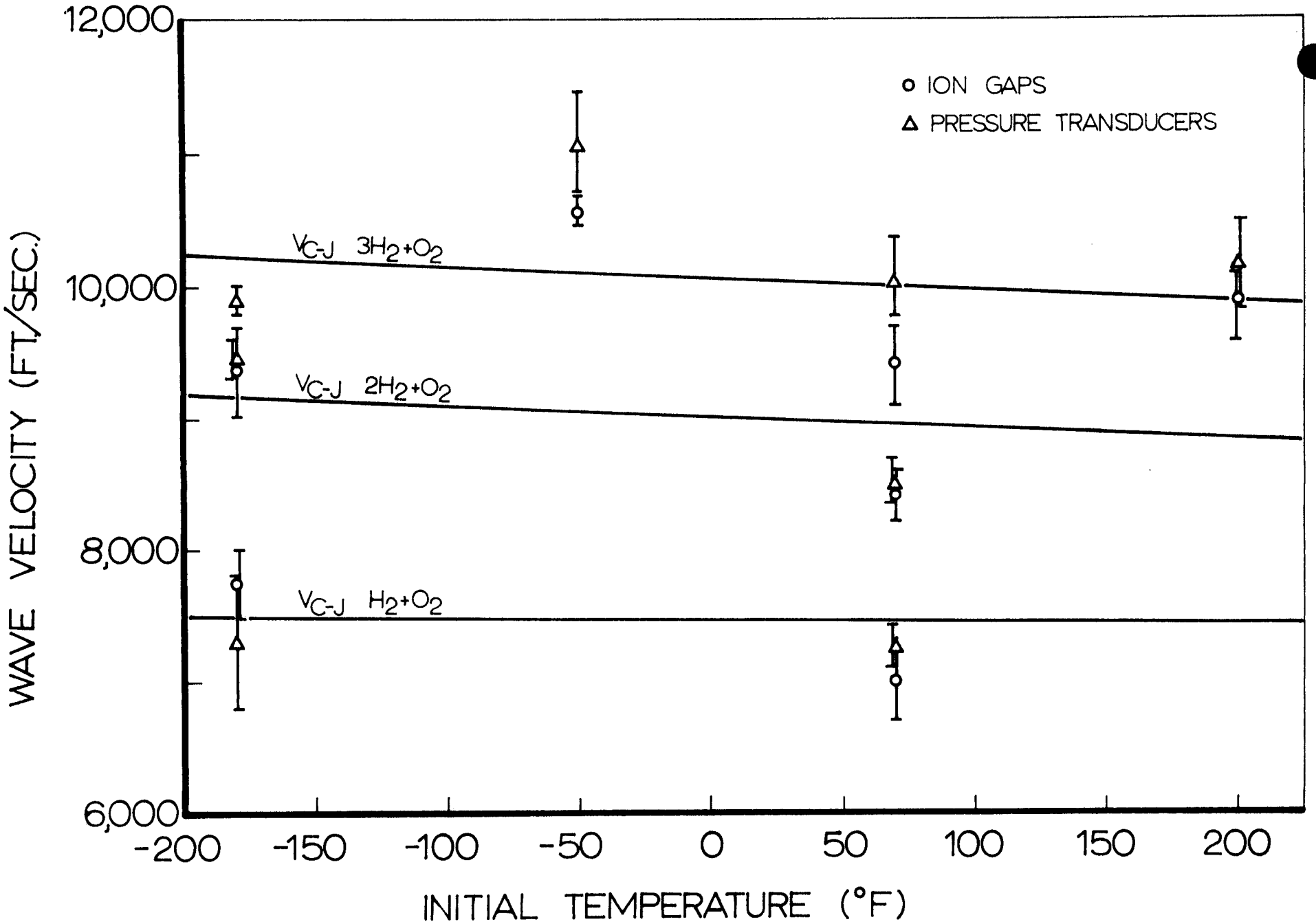

Fig. 112 Wave velocity measured at last position in Vessel CD for hydrogen-oxygen mixtures initially at 100 mmHg versus initial temperature.

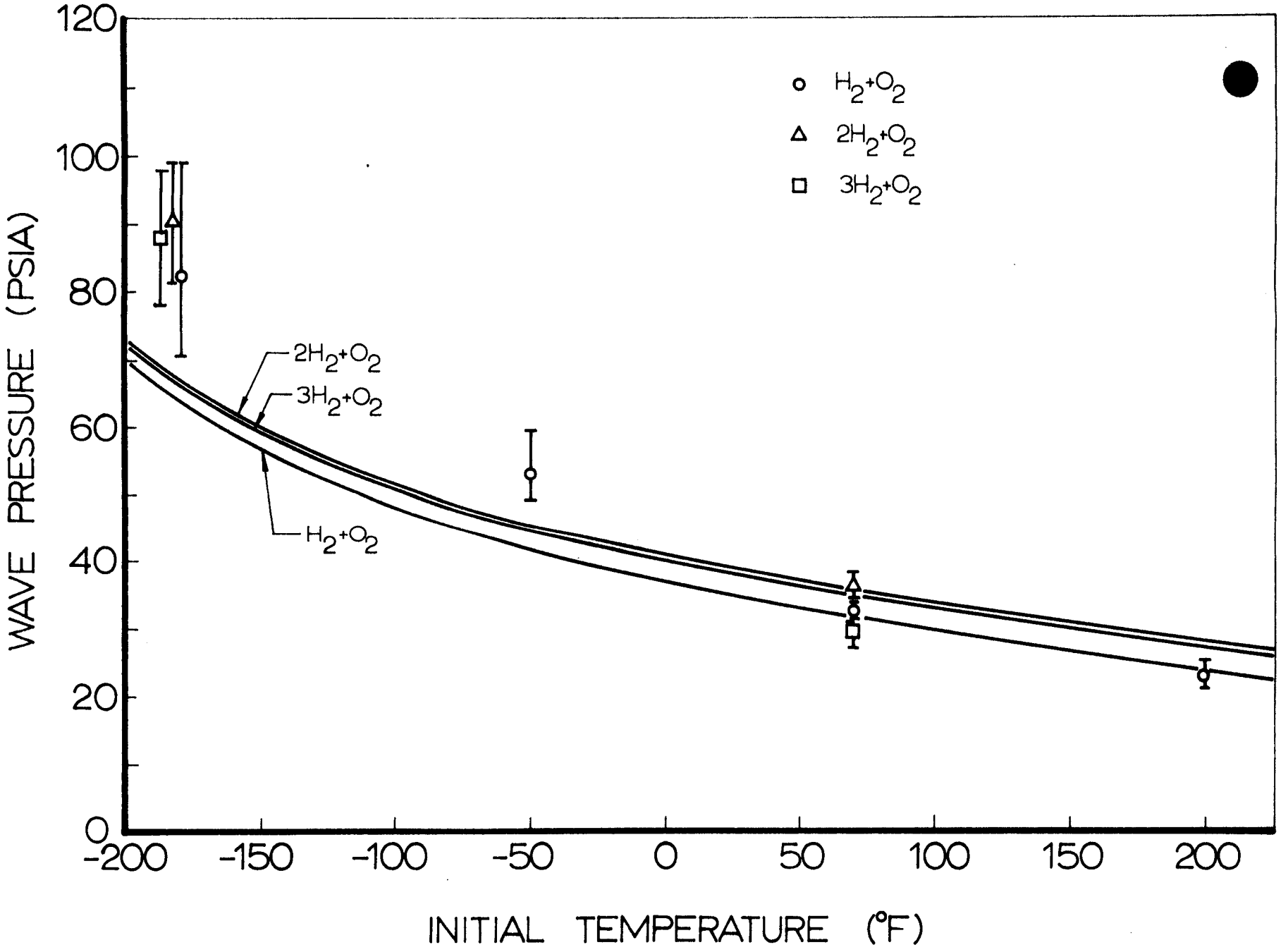

Fig. 113 Peak incident pressure measured at last position in Vessel CD for hydrogen-oxygen mixtures initially at 100 mmHg versus initial temperature.

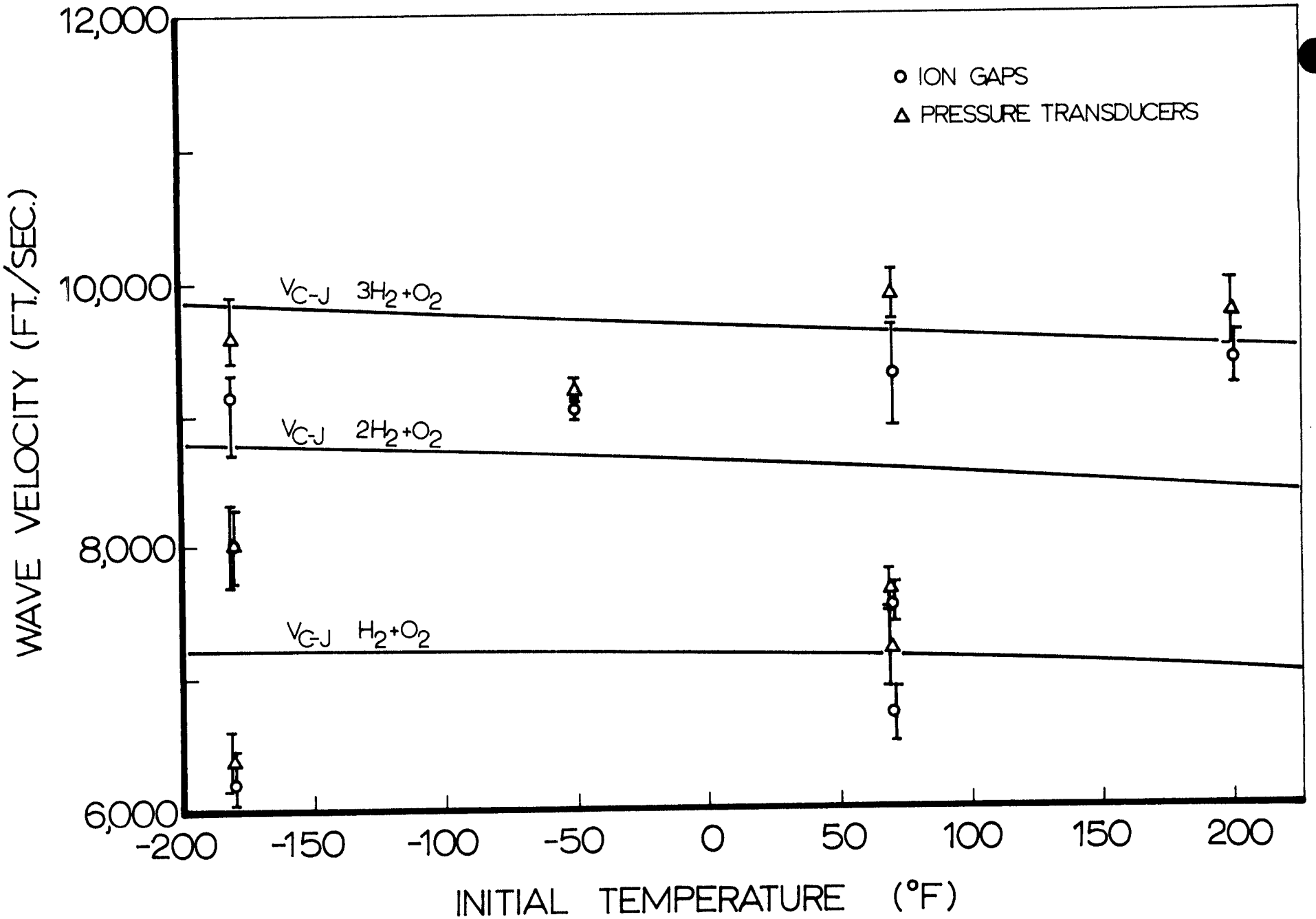

Fig. 114 Wave velocity measured at last position in Vessel CD for hydrogen-oxygen mixtures initially at 10 mmHg versus initial temperature.

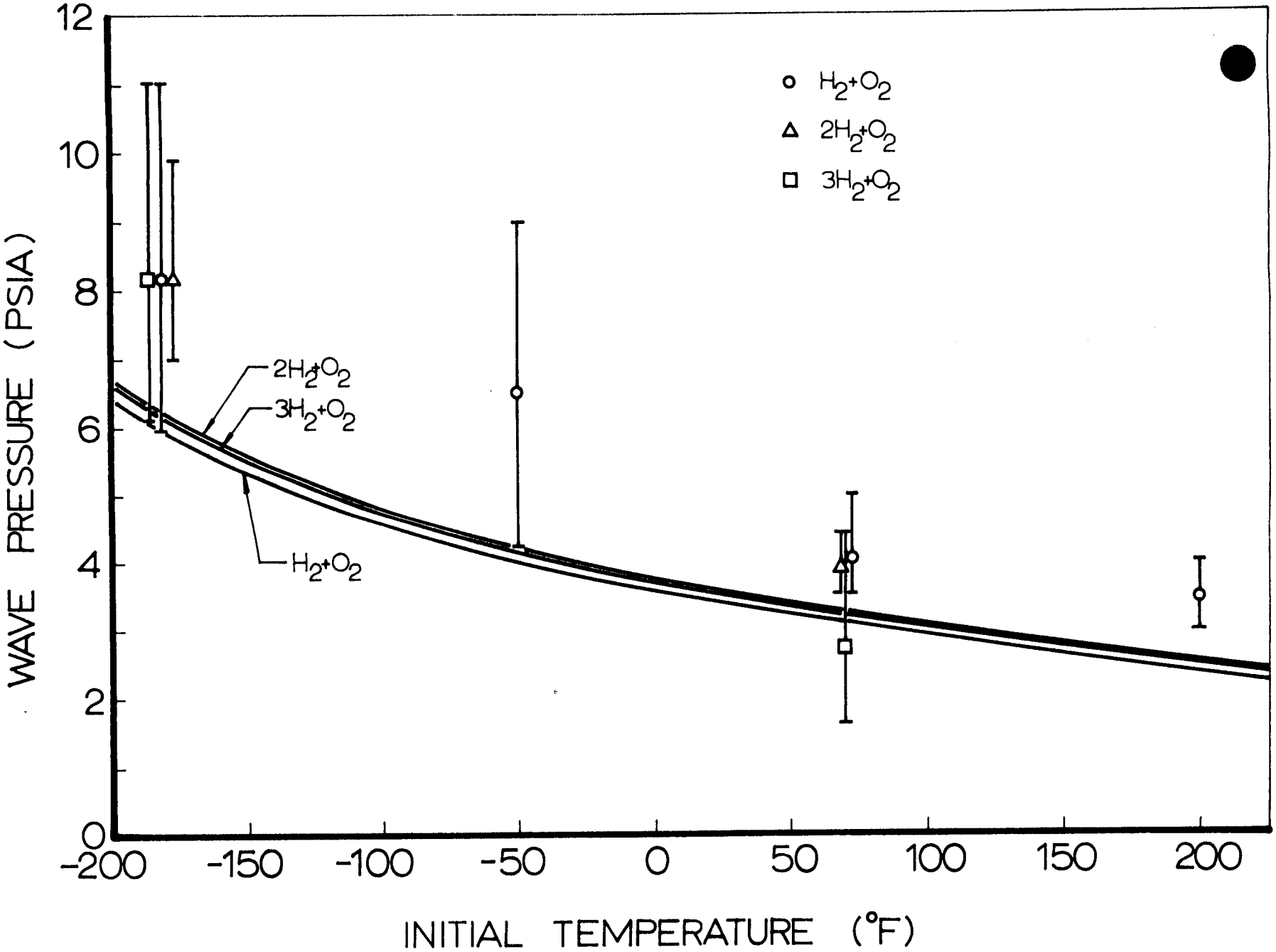

Fig. 115 Peak incident pressure measured at last position in Vessel CD for hydrogen-oxygen mixtures initially at 10 mmHg versus initial temperature.

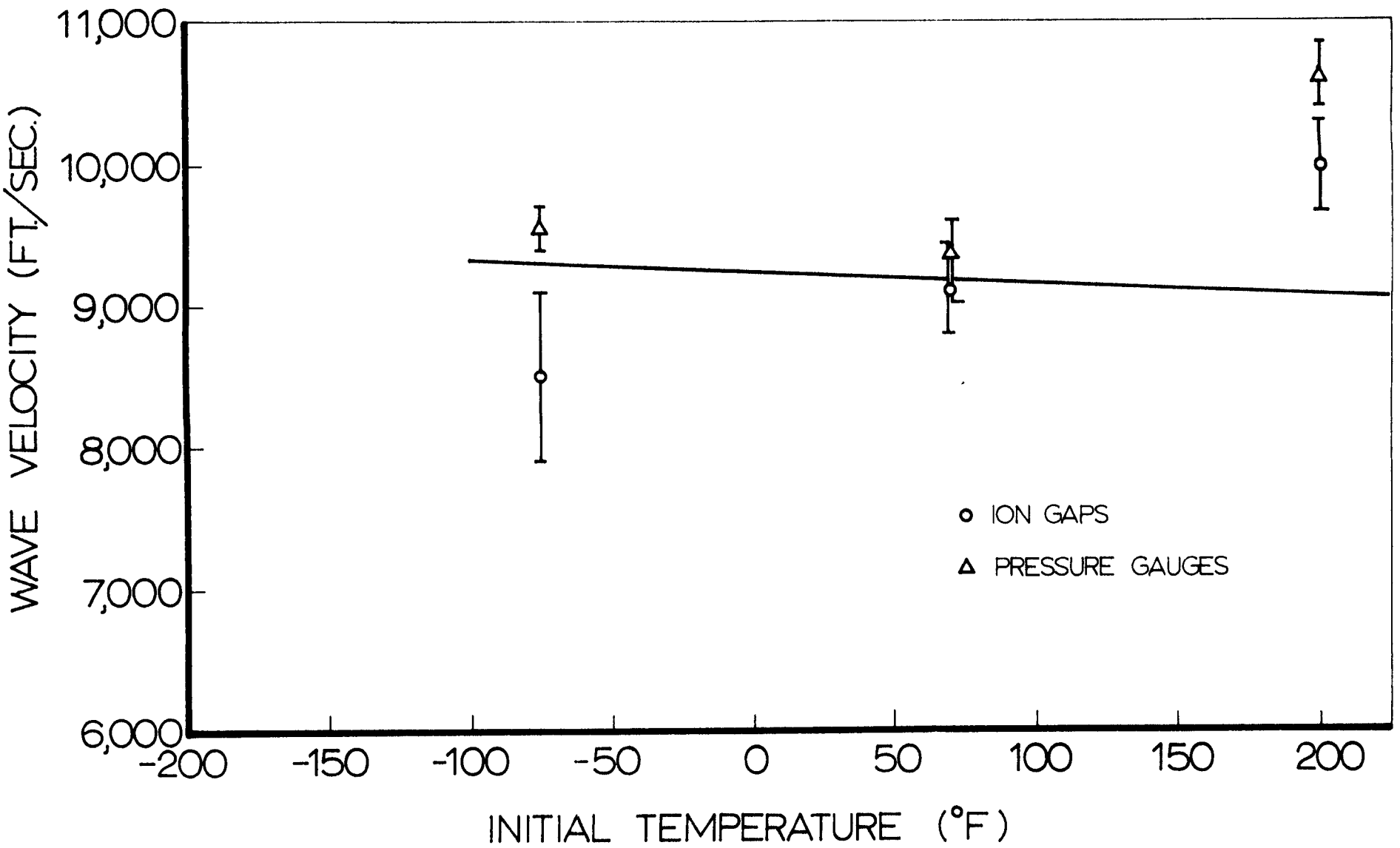

Fig. 116 Wave velocity measured at last position in Vessel CD for $3H_2+O_2$ mixtures initially at 1.0 mmHg versus initial temperature.

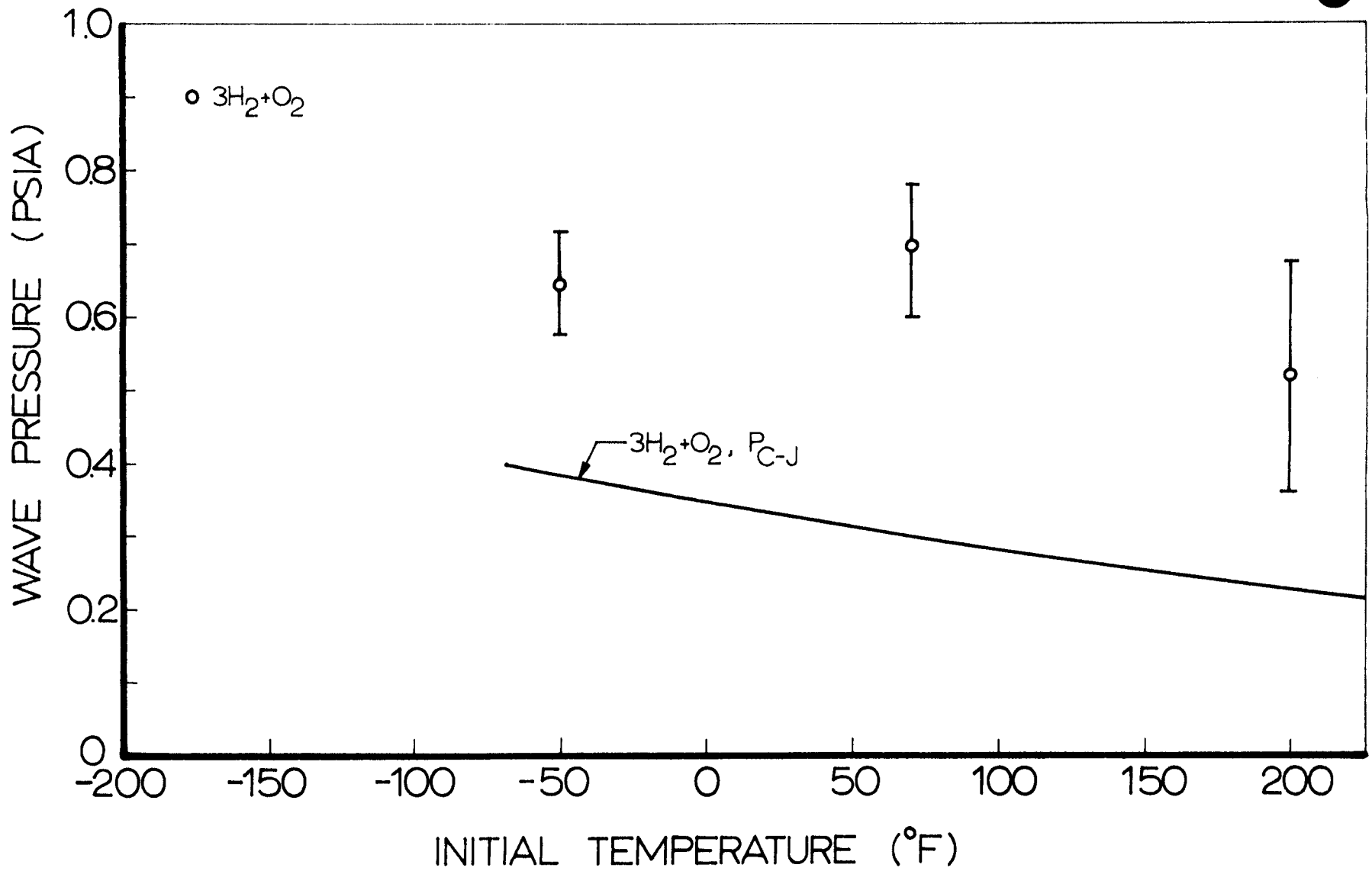

Fig. 117 Peak incident pressure measured at last position in Vessel CD for $3H_2+O_2$ mixtures initially at 1.0 mmHg versus initial temperature.

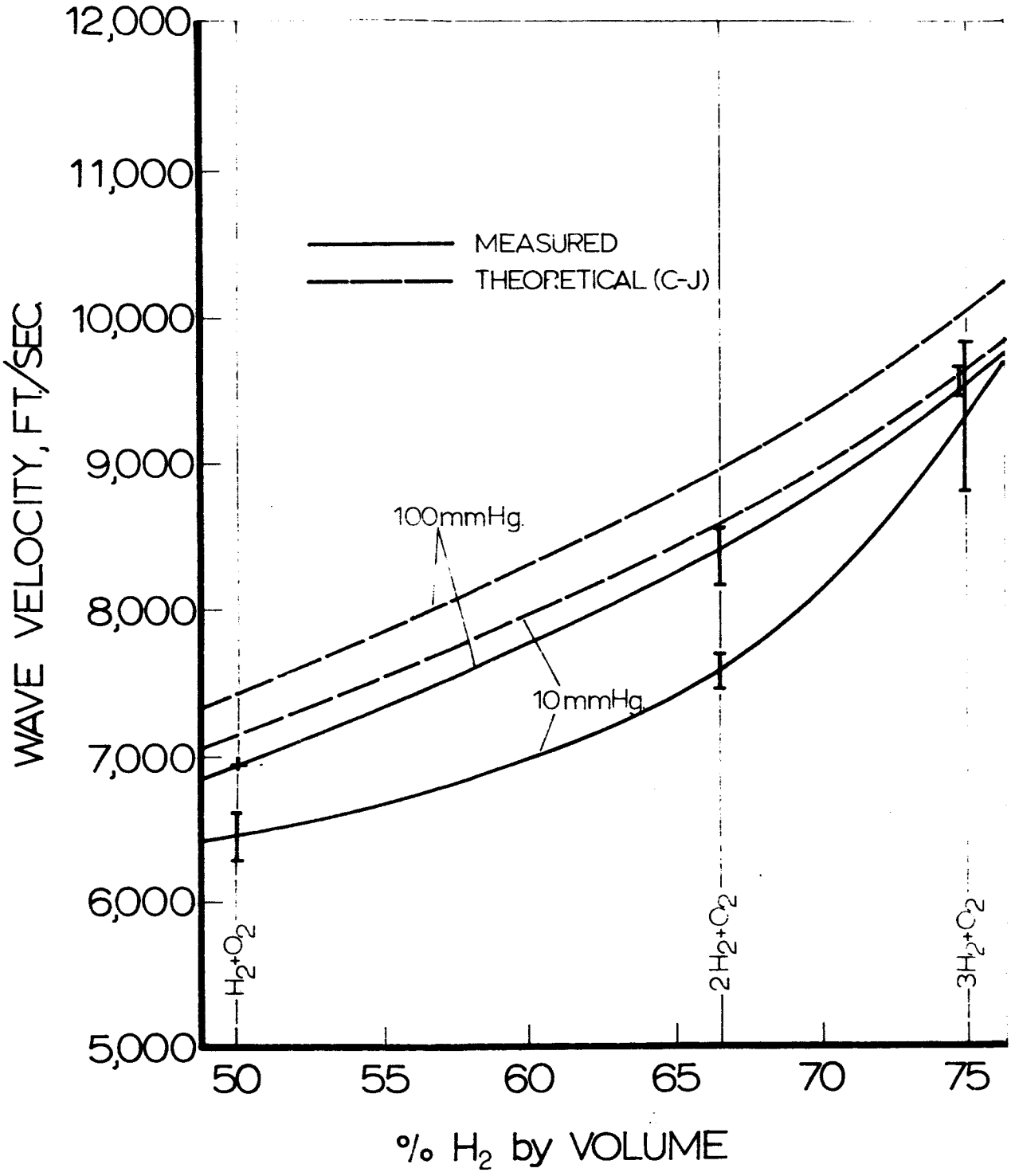

Fig. 118 Wave velocity measured at last position in Vessel CD as a function of volume percent of hydrogen for mixtures initially at pressures of 100 and 10 mmHg and room temperature. Theoretical C-J velocities included for comparison.

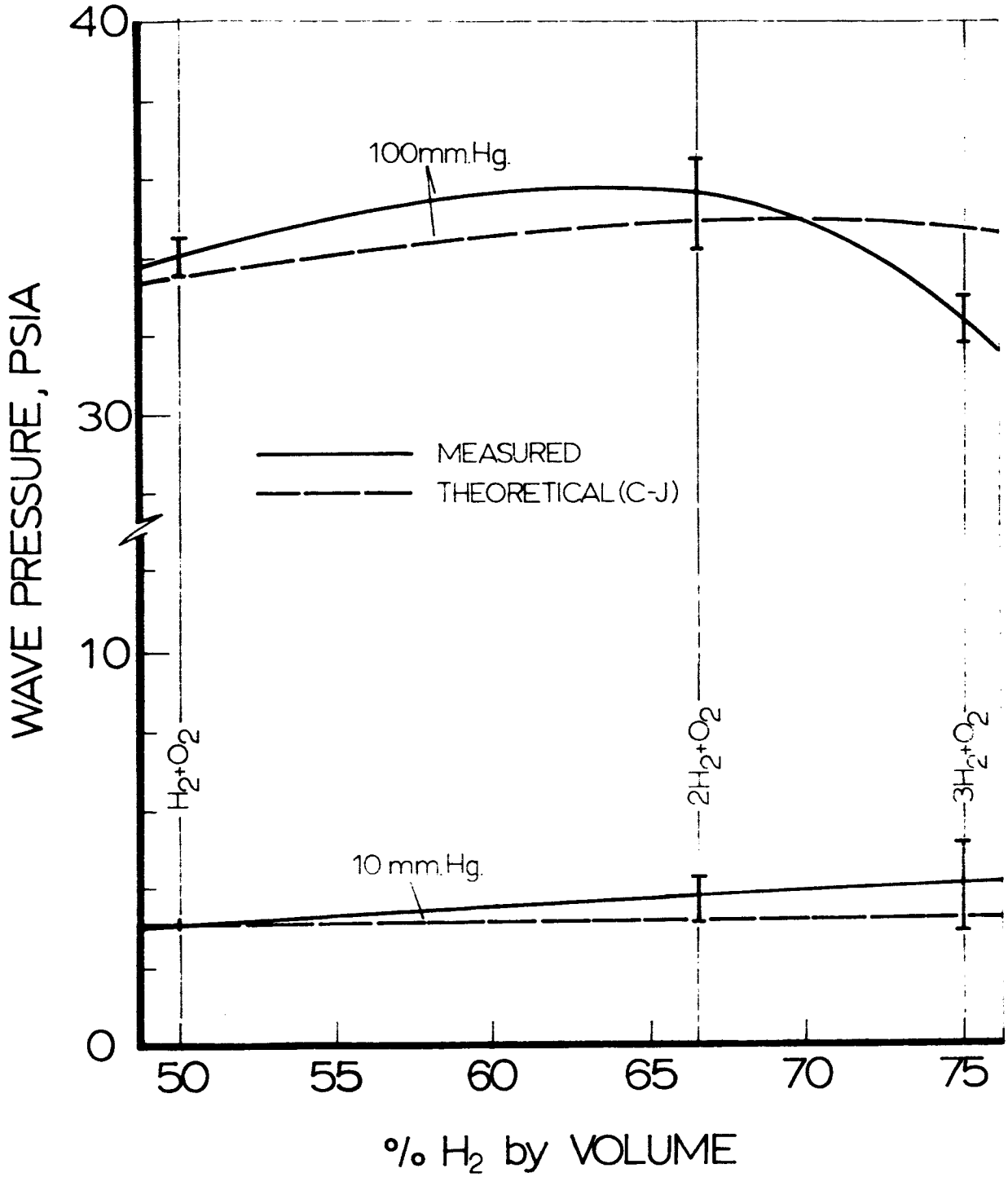

Fig. 119 Incident wave pressure measured at last position in Vessel CD as a function of volume percent of hydrogen for mixtures initially at pressures of 100 and 10 mmHg and temperatures of 70 and -180°F. Theoretical C-J velocities included for comparison.

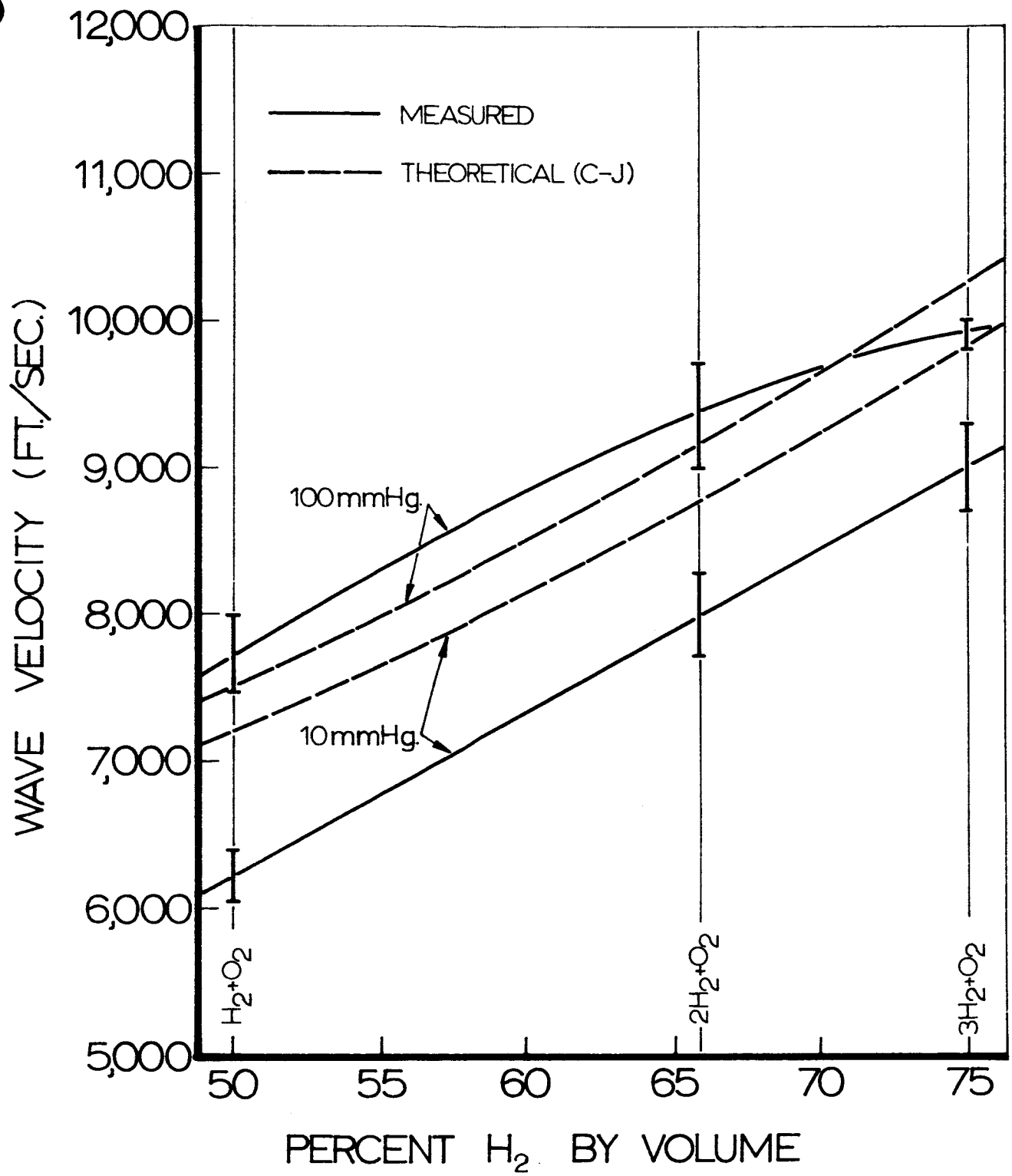

Fig. 120 Wave velocity measured at last position in vessel CD as a function of volume percent of hydrogen for mixtures initially at pressures of 100 and 10 mmHg and -180°F. Theoretical C-J velocities included for comparison.

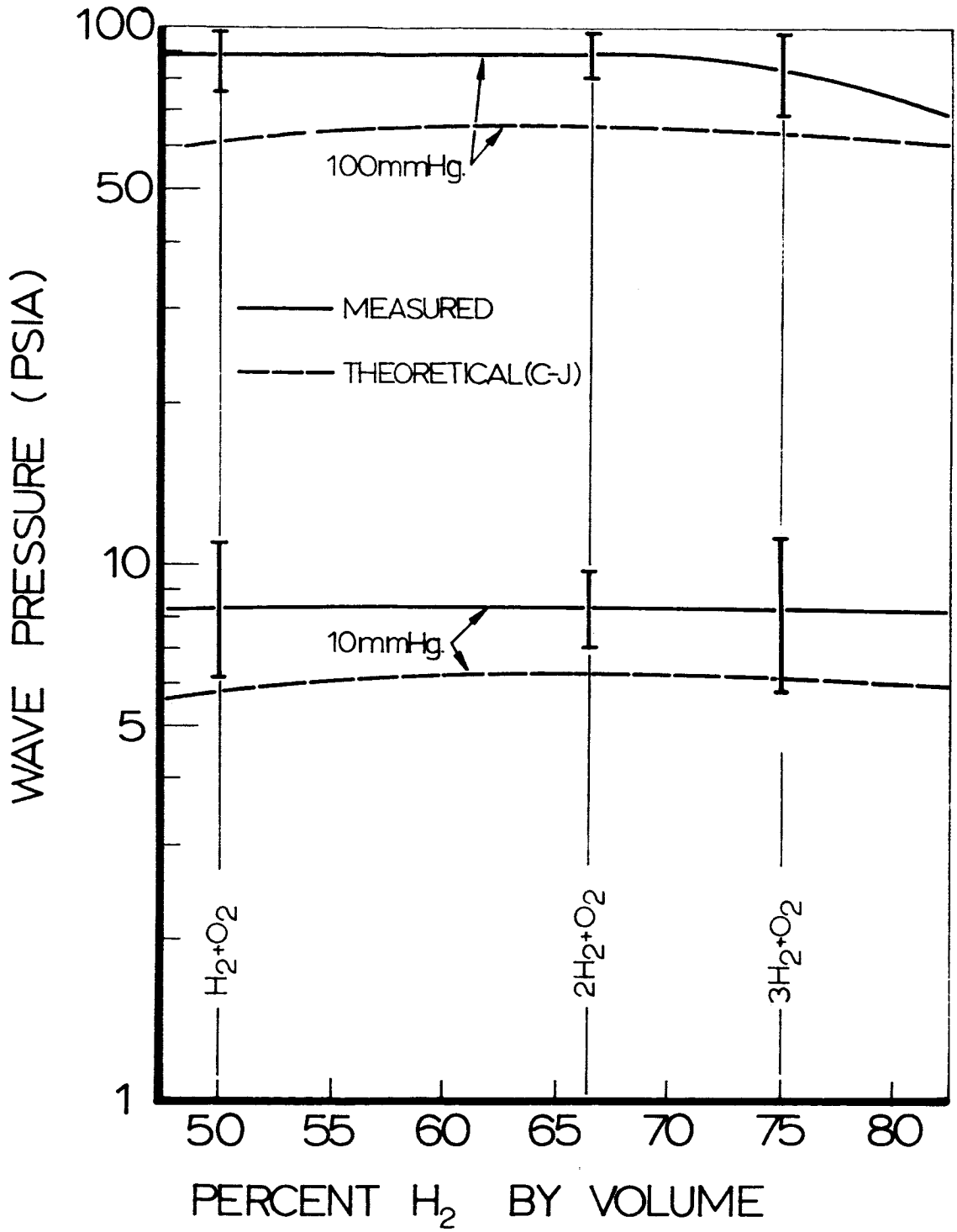

Fig. 121 Incident wave pressure measured at last position in Vessel CD as a function of volume percent of hydrogen for mixtures initially at pressures of 100 and 10 mmHg and -180°F. Theoretical C-J velocities included for comparison.

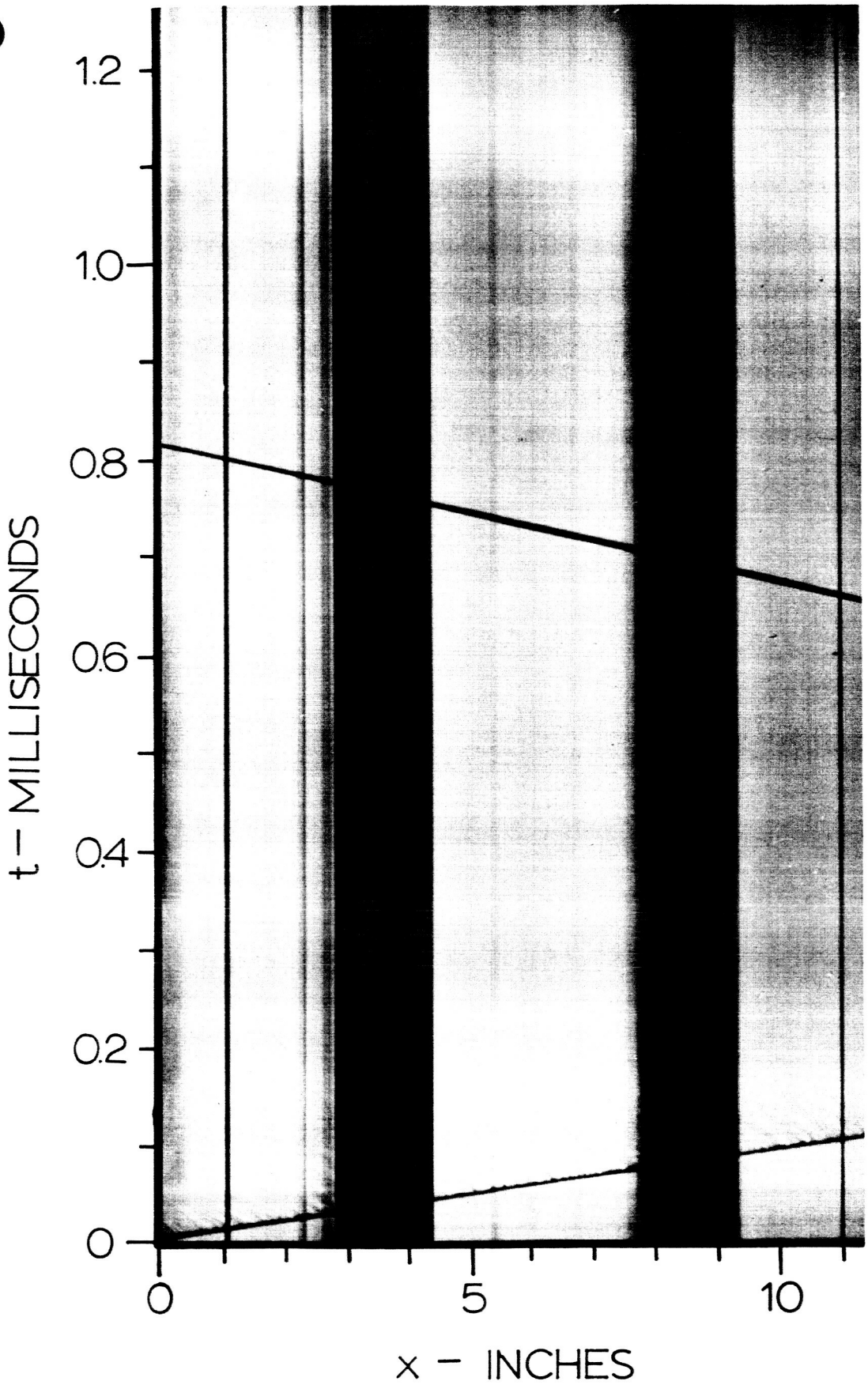

Fig. 122 Streak Schlieren photograph of a steady detonation wave in $3H_2+O_2$ mixture initially at 100 mmHg and room temperature

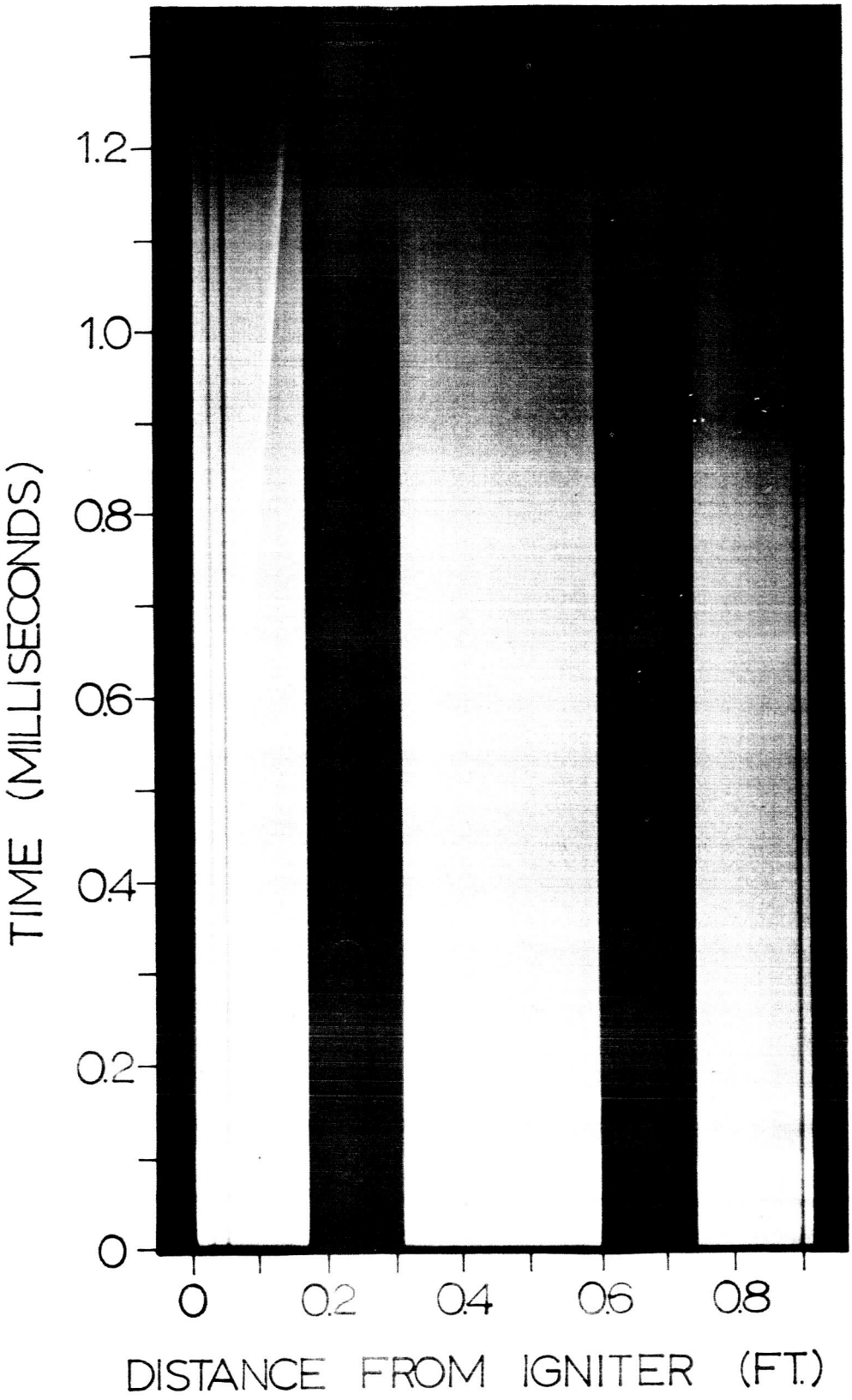

Fig. 124a Streak schlieren photograph of initial flame acceleration in Vessel CD for an H_2+0_2 mixture with spark ignition. Initial pressure 100 mmHg, initial temperature, 70°F. Distance measured from point of ignition. Flame front depicted by bright line curved diagonally up to the right. Similar traces behind front are indicative of flame structure.

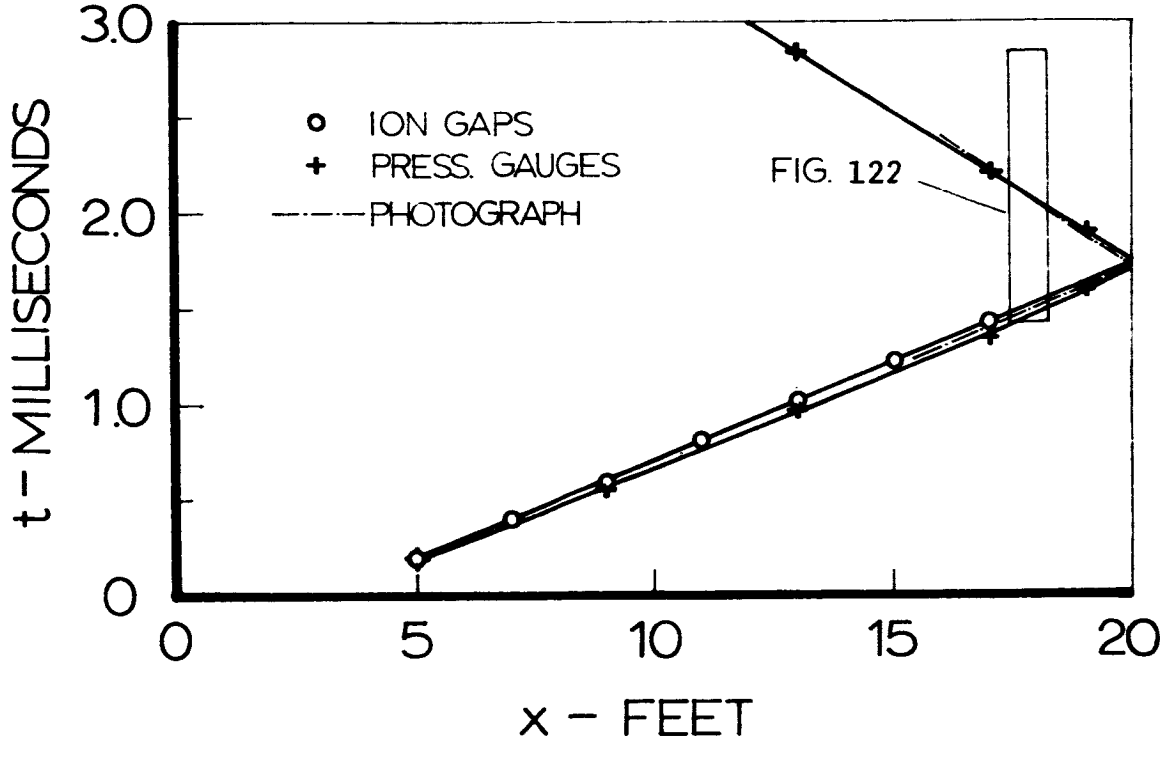

Fig.123 Space-time diagram of detonation wave in Vessel CD for $3H_2+O_2$ mixture with Primacord ignition. Initial pressure 100 mmHg, initial temperature 70°F. Space-time location of Fig.122 shown as insert.

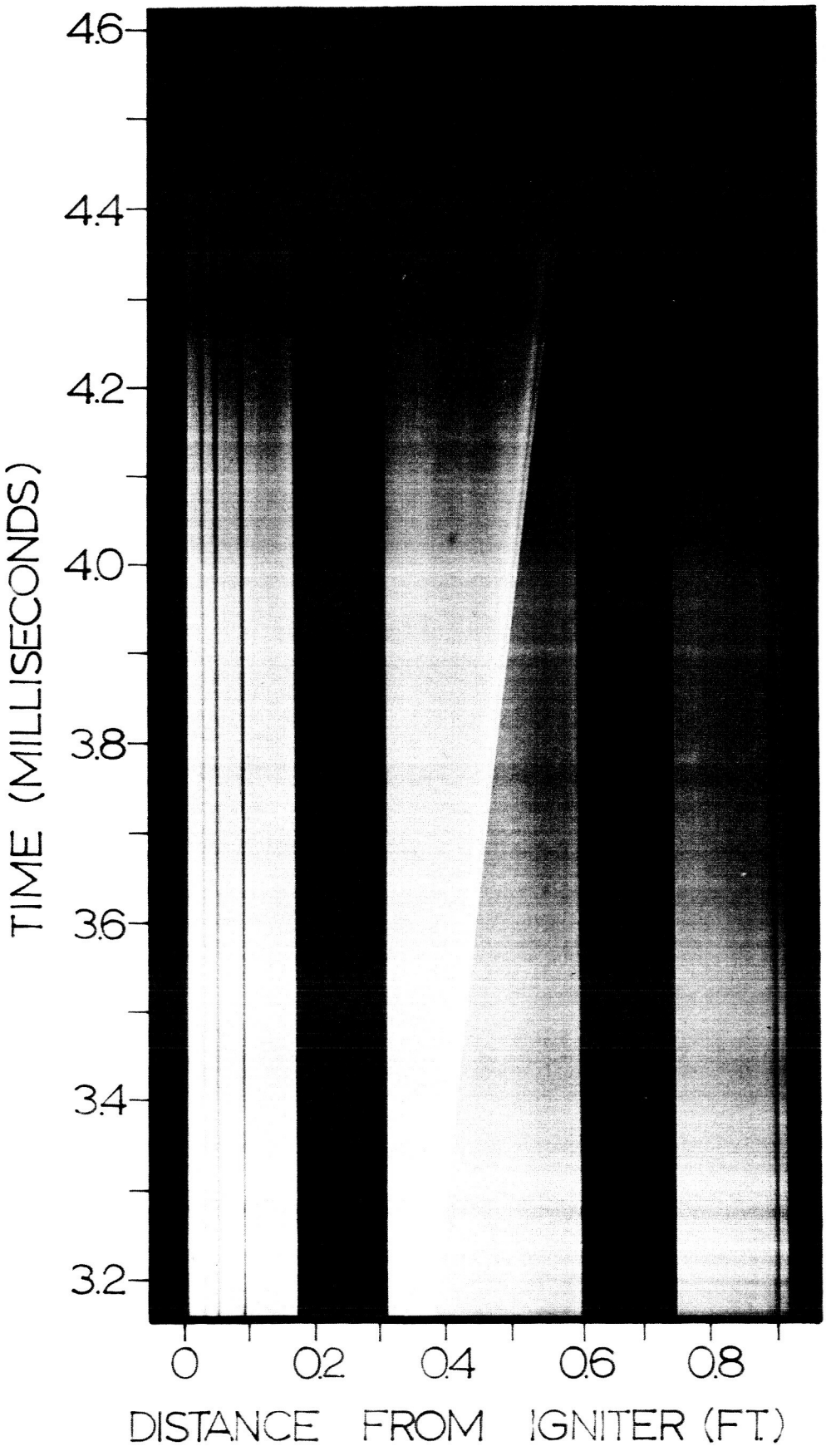

Fig. 124b continued

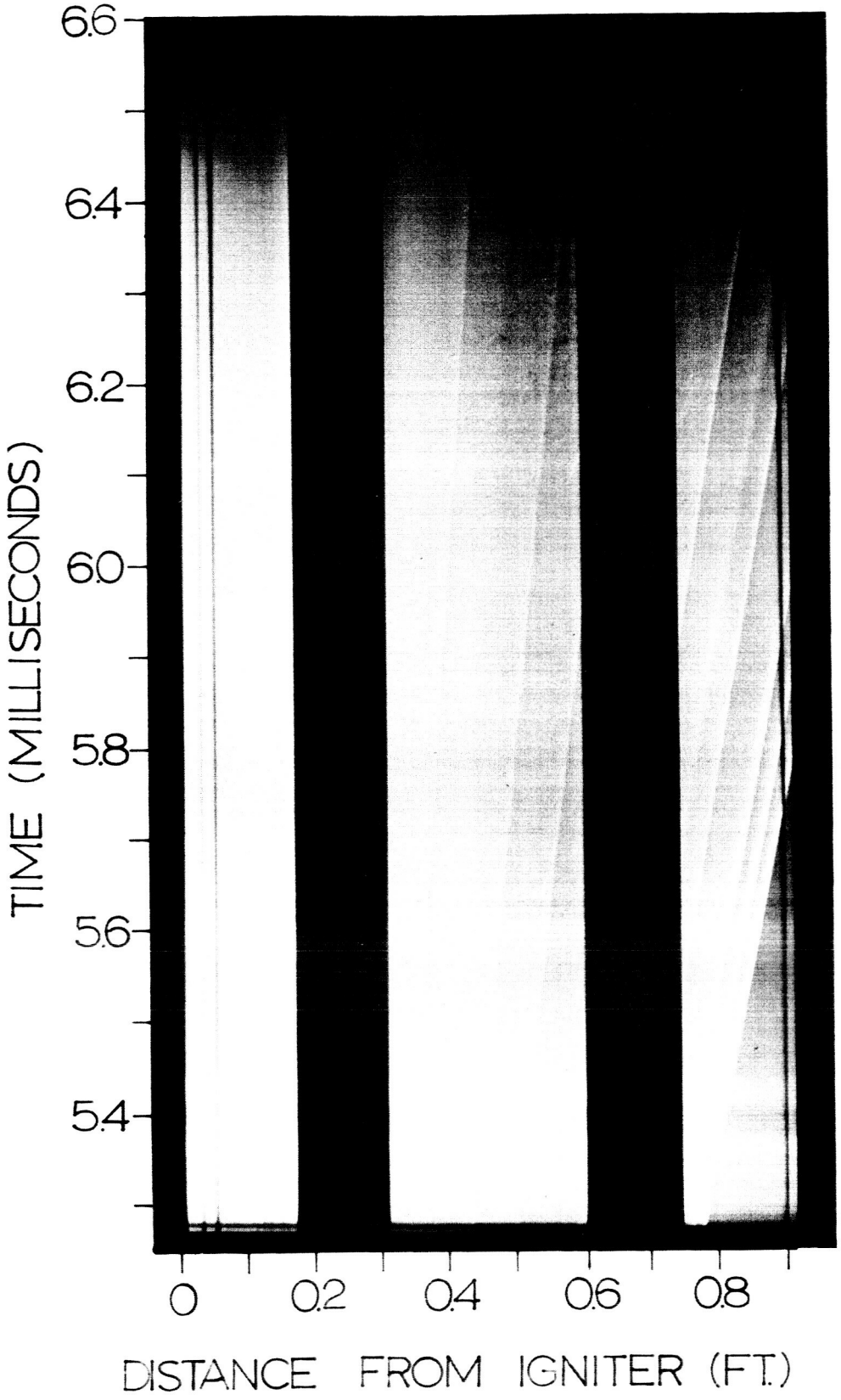

Fig. 124c continued

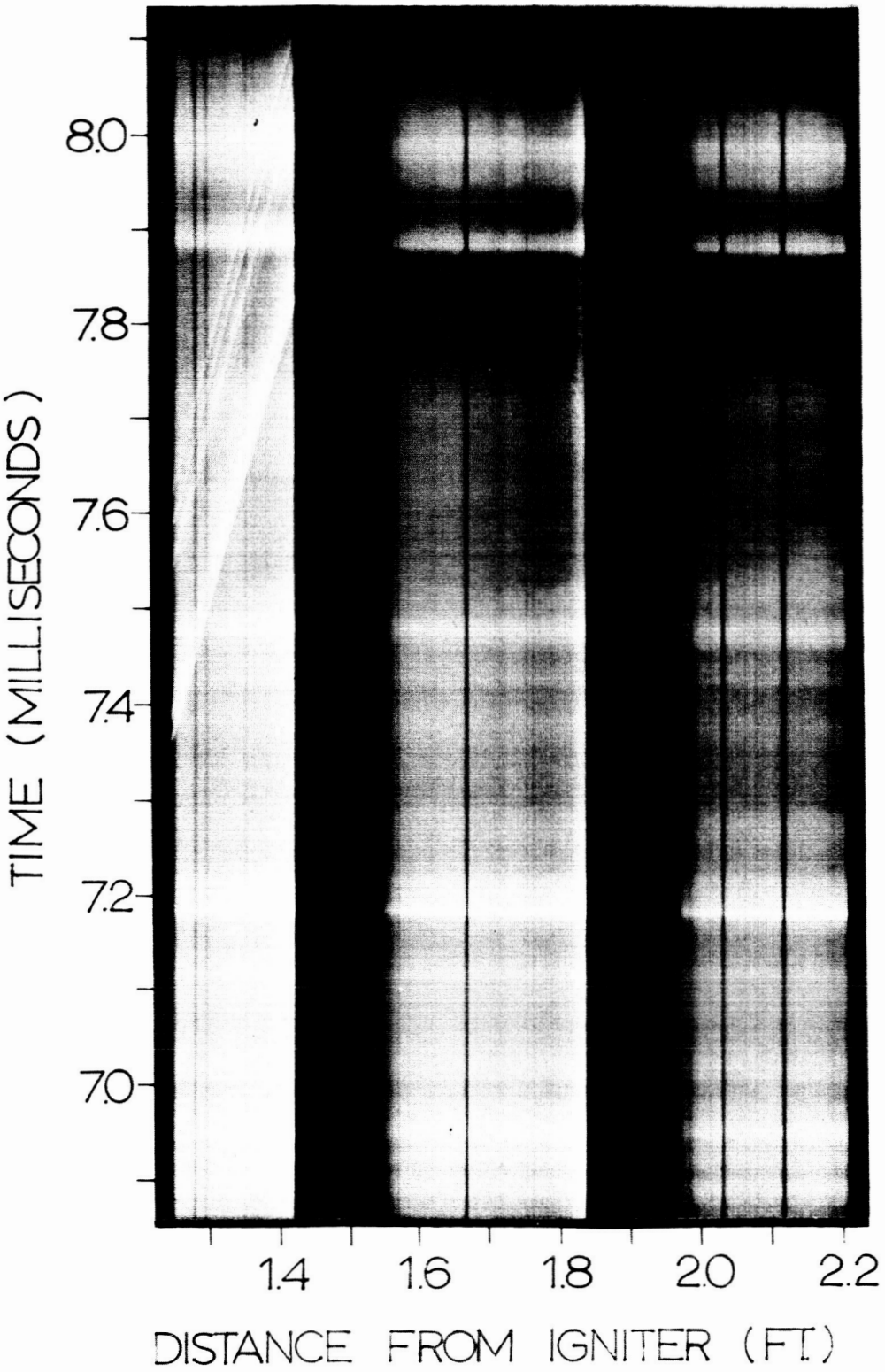

Fig. 124d continued

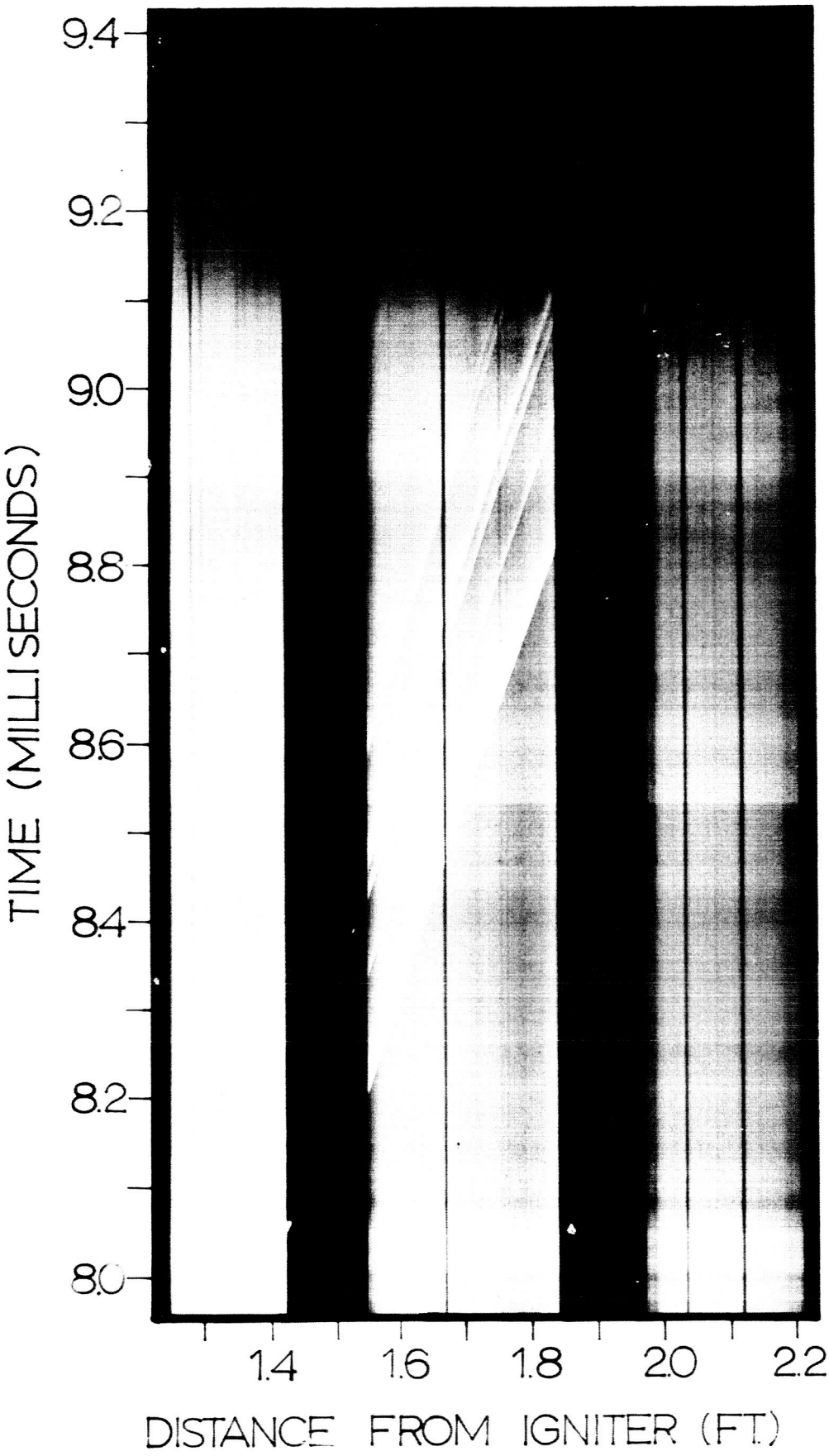

Fig. 124e continued

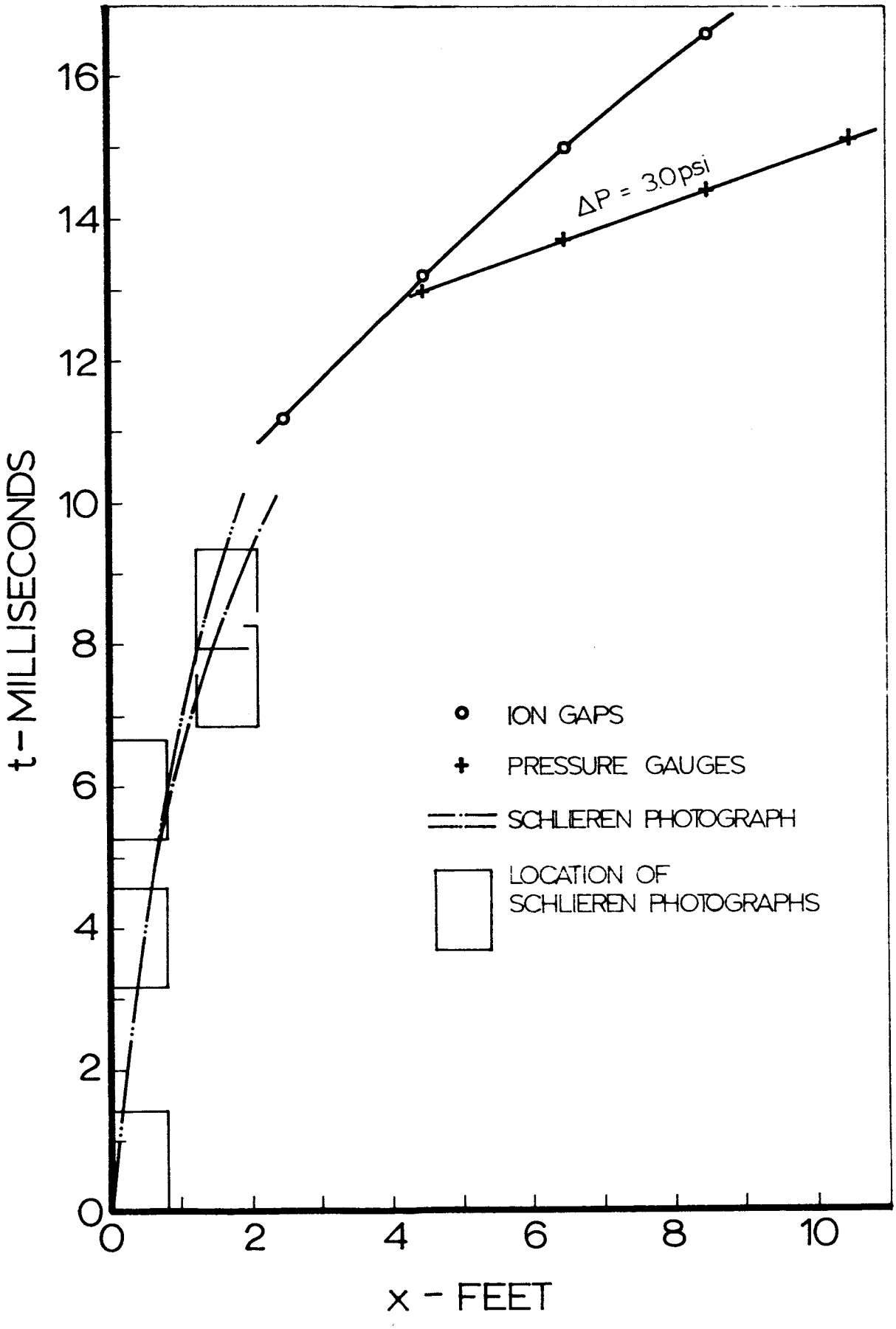

Fig. 125 Space-time diagram of accelerating flame in Vessel C-D for an H_2+O_2 mixture with spark ignition. Initial pressure 100 mmHg, initial temperature 70°F. Distance is measured from point of ignition. Time-space location of photographs of Fig. 124 shown as inserts.

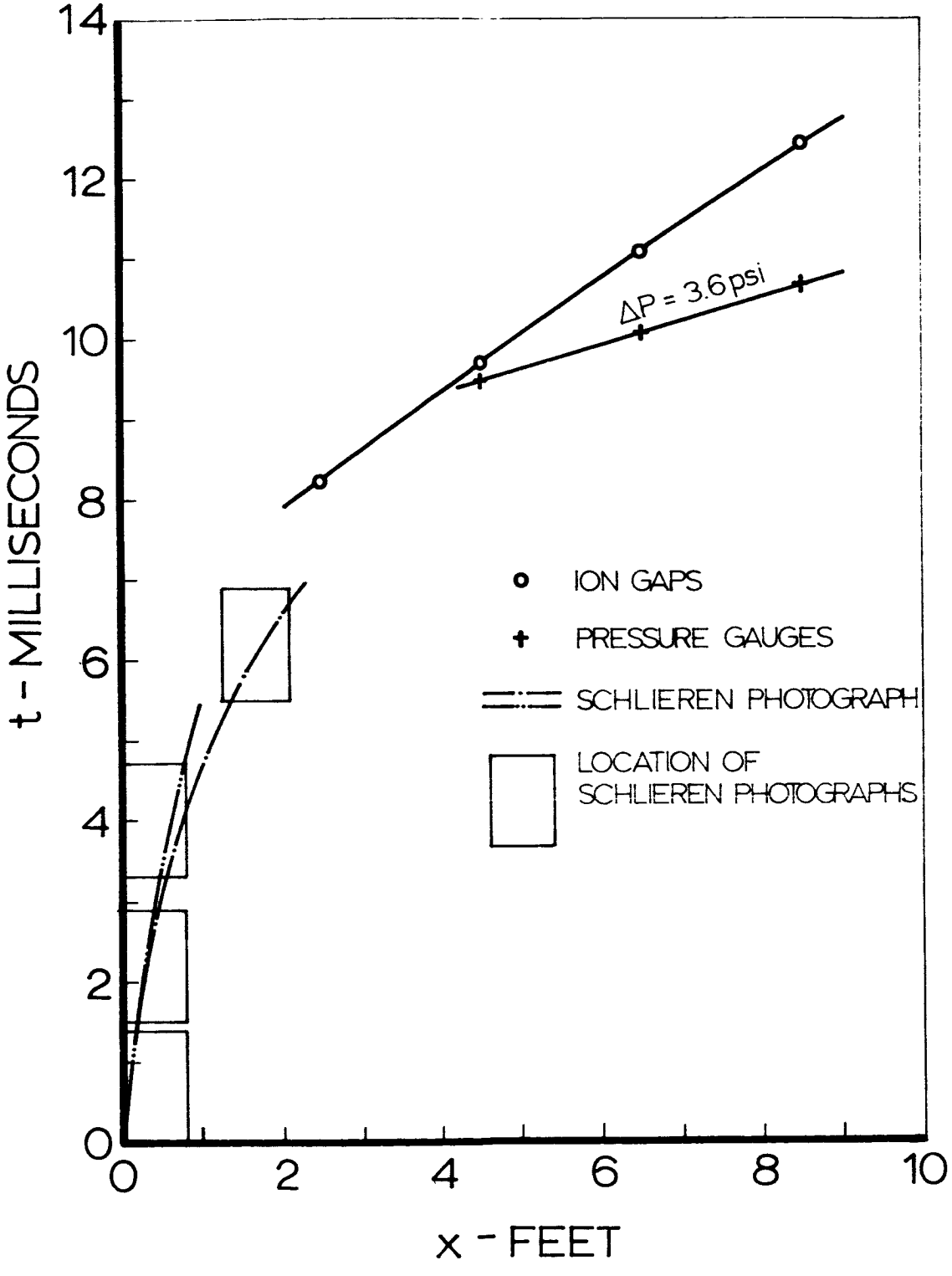

Fig. 126 Space-time diagram of accelerating flame in Vessel C-D for a $2H_2+O_2$ mixture with spark ignition. Initial pressure 100 mm Hg, initial temperature 70°F.

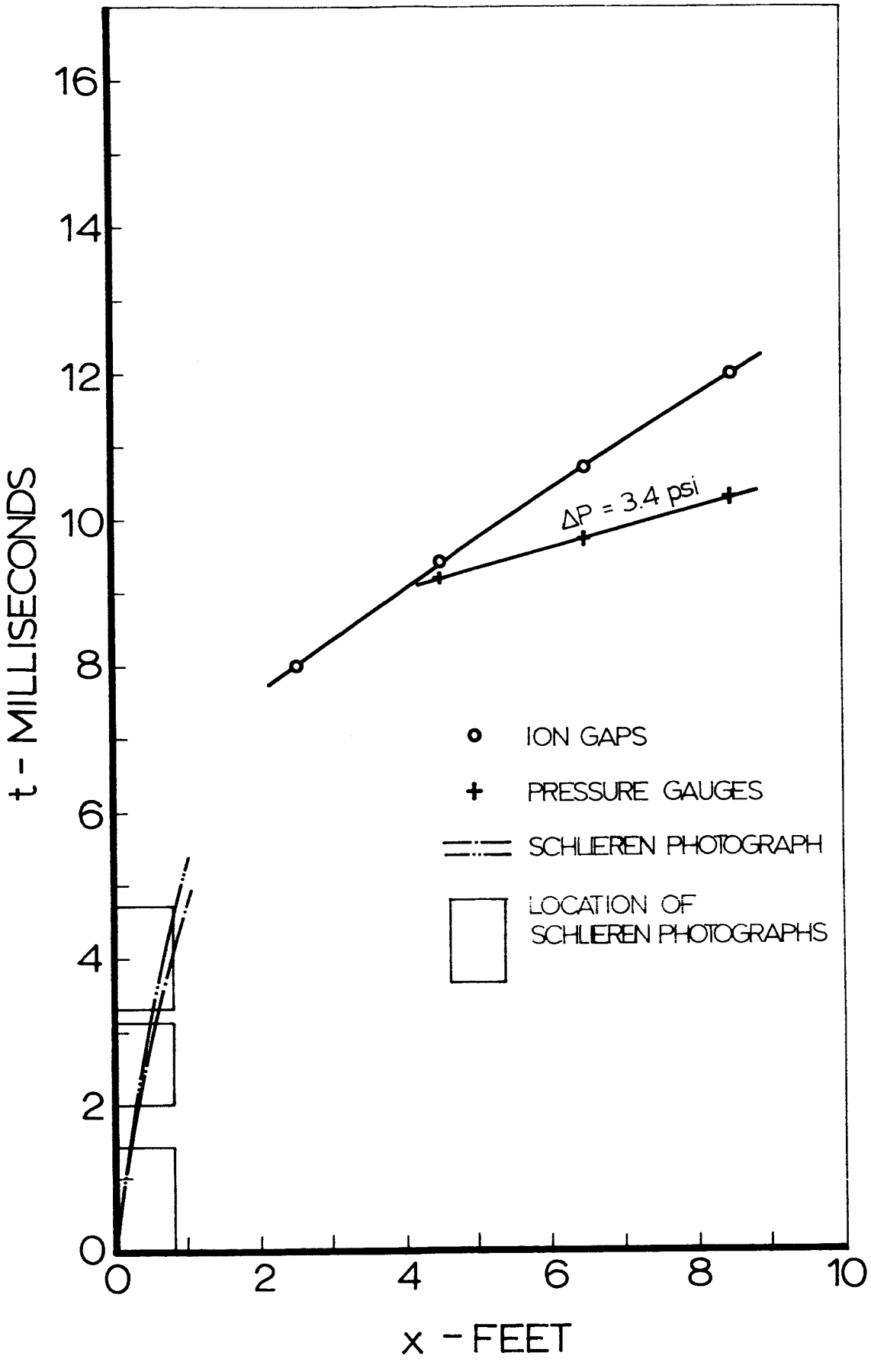

Fig.127 Space-time diagram of accelerating flame in Vessel C-D for a $3H_2+O_2$ mixture with spark ignition. Initial pressure 100 mmHg, initial temperature 70°F.

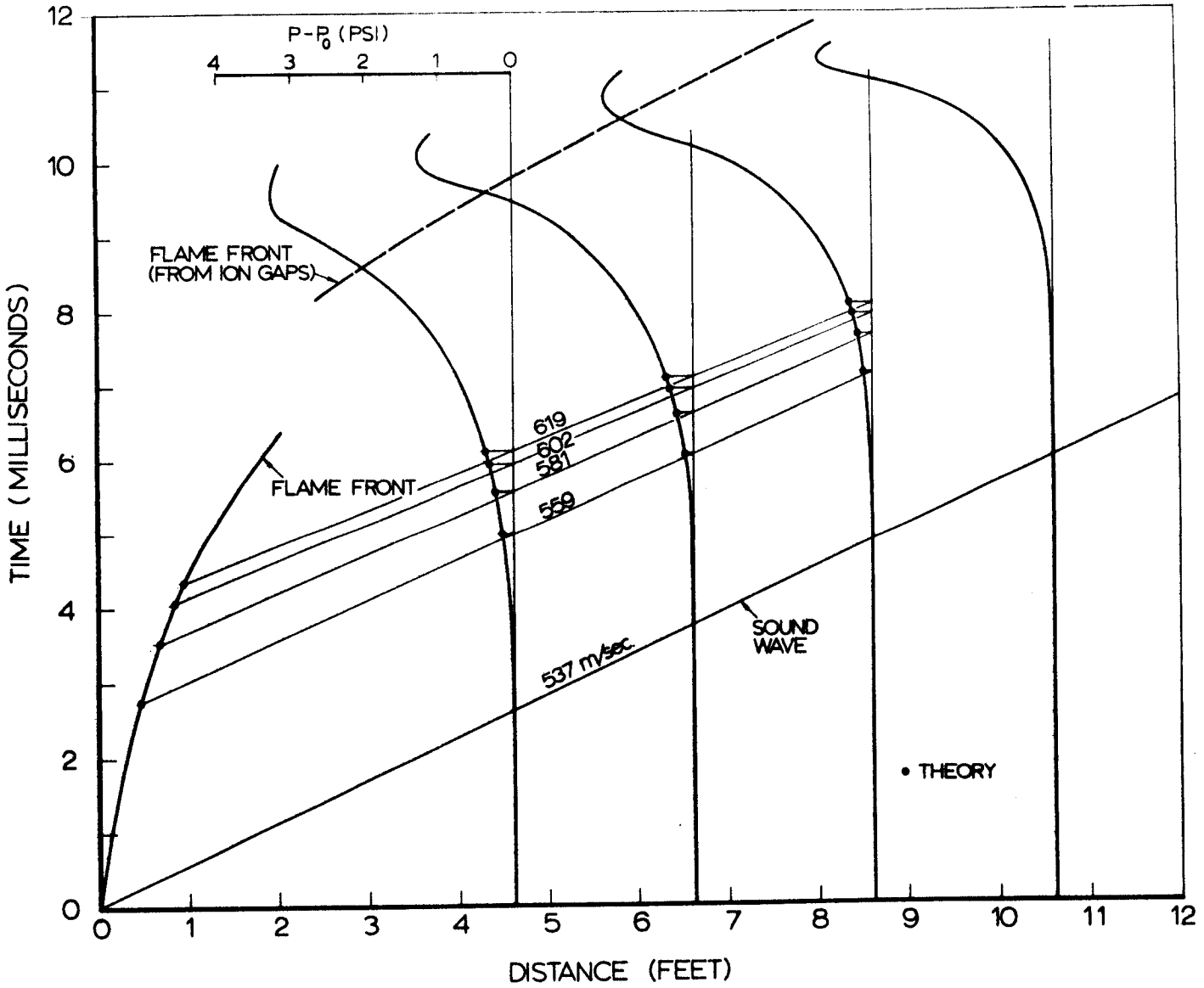

Fig. 128 Space-time diagram of Fig. 126 replotted with pressure records included to demonstrate build-up of pressure pulse.

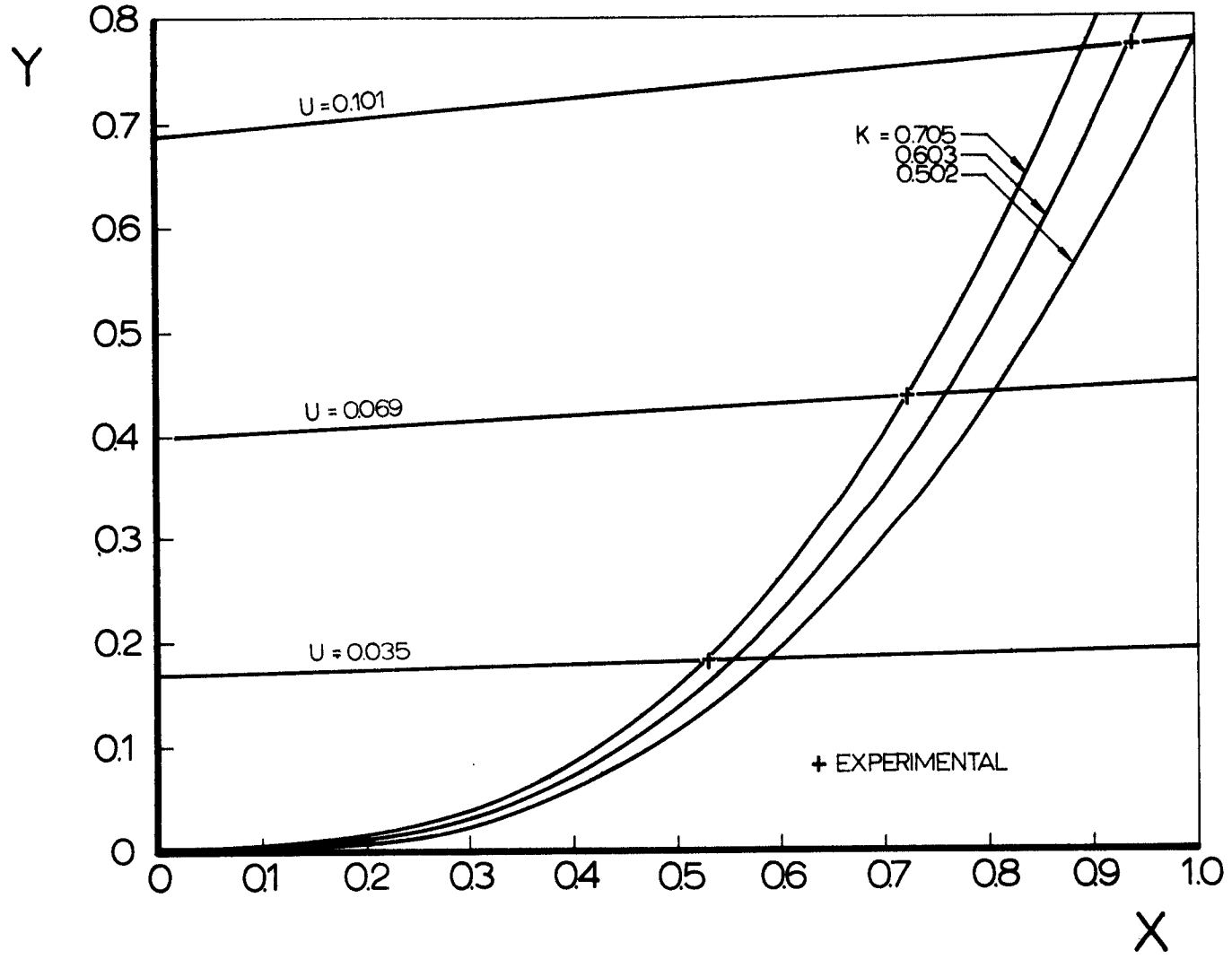

Fig. 129 Graphical representation of the solution for heat of reaction and average flame propagation speed of Fig. 128. The curved lines emanating from the origin represent flame world lines, Eq. (15), while the straight lines describe characteristics of the simple pressure wave, Eq. (16). The crosses, obtained from experiment, establish the value of K.

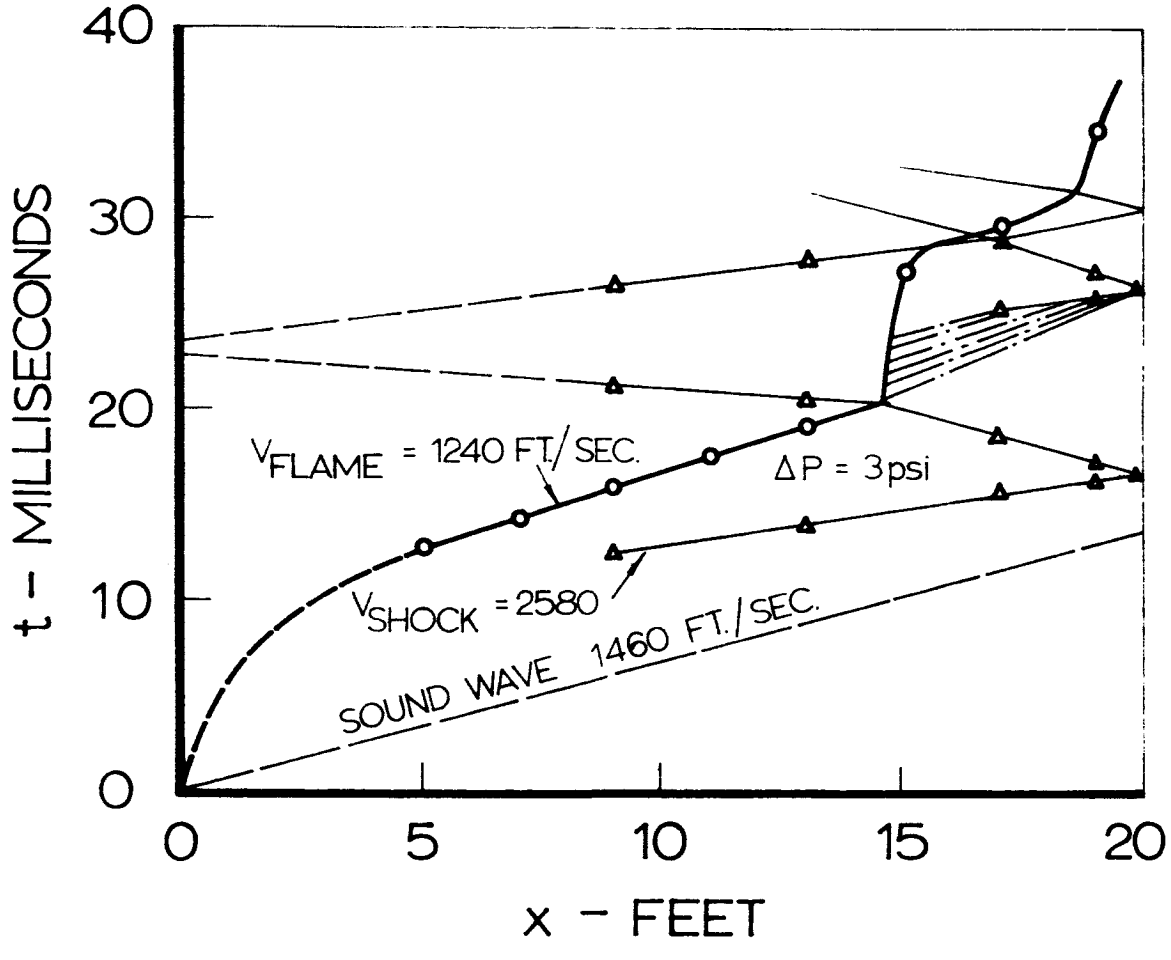

Fig.130 Space-time wave diagram of accelerating flame in 2 ft. dia. vessel. H_2+O_2 mixture at 100 mmHg initial pressure and room temperature. Spark ignition.

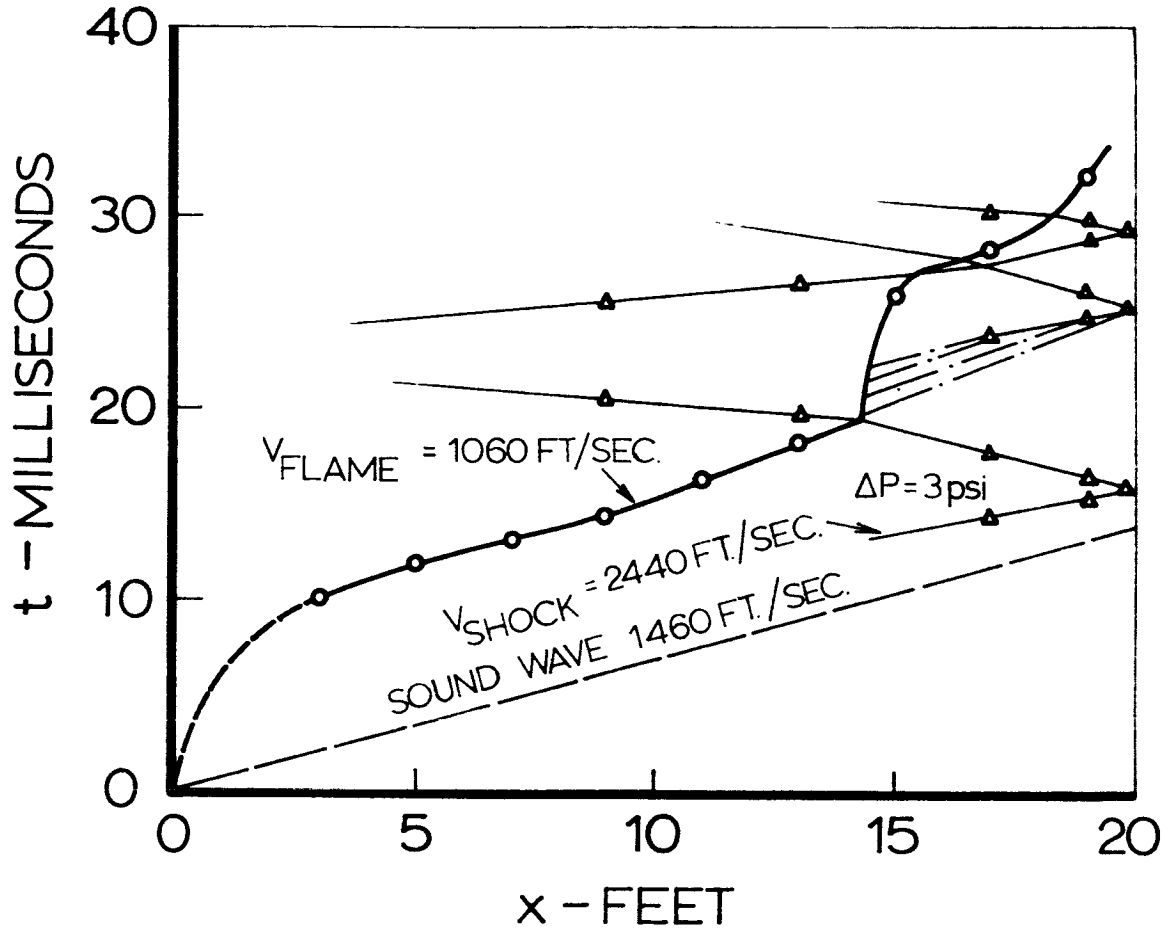

Fig. 131 Space-time wave diagram of accelerating flame in 2 ft. dia. vessel. H_2+O_2 mixture at 100 mmHg initial pressure and room temperature. Hot plate ignition.

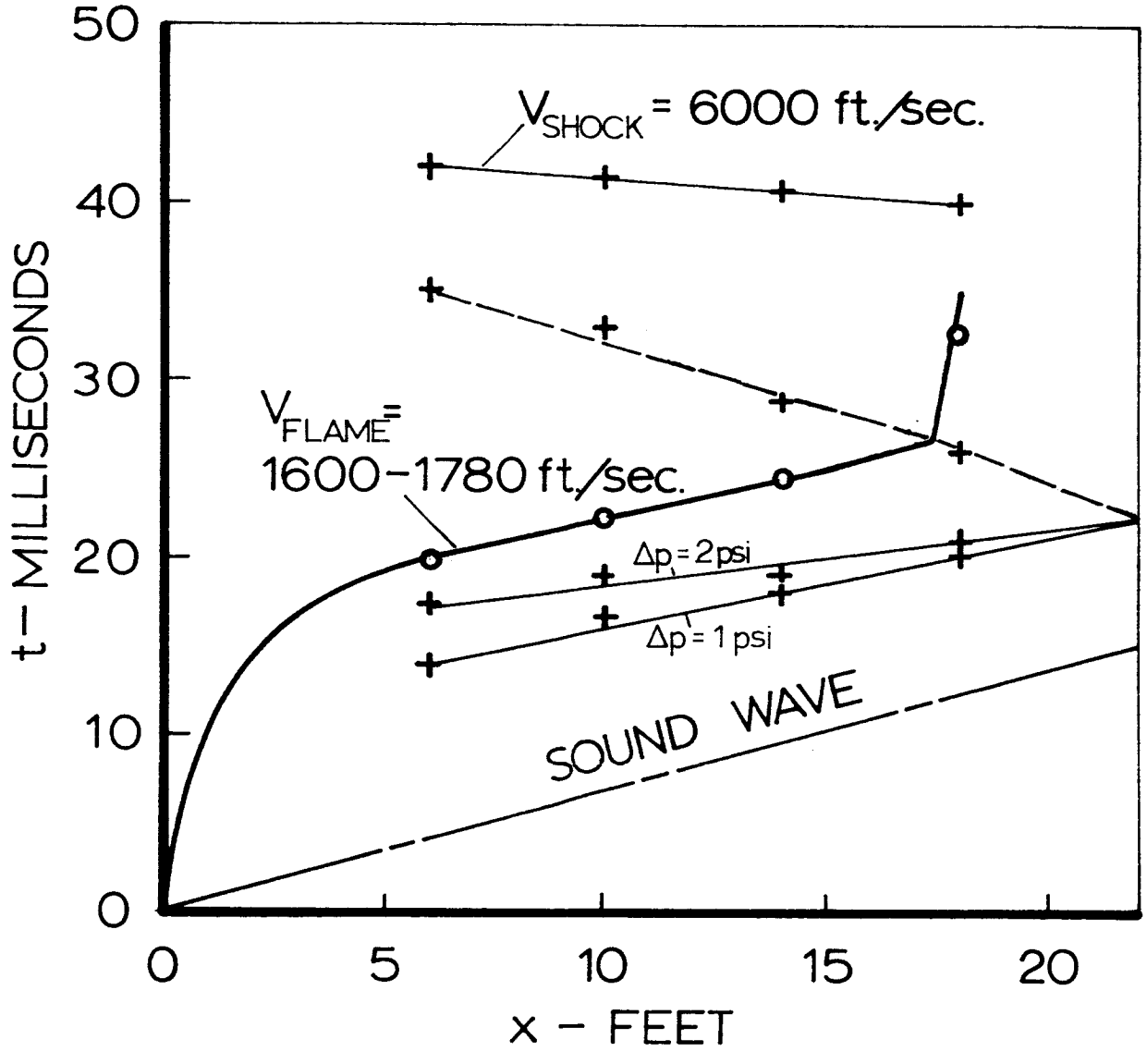

Fig. 132 Space-time wave diagram of accelerating flame in Vessel A. H_2+O_2 mixture at 100 mmHg initial pressure and room temperature. Spark ignition.

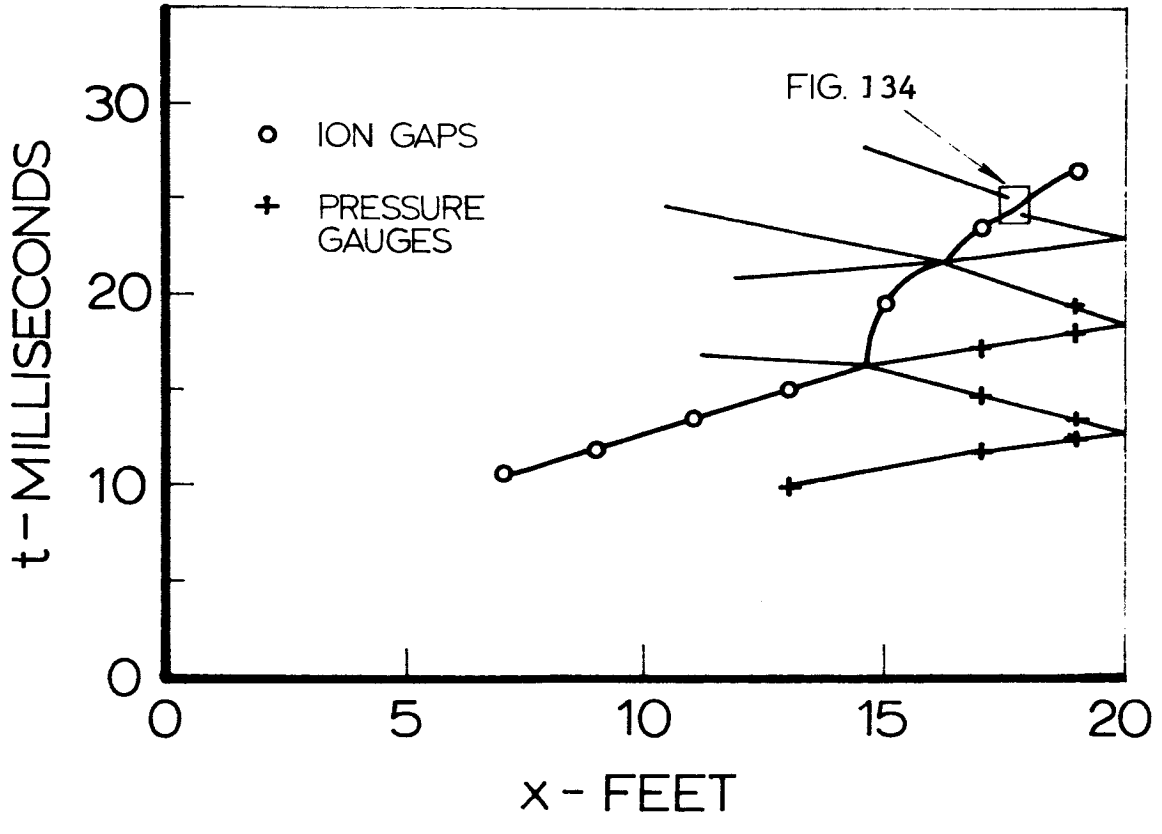

Fig.133 Space-time diagram of accelerating flame in Vessel CD for $2H_2+O_2$ mixture with spark ignition. Initial pressure 100 mmHg, initial temperature 70°F. Space-time location of schlieren photograph of Fig. 134 shown as insert.

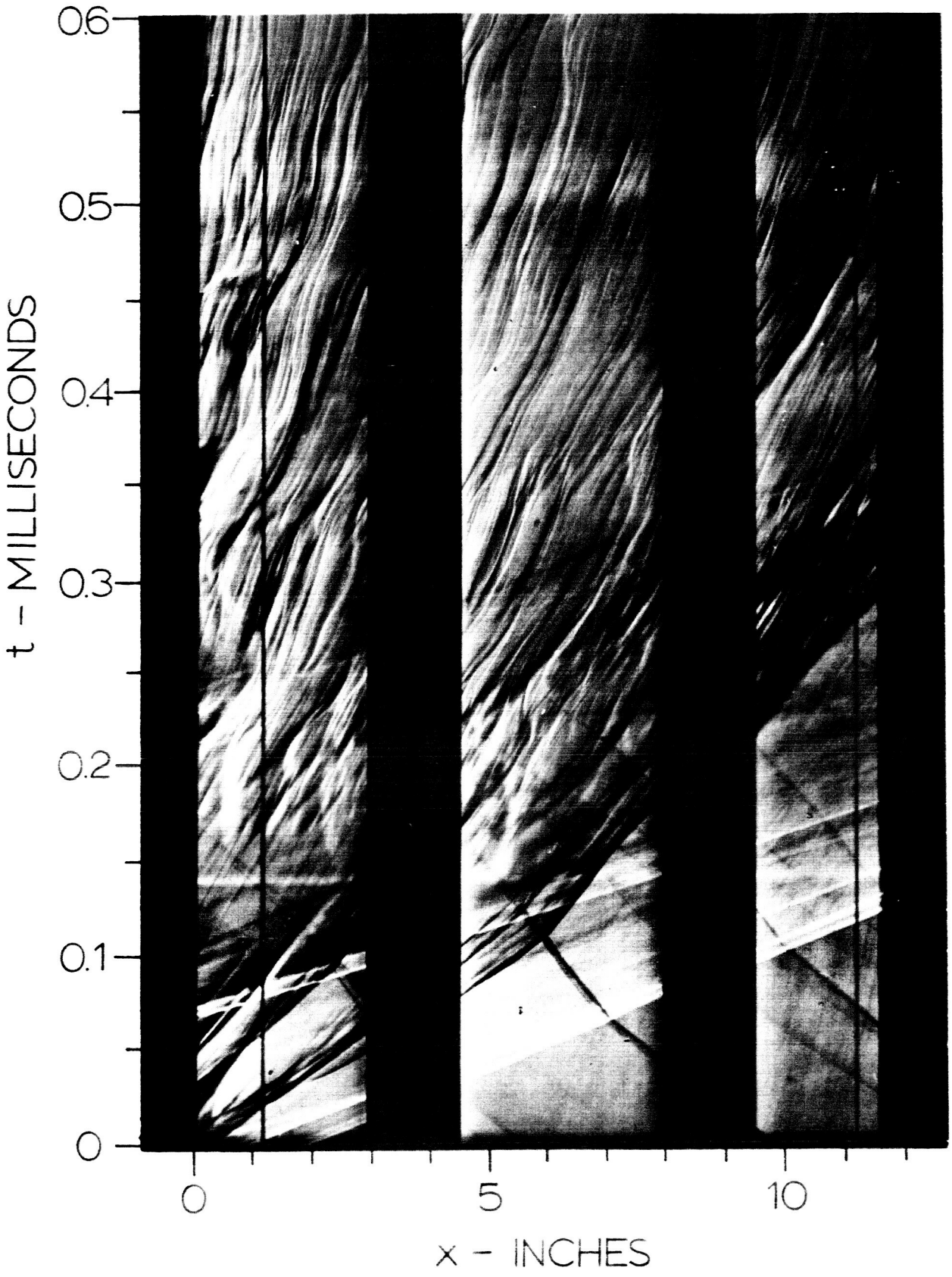

Fig. 134 Streak Schlieren photograph of a flame reflected shock interaction pattern in $2H_2+0_2$ mixture initially at 100 mmHg.

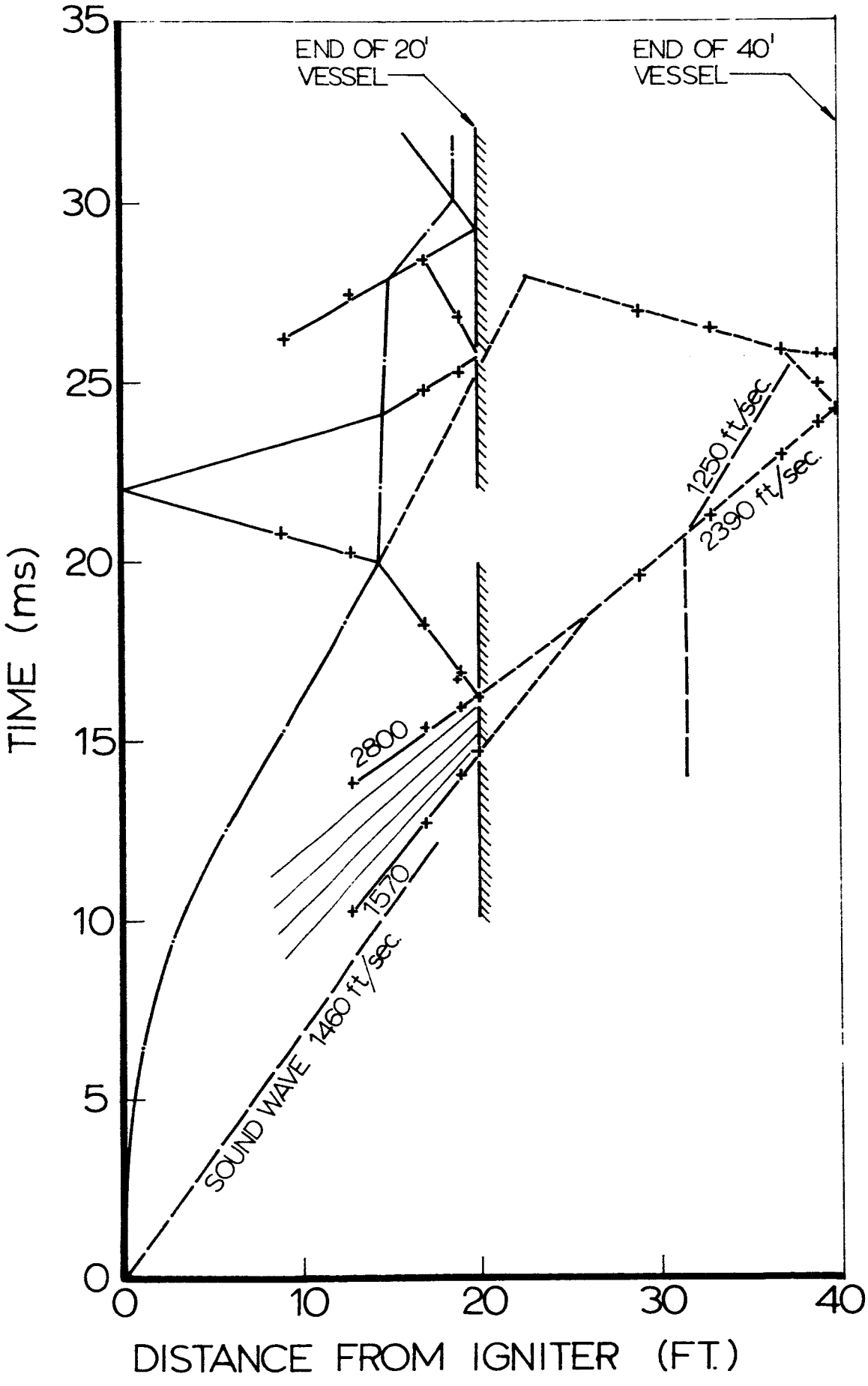

Fig. 135 Space-time diagram of a wave interaction pattern in 40 ft. vessel for H_2+0_2 mixture with spark ignition. Data from 20 ft. vessel is also included. Initial pressure 100 mmHg, initial temperature 70°F.

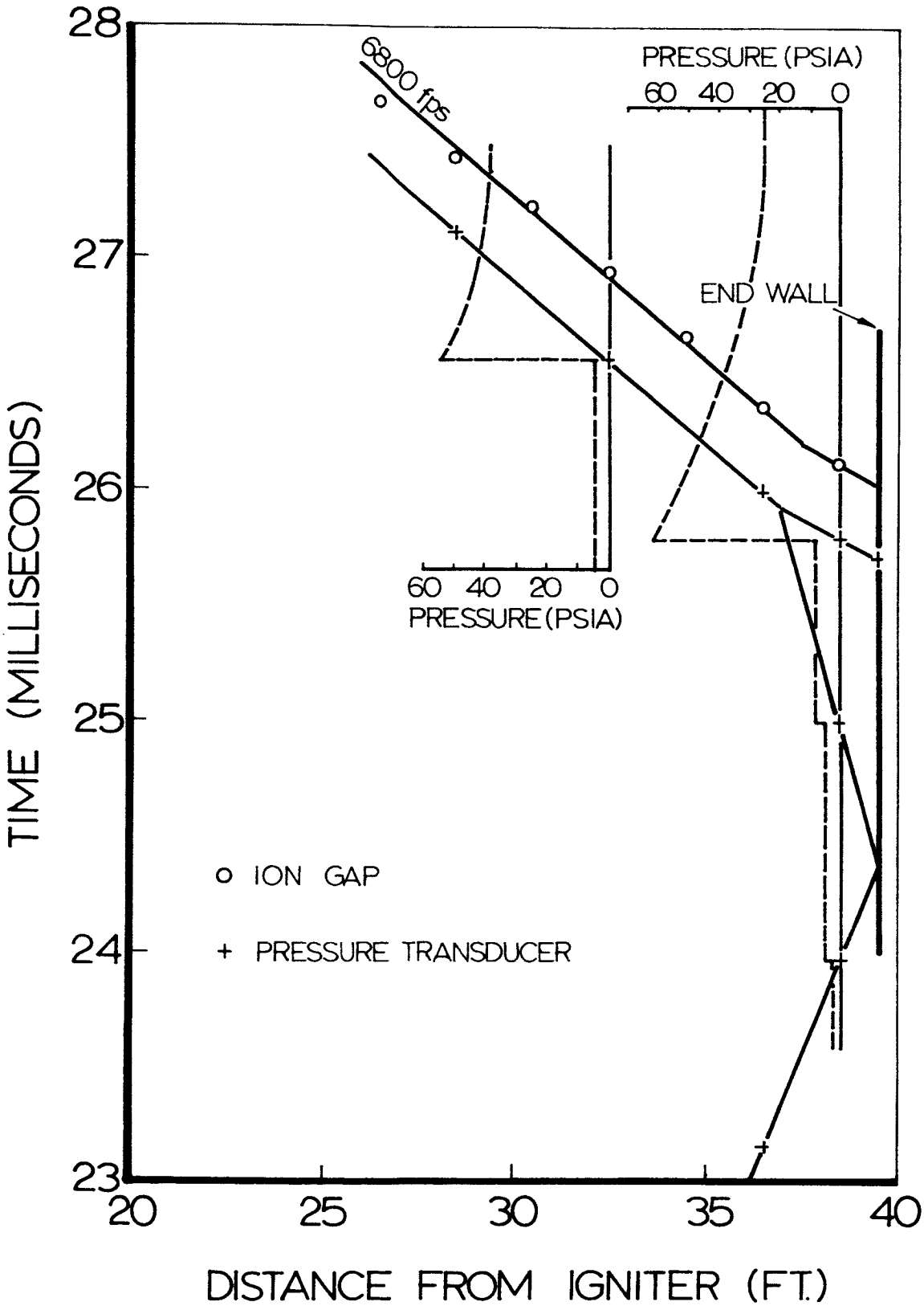

Fig. 136 Space-time diagram with superimposed pressure records of a wave interaction pattern in the 40 ft. vessel for H_2+O_2 mixture with spark ignition. Initial pressure 100 mmHg, initial temperature 70°F.

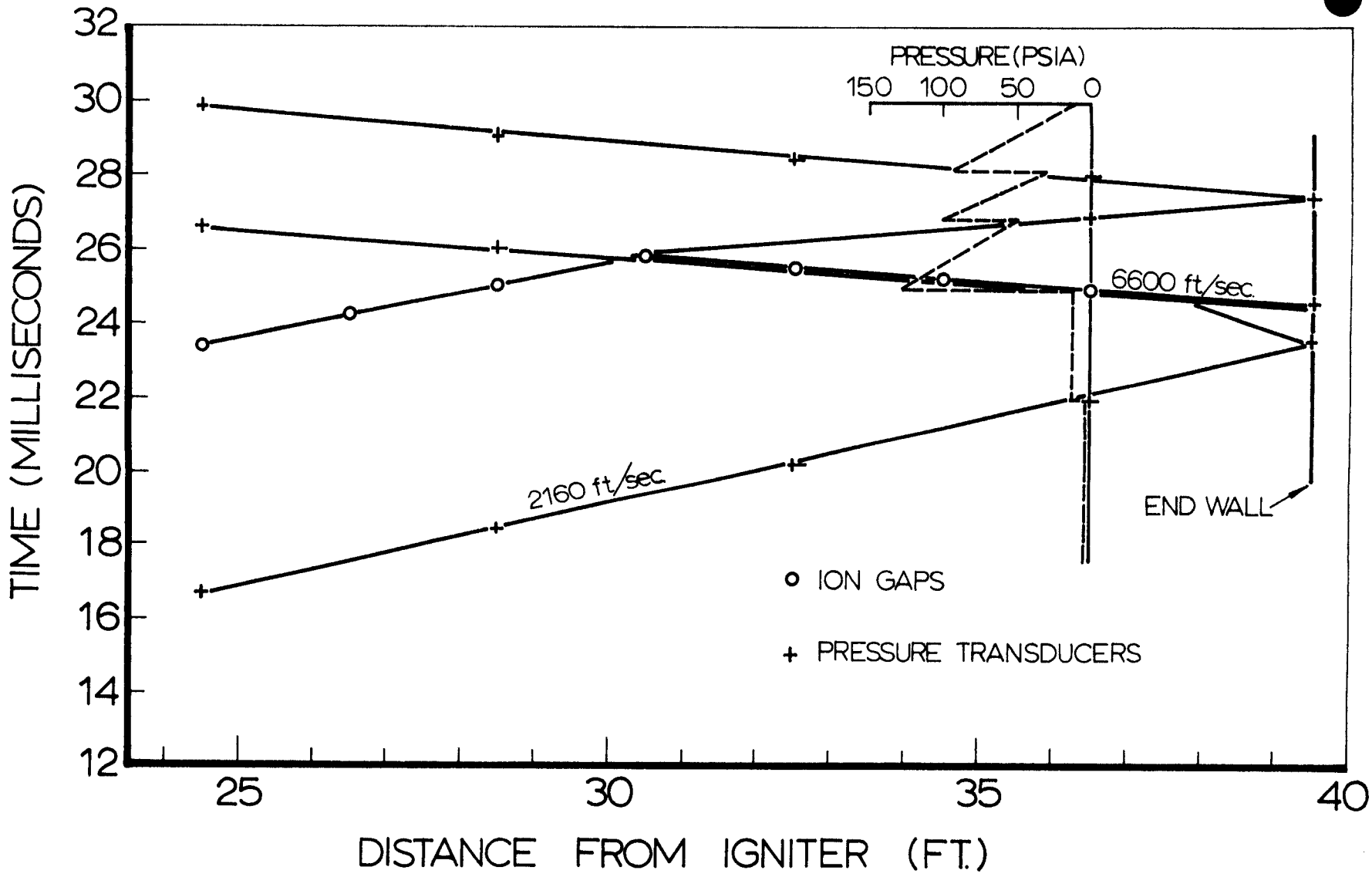

Fig. 137 Space-time diagram with superimposed pressure record of wave interaction pattern in the 2 ft. dia. x 40 ft. long vessel for H_2+0_2 mixture with spark ignition. Initial pressure 200 mmHg, initial temperature 70°F. Initiation of detonation behind reflected shock wave.

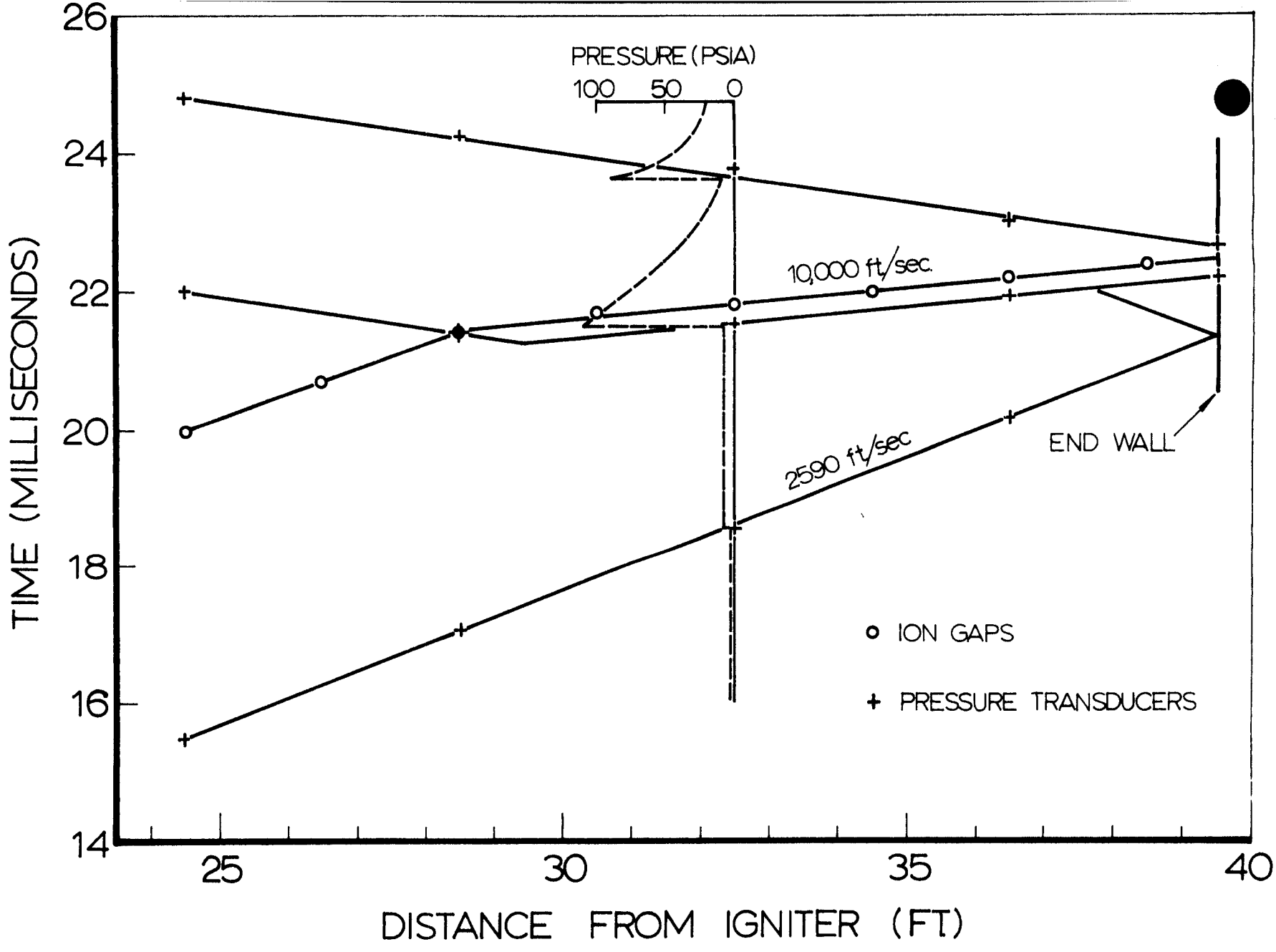

Fig. 138 Space-time diagram with superimposed pressure record of wave interaction pattern in the 2 ft. dia. x 40 ft. long vessel for H_2+0_2 mixture with spark ignition. Initial pressure 200 mmHg, initial temperature 70°F. Initiation of detonation behind precursor shock wave.

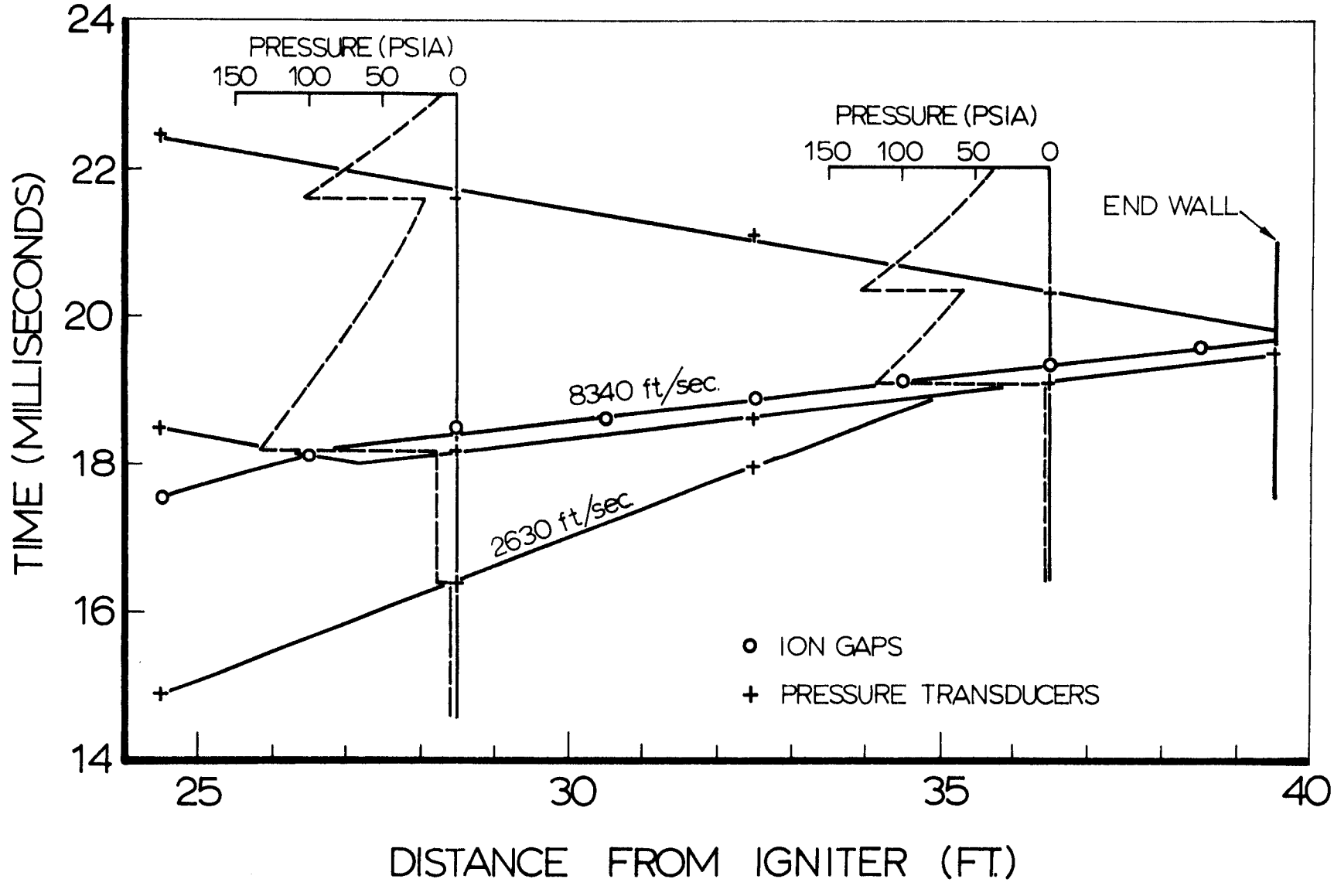

Fig. 139 Space-time diagram with superimposed pressure record of wave interaction pattern in the 2 ft. dia. x 40 ft. long vessel for H_2+0_2 mixture with spark ignition. Initial pressure 250 mmHg, initial temperature 70°F. Initiation of detonation behind precursor shock wave.

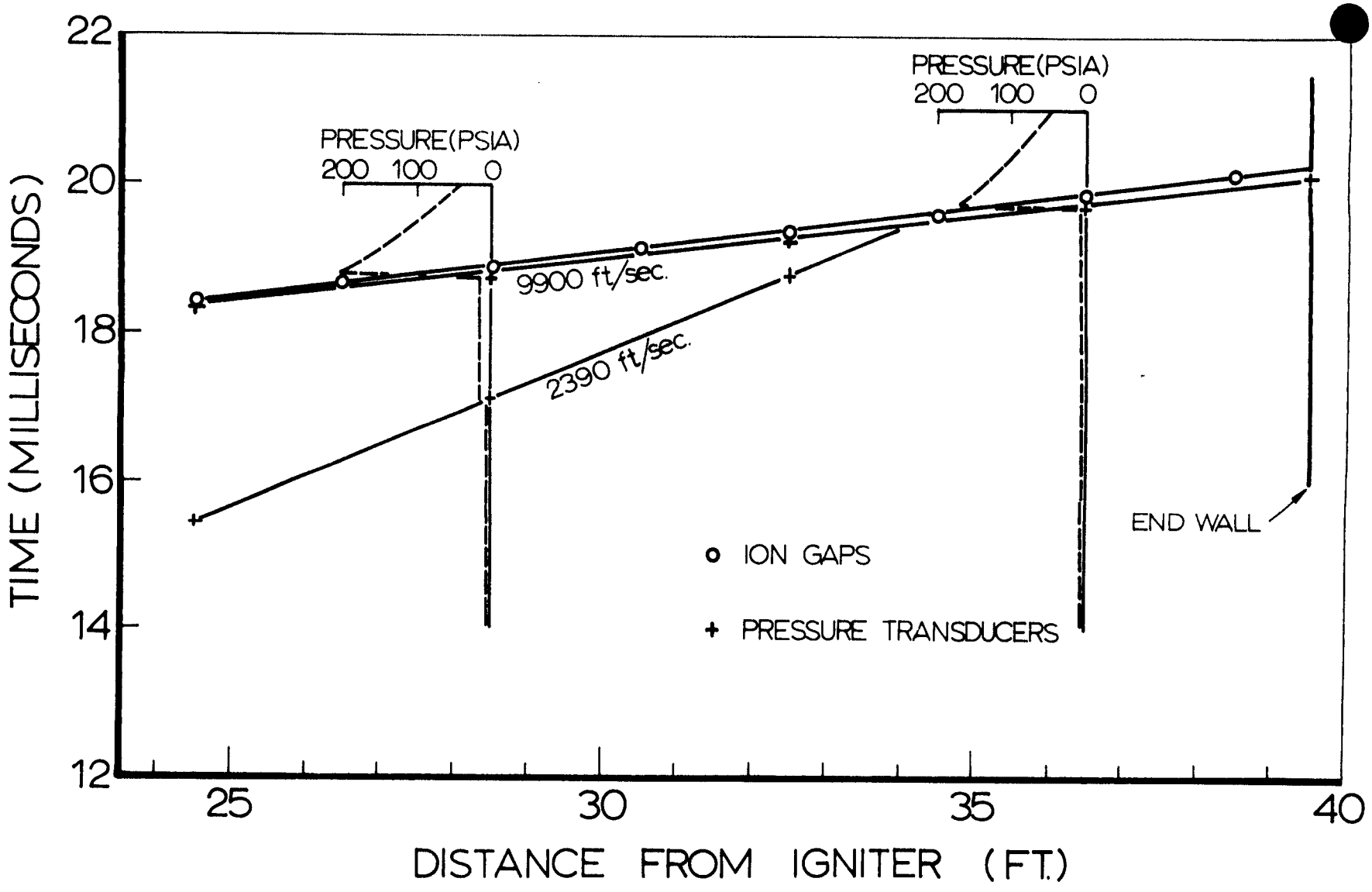

Fig. 140 Space-time diagram with superimposed pressure record of wave interaction pattern in the 2 ft. dia. x 40 ft. long vessel for H_2+O_2 mixture with spark ignition. Initial pressure 300 mmHg, initial temperature 70°F. Initiation of detonation behind precursor shock wave.

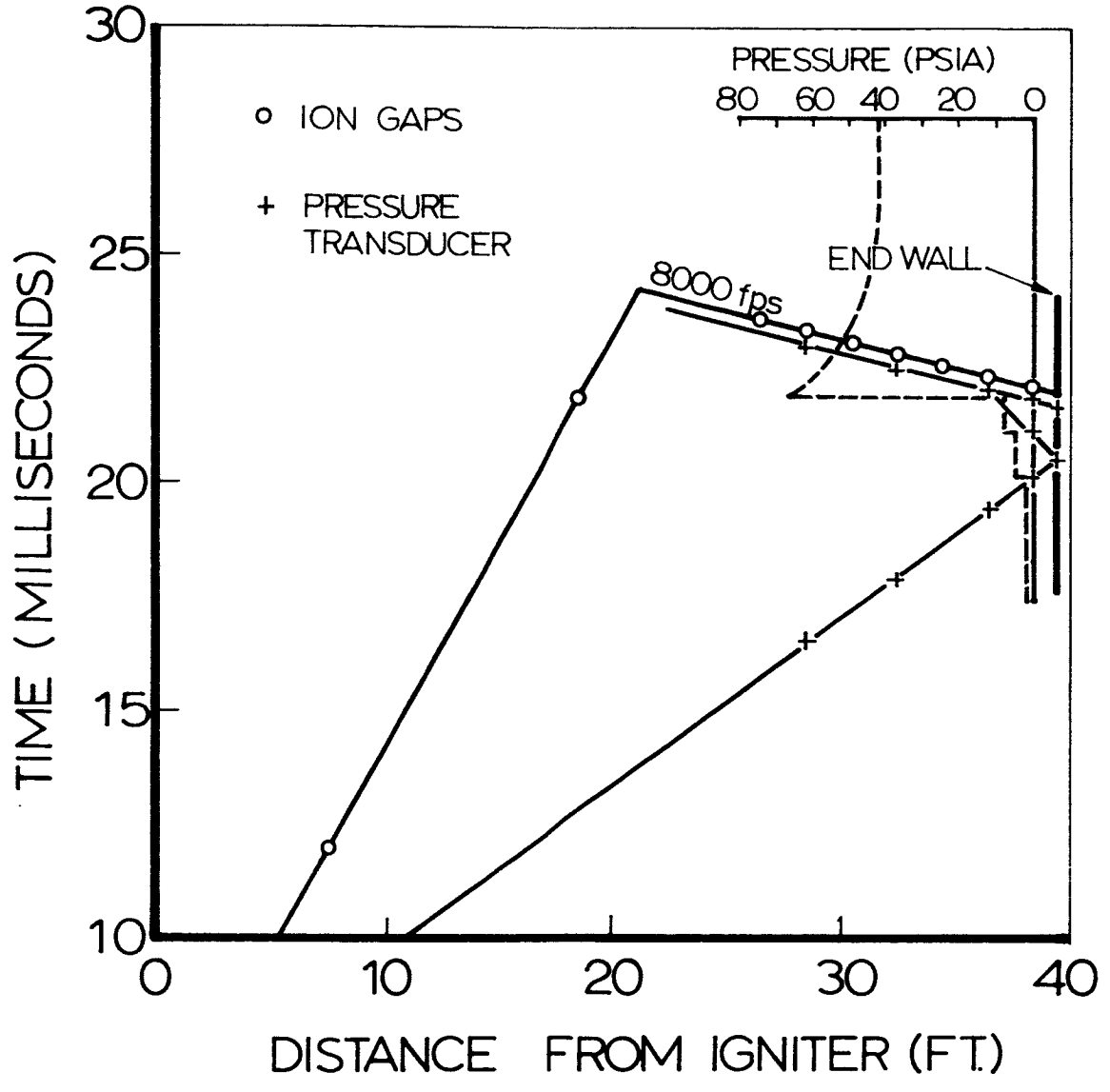

Fig. 141 Space-time diagram with superimposed pressure record of a wave interaction pattern in the 40 ft. vessel for $2H_2+0_2$ mixture with spark ignition. Initial pressure 100 mm Hg, initial temperature 70°F. Initiation of detonation behind reflected shock wave.

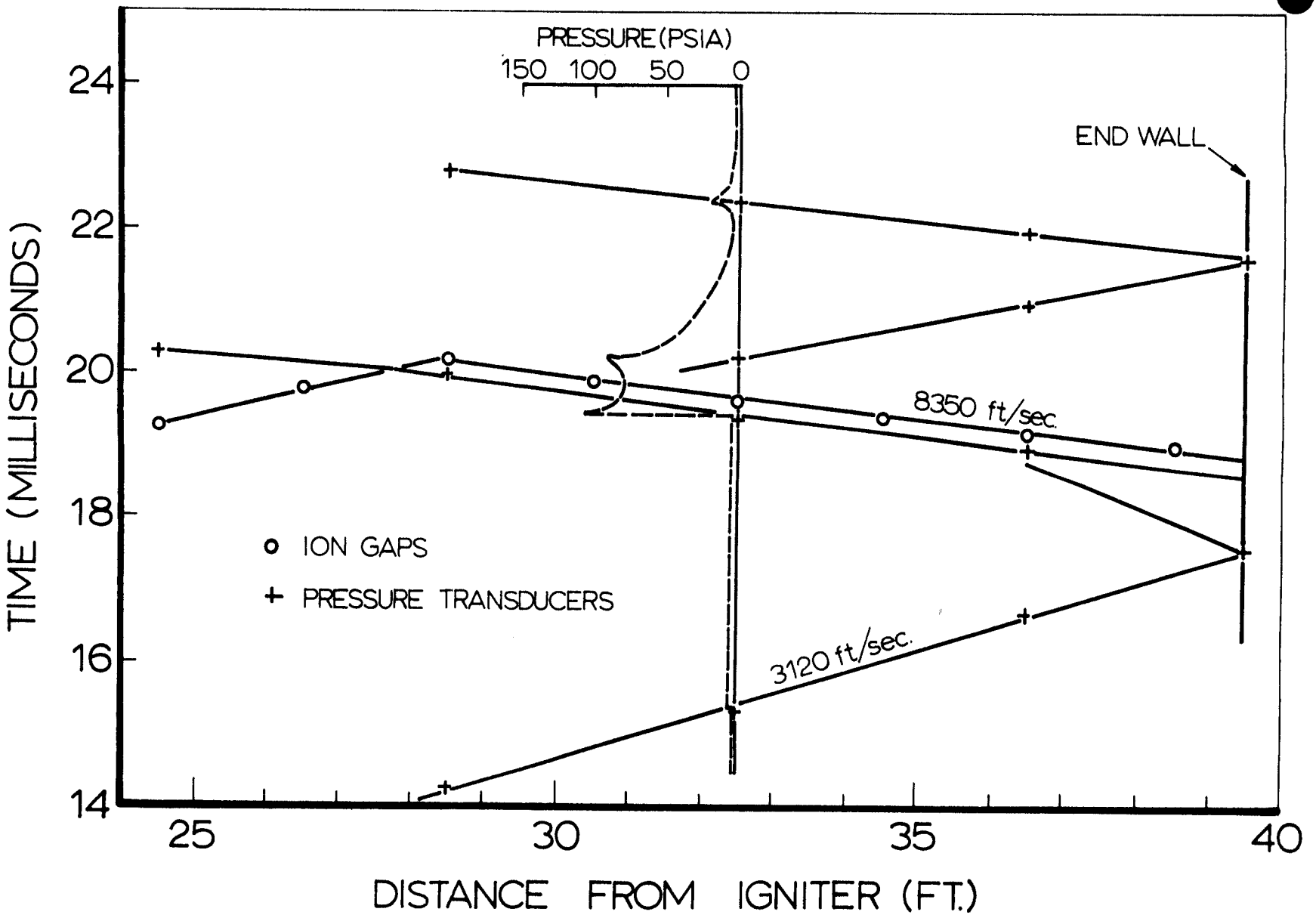

Fig. 142 Space-time diagram with superimposed pressure record of wave interaction pattern in the 2 ft. dia. x 40 ft. long vessel for $3H_2+O_2$ mixture with spark ignition. Initial pressure 200 mmHg, initial temperature 70°F. Initiation of detonation behind reflected shock wave.

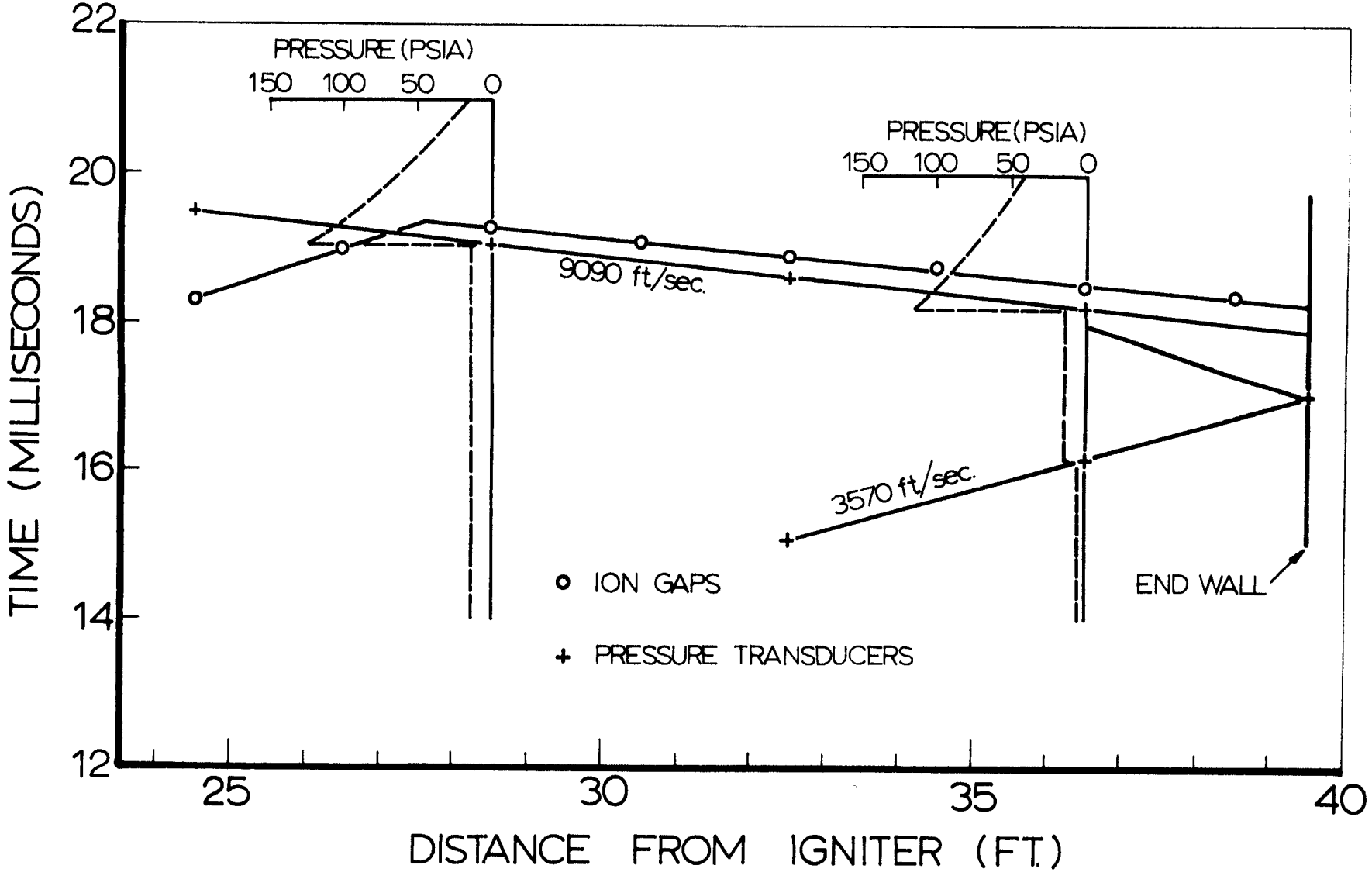

Fig. 143 Space-time diagram with superimposed pressure record of wave interaction pattern in the 2 ft. dia. x 40 ft. long vessel for $3H_2+O_2$ mixture with spark ignition. Initial pressure 250 mmHg, initial temperature 70°F. Initiation of detonation behind reflected shock wave.

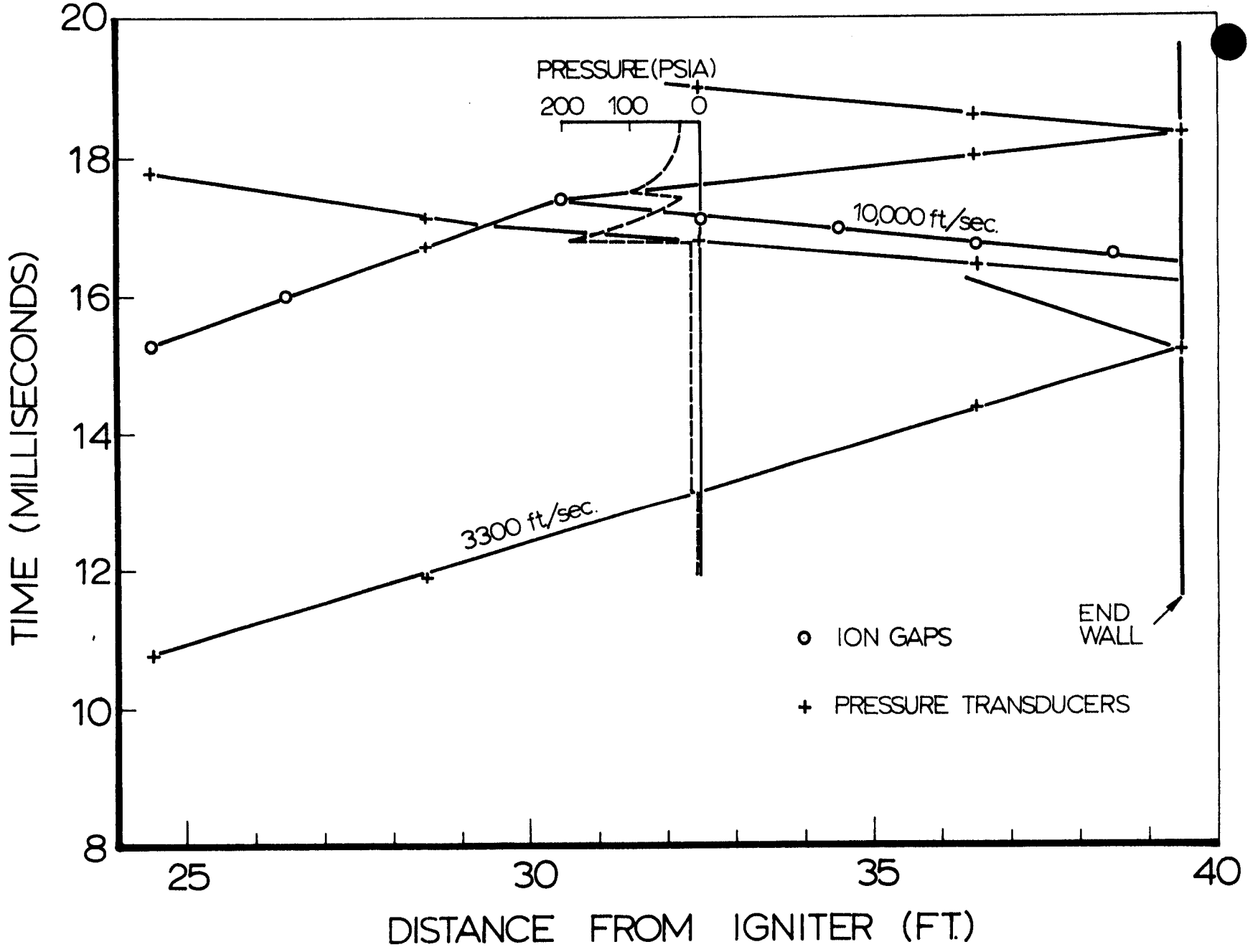

Fig. 144 Space-time diagram with superimposed pressure record of wave interaction pattern in the 2 ft. dia. x 40 ft. long vessel for $3H_2+0_2$ mixture with spark ignition. Initial pressure 300 mmHg, initial temperature 70°F. Initiation of detonation behind reflected shock wave.

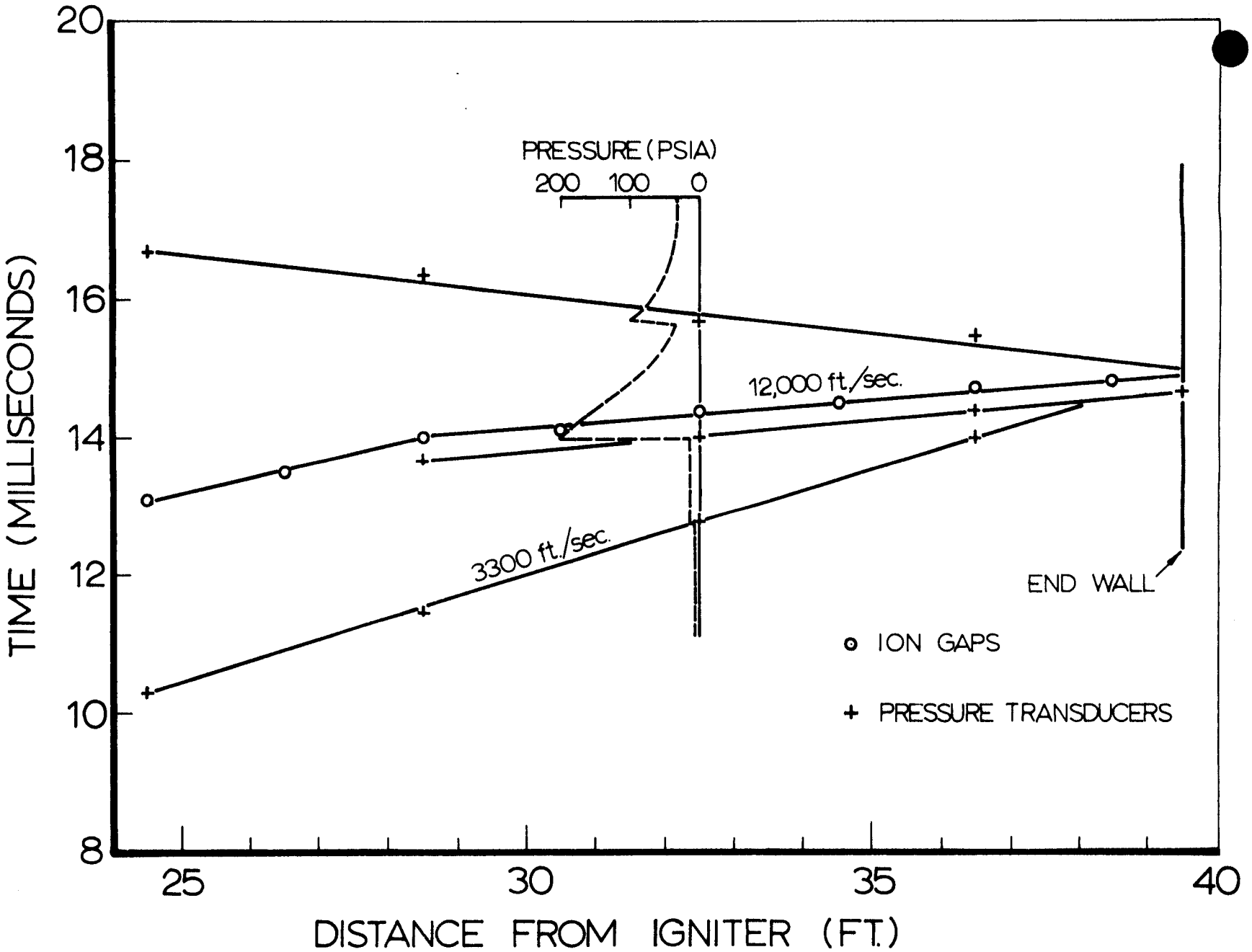

Fig. 145 Space-time diagram with superimposed pressure record of wave interaction pattern in the 2 ft. dia. x 40 ft. long vessel for $3H_2+O_2$ mixture with spark ignition. Initial pressure 300 mmHg, initial temperature 70°F. Initiation of detonation behind precursor shock.

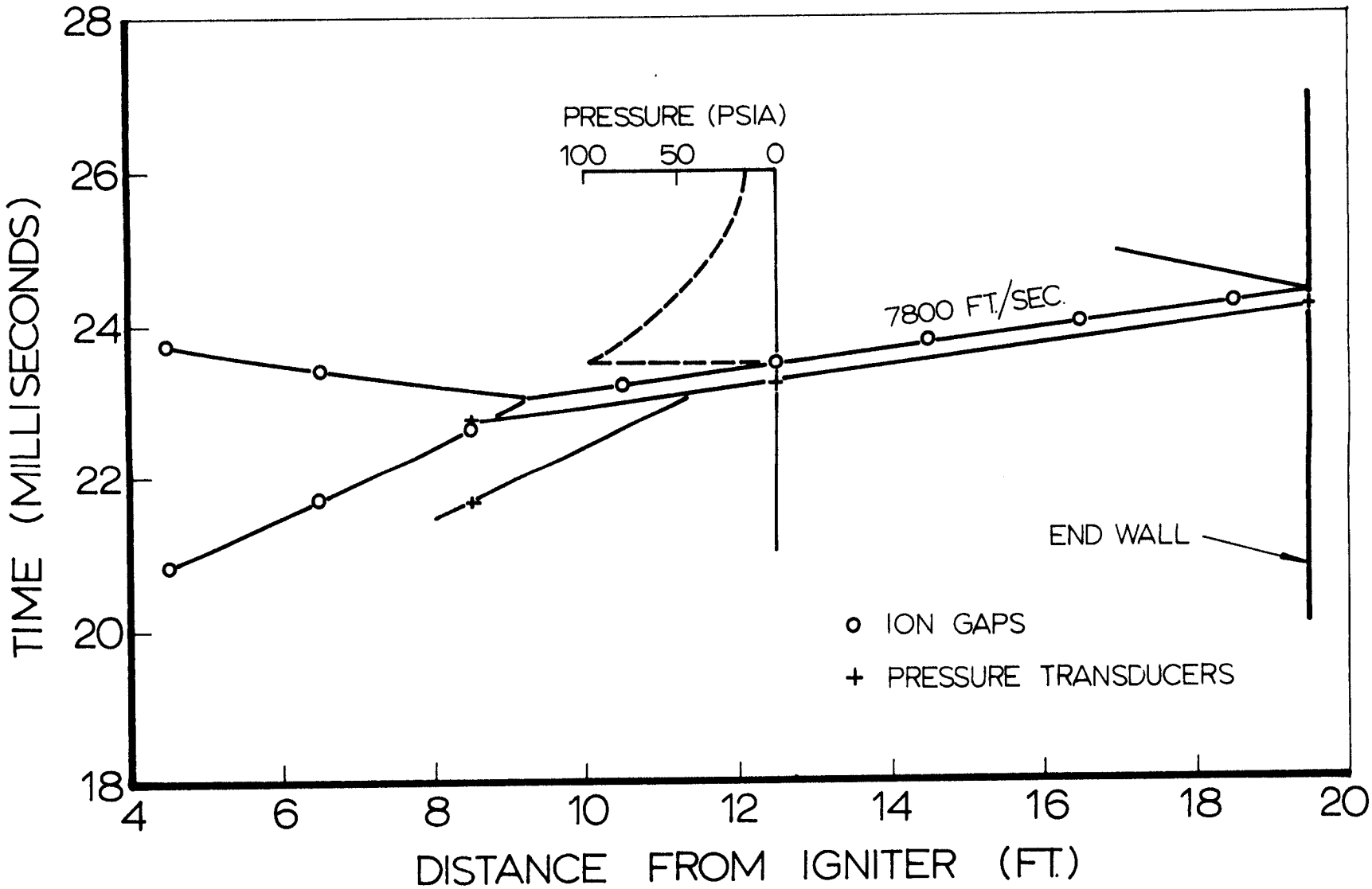

Fig. 146 Space-time diagram with superimposed pressure record of a wave interaction pattern in the 2 ft. dia. x 20 ft. long vessel for H_2+0_2 mixture with spark ignition. Initial pressure 100mmHg, initial temperature -180°F. Initiation of detonation behind precursor shock.

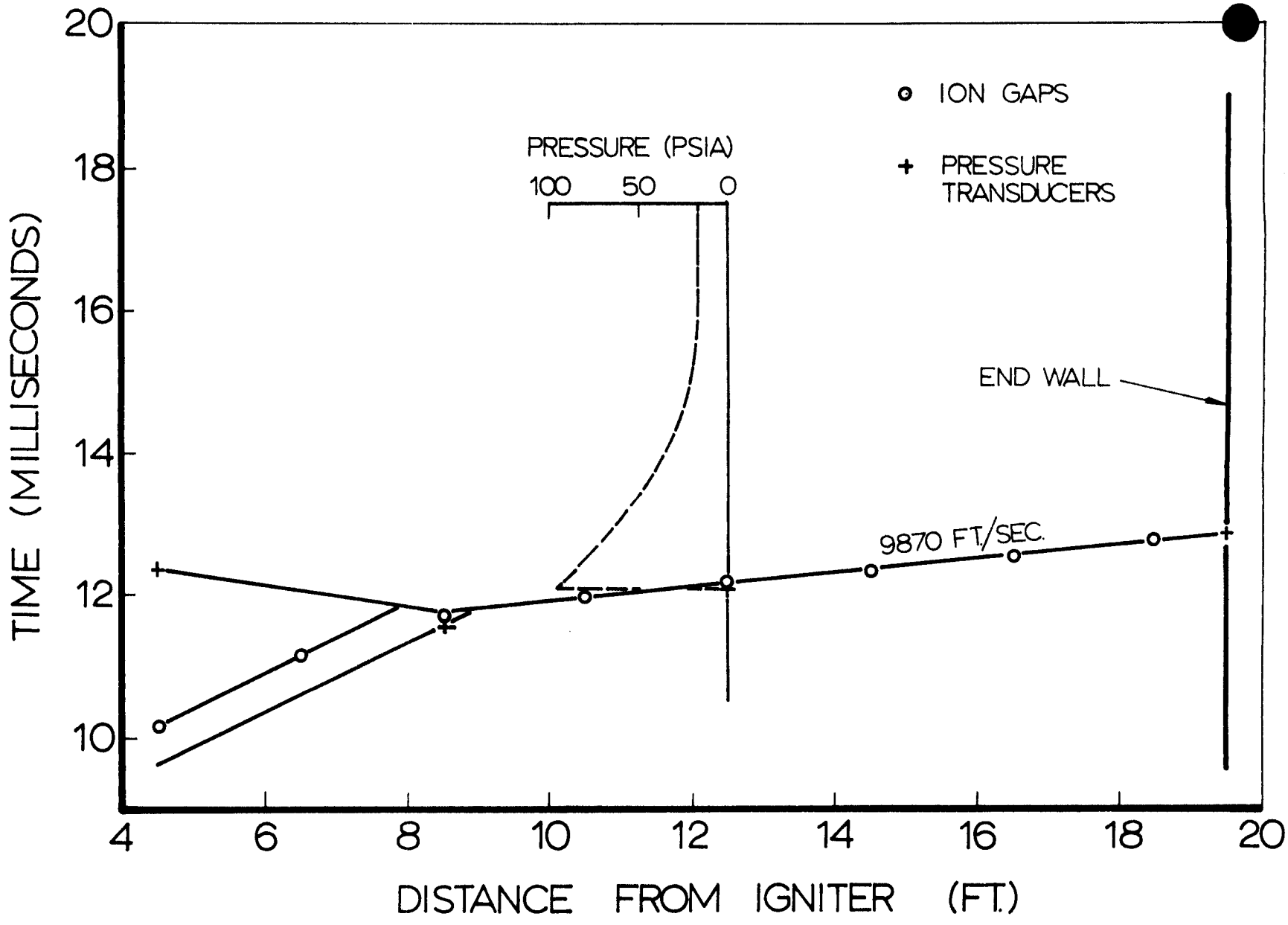

Fig. 147 Space-time diagram with superimposed pressure record of a wave interaction pattern in the 2 ft. dia. x 20 ft. long vessel for $2H_2+0_2$ mixture with spark ignition. Initial pressure 100 mmHg, initial temperature -180°F. Initiation of detonation behind precursor shock.

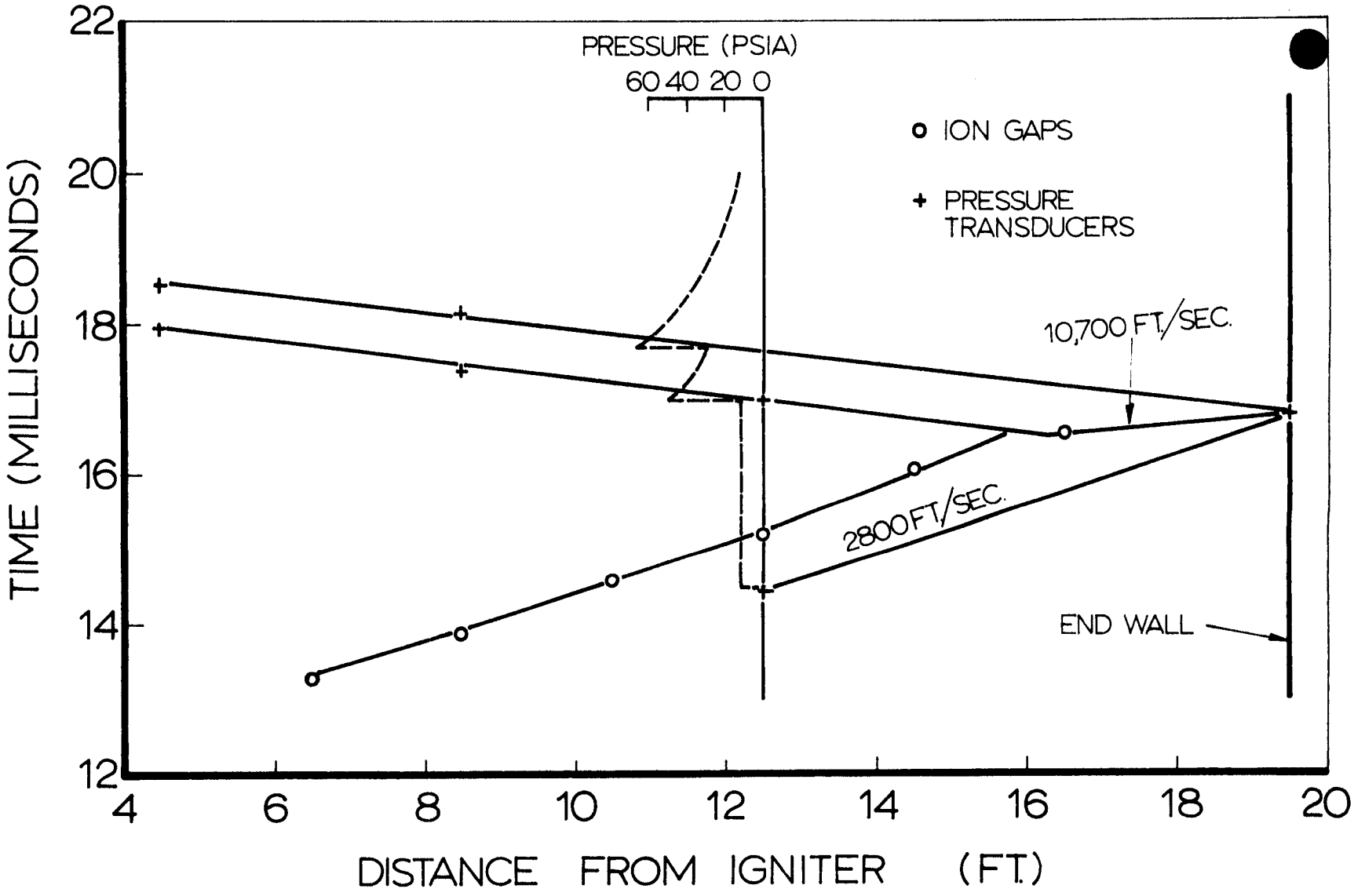

Fig.148 Space-time diagram with superimposed pressure record of a wave interaction pattern in the 2 ft. dia. x 20 ft. long vessel for $3H_2+0_2$ mixture with spark ignition. Initial pressure 100mmHg, initial temperature -180°F. Initiation of detonation behind precursor shock.

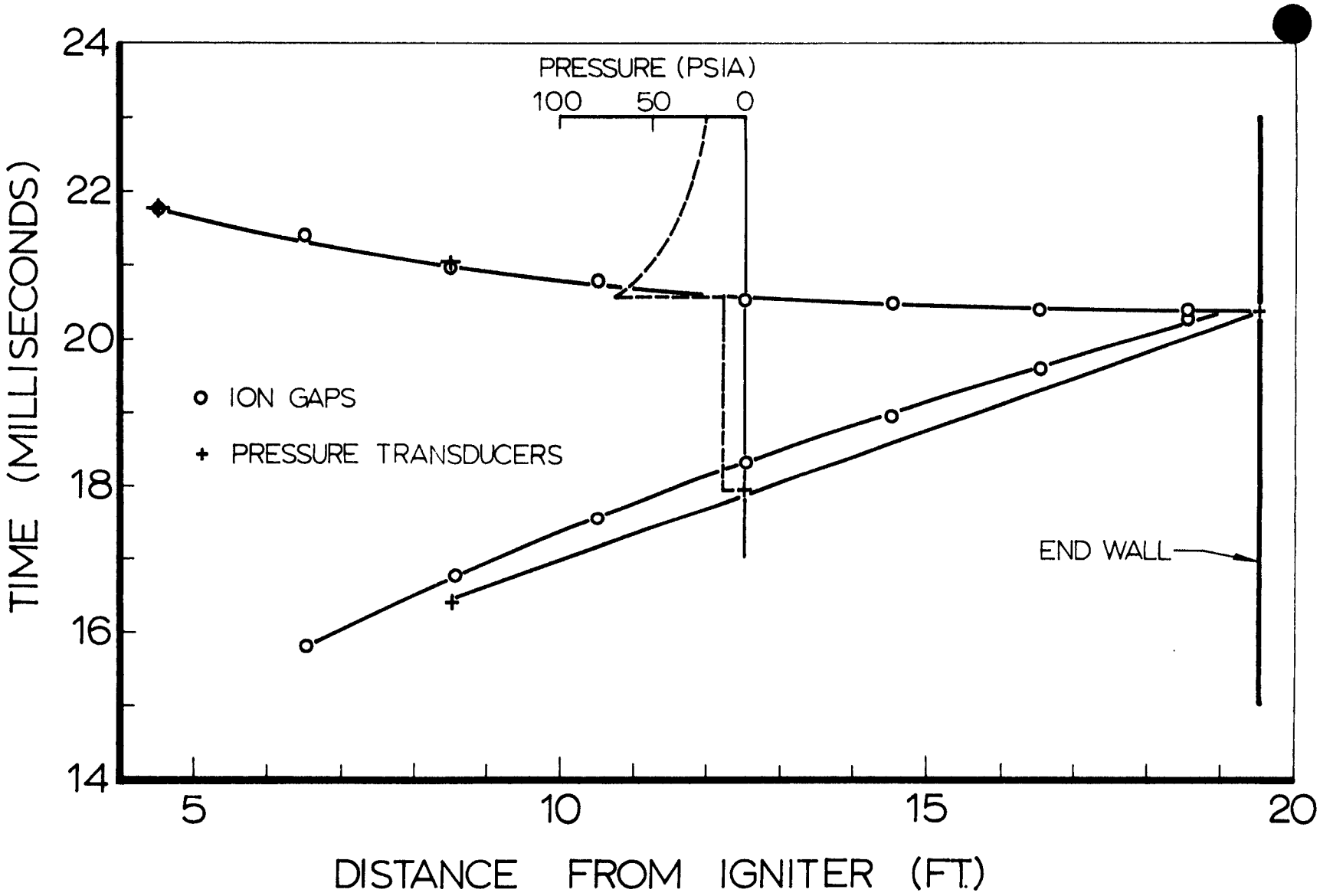

Fig.149 Space-time diagram with superimposed pressure record of a wave interaction pattern in the 2 ft. dia. x 20 ft. long vessel for $3H_2+O_2$ mixture with spark ignition. Initial pressure 100mmHg, initial temperature -260°F.

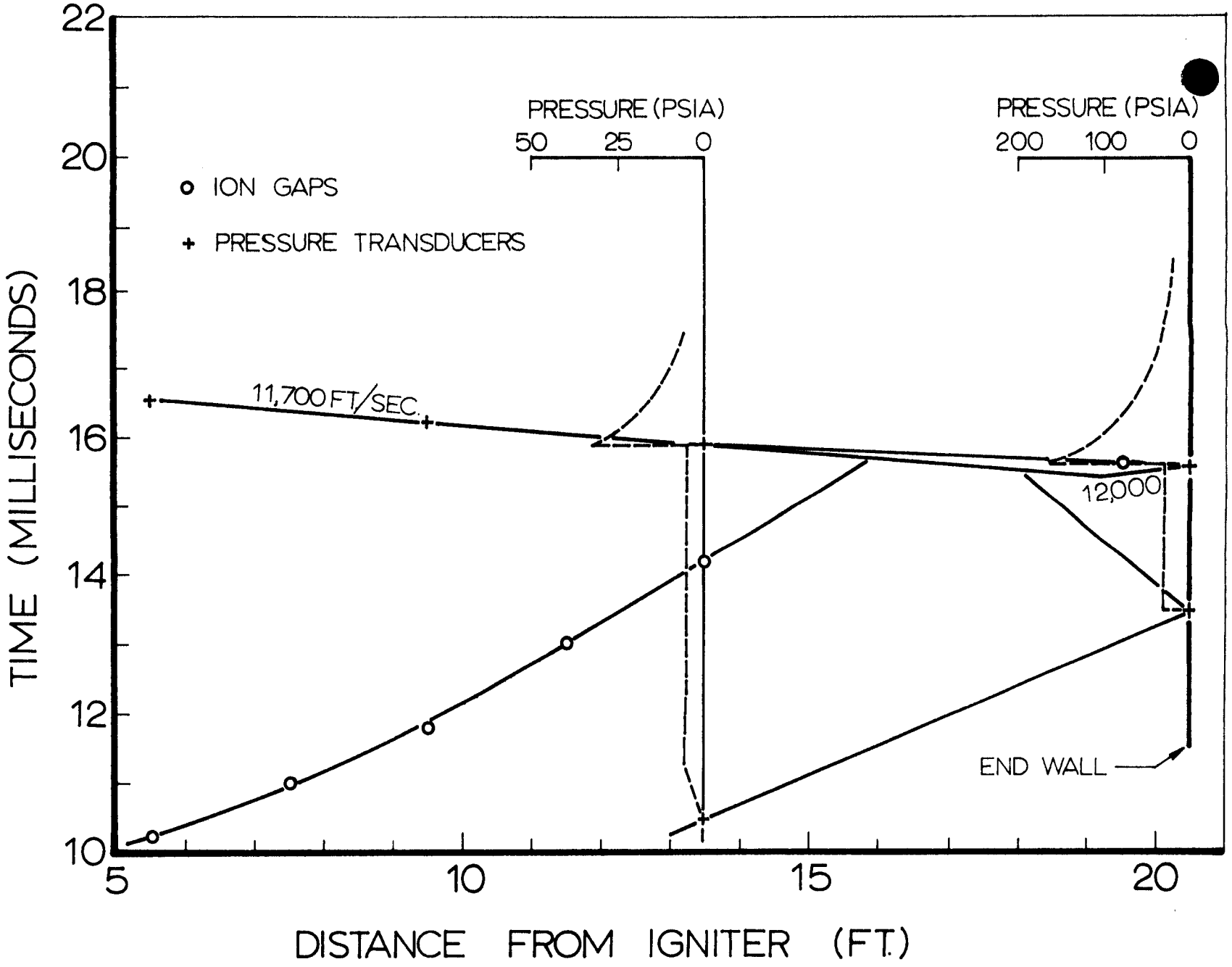

Fig. 150 Space-time diagram with superimposed pressure records of a wave interaction pattern in the 2 ft. dia. x 20 ft. long vessel for $3H_2+O_2$ mixture with spark ignition. Initial pressure 100mmHg, initial temperature -50°F.

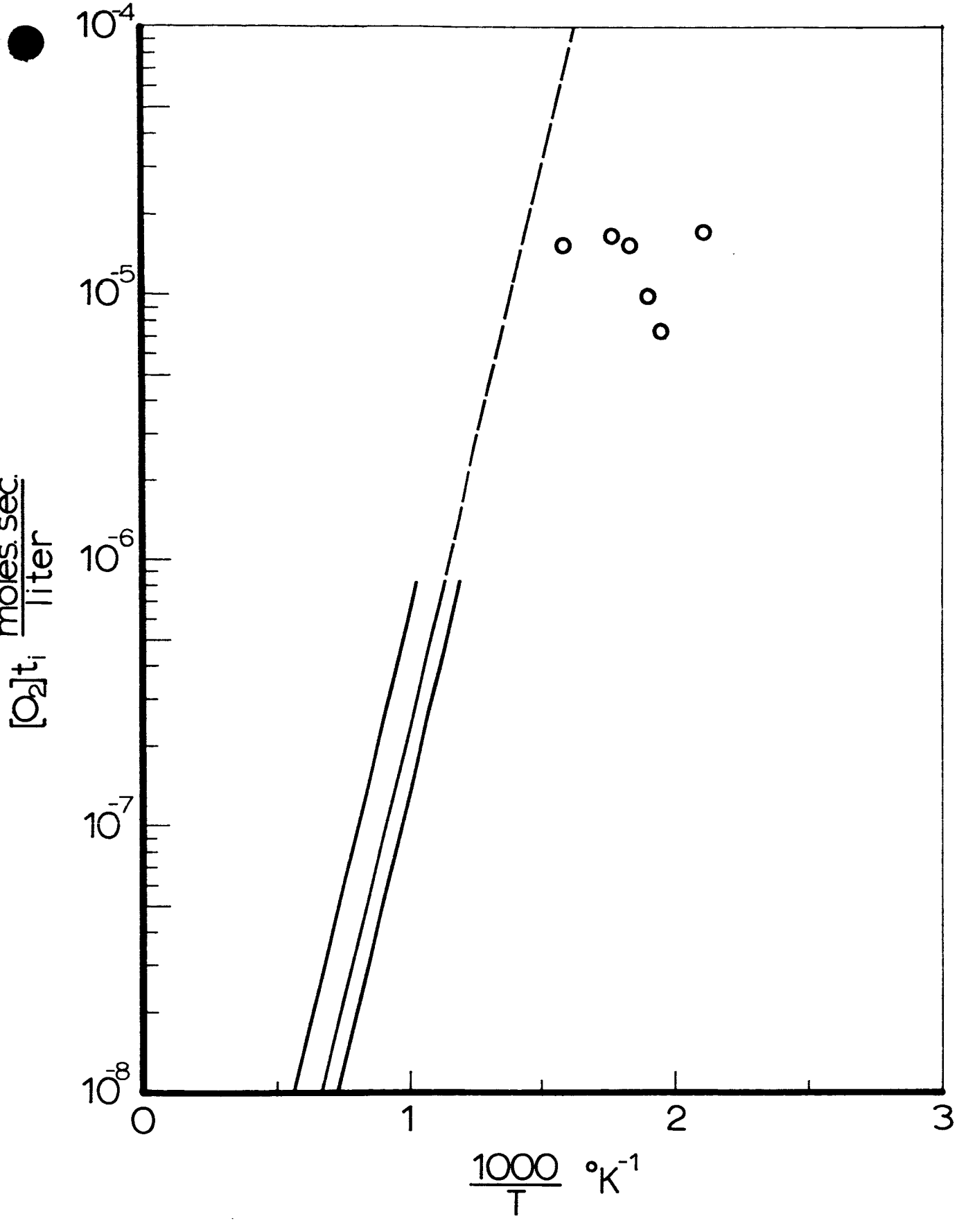

Fig. 151 Product of oxygen concentration and ignition delay time plotted as a function of inverse temperature. Band in lower left hand corner represents data of references 10 and 11.